

IRE Transactions



on ANTENNAS and PROPAGATION

Volume AP-8

NOVEMBER, 1960

Number 6

Published Bimonthly

In This Issue

A Theoretical Analysis of Semi-Infinite Conical Antennas

Electrical Performance of Rigid Ground Radomes

Logarithmically Periodic Antenna

Distribution Functions for Monopulse Antenna Difference Patterns

Radiation from a Tapered Surface Wave Antenna

Near-Field Gain of Aperture Antennas

Duration of Fades in Tropospheric Scatter Transmissions

Fock Approximation for Conducting Cylinders

Frequency Spectra of Transient Electromagnetic Pulses

Reflection Factor of Gradual-Transition Absorbers

A New Sporadic Layer Providing VLF Propagation

PUBLISHED BY THE

Professional Group on Antennas and Propagation

contributions

A Theoretical Analysis of Semi-Infinite Conical Antennas*

S. ADACHI†, MEMBER, IRE

Summary—A theoretical analysis of an antenna consisting of a perfectly conducting semi-infinite cone excited by a thin, linear element directed along its axis is presented. Two different methods are applied; one is a Green's function method, and the other is a mode theory. By the former method, the radiation characteristics of very thin and wide-angle cones excited by a sinusoidal current element are obtained. In the latter method, the linear element at the tip is replaced by a finite cone resulting in a semi-infinite, biconical structure. The variational principle is applied to determine the effective terminating admittance, and thus the input impedance, and the far-zone field. A guided wave which propagates longitudinally on the semi-infinite cone is identified and its properties are discussed.

I. INTRODUCTION

A THEORETICAL analysis is made of an antenna consisting of a perfectly conducting semi-infinite cone excited at its tip by a thin, linear antenna. The physical configuration is illustrated in Fig. 1. The radiation and impedance properties of this structure are of practical interest in cases where a linear antenna is placed at the tip of a missile or aircraft, on the top of a hill or tower, or where a linear antenna is fed by a colinear, coaxial cable (a limiting case of zero cone angle). It is not easy to complete the analysis to the

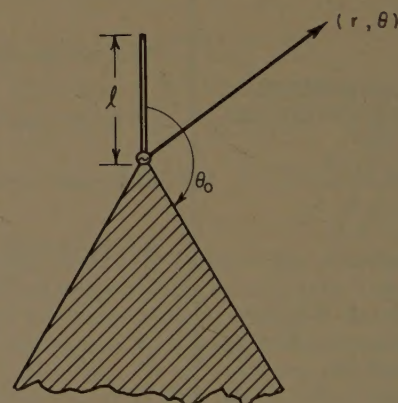


Fig. 1—The semi-infinite conical antenna.

point where numerical results are feasible for infinite cones of arbitrary cone angles; however, the work is greatly simplified for wide-angle or very narrow-angle cones. In this paper the general solution is first obtained and then the cases of the narrow-angle and the wide-angle cones are considered in detail. A problem related to the one being considered here, the radiation from an axially-symmetric circumferential slot close to the tip of a semi-infinite perfectly conducting cone, has been treated by Bailin and Silver.¹

* Received by the PGAP, November 13, 1959; revised manuscript received, April 21, 1960. The research reported in this paper was sponsored in part by U. S. Army Signal Corps, under Contract DA 36(039)sc-70174.

† Antenna Lab., Ohio State University, Columbus 10, Ohio, on leave of absence from Tohoku University, Sendai, Japan.

¹ L. L. Bailin and S. Silver, "Exterior electromagnetic boundary value problems for spheres and cones," IRE TRANS. ON ANTENNAS AND PROPAGATION, vol. AP-H, pp. 5-16; January, 1956.

In Section II the radiation characteristics of a thin, linear antenna placed at the tip of an semi-infinite cone are analyzed using a special Green's function constructed so that it vanishes on the surface of the cone. A sinusoidal current distribution is assumed for the thin, linear antenna. Consequently, in this formulation of the problem the conical surface is considered more as a boundary of the region of radiation than as an integral part of the antenna. The radiation resistance and far-zone field are derived for very narrow-angle and wide-angle cones.

In Section III the linear element at the tip of the semi-infinite cone is replaced by a finite cone as shown in Fig. 6. The fields of this semi-infinite biconical antenna are expressed in terms of appropriate summations of characteristic wave functions. Then, using a variational method in a manner similar to that employed by Tai² in the biconical antenna problem, the input impedance and far-zone field are determined. The case of very narrow cone angles is treated in detail and numerical results are given for both the input impedance and far-zone field.

A guided wave which propagates longitudinally on the semi-infinite conical surface is identified and its properties are discussed. A comparison is made between the power transmitted in this wave and the power in the radiation field.

II. THE RADIATION FROM A THIN, LINEAR ANTENNA AT THE TIP OF A PERFECTLY CONDUCTING CONE

In this section the radiation from a thin linear antenna placed at the tip of a perfectly conducting semi-infinite cone and directed parallel to the symmetry axis of the cone is analyzed (see Fig. 1). The current distribution on the thin, linear antenna is assumed to be sinusoidal, and the boundary conditions at the surface of the cone are met by using a special Green's function given by Felsen.³

A. General Formulation

The electromagnetic field of a dipole positioned so that there is axial symmetry can be derived from a single scalar potential. Let \bar{r}' be the position vector of the dipole and \bar{r} the position vector of the field point; then the axially symmetric solution of the inhomogeneous equation

$$(\nabla^2 + \beta^2)G(\bar{r}, \bar{r}') = -\delta(\bar{r} - \bar{r}'), \quad (1)$$

with the conditions

$$\left. \begin{aligned} G \text{ is finite at } r = 0, \\ r \left(\frac{\partial G}{\partial r} + j\beta G \right) \rightarrow 0 \text{ at } r \rightarrow \infty, \\ G = 0 \text{ at } \theta = \theta_0, \end{aligned} \right\} \quad (2)$$

is given by the expression

$$G(r, r', \theta) = \frac{j}{4\beta r r'} \sum_q (2q + 1) \frac{P_q(\cos \theta) P_q(-\cos \theta_0)}{\sin q\pi \frac{\partial}{\partial q} P_q(\cos \theta_0)} \times j_q(\beta r_<) \hat{h}_q^{(2)}(\beta r_>), \quad (3)$$

where

$$r_< = \begin{cases} r & \text{if } r < r' \\ r' & \text{if } r > r' \end{cases} \quad r_> = \begin{cases} r' & \text{if } r < r' \\ r & \text{if } r > r' \end{cases}.$$

The $j_q(x)$ and $\hat{h}_q^{(2)}(x)$ are spherical Bessel functions defined as follows:

$$j_q(x) = \sqrt{\frac{\pi x}{2}} J_{q+1/2}(x), \quad \hat{h}_q^{(2)}(x) = \sqrt{\frac{\pi x}{2}} H_{q+1/2}^{(2)}(x),$$

and the q is determined from

$$P_q(\cos \theta_0) = 0. \quad (4)$$

The electromagnetic field of an electric current dipole $I dr'$ (I is the current amplitude) at $r', \theta' = 0$, is given in terms of the above Green's function as

$$\left. \begin{aligned} d\bar{E}(\bar{r}, \bar{r}') &= \frac{I dr'}{j\omega\epsilon_0 r'} \nabla \times \nabla \times \bar{r}_0 \{rG(\bar{r}, \bar{r}')\}, \\ d\bar{H}(\bar{r}, \bar{r}') &= \frac{I dr'}{r'} \nabla \times \bar{r}_0 \{rG(\bar{r}, \bar{r}')\}, \end{aligned} \right\} \quad (5)$$

where \bar{r}_0 is a unit radial vector.

For the far field, the following approximation can be made:

$$\begin{aligned} \nabla \times \nabla \times \bar{r}_0[rG] &\simeq \frac{1}{r} \frac{\partial^2}{\partial r \partial \theta} [rG] \bar{\theta}_0, \\ \frac{1}{\beta} \frac{\partial \hat{h}_q^{(2)}(\beta r)}{\partial r} &\approx e^{-j\beta r} e^{j(\pi/2)q}. \end{aligned}$$

Consequently, the far-zone electric field of the linear current distribution is obtained by integrating (5) with respect to r' over the whole current distribution.

$$E_\theta(r, \theta) = \frac{\eta I_0}{4} \frac{e^{-j\beta r}}{r} \sum_q (2q + 1) e^{j(\pi/2)q} S_q(\beta l) \frac{P_q(-\cos \theta_0)}{\sin q\pi \frac{\partial}{\partial q} P_q(\cos \theta_0)} \frac{\partial P_q(\cos \theta)}{\partial \theta}, \quad (6)$$

where

$$S_q(\beta l) = \frac{1}{\beta I_0} \int_0^l \frac{I(r')}{r'^2} j_q(\beta r') dr', \quad (7)$$

and

$$\eta = \sqrt{\frac{\mu_0}{\epsilon_0}}.$$

² C. T. Tai, "Application of the variational principle to biconical antennas," *J. Appl. Phys.*, vol. 20, pp. 1076-1085; November, 1949.

³ L. B. Felsen, "Back-scattering from wide angle and narrow angle cones," *J. Appl. Phys.*, vol. 26, pp. 138-151; February, 1955.

Introducing the approximate current distribution for the thin, linear antenna,

$$I(r') = I_0 \sin \beta(l - r') \quad (8)$$

where I_0 is a sinusoidal current amplitude, or the current at a point $\lambda/4$ from the end of the antenna,

$$S_q(\beta l) = \sin \beta l \int_0^{\beta l} \frac{\cos x}{x^2} \hat{j}_q(x) dx - \cos \beta l \int_0^{\beta l} \frac{\sin x}{x^2} \hat{j}_q(x) dx \quad \text{for } q > 0. \quad (9)$$

Appendix I gives the result of the above integration in terms of spherical Bessel functions. When βl is $(\pi/2)i$, $i = 1, 2, \dots$, $S_q(\beta l)$ is given simply by

$$S_q\left(\frac{\pi}{2}i\right) = \frac{\hat{j}_q\left(\frac{\pi}{2}i\right)}{q(q+1)} \quad q > 0. \quad (10)$$

Using the orthogonality relationship

$$\int_0^{\theta_0} \sin \theta \frac{\partial P_q(\cos \theta)}{\partial \theta} \frac{\partial P_r(\cos \theta)}{\partial \theta} d\theta = \begin{cases} 0, & r \neq q \\ -\sin^2 \theta_0 \frac{q(q+1)}{2q+1} \left[\frac{\partial P_q}{\partial q} \frac{\partial P_q}{\partial x} \right]_{x=\cos \theta_0, q=r}. \end{cases} \quad (11)$$

The radiation resistance with reference to the input current is given by

$$R = \frac{\pi \eta}{8} \frac{\sin^2 \theta_0}{\sin^2 \beta l} \sum_q q(q+1)(2q+1) \left\{ \frac{S_q(\beta l) P_q(-\cos \theta_0)}{\sin q\pi \frac{\partial}{\partial q} P_q(\cos \theta_0)} \right\}^2 \times \left[-\frac{\partial P_q}{\partial q} \frac{\partial P_q}{\partial x} \right]_{x=\cos \theta_0}. \quad (12)$$

B. Narrow-Angle Cones

For a narrow-angle cone, *i.e.*, $\theta_0 \approx \pi$, the eigenvalue q satisfying (4) is approximately given by

$$q \approx n + \frac{1}{2 \ln \frac{2}{\pi - \theta_0}} + 0 \left\{ \left(\ln \frac{2}{\pi - \theta_0} \right)^{-3} \right\} \quad n = 0, 1, 2, 3, \dots \quad (13)$$

and the following expressions are obtained:

$$\frac{P_q(-\cos \theta_0)}{\sin q\pi \frac{\partial}{\partial q} P_q(\cos \theta_0)} \approx \frac{1 - q(q+1) \frac{(\pi - \theta_0)^2}{4}}{\sin 2q\pi \ln \frac{\pi - \theta_0}{2}} = -\frac{1}{\pi}, \quad \theta_0 = \pi, \quad (14)$$

$$-\sin^2 \theta_0 \left[\frac{\partial P_q}{\partial q} \frac{\partial P_q}{\partial x} \right]_{x=\cos \theta_0} \approx 2 + 0 \left(\ln \frac{1}{\pi - \theta_0} \right)^{-2} \quad \theta_0 \approx \pi. \quad (15)$$

Consequently the far-field and the radiation resistance for a narrow-angle cone are approximated by

$$E_\theta(r, \theta) \approx \frac{\eta I_0}{4 \ln \frac{\pi - \theta_0}{2}} \frac{e^{-j\beta r}}{r} \sum_q \frac{(2q+1) \left\{ 1 - q(q+1) \frac{(\pi - \theta_0)^2}{4} \right\}}{\sin 2q\pi} \cdot e^{j(\pi/2)q} \times S_q(\beta l) \frac{\partial P_q(\cos \theta)}{\partial \theta} \quad (16)$$

$$R \approx \frac{\pi \eta}{4 \sin^2 \beta l \left(\ln \frac{\pi - \theta_0}{2} \right)^2} \sum_q \frac{q(q+1)(2q+1)}{\sin^2 2q\pi} \cdot \left\{ 1 - q(q+1) \frac{(\pi - \theta_0)^2}{4} \right\}^2 S_q^2(\beta l). \quad (17)$$

A simplification is obtained, by considering the asymptotic behavior when $\theta_0 \rightarrow \pi$. In these expressions q may be replaced by the integer n .

1) Asymptotic Form for $\sin \beta l \neq 0$:

$$E_\theta(r, \theta) = \frac{-\eta I_0}{4\pi} \frac{e^{-j\beta r}}{r} \left[\sum_{n=1,2,\dots} (-1)^{n/2} (2n+1) S_n(\beta l) \frac{\partial P_n}{\partial \theta} - \sin \beta l \tan \frac{\theta}{2} \right] \quad \theta \leq \theta_0 \quad (18)$$

$$\approx \frac{\eta I_0}{2\pi} \frac{e^{-j\beta r}}{r} \frac{\sin \beta l}{\pi - \theta} \quad \theta(\leq \theta_0) \approx \pi \quad (19)$$

$$R = \frac{\eta}{4\pi} \left[\frac{1}{\sin^2 \beta l} \sum_{n=1,2,\dots} n(n+1)(2n+1) S_n^2(\beta l) + 2 \ln \frac{2}{\pi - \theta_0} \right]. \quad (20)$$

The electric field at $\theta = \theta_0$, the surface of the semi-infinite cone, and the radiation resistance diverge in the order of $(\pi - \theta_0)^{-1}$ and $(\ln 2/\pi - \theta_0)$, respectively, as θ_0 approaches π . Thus, infinite power is required to excite a finite current in the case of a vanishing cone angle and $\sin \beta l \neq 0$.

The second term in (18) is the lowest-order term in the infinite series representation of E_θ in (16); its summation index approaches zero. A physical interpretation of this term may be obtained by recalling that the lowest-order modes (the TEM modes) for the perfectly conducting biconical and cylindrical surfaces are the well-known guided waves, which propagate without attenuation. In the neighborhood of the transmission line these waves are guided along its surface and their

amplitudes are inversely proportional to the distance from the axis of the transmission line. The same properties are described by the second term in (18) and (19); hence this term may be associated with a wave guided along the semi-infinite conical surface. It should be noted that this wave cannot be referred to as a surface wave, because surface waves, as they are customarily defined, have phase velocities less than the free-space phase velocity, and expressions for their field components contain a factor which gives an exponential decay in the direction normal to the guiding surface.

2) *Asymptotic Form for $\sin \beta l = 0$, i.e., $l = i(\lambda/2)$ ($i = 1, 2, \dots$):*

$$E_{\theta}(r, \theta) = \frac{-\eta I_0}{4\pi} \frac{e^{-j\beta r}}{r} \sum_{n=1,2,\dots} (-1)^{n/2} \frac{2n+1}{n(n+1)} j_n(i\pi) \left[\frac{\partial P_n}{\partial \theta} - \frac{(-1)^n \tan \frac{\theta}{2}}{2 \ln \frac{2}{\pi - \theta_0}} \right] \quad \theta \leq \theta_0 \quad (21)$$

$$\approx \frac{\eta I_0}{4\pi(\pi - \theta) \ln \frac{2}{\pi - \theta_0}} \frac{e^{-j\beta r}}{r} \sum_{n=1,2,\dots} (-1)^{n/2} \frac{2n+1}{n(n+1)} j_n(i\pi) \quad \theta(\leq \theta_0) \approx \pi. \quad (22)$$

The electric field at the surface of the cone diverges in the order of $[(\pi - \theta_0) \ln 2/(\pi - \theta_0)]^{-1}$ as θ_0 approaches π ; this is a slower divergence than was encountered in the previous case. The electric field patterns have been calculated for $l = \lambda/2$, $\theta_0 = 179^\circ$; 179.9° and are plotted in Fig. 2. Despite the rapid increase in E_{θ} near the surface of the cone, the power guided along the surface of the infinitely thin cone is zero in this case, so that there is no excitation of a transmission-line wave. A similar result is obtained for the asymmetrically fed linear antenna.⁴ When one of the two linear elements is equal to an integral number of half wavelengths, the current in the other element is a minimum. This phenomenon has also been noted by Butterfield⁵ in connection with antennas placed at the tips of missiles or aircraft.

The radiation resistance referred to the input terminals is infinite because the assumed current is zero at these terminals when $\beta l = i\pi$. The difficulty can be overcome by referring the radiation resistance to the point of maximum current instead of the input terminals. This definition of radiation resistance is frequently used for the very thin, linear antenna, where

⁴ C. T. Tai, "Asymmetrically-Fed Antennas," Stanford Res. Inst., Menlo Park, Calif., Rept. No. 2, SRI Project No. 188, Contract No. AF 19(122)78; 1949.

⁵ F. E. Butterfield, "Aircraft telemetry antenna," IRE TRANS. ON ANTENNAS AND PROPAGATION, vol. AP-5, p. 143; January, 1957.

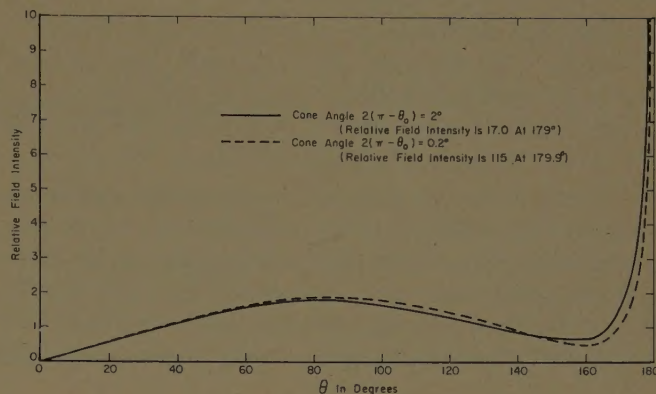


Fig. 2—Radiation patterns of thin, semi-infinite conical antennas.

the same problem arises. Thus,

$$R_0 \approx \frac{\eta}{4\pi} \sum_q q(q+1)(2q+1) S_q^2(i\pi), \quad \theta_0 \approx \pi \quad (23)$$

$$= \frac{\eta}{4\pi} \sum_{n=1,2,\dots} \frac{2n+1}{n(n+1)} j_n^2(i\pi), \quad \theta_0 \rightarrow \pi. \quad (24)$$

This expression is identical with that obtained for a very thin, linear antenna with the same current distribution. For example, $R_0 = 73.13$ ohms when $i = 1$. The result is not surprising, because both antennas have identical current distributions on the linear element, and the current on the semi-infinite cone is zero as $\theta_0 \rightarrow \pi$. Note that the current on the conical surface is

$$j \frac{2\pi(\pi - \theta_0)}{\omega\mu} \frac{\partial}{\partial r} (rE_{\theta}),$$

where E_{θ} is given by (22).

C. Wide-Angle Cones⁶

In order to obtain the eigenvalues q for wide-angle cones in an approximate, but analytical form, Legendre function $P_q(\cos \theta)$ is represented by trigonometric functions in the neighborhood of 90° . When θ_0 is not too near 0 or π , and $q \gg 1$, $P_q(\cos \theta_0)$ can be expressed, approximately, by⁷

$$P_q(\cos \theta_0) \approx \frac{\cos \left[\left(q + \frac{1}{2} \right) \theta_0 - \frac{\pi}{4} \right]}{\sqrt{\frac{1}{2} q \pi \sin \theta_0}} = 0. \quad (25)$$

⁶ S. Adachi, "A Theoretical Analysis of Infinite Conical Antennas—Part II," Antenna Lab., The Ohio State University Res. Foundation, Columbus, Rept. No. 622-32, prepared under contract DA 36-039-sc-70174, U. S. Army Signal Res. and Dev. Lab., Fort Monmouth, N. J.; June, 1959.

⁷ S. A. Schelkunoff, "Advanced Antenna Theory," John Wiley and Sons, Inc., New York, N. Y., p. 45; 1952.

Solving (25) leads to

$$q = \frac{\pi(n + \frac{1}{2}) - \theta_0}{2\theta_0} \quad n = \text{an odd integer.} \quad (26)$$

It is found that (26) gives a fairly good approximation even for the eigenvalue corresponding to $n=1$, notwithstanding that (25) has been approximated under the condition that $q \gg 1$; therefore, $n \gg 1$. It can be shown that (26) is valid for small values of q also, if θ_0 is near 90° . This simple, approximate expression for the

eigenvalue is very useful in transforming (6) and (12) into the forms for which numerical computation is feasible; that is,

$$\frac{P_q(-\cos \theta_0)}{\sin q\pi \frac{\partial}{\partial q} P_q(\cos \theta_0)} \approx -\frac{1}{\theta_0}$$

$$-\sin^2 \theta_0 \left[\frac{\partial P_q}{\partial q} \frac{\partial P_q}{\partial x} \right]_{x=\cos \theta_0} \approx \frac{2\theta_0}{\pi}$$

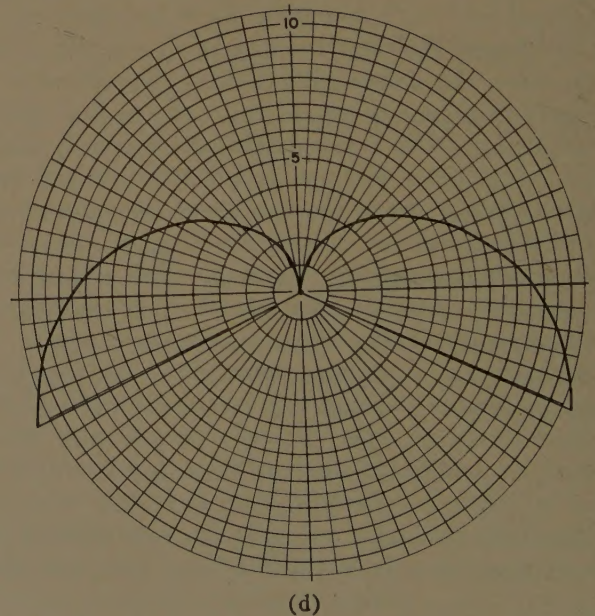
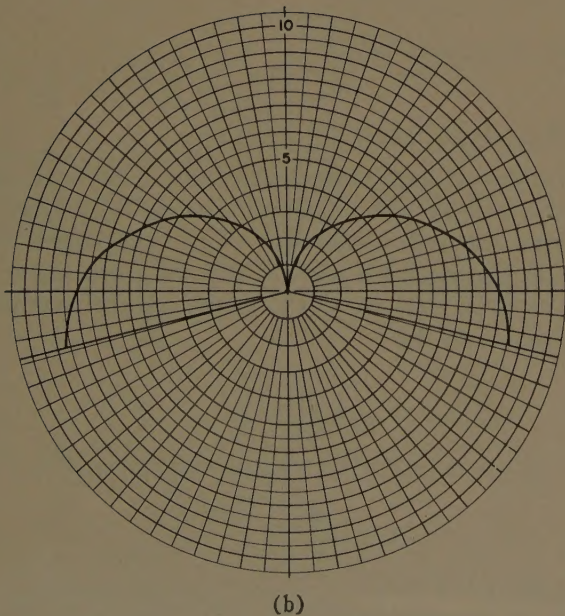
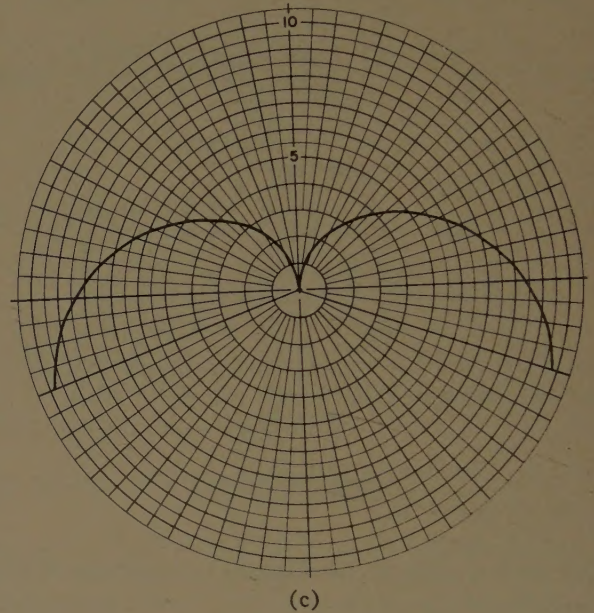
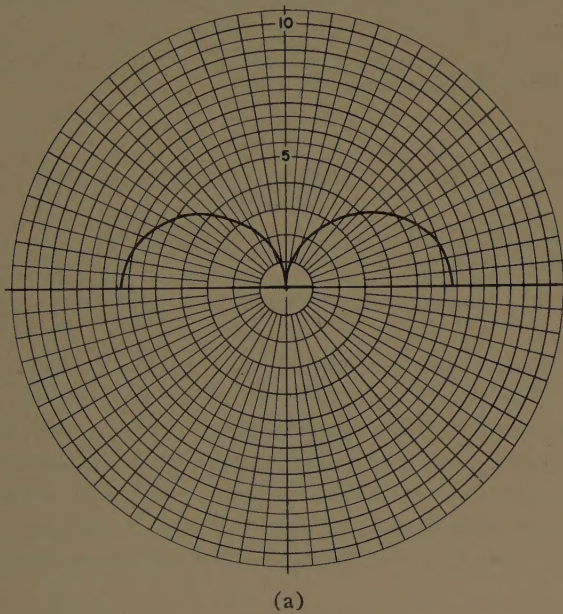


Fig. 3—The electric field patterns of the infinite wide-angle conical antennas, $l=\lambda/4$. (a) $\theta_0=90^\circ$, (b) $\theta_0=103.81^\circ$, (c) $\theta_0=109.88^\circ$, (d) $\theta_0=115.5^\circ$.

Introducing the above equations into (6) and (12) respectively, leads to

$$E_\theta(r, \theta) \approx -\frac{\eta I_0}{4\theta_0} \frac{e^{-i\beta r}}{r} \sum_q e^{i(\pi/2)q} (2q+1) S_q(\beta l) \frac{\partial P_q(\cos \theta)}{\partial \theta} \quad (27)$$

$$R \approx \frac{\eta}{4\theta_0 \sin^2 \beta l} \sum_q q(q+1)(2q+1) S_q(\beta l)^2. \quad (28)$$

It is found that (28) is equal to the infinite series term in (20), if θ_0 and q are replaced by π and n , respectively. The far-zone field patterns have been calculated for $l=\lambda/4$ and $\lambda/2$; $\theta_0=90^\circ$, 103.81° , 109.88° , and 115.50° . These are shown in Figs. 3 and 4. The radiation resistances of the infinite narrow- and wide-angle cones excited by a quarter-wavelength antenna have been calculated by using (20) and (28), respectively, and plotted in Fig. 5 by solid lines. When θ_0 is equal to $\pi/2$, *i.e.*, in the case of the flat plane, the radiation resistance is a well-known value, 15 (ln

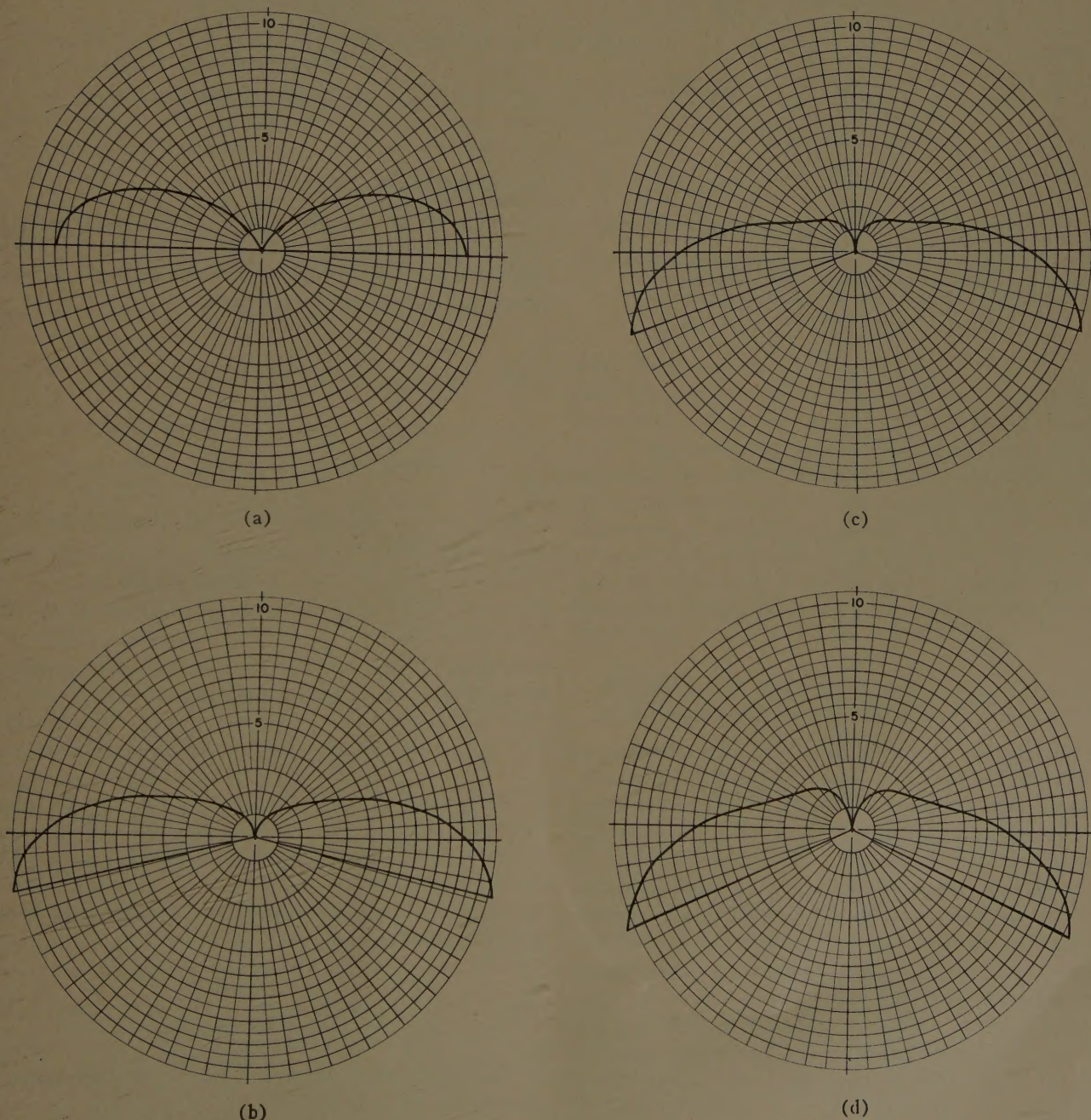


Fig. 4—The electric field patterns of the wide-angle infinite conical antennas, $l=\lambda/2$. (a) $\theta_0=90^\circ$, (b) $\theta_0=103.81^\circ$, (c) $\theta_0=109.88^\circ$, (d) $\theta_0=115.5^\circ$.

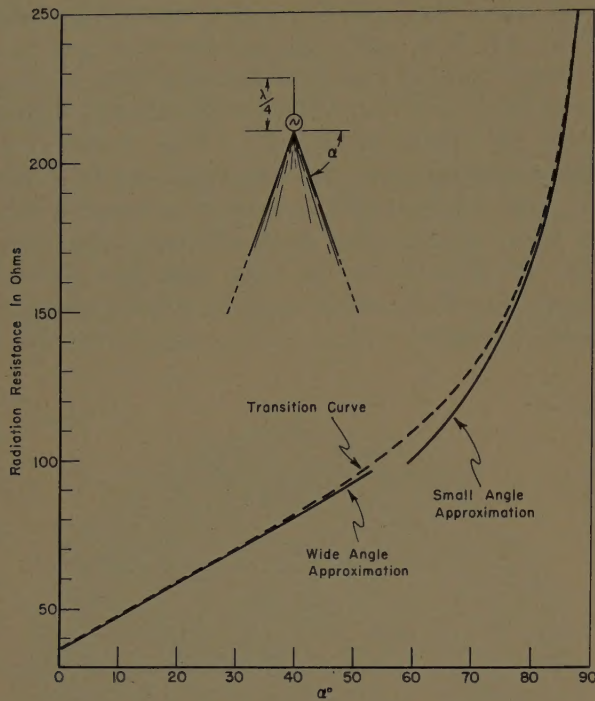


Fig. 5—The radiation resistance of the infinite conical antenna excited by a quarter-wavelength antenna.

$2\pi + c) = 15 \text{ Cin } 2\pi = 73.13/2$. It is interesting to note that the radiation resistance of the wide-angle cone increases almost linearly with the increasing cone angle θ_0 . The expression for the wide-angle cone case (28) is valid in the region about $\theta_0 \lesssim 140^\circ$, while the equation for the very small-angle cone (20) is an asymptotic expression. Considering the above facts it is reasonable to connect these two curves by the transition curve as shown by the broken line in Fig. 5. Thus the radiation resistance for an arbitrary cone angle can be estimated from this curve.

III. THE RADIATION AND IMPEDANCE PROPERTIES OF A SEMI-INFINITE BICONICAL ANTENNA

In this section a semi-infinite biconical antenna, as shown in Fig. 6, is analyzed as a boundary value problem using mode theory. In region I, the electric and magnetic fields are represented as the sum of a principal (transmission-line) wave and an infinite number of complementary waves. In region II, the fields are represented by an infinite series of complementary waves. Boundary conditions at the aperture and over the end surface of the finite cone are used to obtain a basic set of equations from which the amplitudes of the complementary waves and the effective terminating admittance of the principal wave can be determined. The basic set of equations is then solved by a variational method used by Tai on the biconical antenna problem.² A stationary expression for the effective terminating admittance is derived and the amplitudes of the exterior complementary waves are determined.

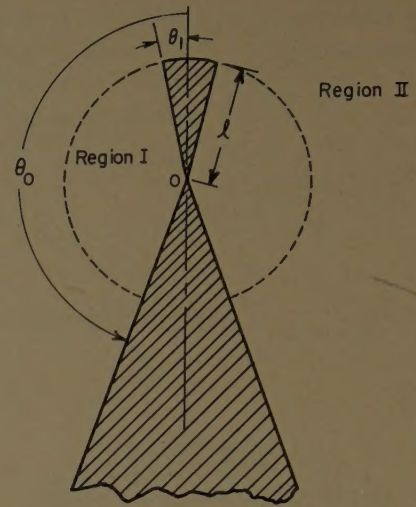


Fig. 6—The semi-infinite biconical antenna.

A. General Formulation

The fields are assumed to be axially symmetric and transversely magnetic. The field components E_θ^I and H_ϕ^I in region I can be expressed as a sum of a principal wave and complementary waves.

$$E_\theta^I = \frac{\eta I_0}{2\pi r \sin \theta} [K Y_l \sin \beta(l-r) - j \cos \beta(l-r)] - \frac{j\eta}{2\pi r} \sum_u \frac{a_u}{u(u+1)} \frac{j_u'(\beta r)}{j_u(\beta l)} \frac{\partial \Theta_u(\theta)}{\partial \theta} \quad (29)$$

$$H_\phi^I = \frac{I_0}{2\pi r \sin \theta} [\sin \beta(l-r) - jK Y_l \cos \beta(l-r)] - \frac{1}{2\pi r} \sum_u \frac{a_u}{u(u+1)} \frac{j_u(\beta r)}{j_u(\beta l)} \frac{\partial \Theta_u(\theta)}{\partial \theta} \quad (30)$$

The field components E_θ^{II} , H_ϕ^{II} in region II can be expressed as a sum of complementary waves:

$$E_\theta^{II} = -\frac{j\eta}{2\pi r} \sum_q \frac{b_q}{q(q+1)} \frac{\hat{h}_q^{(2)'}(\beta r)}{\hat{h}_q^{(2)}(\beta l)} \frac{\partial P_q(\theta)}{\partial \theta} \quad (31)$$

$$H_\phi^{II} = -\frac{1}{2\pi r} \sum_q \frac{b_q}{q(q+1)} \frac{\hat{h}_q^{(2)}(\beta r)}{\hat{h}_q^{(2)}(\beta l)} \frac{\partial P_q(\theta)}{\partial \theta} \quad (32)$$

where the prime indicates the derivative with respect to the argument, and

$$\Theta_u(\theta) = \frac{1}{2} \left[P_u(\cos \theta) - \frac{P_u(\cos \theta_1)}{P_u(-\cos \theta_1)} P_u(-\cos \theta) \right] \quad (33)$$

The summation indexes u and q are solutions, respectively, of

$$P_u(\cos \theta_1) P_u(-\cos \theta_0) = P_u(\cos \theta_0) P_u(-\cos \theta_1) \quad (34)$$

$$P_q(\cos \theta_0) = 0. \quad (35)$$

It should be noted here that

$$[\Theta_u(\theta)]_{\theta_1}^{\theta_0} = 0.$$

In (29) and (30) I_0 , K , and Y_t are constants defined as follows:

$$\left. \begin{aligned} I_0 &= j \frac{V(l)}{K} = \frac{j}{K} \int_{\theta_1}^{\theta_0} l E_{\theta}^I(l, \theta) d\theta \\ K &= \frac{\eta}{2\pi} \int_{\theta_1}^{\theta_0} \frac{d\theta}{\sin \theta} = \frac{\eta}{2\pi} \ln \left(\cot \frac{\theta_1}{2} \tan \frac{\theta_0}{2} \right) \\ KY_t &= \frac{\eta}{V(l)} \int_{\theta_1}^{\theta_0} l H_{\phi}^I(l, \theta) d\theta. \end{aligned} \right\} \quad (36)$$

It is seen from (30) that I_0 may be interpreted as a current associated with the TEM wave at a point $\lambda/4$ from the end of the finite cone. K is the characteristic impedance of the biconical transmission line, and Y_t is the effective terminating admittance for the principal wave.

In (29) and (30) I_0 and Y_t are not independent; they are related through the input current $I(0)$ as follows:

$$I(0) = I_0(\sin \beta l - jKY_t \cos \beta l), \quad (37)$$

which can be easily shown from (30). From (29) the input voltage is given by

$$V(0) = V(l)(\cos \beta l + jKY_t \sin \beta l). \quad (38)$$

Therefore, the normalized input admittance is given by

$$KY_t = \frac{KY_t \cos \beta l + j \sin \beta l}{\cos \beta l + jKY_t \sin \beta l}. \quad (39)$$

Eqs. (29)–(32) satisfy the boundary conditions at the cone surfaces $\theta = \theta_0$ and $\theta = \theta_1$, and the proper behavior of the fields at the input terminal. The three constants a_u , b_q , and Y_t are determined by three remaining boundary conditions, *i.e.*, the continuity of the tangential components of the electric and magnetic fields at the aperture and the vanishing of the tangential component of the electric field on the end surface of the upper cone.

Now, let the aperture electric field be represented by $E_a(\theta)$, and let the constants a_u , b_q and Y_t be expressed in terms of $E_a(\theta)$ by introducing the boundary conditions just mentioned. Later $E_a(\theta)$ will be determined by a stationary property of Y_t with respect to $E_a(\theta)$.

Introduction of the boundary condition for the tangential component of the electric field at the aperture leads to

$$\frac{-j\eta}{2\pi l} \sum_q \frac{b_q}{q(q+1)} M_q P_q'(\theta) = \begin{cases} E_a(\theta) & \theta_1 \leq \theta \leq \theta_0 \\ 0 & 0 \leq \theta \leq \theta_1 \end{cases} \quad (40)$$

$$\frac{-j\eta I_0}{2\pi l \sin \theta} - \frac{j\eta}{2\pi l} \sum_u \frac{a_u}{u(u+1)} N_u \Theta_u' = E_a(\theta) \quad \theta_1 \leq \theta \leq \theta_0, \quad (41)$$

where the notation is similar to that used by Tai,⁸ *i.e.*,

$$\left. \begin{aligned} P_q'(\theta) &= \frac{\partial P_q(\theta)}{\partial \theta}, & \Theta_u' &= \frac{\partial \Theta_u(\theta)}{\partial \theta} \\ M_q &= \frac{\hat{h}_q^{(2)'}(\beta l)}{\hat{h}_q^{(2)}(\beta l)}, & N_u &= \frac{\hat{j}_u'(\beta l)}{\hat{j}_u(\beta l)} \end{aligned} \right\}. \quad (42)$$

Multiplying both sides of (40) by $P_q'(\theta) \sin \theta$ and integrating with respect to θ from $\theta = 0$ to $\theta = \theta_0$,

$$b_q = \frac{j2\pi l}{\eta} \frac{I}{M_q I_{qq}} \int_{\theta_1}^{\theta_0} E_a(\theta) P_q'(\theta) \sin \theta d\theta, \quad (43)$$

where

$$\begin{aligned} I_{qq} &= \frac{1}{q(q+1)} \int_0^{\theta_0} [P_q'(\theta)]^2 \sin \theta d\theta \\ &= \frac{-\sin^2 \theta_0}{2q+1} \left[\frac{\partial P_q}{\partial q} \frac{\partial P_q}{\partial x} \right]_{\cos \theta_0}. \end{aligned} \quad (44)$$

The following equation is obtained in a similar manner:

$$a_u = \frac{j2\pi l}{\eta} \frac{1}{N_u I_{uu}} \int_{\theta_1}^{\theta_0} E_a(\theta) \Theta_u'(\theta) \sin \theta d\theta, \quad (45)$$

where

$$\begin{aligned} I_{uu} &= \frac{1}{u(u+1)} \int_{\theta_1}^{\theta_0} [\Theta_u'(\theta)]^2 \sin \theta d\theta \\ &= \frac{-1}{2u+1} \left[(1-x^2) \frac{\partial \Theta_u}{\partial u} \frac{\partial \Theta_u}{\partial x} \right]_{\cos \theta_1}^{\cos \theta_0}. \end{aligned} \quad (46)$$

Next, the continuity of the tangential component of the magnetic field at the aperture is expressed by

$$\begin{aligned} &\frac{-jKY_t I_0}{2\pi l \sin \theta} - \frac{1}{2\pi l} \sum_u \frac{a_u}{u(u+1)} \Theta_u'(\theta) \\ &= -\frac{1}{2\pi l} \sum_q \frac{b_q}{q(q+1)} P_q'(\theta) \quad \theta_1 \leq \theta \leq \theta_0. \end{aligned} \quad (47)$$

Substituting a_u , b_q , and I_0 [from (36)] into (47) leads to

$$\begin{aligned} &\frac{Y_t}{2\pi \sin \theta} \int_{\theta_1}^{\theta_0} E_a(\theta) d\theta \\ &- \frac{j}{\eta} \sum_u \frac{\Theta_u'(\theta)}{u(u+1) N_u I_{uu}} \int_{\theta_1}^{\theta_0} E_a(\theta) \Theta_u'(\theta) \sin \theta d\theta \\ &= \frac{-j}{\eta} \sum_q \frac{P_q'(\theta)}{q(q+1) M_q I_{qq}} \int_{\theta_1}^{\theta_0} E_a(\theta) P_q'(\theta) \sin \theta d\theta. \end{aligned} \quad (48)$$

⁸ Tai, *op. cit.*, p. 1077.

Multiplying both sides of (48) by $E_a(\theta) \sin \theta$, integrating with respect to θ from $\theta = \theta_1$ to $\theta = \theta_0$, and then solving for Y_t leads to

$$Y_t = \frac{j2\pi}{\eta} \sum_u \frac{1}{u(u+1)N_u I_{uu}} \frac{\left[\int_{\theta_1}^{\theta_0} E_a(\theta) \Theta_u'(\theta) \sin \theta d\theta \right]^2}{\left[\int_{\theta_1}^{\theta_0} E_a(\theta) d\theta \right]^2} - \frac{j2\pi}{\eta} \sum_q \frac{1}{q(q+1)M_q I_{qq}} \frac{\left[\int_{\theta_1}^{\theta_0} E_a(\theta) P_q'(\theta) \sin \theta d\theta \right]^2}{\left[\int_{\theta_1}^{\theta_0} E_a(\theta) d\theta \right]^2}. \quad (49)$$

This is a stationary expression for Y_t with respect to variations of $E_a(\theta)$ about its correct value. Now, let $E_a(\theta)$ be expanded in the same form of complete orthogonal series as that used for the electric field in region I, i.e., let

$$E_a(\theta) = A \left[-\frac{1}{\sin \theta} + \sum_u A_u \Theta_u'(\theta) \right]. \quad (50)$$

Introducing (50) into (49) leads to

$$Y_t = Y_{t0} + 2 \sum_u \alpha_u A_u + \sum_u \beta_u A_u^2 + \sum_u \sum_v \gamma_{uv} A_u A_v, \quad (51)$$

where the symbols are defined in the same manner as in Tai's paper.²

$$\left. \begin{aligned} Y_{t0} &= \frac{-j\eta}{\pi K^2} \sum_q \frac{P_q^2(\theta_1)}{2q(q+1)I_{qq}M_q}, \\ \alpha_u &= \frac{-j\eta}{2\pi K^2} \sum_q \frac{P_q(\theta_1)I_{uq}}{I_{qq}M_q}, \\ \beta_u &= \frac{j\eta}{2\pi K^2} \frac{u(u+1)I_{uu}}{N_u}, \\ \gamma_{uv} &= \gamma_{vu} = \frac{-j\eta}{2\pi K^2} \sum_q \frac{q(q+1)I_{uq}I_{vq}}{I_{qq}M_q}, \end{aligned} \right\} \quad (52)$$

and where

$$I_{uq} = \frac{1}{q(q+1)} \int_{\theta_1}^{\theta_0} \Theta_u'(\theta) P_q'(\theta) \sin \theta d\theta = \frac{-\sin^2 \theta_1}{(u-q)(u+q+1)} \left[P_q \frac{\partial \Theta_u}{\partial x} \right]_{\cos \theta_1}. \quad (53)$$

Using the stationary property, $\partial Y_t / \partial A_u = 0$, one obtains the following equation for all of u :

$$\alpha_u + \beta_u A_u + \sum_v \gamma_{uv} A_v = 0. \quad (54)$$

From (51) and (54), one obtains

$$Y_t = Y_{t0} + \sum_u \alpha_u A_u. \quad (55)$$

Thus, the terminating admittance Y_t can be obtained by using (55), if (54) can be solved for the A_u . It is not easy, however, to solve (54) rigorously for the general case.

B. The Terminating Admittance for Narrow-Angle Cones

The approximate terminating admittance for a very narrow-angle semi-infinite biconical antenna is obtained in this section. The approximate solution is presented for the case where θ_0 and θ_1 are very near π and 0, respectively.

When $\theta_0 \approx \pi$, $\theta_1 \approx 0$, the parameter q can be determined approximately from (13), and the parameter u from⁹

$$u \approx m + \frac{1}{\pi} \tan^{-1} \frac{\pi \ln \frac{4}{\theta_1(\pi - \theta_0)}}{2 \ln \frac{2}{\theta_1} \ln \frac{2}{\pi - \theta_0}} \quad m = 0, 1, 2, \dots \quad (56)$$

For simplicity, the angles of both cones are assumed to be equal; i.e., $\theta_1 = \pi - \theta_0$. Then, u is given by

$$u \approx m + \frac{1}{2} + 0 \left\{ \left(\ln \frac{2}{\theta_1} \right)^{-3} \right\} \quad m = 0, 1, 2, \dots \quad (57)$$

Now, consider γ_{uv} in (52); the integrals I_{uq} and I_{vq} have the following asymptotic expressions when the cone angles are very small:

$$I_{uq} \left\{ \begin{aligned} &= \frac{2}{2n+1} \equiv I_{kk}, \quad \text{if } m = n = k \\ &\approx \frac{1}{(m+n+1)(m-n) \ln \frac{2}{\theta_1}} \rightarrow 0, \quad \text{if } m \neq n. \end{aligned} \right. \quad (58)$$

Consequently,

$$\gamma_{uv} \approx 0 \left(\ln \frac{2}{\theta_1} \right)^{-1} \rightarrow 0 \quad \text{if } u \neq v. \quad (59)$$

Due to the relation expressed in (59), A_u in (54) can be obtained in the following simple form:

$$A_u = \frac{-\alpha_u}{\beta_u + \gamma_{uu}}. \quad (60)$$

⁹ S. Adachi, "A Theoretical Analysis of Infinite Conical Antennas—Part I," Antenna Lab., The Ohio State University Res. Foundation, Columbus, Rept. No. 662-20, prepared under Contract DA 36-039, sc-70174, U. S. Army Signal Res. and Dev. Lab., Fort Monmouth, N. J.; February, 1959.

In a similar way the following asymptotic expressions for I_{qq} and I_{uu} are derived:

$$I_{qq} = \frac{2}{2q+1} + O\left(\ln \frac{2}{\theta_1}\right)^{-2} \approx \frac{2}{2n+1} = I_{kk} \quad (61)$$

$$I_{uu} = \frac{2}{2u+1} + O\left(\ln \frac{2}{\theta_1}\right)^{-2} \approx \frac{2}{2m+1} = I_{kk} \quad \text{for } n = m = k. \quad (62)$$

Substituting (52), (58), (61), (62) into (60),

$$A_u = A_k = \frac{2k+1}{2k(k+1)} \frac{N_k}{M_k - N_k} \quad k = 1, 2, 3, \dots \quad (63)$$

and

$$A_0 = \ln \frac{2}{\theta_1} \frac{N_0}{2M_0 - N_0}. \quad (64)$$

Introducing (63) and (64) into (55) yields

$$Y_t = -\frac{j\eta}{4\pi K^2} \left[\frac{4 \ln \frac{2}{\theta_1}}{2M_0 - N_0} + \sum_k \frac{2k+1}{k(k+1)} \frac{1}{M_k - N_k} \right] \quad k = 1, 2, 3, \dots \quad (65)$$

By using the well-known Wronskian relation for Bessel functions, the above equation can be written in the form

$$Y_t = \frac{\eta}{4\pi K^2} \left[\frac{4 \ln \frac{2}{\theta_1}}{2 - j \cot \beta l} + \frac{\pi \beta l}{2} \sum_{k=1,2,3,\dots} \frac{2k+1}{k(k+1)} J_{k+1/2}(\beta l) H_{k+1/2}^{(2)}(\beta l) \right],$$

$$K = \frac{\eta}{\pi} \ln \cot \frac{\theta_1}{2} \approx \frac{\eta}{\pi} \ln \frac{2}{\theta_1}. \quad (66)$$

The first term in the bracket of (66) is proportional to the characteristic impedance of the biconical transmission line. On the other hand, the second term in the bracket is independent of the cone angle. It will be shown in Section III-C that the conductances of the first and second terms are associated with the transmission-line wave power and the usual radiation power, respectively.

The real part of the infinite summation in (66) converges very rapidly, but the imaginary part does not

converge rapidly enough to permit the numerical computation easily. By using the asymptotic expression for Bessel functions of large order, (66) can be rewritten in the following more rapidly convergent expression (see Appendix II):

$$Y_t = \frac{\eta}{4\pi K^2} \left[j\beta l + \frac{4 \ln \frac{2}{\theta_1}}{2 - j \cot \beta l} + \frac{\pi \beta l}{2} \sum_{k=1,2,\dots} \frac{1}{k(k+1)} \cdot \left\{ (2k+1) J_{k+1/2}(\beta l) H_{k+1/2}^{(2)}(\beta l) - j \frac{2}{\pi} \right\} \right]. \quad (67)$$

From the viewpoint of determining the input impedance, the formulation of the problem given in this section is clearly superior to that in the previous section, where only the radiation resistance was determined. The terminating admittance $Y_t = G_t + jB_t$ has been calculated for the cone angles $2\theta_1 = 2(\pi - \theta_0) = 2^\circ, 0.5^\circ$, and 0.2° . The terminating conductance is plotted in Fig. 7 and the terminating susceptance is plotted in Fig. 8. The input impedance can be easily calculated by introducing Y_t into (39).

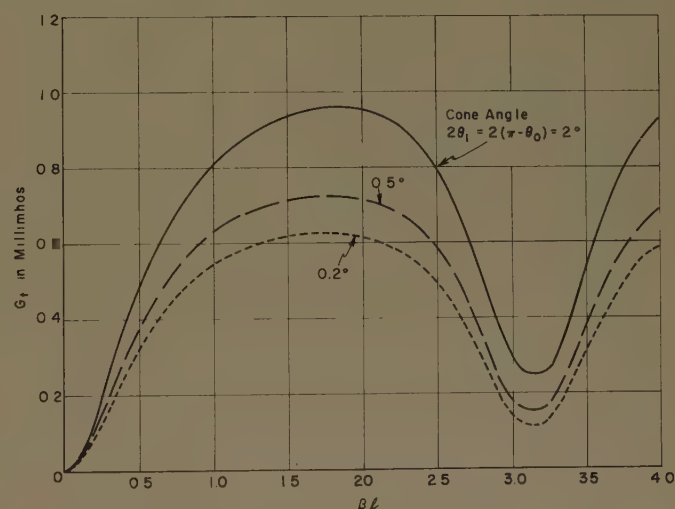


Fig. 7—Terminating conductances of thin, semi-infinite biconical antennas.

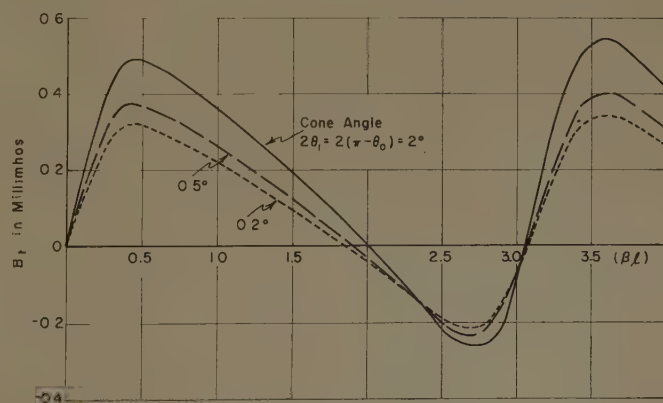


Fig. 8—Terminating susceptances of thin, semi-infinite biconical antennas.

Figs. 9 and 10 show the input resistance and reactance, respectively, for the cone angles given in the previous paragraph. Although similar in form to the input resistance and reactance curves for the biconical antenna, the curves for the semi-infinite biconical antenna are seen to be more sharply antiresonant with larger maxima than occur for corresponding biconical antennas. Furthermore, it is interesting to note in Fig. 9 that the input resistance remains finite as βl approaches zero. In this limit, it is associated with the guided term in the terminating admittance (66), and the input resistance is equal to half the value of the characteristic impedance of the biconical transmission line. The nonvanishing input resistance in the limit of zero βl can be explained in the following manner. As βl approaches zero, the input resistance depends increasingly on the form of the current distribution on the semi-infinite cone, and less on the form of the current distribution on the finite cone of length l . Furthermore, as l becomes vanishingly small, the form of the current distribution on the semi-infinite cone becomes independent of l . Despite the fact that the input resistance is finite as βl approaches zero, no generator power is radiated in this limit, because the input reactance is infinite.

C. The Far-Zone Field for Narrow-Angle Cones

In the preceding section the coefficient b_q has been expressed in terms of the aperture field $E_a(\theta)$ which is given by (50). By integrating (50) with respect to θ , the amplitude coefficient A is determined as

$$A = -\frac{\eta}{2\pi l K} V(l) = \frac{j\eta}{2\pi l} I_0. \quad (68)$$

Introducing (50) and (68) into (43) and carrying out the indicated integration leads to

$$b_q = \frac{-I_0}{M_q I_{qq}} \left[P_q(\theta_1) + q(q+1) \sum_u A_u I_{uq} \right]. \quad (69)$$

For a very narrow-angle biconical antenna the following simple expressions are obtained by a procedure similar to that used in the preceding section:

$$\left. \begin{aligned} b_k &= -I_0 \frac{2k+1}{2} \frac{1}{M_k - N_k} \\ k &= 1, 2, 3, \dots \\ b_0 &= -\frac{I_0}{2M_0 - N_0} \end{aligned} \right\} \quad (70)$$

Approximately,

$$\frac{\partial P_q}{\partial \theta} \approx \frac{\partial P_k}{\partial \theta} - \frac{(-1)^k}{2 \ln \frac{2}{\theta_1}} \tan \frac{\theta}{2}$$

$$k = 0, \theta \leq \theta_0$$

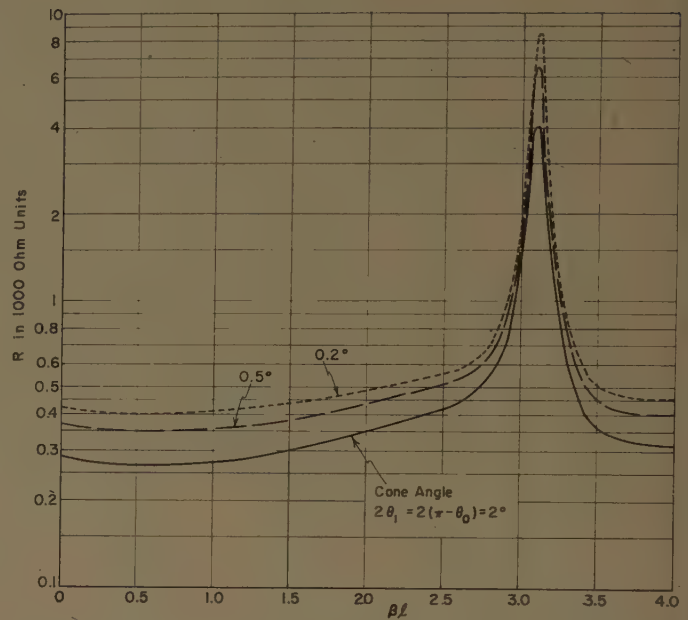


Fig. 9—The input resistances of thin, semi-infinite biconical antennas.

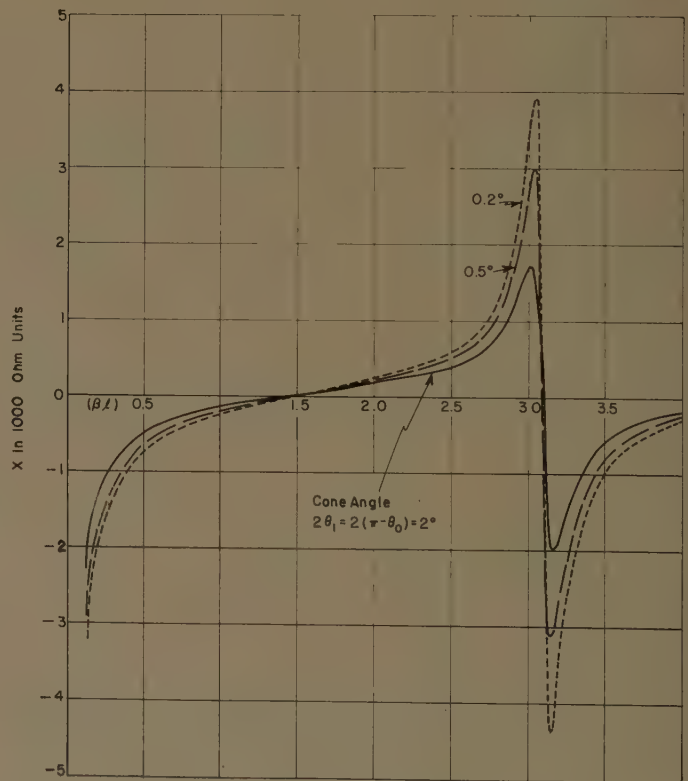


Fig. 10—The input reactances of thin, semi-infinite biconical antennas.

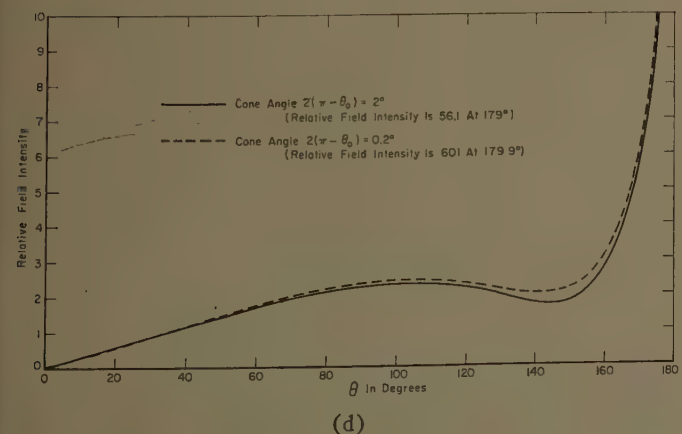
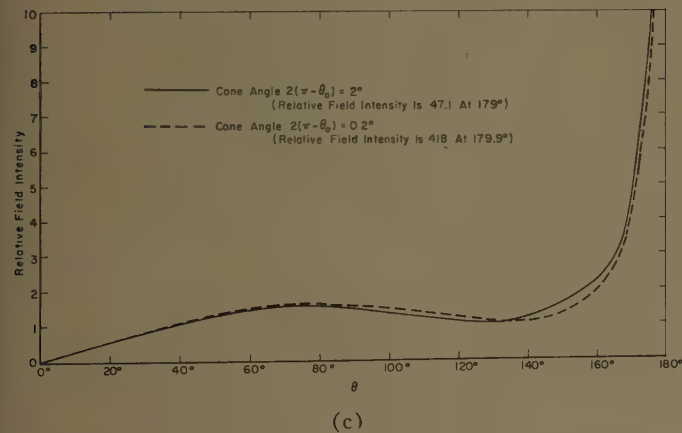
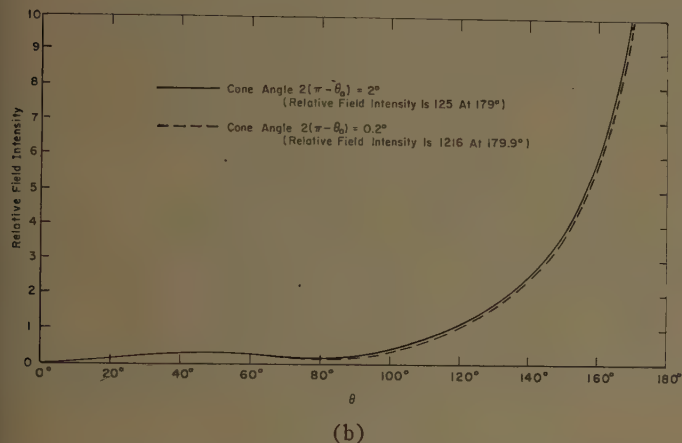
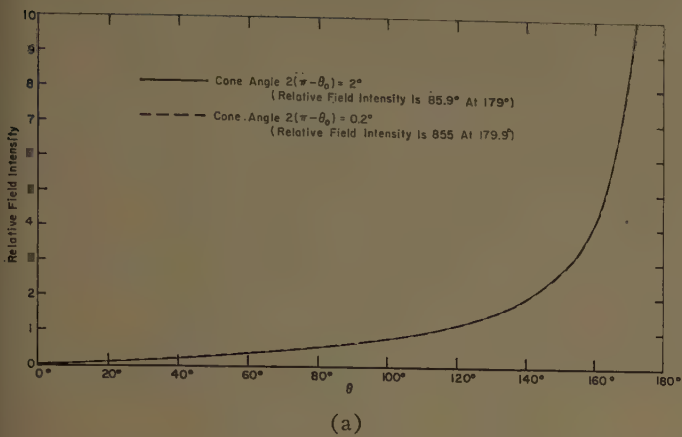


Fig. 11—Radiation patterns of thin semi-infinite biconical antennas.
(a) $\beta l = 0.5$, (b) $\beta l = 1.5$, (c) $\beta l = 3.0$, (d) $\beta l = 3.5$.

and

$$k = 1, 2, 3, \dots, \theta(\leq \theta_0) \approx \pi. \quad (71)$$

Introducing (70) and (71) into (31) leads to the following expression for the far-zone field:

$$E_{\theta}^{\text{II}} \approx \frac{\eta I_0}{4\pi} \frac{e^{-j\beta r}}{r} \left[\tan \frac{\theta}{2} \left\{ \frac{2}{h_0^{(2)}(\beta l) \{2j + \cot \beta l\}} \right. \right. \\ \left. \left. + \frac{1}{2 \ln \frac{2}{\theta_1}} \sum_{k=1,2,\dots} (-1)^{-k/2} \frac{2k+1}{k(k+1)} j_k(\beta l) \right\} \right. \\ \left. - \sum_{k=1,2,\dots} (-1)^{k/2} \frac{2k+1}{k(k+1)} j_k(\beta l) \frac{\partial P_k}{\partial \theta} \right]. \quad (72)$$

Consider the limiting case as $\theta_1 \rightarrow 0$. For $\sin \beta l \neq 0$, the second term in the brace can be neglected compared with the first term, and the field pattern becomes independent of the cone angle as $\theta_1 \rightarrow 0$, in the same manner as (18) which was derived using a Green's function.

For $\sin \beta l = 0$, $\beta l = i\pi$, (72) is identical with (21) which was obtained by the use of a Green's function.

The field patterns of E_{θ}^{II} as computed from (72) are shown in Fig. 11 for $\beta l = 0.5, 1.5, 3.0, 3.5$ and for cone angles of 2° and 0.2° . It is seen that the patterns become less dependent on the cone angles as the length of the finite cone decreases. The patterns for the 2° cone angle in Fig. 11, together with the pattern for the 2° cone angle in Fig. 2, are replotted in Fig. 12 with the pattern maxima normalized to 100. In each case a sharp maximum in the pattern occurs at the conical surface; however, this maximum is least pronounced with respect to the rest of the pattern when $\beta l = \pi$. This is in agreement with the results deduced from the asymptotic expressions for E_{θ}^{II} that a wave guided along the conical surface is excited when $\beta l \neq i\pi$, but no guided wave is excited when $\beta l = i\pi$.

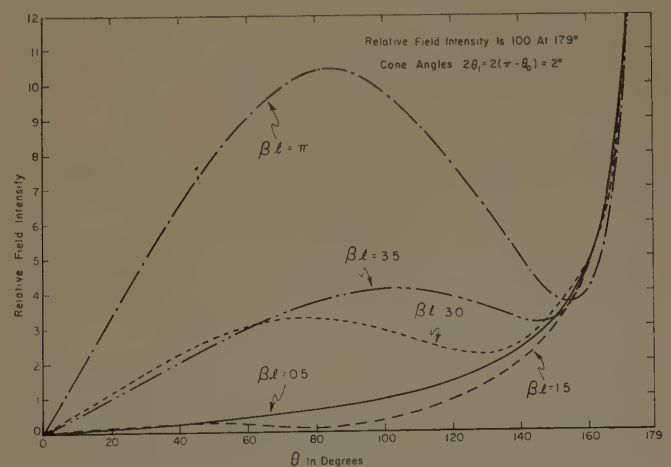


Fig. 12—Normalized radiation patterns of thin, semi-infinite biconical antennas.

A maximum in the field pattern at the conical surface is also evident in the case where the semi-infinite cone is excited by an annular slot near its tip. However, for the 30° cone angle used in the calculations of Bailin and Silver, this maximum is reduced to the same order of magnitude as other maximum points in the pattern.

The ratio of the power in the guided-wave (transmission-line) component to the power in the radiation field is of interest. This will be determined for the limiting case of $\theta_1 \rightarrow 0$. The total energy flux is

$$\begin{aligned}
 P &= \frac{2\pi}{\eta} \int_0^{\pi-\theta_1} |E_\theta|^2 r^2 \sin \theta d\theta \\
 &= \frac{\eta |I_0|^2}{8\pi} \left\{ \frac{4}{|2 - j \cot \beta l|^2} \int_0^{\pi-\theta_1} \tan^2 \frac{\theta}{2} \sin \theta d\theta \right. \\
 &\quad + \sum_{k=1,2,\dots} \left(\frac{2k+1}{k(k+1)} \right)^2 j_{k+1/2}^2(\beta l) \int_0^{\pi-\theta_1} \left(\frac{\partial P_k}{\partial \theta} \right)^2 \sin \theta d\theta \Big\} \\
 &\quad + 0 \left(\ln \frac{2}{\theta_1} \right)^{-1} \\
 &\approx \frac{\eta |I_0|^2}{4\pi} \left\{ \frac{8 \ln \frac{2}{\theta_1}}{4 + \cot^2 \beta l} \right. \\
 &\quad \left. + \frac{\pi \beta l}{2} \sum_{k=1,2,\dots} \frac{2k+1}{k(k+1)} j_{k+1/2}^2(\beta l) \right\}. \quad (73)
 \end{aligned}$$

Let the radiation resistance R_a be defined in terms of I_0 , the current associated with the TEM wave at a point $\lambda/4$ from the end of the biconical transmission line.

$$\begin{aligned}
 R_a &= \frac{\eta}{4\pi} \left\{ \frac{8 \ln \frac{2}{\theta_1}}{4 + \cot^2 \beta l} \right. \\
 &\quad \left. + \frac{\pi \beta l}{2} \sum_{k=1,2,\dots} \frac{2k+1}{k(k+1)} j_{k+1/2}^2(\beta l) \right\}. \quad (74)
 \end{aligned}$$

Noting that the radiated energy is entirely transmitted in the principal wave, it follows that R_a is the real part of the principal wave impedance at a point $\lambda/4$ from the termination of the biconical transmission line. Thus from the theory of transmission lines,

$$R_a = K^2 G_t. \quad (75)$$

This relationship provides a useful check between (74) and (66). Schelkunoff refers to $K^2 G_t$ as the inverse radiation resistance.⁷ Thus, with the discussion following (20) it is reasonable to associate the first term of (74) or (66) with the guided wave and the second term with the radiation field for very narrow-angle cones. The ratio of the first term to the second term, R_s/R_r , is plotted as a function of βl in Fig. 13. At the first resonance the ratio of guided wave power to radiation power for a cone angle of 2° is 12.3 db, and the ratio can be further increased by decreasing the cone angle or the length of the finite conical element.

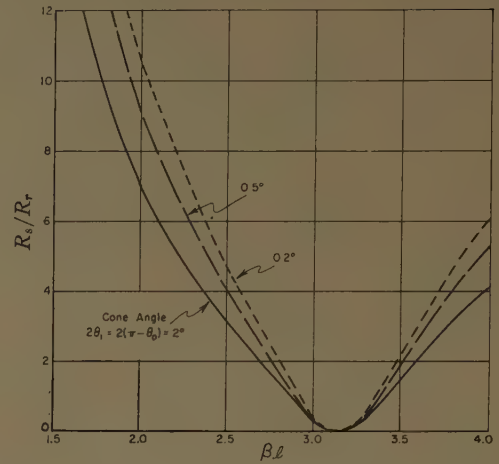


Fig. 13—Ratios of guided wave power to radiation power for thin, semi-infinite biconical antennas.

IV. CONCLUSIONS

A theoretical analysis of the infinite conical antenna is carried out using two different formulations. In the first formulation a Green's function is used which satisfies the boundary condition that it vanish on the surface of the cone. Expressions are obtained for the radiation resistance and far-zone field. In the second formulation a similar structure, the semi-infinite biconical antenna, is analyzed using mode theory and applying the variational method. Expressions are obtained for the far-zone field and the terminating admittance, from which the input impedance is readily determined. Since it is not feasible to obtain numerical results for arbitrary cone angles, the special cases of narrow- and wide-angle cones are considered.

A notable feature of the far-zone patterns is the sharp increase in the field in the vicinity of the conical surface, which depends not only on cone angle, θ_0 , but also on the length of the linear exciting element. If the linear element does not equal an integral number of half wavelengths, there is a finite amount of power guided along the conical surface, and the behavior of the field in the vicinity of the cone is similar to that of the biconical transmission line. The excitation efficiency of this guided wave has been computed. It decreases with increasing cone angle, and it is a quite sensitive function of the length of the linear element. If the linear element is equal to an integral number of half wavelengths (the linear element is resonant) there is negligible power guided along the very thin cone.

The input impedance of the semi-infinite biconical antenna in the vicinity of the first resonance is much less frequency sensitive than biconical or linear antennas of comparative thickness. This desirable broadband property with regard to impedance improves with increasing cone angle. It is interesting to note that the semi-infinite biconical antenna is more sharply antiresonant than the corresponding biconical antenna.

The fact that a guided wave is readily excited on a

narrow cone suggests that it may have potential use as part of the primary feed for a surface wave structure where efficient surface wave excitation is desired. This application merits further study in connection with surface wave geometries which are axially or radially cylindric or conical.

APPENDIX I

THE INTEGRALS $S_q(\beta l)$

$$S_q(\beta l) = \sin \beta l \int_0^{\beta l} \frac{\cos x}{x^2} \hat{f}_q(x) dx - \cos \beta l \int_0^{\beta l} \frac{\sin x}{x^2} \hat{f}_q(x) dx$$

$$I_1(\beta l) \equiv \int_0^{\beta l} \frac{\cos x}{x^2} \hat{f}_q(x) dx = \int_0^{\beta l} \frac{1}{x^2} \hat{f}_{-1}(x) \hat{f}_q(x) dx \quad q > 0$$

$$I_2(\beta l) \equiv \int_0^{\beta l} \frac{\sin x}{x^2} \hat{f}_q(x) dx = \int_0^{\beta l} \frac{1}{x^2} \hat{f}_0(x) \hat{f}_q(x) dx \quad q \geq 0.$$

Using Lommel's integral formula, one obtains

$$I_1(\beta l) = \frac{1}{q(q+1)} \left[\hat{f}_{-1}(\beta l) \hat{f}_{q-1}(\beta l) - \hat{f}_{-2}(\beta l) \hat{f}_q(\beta l) - \frac{q+1}{\beta l} \hat{f}_{-1}(\beta l) \hat{f}_q(\beta l) \right], \quad q > 0 \quad (76)$$

$$I_2(\beta l) = \frac{1}{q(q+1)} \left[\hat{f}_0(\beta l) \hat{f}_{q-1}(\beta l) - \hat{f}_{-1}(\beta l) \hat{f}_q(\beta l) - \frac{q}{\beta l} \hat{f}_0(\beta l) \hat{f}_q(\beta l) \right] \quad q \geq 0 \quad (77)$$

$$S_q(\beta l) = I_1(\beta l) \sin \beta l - I_2(\beta l) \cos \beta l. \quad (78)$$

If βl is $(\pi/2) i$, $i=1,2,3 \dots$, $S_q(\beta l)$ is given simply by

$$S_q\left(\frac{\pi}{2} i\right) = \frac{\hat{f}_q\left(\frac{\pi}{2} i\right)}{q(q+1)}. \quad (79)$$

APPENDIX II

THE SUMMATION OF AN INFINITE SERIES

When k is large, or $k \gg \beta l$, the following asymptotic expressions can be used:

$$J_{k+1/2}(\beta l) \approx \frac{1}{\Gamma(k + \frac{1}{2} + 1)} \left(\frac{\beta l}{2}\right)^{k+1/2} \quad (80)$$

$$N_{k+1/2}(\beta l) \approx -\frac{\Gamma(k + \frac{1}{2})}{\pi} \left(\frac{2}{\beta l}\right)^{k+1/2}. \quad (81)$$

Therefore, for a large k

$$J_{k+1/2}(\beta l) N_{k+1/2}(\beta l) \approx -\frac{2}{\pi} \frac{1}{2k+1} \quad (82)$$

and, since we have

$$\sum_{k=1}^{\infty} \frac{1}{k(k+1)} = 1, \quad (83)$$

the following transformation can be made:

$$\sum_{k=1}^{\infty} \frac{2k+1}{k(k+1)} J_{k+1/2}(\beta l) N_{k+1/2}(\beta l) = -\frac{2}{\pi} + \sum_{k=1}^{\infty} \frac{1}{k(k+1)} \left[\frac{2}{\pi} + (2k+1) J_{k+1/2}(\beta l) N_{k+1/2}(\beta l) \right]. \quad (84)$$

ACKNOWLEDGMENT

The author wishes to thank Dr. R. G. Kouyoumjian, of The Ohio State University, and Dr. Y. Mushiaki, of Tokohu University, Japan for their critical reading of this paper and for their many valuable suggestions. Thanks are also due to Dr. T. E. Tice and R. A. Fouty at the Antenna Laboratory, The Ohio State University, for their advice and encouragement.

Electrical Performance of Rigid Ground Radomes*

W. LAVRENCH†, MEMBER, IRE

Summary—The main purpose of a radome is to protect an antenna from the weather. Many designs of radomes can be evolved which will meet the mechanical requirements dictated by such factors as wind and snow load; however, these requirements are not sufficient. The radome must also have certain electrical characteristics in order that operation of the enclosed antennas is not degraded. This paper summarizes the many electrical measurements made on rigid ground radomes to date at the National Research Council to study the effect of the radomes on the performance of radar antennas.

Ground radomes made of thin single-skin, sandwich, and thick foam walls have been studied. Performance of single-skin radomes was found to be adequate for wavelengths of about ten centimeters and longer. In order to obtain maximum transmission, the skins must be thin and the panel joints must be small, few in number, and randomly spaced. Sandwich radomes provide a good design for wavelengths of five to ten centimeters. At wavelengths of three centimeters and shorter, the thick foam wall is believed to be the best solution, because in this construction joints between panels can be made practically invisible to the radiation. Transmission losses as low as one per cent have been measured.

INTRODUCTION

GROUND radomes are used over antennas to protect the latter from the elements and to simplify the problem of constant antenna rotation in gusty air. In order that the operation of the enclosed radar antenna will not be impaired, the radome must satisfy many electrical requirements.

To ensure ease of transportation and erection, large rigid radomes almost invariably consist of many individual sections or panels. This arrangement introduces the problem of joining the panels in some fashion. Some form of fastener is now required, and furthermore—for mechanical reasons—the edges of the panels are usually quite different from the rest of the panel. The ideal uniform wall mentioned previously has now become one with many discontinuities. These discontinuities, whether they be flanges, reinforced edges, or glue lines, are the largest source of trouble in a rigid radome, and can have quite serious effects on the performance of a radar antenna.

Before considering various radome designs and their performance, it may be pertinent to list briefly the most important of the electrical characteristics that a radome must have.

- 1) Transmission coefficient: In order to realize the maximum sensitivity (range) of which a radar is capable, the radome must introduce little or no loss in the transmitted or received energy.

- 2) Sidelobes: Power transmitted in the sidelobes is power wasted. Reception on a sidelobe will result in spurious and misleading information. The ease with which a radar can be jammed is increased with increasing sidelobe amplitude. It follows, therefore, that the presence of a radome over the antenna must not result in an appreciable increase in sidelobe levels.
- 3) Reflection: Reflections from the radome must be held to a minimum. If sizable reflections exist and vary in amplitude or phase as the radar antenna is rotated, the magnetron in some radars may be pulled in frequency, initiating possible AFC and MTI problems.
- 4) Boresight error: This is also known as "pointing error" or "beam shift." The bearing of a target is determined from the position of the antenna beam when maximum signal is received, or in the case of a split beam, when minimum signal is received. In either case, any shift produced in the position of the beam by the radome would lead to errors in determining the true bearing of the target. If the beamshift produced by a radome remained constant, or followed some other simple law, as the antenna rotated, suitable corrections could be applied; however, such is not usually the case. In practice it is found that the boresight error varies quite randomly in magnitude and direction for different positions of the antenna in the radome. This dictates that the beam shift produced by the radome should be very small, usually a fraction of a milliradian.

The remainder of this paper will deal with tests carried out on radomes and portions of radomes to gain a better understanding of how the various ill effects of a radome on the performance of a radar are brought about, to determine their magnitudes, and to find what steps can be taken to reduce these effects.

TRANSMISSION LOSS

Loss in transmission through a radome can be brought about in several ways:

- 1) Attenuation in the radome wall because of use of lossy materials;
- 2) Reflection of energy from the radome wall because of a mismatch;
- 3) Reflection or scatter of energy by the discontinuities in the radome wall such as ribs, flanges, and panel fasteners;

* Received by the PGAP, December 1, 1959; revised manuscript received, April 4, 1960.

† Radio and Elec. Engrg. Div., Natl. Res. Council, Ottawa, Can.

- 4) Scatter of energy by the radome wall because of a nonuniform delay of phase of the incident wave front.

Attenuation caused by the use of a lossy material can be considered negligible since the materials that are normally employed either have a very low loss tangent, or are very thin in terms of wavelength. The skins in thin-walled radomes may range in thickness from $\frac{1}{16}$ inch to $\frac{1}{8}$ inch. Using a glass-cloth laminate with a dielectric constant of about 4, and operating at a wavelength of 10 centimeters (S band), the electrical thickness in question ranges from $\lambda/32$ to $\lambda/16$. If a loss tangent of about 0.015 is assumed, the reduction in field strength due to absorption varies from 0.15 per cent to 0.3 per cent for the thicknesses being considered. Even when the thickness is increased to half a wavelength, the loss is only 2.4 per cent.¹ When this type of material is used in dielectric lenses, the thickness involved may be of the order of several wavelengths, and absorption loss would certainly be significant.

Several types of construction can be used in the wall of the radome to minimize losses due to reflection. The first obvious type is the single-skin wall² of a thickness which is small in terms of wavelength. In this particular case, reflections from the first interface and the second interface are nearly equal in amplitude and opposite in phase, and the resultant total reflection is small. If the skin thickness is increased for mechanical reasons, the reflection loss increases to a maximum value dependent on the dielectric constant of the material. This occurs at a thickness of $\lambda/4$. Further increases in skin thickness result in a reduced reflection loss. This loss eventually reaches zero when the panel is exactly one-half wavelength thick. The panel may be considered to be a half-wavelength transmission line coupling the load (free space) on one side to the generator on the other. In this manner the load impedance is transformed to an identical impedance on the input side of the panel and no reflections occur. Theoretical analysis shows that reflection loss varies periodically with increasing panel thickness. The maximum power loss occurs when the panel is an odd number of quarter-wavelengths thick and is equal to

$$\frac{(\epsilon - 1)^2}{(\epsilon + 1)^2} \cdot 100 \text{ per cent}$$

where ϵ is the dielectric constant of the material. Zero loss occurs when the panel is a multiple of a half wavelength.

It is thus obvious that if a very thin wall is inadequate for mechanical reasons, other thicknesses can be chosen which will also satisfy the electrical requirement of zero reflection. However, it usually turns out that the $\lambda/2$ thickness calls for an excessive amount of material. For example, if a glass-cloth laminate ($\epsilon=4$) is considered, it turns out that $\lambda/2$ at S band is equal to one inch. It is evident why this solution is hardly every considered.

If a thin skin is ruled out because of unsuitable physical properties and the $\lambda/2$ wall because of excessive material, a satisfactory solution is still available. This is the sandwich construction.³

The typical sandwich consists of two thin, high-density skins (such as glass-cloth laminates) spaced by a low-density core. The core may be either a foam or a paper honeycomb.⁴ In this design the reflection loss can be reduced to zero by use of the correct core thickness. The core thickness required for maximum transmission depends upon the skins used. This can be calculated theoretically; however, with the thin skins normally used there is some uncertainty as to the actual dielectric constant of the material. It is therefore advisable to make laboratory tests on sample sandwiches to verify that an optimum sandwich has indeed been designed for the materials in question.

Most of the early rigid ground radomes were of the single-skin variety, as shown in Fig. 1. This radome consists of many individual panels with a membrane of the order of $\frac{1}{16}$ inch. The panels are held together by bolting the flanges, which are molded to the membrane. In this particular design, the flanges were about 3 inches in radial depth, and about $\frac{3}{8}$ inch thick, making the total joint about $\frac{3}{8}$ inch thick.



Fig. 1—Typical thin-skin radome.

¹ W. M. Cady, M. B. Karelitz, and L. A. Turner, "Radar Scanners and Radomes," McGraw-Hill Book Co., Inc., New York, N. Y., pp. 265-272; 1948.

² *Ibid.*, pp. 260-265 and pp. 354-360.

³ *Ibid.*, pp. 272-285 and pp. 360-365.

⁴ J. A. Simpson, "Development of 55-foot diameter honeycomb sandwich radome," *Proc. OSU-WADC Radome Symp.*, vol. 1, pp. 460-482; June, 1958.

Radomes of this size (31-foot major diameter) and smaller, have been tested over various antennas by handling them with a crane,⁵ as shown in Fig. 2. The usual procedure is to measure the antenna pattern without the radome, set the radome down, then repeat the measurements. The two patterns can be taken on the same sheet of paper and an immediate evaluation of the effect of the radome on the transmission can be made.

Using the theoretical expression for reflection loss, it can be shown that when a glass-laminate wall ($\epsilon \cong 4$) is used at S band, the reductions in transmitted field strength to be expected are about 1 per cent, 4 per cent, and 12 per cent for wall thicknesses of $\frac{1}{8}$ inch, $\frac{1}{4}$ inch, and $\frac{1}{2}$ inch, respectively.

A typical pattern obtained with the radome in Fig. 1 is shown in Fig. 3. The loss on the peak is 6 per cent. As was the case with many other tests, the actual measured loss is higher than that predicted on the basis of panel reflection alone. The source of this increased loss is the scatter of energy by the panel flanges. This can be seen in the modified sidelobe structure.

This brings us to the third source of loss. Since the flanges on the panel edges constitute a marked discontinuity in the radome wall, some distortion in the radiated wavefront is to be expected. The effect of this distortion on the far-field radiation patterns may be examined in several ways.

One procedure followed at Ohio State University⁶ has been to find the equivalent induced currents on a sample rib, then calculate the pattern obtained when many such ribs are illuminated by the antenna in the radome. This procedure predicts a secondary radiation pattern which must be superimposed on the radiation pattern of the undisturbed antenna. This secondary pattern is, in general, a scatter pattern with no "main beam." The amplitude of the main beam from the antenna is reduced by the addition of the secondary pattern.

Another approach that can be used is to consider the discontinuities as blocking agents. This, of course, reduces the energy available on the peak of the main beam. This point of view is quite useful when considering such items as panel fasteners (sometimes known as locks) molded inside sandwich panels. It has been verified experimentally that for discontinuities such as locks which are of the order of a wavelength or larger in size, a very close estimate of the reduction in transmission can be made simply by calculating the percentage of the area in front of the antenna that is blocked. In other words,

$$E = E_0 \frac{A - a}{A},$$

⁵ W. Lavrench, "Microwave transmission tests on large rigid radomes," *Proc. OSU-WADC Radome Symp.*, vol. 1, pp. 359-377; June, 1957.

⁶ P. D. Kennedy, J. R. Baechle, and S. Chen, "Electrical effects of the ribs of large radomes," *Proc. OSU-WADC Radome Symp.*, vol. 1, pp. 483-489; June, 1958.



Fig. 2—A radome being lowered by a crane during transmission tests.

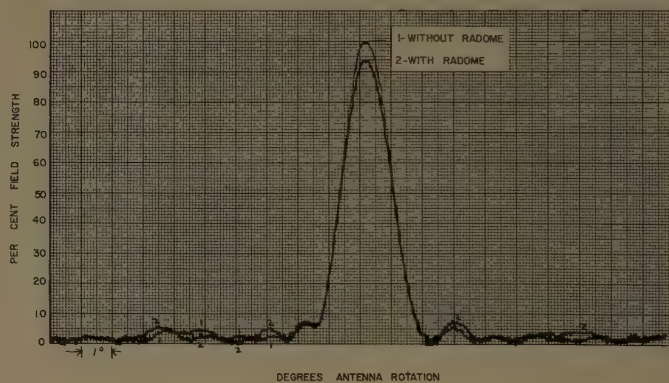


Fig. 3—Radiation pattern of an S-band antenna in the radome of Fig. 1.

where

E_0 = the undisturbed field strength on the main beam,
 E = the field strength with scatterers in front of the antenna,
 a = the total area occupied by the scatterers, and
 A = the antenna aperture area.

Detailed discussion of the effect of the flanges on transmission loss will be left until sidelobes have been discussed, since the two are very closely tied together.

The fourth source of reduction in transmission is a distortion of the wavefront by the radome wall. A radome wall can be designed to produce negligible reflection loss and can still exhibit a reduction of field strength on the peak of the main beam simply because of phase errors. Mathematical analysis of such a case will show the existence of scattered energy which of

course must come from the main beam. Again, examples will be left until after the discussion of sidelobes.

SIDELOBES

The presence of discontinuities such as flanges and ribs in a radome wall leads to scattering of energy which not only reduces the amount of power in the main beam, as mentioned above, but also changes the sidelobe structure of the antenna in question. It has been found experimentally that for a given number of ribs in front of the antenna, the reduction in transmission is practically independent of the orientation of the ribs. This is so since the amount of scattered energy is the same, to a first approximation. The behavior of sidelobe structure, however, is quite closely connected with the orientation of the ribs. When the ribs or flanges are placed in a uniform fashion (parallel and equidistant), the scatter from the ribs adds at certain angles to produce definite sidelobes. If the ribs are placed at random, the scattered energy does not form distinct sidelobes but tends to smear the existing antenna sidelobes. It will be appreciated that some of the scatter sidelobes may be out of phase with an antenna lobe, thereby reducing the latter in size. The converse is just as apt to happen—an antenna sidelobe can be increased. This can be seen in Fig. 3. It may be thought that this scatter of energy could be avoided by covering the flanges with absorbing material. This, of course, is a fallacy, since such a procedure produces "holes" in the aperture distribution of the antenna, and theoretical analysis shows that new sidelobes will still be formed.

If we assume constant amplitude and equiphase distribution across an aperture which is blocked by n equidistant strips as shown in Fig. 4, it can be shown that the pattern of the antenna can be given by

$$F = 2a \frac{\sin \beta}{\beta} - 2b \left\{ 1 + 2 \sum_{l=1}^{(n-1)/2} \cos l\phi \right\} \quad \text{for } n \text{ odd,}$$

$$= 2a \frac{\sin \beta}{\beta} - 2b \left\{ 2 \sum_{l=1}^{n/2} \cos \left(l - \frac{1}{2} \right) \phi \right\} \quad \text{for } n \text{ even,}$$

where

$$\beta = \frac{2\pi a}{\lambda} \sin \theta,$$

and

$$\phi = \frac{2\pi d}{\lambda} \sin \theta.$$

These expressions indicate a loss on the peak of the main beam of $n(b/a) \cdot 100$ per cent, and new sidelobes, the largest of which are $n(b/a) \cdot 100$ per cent of the main

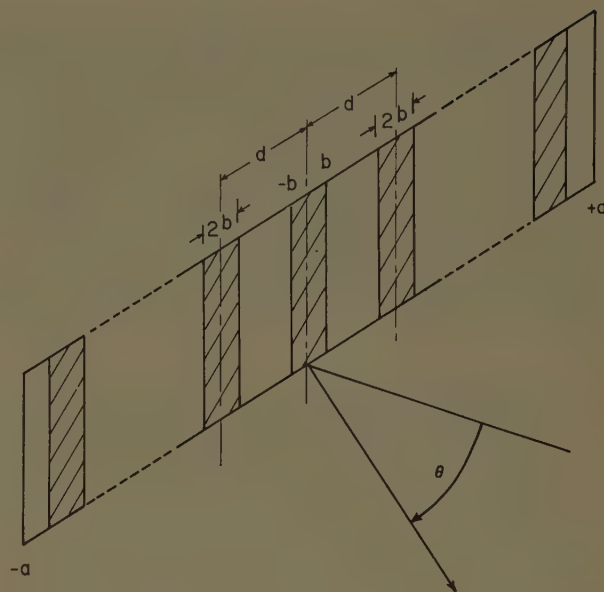


Fig. 4—Aperture blocked by n strips.

undisturbed beam and which are separated by an angle

$$\theta = \sin^{-1} (\lambda/d)$$

$$\cong \lambda/d.$$

This has been verified experimentally. A fourteen-foot wide S-band antenna was used. Three 6-inch strips on the antenna were covered with absorbing material, one in the center and one 5 feet each side of center, to produce three gaps in the aperture distribution. Fig. 5 shows radiation patterns obtained with and without the absorbing material on the antenna. It is evident that sizable sidelobes are produced. Calculations indicate that the loss on the main beam and the size of the new sidelobes should be about 11 per cent of the main undisturbed beam. The patterns show that these items run around 12 per cent.

Fig. 6 shows patterns obtained with a different arrangement of the same absorbing material. In this case the three discontinuities did not form a periodic structure and no new distinct sidelobes were produced. However, the loss on the peak of the main beam remains about the same. This is to be expected since the same amount of antenna is blocked.

Antenna patterns were taken with and without the radome over the antenna. Symmetrical and asymmetrical ribs were tested in turn. It was found that the reduction of the main beam amplitude was the same in both cases, but the sidelobe structure was vastly different, as shown in Figs. 7 and 8.

To study the variation of loss and sidelobes with radial depth of the ribs, simulated ribs consisting of three glass-cloth laminate strips $\frac{1}{2}$ inch thick and of various widths, were tested in front of a fourteen-foot S-band antenna. The strips were placed so that propagation was parallel to the wide dimension of the strips, as would be the case in a radome. The results are

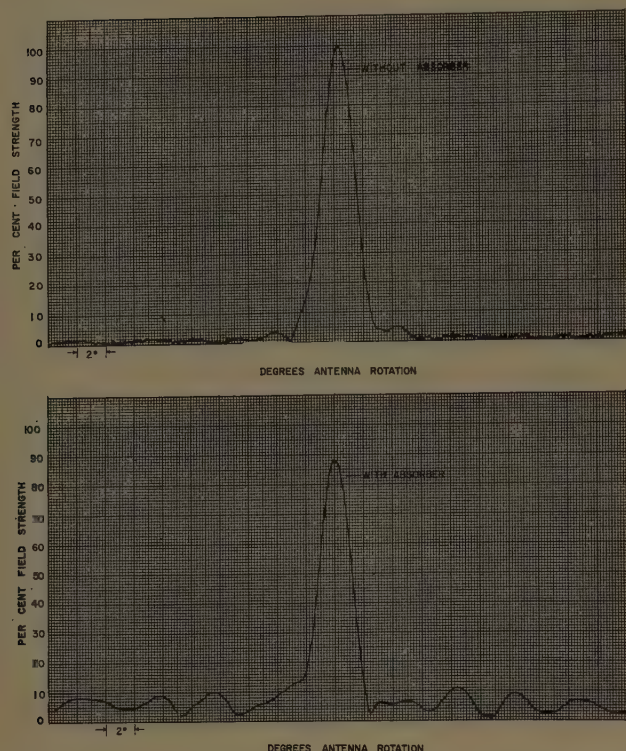


Fig. 5—Radiation patterns with and without three symmetrical absorbing strips in front of an antenna.

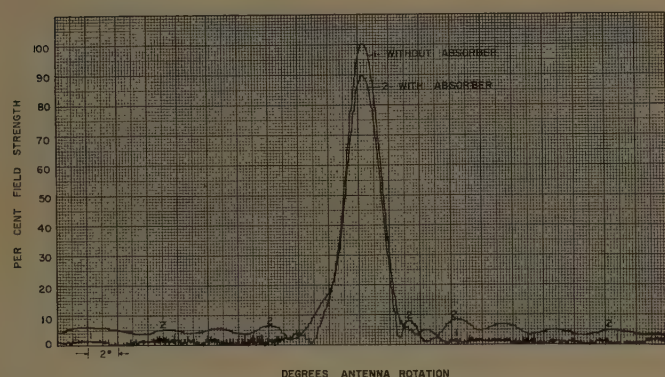


Fig. 6—Radiation patterns with and without three asymmetrical absorbing strips in front of an antenna.

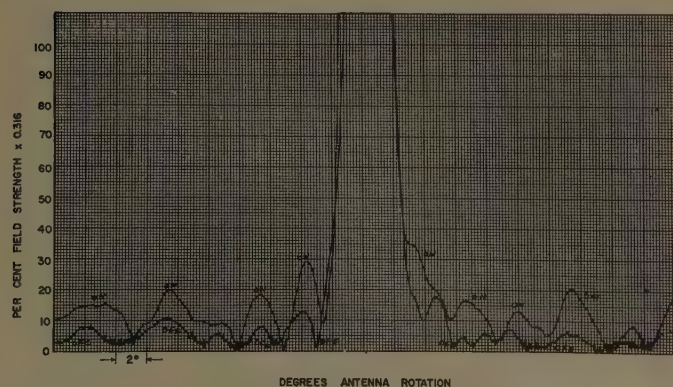


Fig. 7—Radiation patterns with and without symmetrical radome flanges in front of an antenna. Main beam taken as 100 per cent.

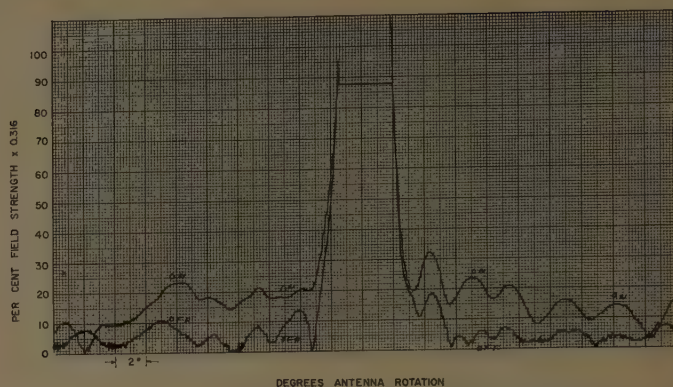


Fig. 8—Radiation patterns with and without asymmetrical radome flanges in front of an antenna. Main beam taken as 100 per cent.

plotted in Fig. 9. Amplitude of sidelobes has been plotted as a percentage of main beam amplitude. It can be seen that the scatter sidelobes grow in almost a linear fashion with increase in radial depth of the strips.

In order to check the variation of loss with the number of ribs in front of an antenna, a different experiment was performed. Strips of 1 inch \times 2 inch wood, covered with metal foil, were placed in front of an antenna to simulate radome ribs. Antenna patterns were plotted with different numbers of strips in front. In all cases the total antenna aperture was equally divided by the strips in use. A summary of these tests appears in Fig. 10. The reduction in field strength is about proportional to the total number of ribs in front of the antenna, and the scatter sidelobes increase in amplitude with increase in number of ribs.

METAL FLANGES

Larger radomes of the space-frame variety call for stronger and therefore larger flanges. One solution could be the use of metal flanges⁷ to produce the space frame, and a dielectric membrane to complete the surface of the radome. Acting on a suggestion from Lincoln Laboratory of the Massachusetts Institute of Technology, metal flanges were tested by covering the existing flanges in a radome with metalized tape. In a typical case (see Fig. 11), very little difference in transmission was noted with the flanges covered or uncovered, which indicated that for the particular radome used the flanges could be of either metal or glass-cloth laminate. Metal ribs should prove superior electrically, since for a given mechanical strength they can be smaller than glass-cloth laminate flanges. The conclusions to be drawn from the various tests described are that for best electrical performance, the flanges in a radome should be small in cross section and few in number for low attenuation, and irregularly spaced to avoid prominent scatter sidelobes.

⁷ A. Cohen, P. Davis, S. C. Nilo, and J. F. Orabona, "A 150-foot metal space-frame radome," *Proc. OSU-WADC Radome Symp.*, vol. 1, pp. 343-358; June, 1957.

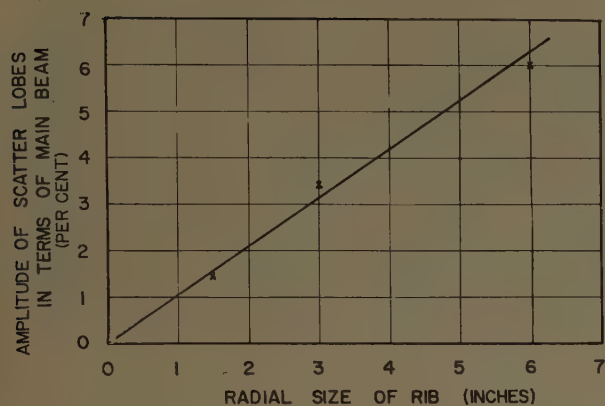


Fig. 9—Amplitude of scatter sidelobes produced by dielectric ribs of various radial depth. Main beam taken as 100 per cent.

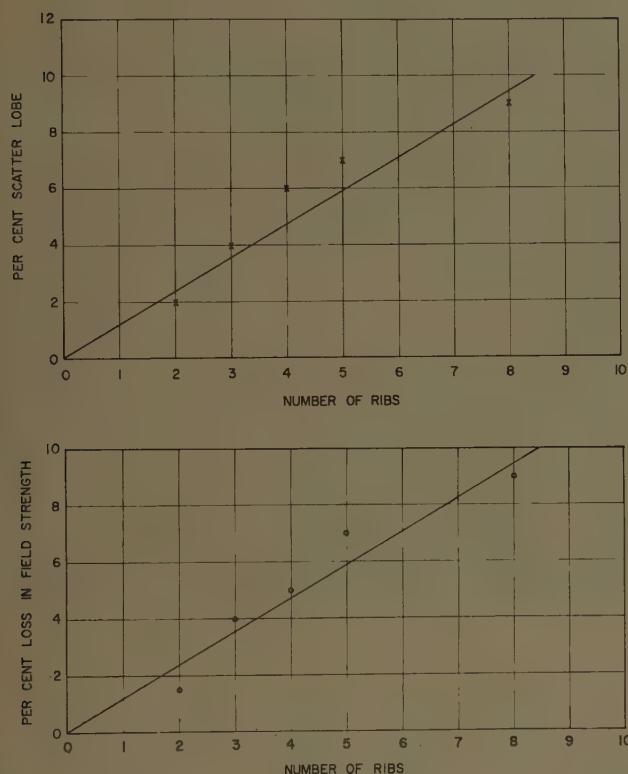


Fig. 10—Variation of scatter sidelobe amplitude and transmission loss caused by various numbers of ribs. Main beam taken as 100 per cent.

PANEL FASTENERS

When the sandwich-type of radome with its embedded locks was under consideration, some measurements were made to evaluate the effect of the locks. The Simmons lock, as supplied by the manufacturer, is encased in metal. It seemed desirable to remove as much of the metal as possible without impairing the mechanical strength of the lock. With this in mind, several panels were made for test purposes wherein the lock had a reduced amount of metal. Transmission tests made through the panels as received, and also with metal foil covering the locks to simulate the original locks, showed that there was no difference in performance. It therefore appears that for scatterers of this

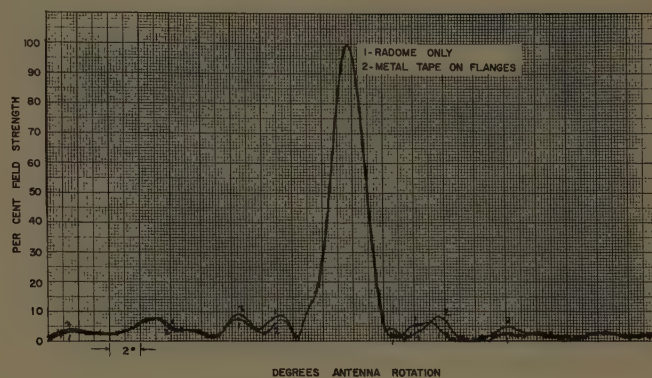


Fig. 11—Metal tape on radome flanges.

size it matters little whether the locks are embedded in a dielectric (to strengthen the bond to the rest of the panel) or metal.

A further test was made to check the magnitude of the effect of the locks. In this test an experimental foam radome (to be described later) was used as a support for simulated locks. The performance of the radome itself had been found previously to be excellent at 3000 mc; therefore its effect in this particular test could be taken as nil. The locks were simulated by cutting pieces of cardboard of the same cross section as the locks, and covering them with metal foil. These "locks" were then stapled to long narrow strips of thin plastic and these strips of plastic were in turn tacked to the inside surface of the foam radome. The strips were placed in such a fashion as to duplicate the lock arrangement of a radome design being considered at that time. Antenna patterns were taken with and without the "locks" on the radome wall. Since the plastic strips were held on only by a few thumb tacks they could be removed rapidly and the two patterns taken very quickly. The results of several such tests showed that the reduction in field strength of the transmitted signal was practically equal to the percentage of the aperture area that was blocked by the "locks." The locks in this case were irregular in shape, with maximum and minimum dimensions of 7.5 and 4 inches.

Similar tests have been carried out elsewhere⁸ and have also demonstrated that when the size of scatterers is of the order of a wavelength or more, the reduction in signal can be very closely approximated by calculating the area that is blocked by the scatterers. No attempt has been made to study the effect of panel bolts on the performance of a radome; however, since the area blocked by the bolts is so small, the effect would be extremely small.

The remaining source of transmission loss and sidelobe deterioration to be mentioned is the distortion of the phase front by a radome wall whose electrical thickness is nonuniform. This effect became evident when attention was turned to a thick foam wall.

⁸ J. Vaccaro, Rome Air Dev. Center, Rome, N. Y., private communication.

TABLE I
LOSS IN TRANSMISSION WITH VARIOUS ANTENNA/RADOME COMBINATIONS
(ALL TESTS AT S BAND)

Radome	Antenna	FPS-14 12×17 feet	MPS-501 2×14 feet	FPS-502 4×21 feet	ASR-3 9×9 feet
1)	Space Frame: 31-foot diameter, 9-foot triangular panels with $\frac{3}{16}$ -inch×3-inch flanges and membrane about $\frac{1}{16}$ inch to $\frac{1}{8}$ inch.	—	8 per cent	—	—
2)	Space Frame, shown in Fig. 1: 31-foot diameter, hexagonal and pentagonal panels with $\frac{3}{16}$ -inch×3-inch flanges and $\frac{1}{16}$ -inch or thinner membrane.	7 per cent	6 per cent	—	—
3)	Stressed Skin, shown in Fig. 2: 26-foot diameter, 4-foot×8-foot panels with $\frac{1}{8}$ -inch×1½-inch flanges and a $\frac{1}{8}$ -inch membrane.	7 per cent	—	10 per cent	6 per cent
4)	Stressed Skin: essentially identical with radome 3) except for a wall thickness of $\frac{1}{16}$ inch.	6 per cent	—	—	—

Table I summarizes the results obtained in transmission tests with various S-band antennas in several different radomes. It is not surprising to note that different radomes produce different losses with a given antenna. This is so because of the geometry of the flanges and the thickness of the membrane. The interesting point to note is that a given radome has different effects on different antennas.

As indicated in Table I, the lowest transmission loss obtained at S band was 6 per cent. The operation of these radomes at X band was much poorer. In order to increase the transmission, reduce the sidelobe effect, and permit the use of a radome at X band, a new wall design was studied. This design consisted of a thick wall made of blocks or panels.⁹ The use of a thick wall would permit simple glued V or tongue-and-groove joints, thereby reducing the amount of discontinuity at the edges of the panels. In order to use thick walls and keep down the cost and weight of the radome it was decided to use a foam material. The most readily available material at the time was foamed polystyrene, and as a result the first foam radome was made of expanded Dylite beads. The density was of the order of 2.5 pounds per cubic foot, and the panels were about 3 feet by 4 feet by 4 inches thick. This radome is shown in Fig. 12. Both sides of the panels were covered with a single layer of glass cloth. It must be pointed out that this type of construction falls into none of the types previously outlined. Even though it is basically a sandwich, the skins are so thin in terms of wavelength (S band) that the reflection from each skin is very small. Because of this, electrical effects were neglected and the thickness of the core was based entirely on mechanical considerations. In order to increase the usefulness of the radome for test purposes, the panels were assembled in three different ways. One-third of the radome was



Fig. 12—Expanded Dylite foam radome.

joined with a high-density glue (approximately 70 pounds per cubic foot); another third with a medium density glue (25 pounds per cubic foot); and the remaining third was assembled by bonding 2-inch strips of glass cloth on the inside and outside of joints. This procedure was possible because any antenna usually looks through less than one-third of the radome's circumference at any given time.

Results at S band were very good. As can be seen in a typical pattern (Fig. 13), the loss in transmission is 1 per cent, with negligible effect on the sidelobe structure. The transmission loss was found to be 2 per cent, 1 per cent, and 1 per cent for the portions with high-density glue, medium-density glue, and taped joints, respectively.

Tests at X band⁹ showed the transmission loss to be about 8 per cent (see Fig. 14). Small scatter sidelobes are evident. At first these were considered to be caused by the glue line at the joint and the extra glass-cloth

⁹ W. Lavrench, "Electrical and mechanical tests on a 26-foot foam radome," *Proc. OSU-WADC Radome Symp.*, vol. 1, pp. 523-538; June, 1958.

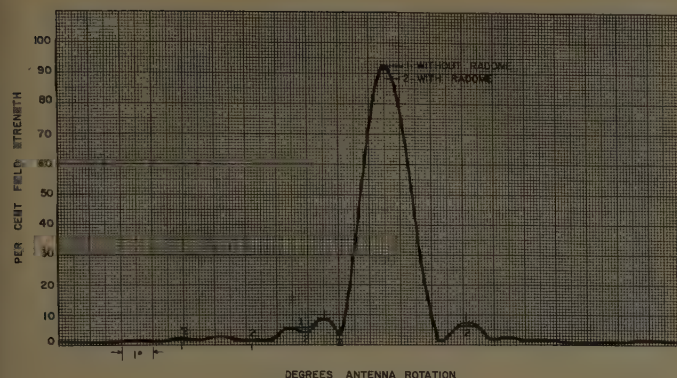


Fig. 13—Transmission test of foam radome at S band.

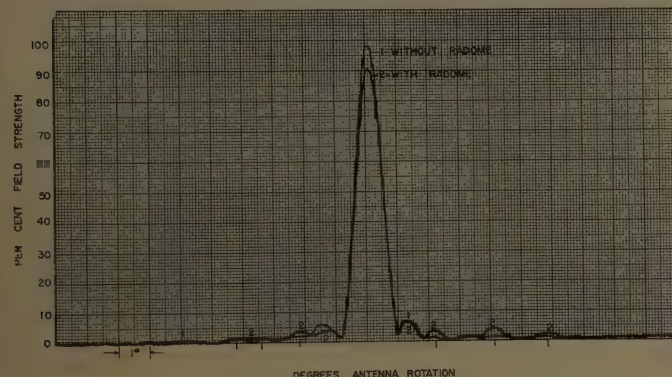


Fig. 14—Transmission test of foam radome at X band.

tape, but later tests showed a new source of trouble at X band.

Additional panels were obtained to study the effect of the joints at X band. The new panels were assembled in front of an antenna with no glue at the joints, and it was found that the sidelobes and loss were now much larger than those produced by the radome (see Fig. 15). Extensive tests disclosed that if the skins on the panels were removed and the panels allowed to age, this effect disappeared. Measurements of the insertion phase delay produced by the panels at X band showed that the phase delay varied considerably over the panel surface even though the physical thickness was quite uniform. A typical set of measurements is shown in Fig. 16. A wall formed from panels of this type would show a periodic variation in phase delay; hence the production of scatter lobes. The scattered energy results in a reduction in the main beam. When the skins were removed and the phase measurements made from day to day, it was found that the path lengths through the central portions of the panels diminished slowly until the electrical thickness of the entire panel was uniform to within two to three degrees. It appears that the panels had entrapped water vapor near the central portion which raised the dielectric constant. This water vapor originated during the process of manufacturing the panels. When the skins were removed, the water vapor escaped.

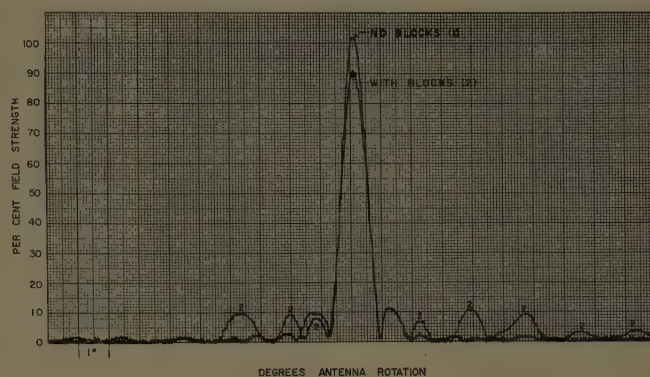


Fig. 15—Transmission tests at X band through foam blocks of the type used in the radome of Fig. 12.

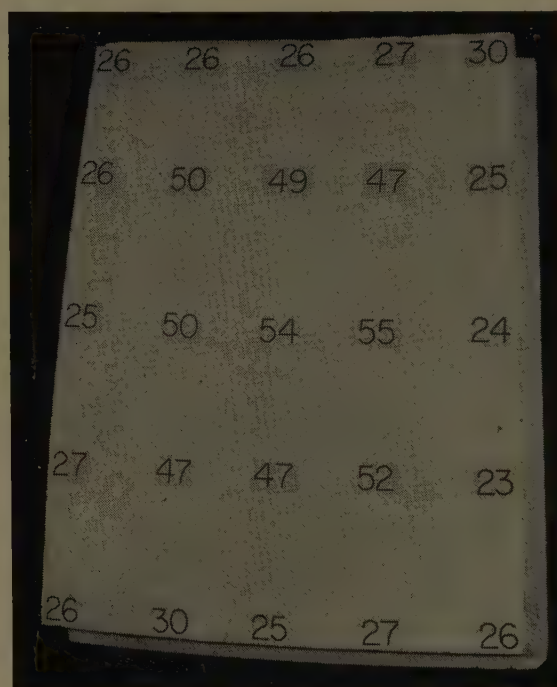


Fig. 16—Variation of insertion phase delay in degrees over a sample foam block.

FOAMED JOINTS

In order to reduce the effect of the glue line in a foam radome, studies were made on the possibility of foaming a joint between two foam panels. Foam panels with a density of 4 pounds per cubic foot were cut into sections about 12 inches wide and then joined with a new foam mixture. The same type of foam was used and different densities were tested. The density of the foamed-in-place joints ranged from 4 to 12 pounds per cubic foot (see Fig. 17). The foam joints were placed much closer together than would be the case in a full-sized radome. This was done in order to exaggerate the effect of the joints. In actual practice, such joints are expected to be of the order of four to five feet apart, hence scatter sidelobes and loss can be estimated by dividing the measured values by four or five.

The worst case occurred when the 12-pound foam was used in the joint. Fig. 18 is a sample of the results obtained. The sidelobes are very large; however, in practice, with a five-foot panel they would be about one-fifth this size, which would make them of the same order as the sidelobes of the antenna. Lower density joints gave still better performance. It thus appears that a foamed-in-place joint should be quite satisfactory electrically.

If an antenna having a maximum sidelobe of -26 db is used in a radome made of 4 pounds per cubic foot foam, it is estimated that joints spaced four feet apart can vary in density from about three to five pounds per cubic foot for a rise in the sidelobe not greater than 1 db. If a 2-db rise in sidelobe is permissible, the joint density can be between 2 and 6 pounds per cubic foot. These two cases would correspond to scatter sidelobes of about -42 and -38 db. Loss due to scatter would be of the order of 1 per cent.

A comparison between a glued joint and a foamed-in-place joint is shown in Fig. 19. In both cases, 4-pound foam was used in the joint. In one case the joint was

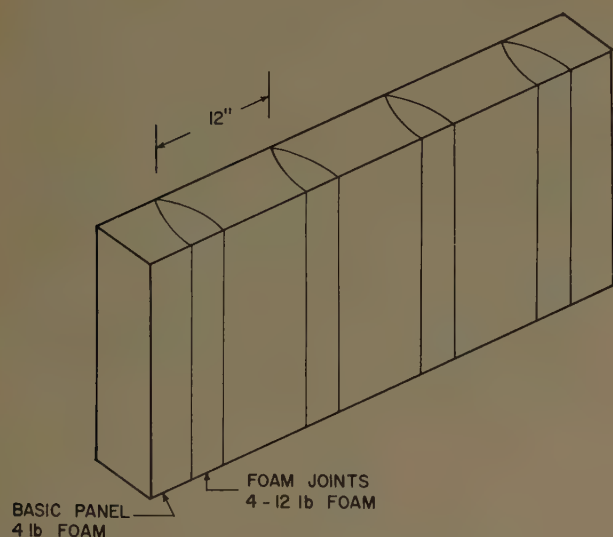


Fig. 17—Foamed joints in foam panel.

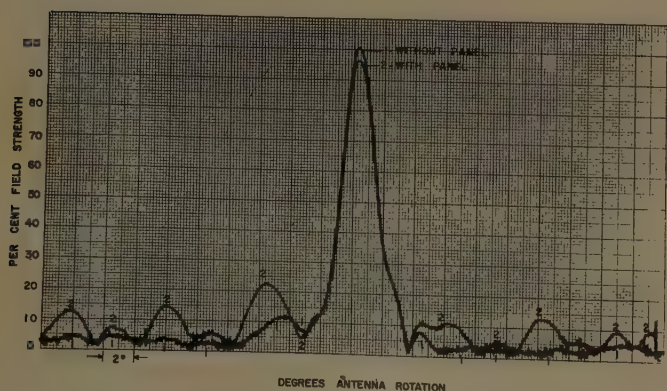


Fig. 18—Transmission through 4 pound per cubic foot panel with 12 pound per cubic foot joints.

foamed as shown in Fig. 17, and in the other, wedges were cut from the same blocks that were to be joined and then cemented in place as shown in Fig. 20. The superiority of the foamed joint is evident.

CHANGES IN ANTENNA VOLTAGE STANDING WAVE RATIO CAUSED BY REFLECTIONS

Reflections from the radome wall not only reduce the useful transmitted energy but may also adversely affect the operation of the enclosed antenna. Reflections picked up by the antenna are fed down the cable or

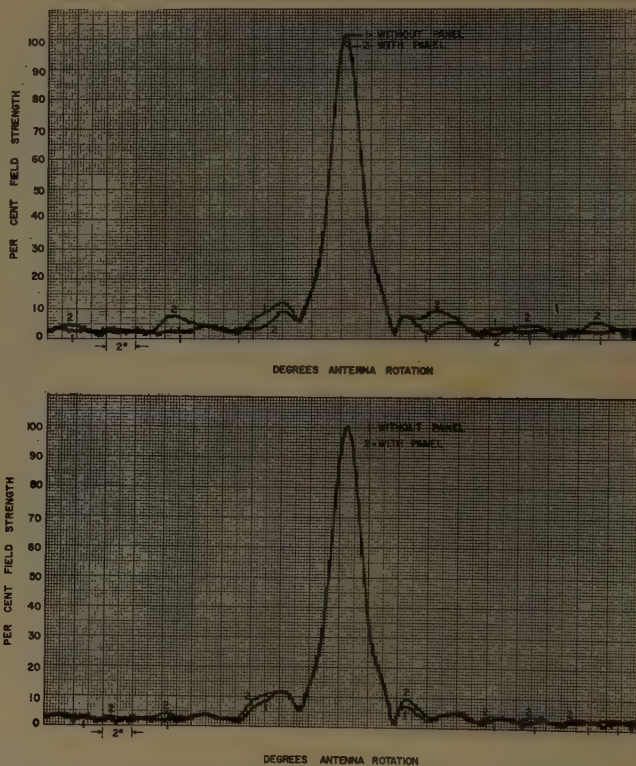


Fig. 19—Comparison of (top) glued and (bottom) foamed joints.

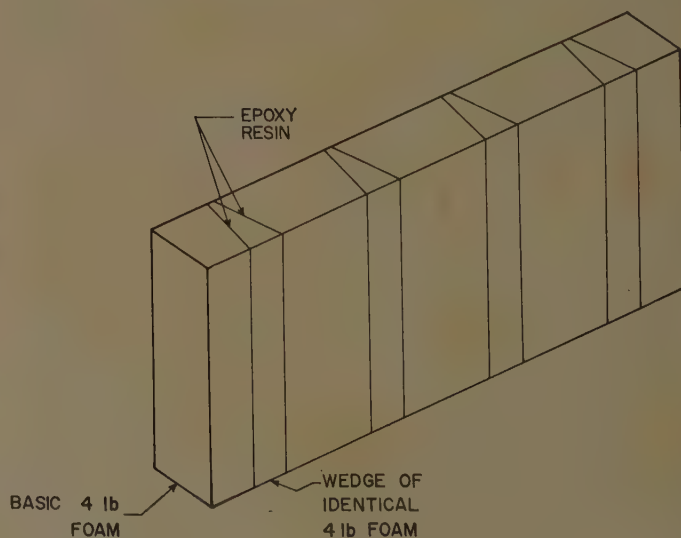


Fig. 20—Foam wedges glued between foam panel sections.

waveguide to the transmitter. The resultant voltage standing wave ratio (VSWR) can be measured in several ways. A slotted line can be inserted in the transmission line or waveguide which feeds the antenna and the VSWR checked for the case of no radome and also with the radome over the antenna. This method of measurement has two disadvantages. First, since the VSWR is likely to vary with radome-antenna orientation, many separate readings must be taken, and even then important spots may still be missed. Second, for small variations in VSWR near the matched condition ($VSWR=1$) the method is not very sensitive. The procedure adopted here was to insert a directional coupler in the transmission line and to record on a chart the reflected energy, while either the antenna or the radome was being rotated. The directional coupler is made ideal by matching it with a sliding screw tuner when a flat load is connected in place of the antenna feed. The tuner is adjusted for zero reflected signal. The complete system is calibrated by placing a short circuit at the end of the transmission line to give a known reflection. A typical plot is shown in Fig. 21; this was obtained with a 12-foot by 17-foot *S*-band antenna in a 26-foot thin-skin radome. It can be seen that once the calibration has been performed, the gain of the system can be increased by a known amount so that full-scale deflection is not equal to a reflection coefficient of unity, but something much smaller. In this case, the gain has been increased by 10 db to make full-scale equal to a reflection coefficient of 0.316. In this manner the recorder is capable of detecting extremely small variations in VSWR.

Reflections cause frequency pulling where a magnetron is used as the transmitter. An example of this occurred when the radome of Fig. 2 was used over a 9-foot by 9-foot *S*-band antenna. The radome was placed over the antenna, which was installed on a tower. The original design of the tower dictated that the center of the antenna be located on the major diameter of the radome and three to four feet from the vertical center. When the antenna was rotated, rapid fluctuations in reflection were observed. The worst reflections

occurred when the antenna was looking at the nearest and furthest points of the radome. In these cases the radome wall was largely normal to the direction of propagation. The rapid variations in reflection resulted in magnetron pulling of such an order that the use of an echo box was impossible while the antenna was rotating. Further, it was stated by the radar operators that MTI operation was affected.

The solution to this particular problem was to elevate the antenna by three feet to avoid hitting the radome wall at normal incidence. This proved quite effective. It must be remembered that this sort of solution would be impossible in cases where very large antennas are used and antenna-radome clearances are small. However, it has been found that variations in VSWR are smaller for antennas which are larger relative to the radome.

BORESIGHT TESTS

This laboratory has been involved in the design and testing of ground radomes for three or four years, but boresight measurements have been undertaken only within the past year, and to date boresight information has been obtained for only one antenna-radome combination. The radome tested was a 55-foot paper honeycomb sandwich designed for use at *S* band. A radome of this size is difficult to handle with a crane; therefore, a special test site was erected. The test stand consists of two platforms resting on individual footings. A stationary circular central platform supports the antenna. Surrounding this platform is an annular platform which rides on a circular track. The radome is erected over three metal supports on the annular platform. The supports are spaced 120° apart. After the radome has been completely assembled, it is blocked up so that a large part of its weight rides on the supports. Following this, one-third of the radome is removed to provide a window, as shown in Fig. 22. The radome can now be rotated about the antenna in order to make various measurements "with and without" the radome.

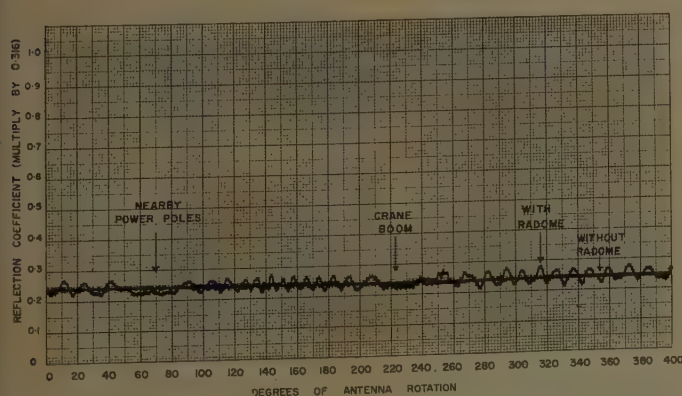


Fig. 21—Variation of radome reflection with antenna rotation. 12-foot \times 17-foot *S*-band antenna in a 26-foot thin-skin radome.



Fig. 22—Boresight tests on CW-423 radome over an AN/FPS-6 antenna.

The antenna used in this test was part of a single-beam height-finder radar. In order to facilitate boresight measurements, the feed in the antennas was modified to produce a split beam to simulate an amplitude-comparison monopulse system. The signals received by the two separate horns at the feed were detected and subtracted to produce a null axis. An upward shift of the beam produces an error signal of one polarity and a downward shift of the beam produces an error signal of opposite polarity. The error signal drives a recording pen. The entire system is first calibrated by nulling the antenna under test on the transmitting antenna while looking through the open section of the radome. The distant transmitting antenna is then moved known amounts on a linear track to position the recording pen at various spots on the chart. The transmitting antenna is then returned to the null position and locked. Subsequent rotation of the radome shifts the antenna beam and produces error signals. These are plotted on a chart whose rotation is linked to the rotation of the radome.

Boresight errors have been measured for both the vertical and horizontal planes, and typical results are shown in Figs. 23 and 24. In the vertical plane, large boresight errors can be noted when each of the three metal supports passes in front of the antenna. The remainder of the pattern shows the errors produced by the radome wall. It will be noted that there is a negligible variation in the beam position between 40° and 120° , and between 310° and 30° , in Figs. 23 and 24 respectively. In these angular intervals the open section of the radome passes by. The maximum boresight shift in the vertical is $\frac{1}{4}$ milliradian, and in the horizon-

tal, 2 milliradians. The horizontal shift was measured by replacing the feed with a pair of horns to provide a split beam in the horizontal plane.

The explanation for the difference in boresight error is thought to be as follows. Near the equator of the radome where the maximum radiation from the antenna is incident, the panel joints are spaced about six feet apart. The antenna is 7.5 feet wide. Therefore, at any one time, there is only one joint in front of the antenna in the horizontal dimension, and as this joint moves across the antenna aperture a sizable boresight error occurs. On the other hand, the antenna is 30 feet high, and thus the vertical dimension of the antenna sees several joints at any one time. The errors produced would thus tend to cancel.

CONCLUSIONS

It is certainly no surprise that the behavior of a radome is different at different frequencies, but an important point to note is that the same radome will have different effects on various antennas operating on the same frequency. This is particularly true for radomes with discontinuities in the walls. The resultant transmission coefficient and sidelobe effect is closely tied to the radome-antenna geometry. This comes about because the antenna's operation is disturbed largely by that portion of the radome directly in front of it. Thus, final results depend on whether the antenna is short and wide, tall and narrow, or falls somewhere in between. This was shown in Table I where transmission losses of three different antennas were compared.

These results point out the need to investigate all antennas under consideration rather than to attempt to extrapolate from previous measurements.

In order to design and build adequate radomes, the results of the many tests may be summarized as follows:

Stressed-Skin or Space-Frame Radomes

- 1) Skin should be very thin in terms of wavelength.
- 2) Use as few joints as possible.
- 3) Make joints as small as possible.
- 4) Space joints in a random fashion.

Sandwich Radomes

- 1) Core thickness should be chosen for maximum transmission.
- 2)-4) As stated above for single-skin radomes.

Foam Radomes

- 1) Foam should be uniform to avoid wave-front phase distortion.
- 2) Foam joints instead of glued joints should be used. Tolerance on foam in joint is not too strict.

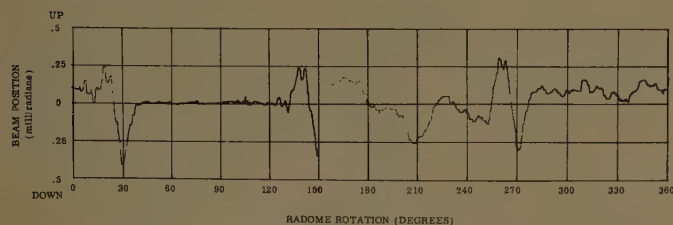


Fig. 23—Vertical beamshift. Antenna and radome of Fig. 22.

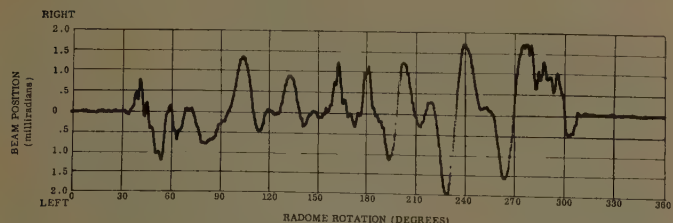


Fig. 24—Horizontal beamshift. Antenna and radome of Fig. 22.

Near-Field Measurements on a Logarithmically Periodic Antenna*

R. L. BELL†, MEMBER, IRE, C. T. ELFVING‡, MEMBER, IRE, AND R. E. FRANKS‡, MEMBER, IRE

Summary—Near-field measurements on a triangular-tooth log periodic antenna reveal that two waves exist on the structure. A transmission line wave travels from the apex to the “active region” of the antenna and excites currents in the teeth or radiating elements in this region. These currents, in turn, launch a radiated wave which accounts for the far-field pattern characteristics of the antenna. The antenna is shown to exhibit a pronounced degree of increased directivity.

Near-field measurements made through one period of operation show smooth variations of the field distributions with frequency.

I. INTRODUCTION

A NEW CONCEPT, in which an antenna is specified entirely by angles, was formulated by Rumsey¹ for frequency independent antenna designs. Application of this concept to any finite antenna, however, results in the appearance of at least one characteristic length. The problem then becomes one of finding a finite angular structure which has electrical properties that converge rapidly to those of the infinite structure.

An investigation by Dyson² revealed that the electrical characteristics of the equiangular or logarithmic spiral structures are essentially independent of frequency which indicates rapid convergence. These structures are circularly polarized and may be made unidirectional by folding the spiral back on a cone.³

A linearly polarized antenna with similar broad-band characteristics was developed by DuHamel and Isbell⁴⁻⁶ by modifying a planar angular structure to include logarithmically periodic discontinuities. The introduction of these discontinuities increased the rate of con-

vergence of the finite structure or, in other words, decreased the “end effects.” More precisely, the resulting structure is pseudo frequency-independent, since the electrical characteristics vary periodically with the logarithm of the frequency. The principles underlying the unlimited bandwidth properties of this type of structure, used singly and in arrays, have been well developed; however, little explanation has been offered as to why the basic periodic structure should radiate at any frequency. While many variations of this structure have been developed experimentally,⁶⁻⁹ applications may have been limited and designs may have been less than optimum because of a lack of knowledge of the basic means by which radiation occurs from these structures.

To gain better understanding of the theory of operation, near-field measurements were made on a logarithmically periodic antenna. The electric field distribution measured near the structure and the currents measured in the elements are presented in this report, along with a discussion of the waves on the antenna. No complete analysis of the operation of the antenna is attempted at this time; however, it is hoped that the data presented here will contribute to a better understanding of how these structures operate.

II. DESCRIPTION OF ANTENNA AND TEST SETUP

The type of antenna on which all data were taken is a nonplanar, log-periodic antenna with triangular teeth,⁶ as shown in Fig. 1. The angles α and ψ define the extremities of the teeth and the angle between the two half structures, respectively.

The logarithmic design ratio τ is the ratio of two adjacent similar dimensions on the antenna. In terms of the antenna lengths measured from the apex (see Fig. 1), τ is equal to R_{n+2}/R_n and R_{n+1}/R_n is equal to $\tau^{1/2}$.

Values selected for the above parameters are

$$\tau = 0.85,$$

$$\alpha = 28^\circ,$$

$$\psi = 32^\circ.$$

* Received by the PGAP, January 13, 1960; revised manuscript received, May 23, 1960. The work described in this paper has been supported by the Signal Corps under Contract DA 36-039 SC-78281.

† Granger Associates, Electronic Res., Palo Alto, Calif. Formerly at Sylvania Electronic Defense Labs., Mountain View, Calif.

‡ Sylvania Electronic Defense Labs., Sylvania Electric Products, Inc., Mountain View, Calif.

¹ V. H. Rumsey, “Frequency independent antennas,” 1957 IRE NATIONAL CONVENTION RECORD, pt. 1, pp. 144-148.

² J. D. Dyson, “The Equiangular Spiral Antennas,” Antenna Lab., University of Illinois, Urbana, Tech. Rept. No. 21, Contract AF 33(606)3223; September 15, 1957. Also, IRE TRANS. ON ANTENNAS AND PROPAGATION, vol. AP-7, pp. 181-187; April, 1958.

³ J. D. Dyson, “The Unidirectional Equiangular Spiral Antenna,” Antenna Lab., University of Illinois, Urbana, Tech. Rept. No. 33, Contract AF 33(606)3220; July 10, 1958. Also, IRE TRANS. ON ANTENNAS AND PROPAGATION, vol. AP-7, pp. 329-334; October, 1959.

⁴ R. H. DuHamel and D. E. Isbell, “Broadband logarithmically periodic antenna structures,” 1957 IRE NATIONAL CONVENTION RECORD, pt. 1, pp. 119-128.

⁵ D. E. Isbell, “Nonplanar Logarithmically Periodic Antenna Structures,” Antenna Lab., University of Illinois, Urbana, Tech. Rept. No. 30, Contract AF 33(616)3220; February 20, 1958.

⁶ R. H. DuHamel and F. R. Ore, “Logarithmically periodic antenna designs, 1958” IRE NATIONAL CONVENTION RECORD, pt. 1, pp. 139-151.

⁷ R. H. DuHamel and D. G. Berry, “Logarithmically periodic antenna arrays,” 1958 IRE WESCON CONVENTION RECORD, pt. 1, pp. 161-174.

⁸ R. E. Franks and C. T. Elfving, “Reflector-type periodic broad-band antennas,” 1958 IRE WESCON CONVENTION RECORD, pt. 1, pp. 262-271.

⁹ R. H. DuHamel and F. R. Ore, “Log periodic feeds for lens and reflectors,” 1959 IRE NATIONAL CONVENTION RECORD, pt. 1, pp. 128-137.

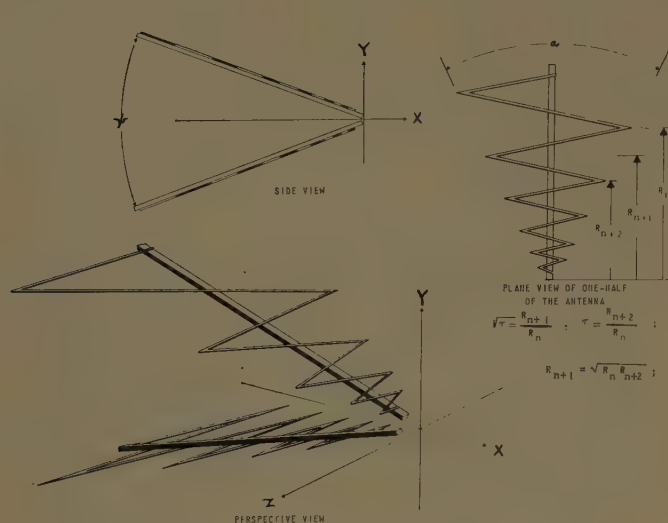


Fig. 1—Parameters and coordinate system for triangular-tooth antenna.

The antenna is approximately 20 feet long and provides essentially frequency independent operation from 50 to 300 Mc. The far-field radiation pattern from this antenna is unidirectional with a maximum in the positive x direction (Fig. 1), and the E plane is parallel to the x - z plane.

The geometry of this type of structure is such that the electrical properties repeat periodically with the logarithm of the frequency. This means, for example, that if one tooth is of resonant length, *e.g.*, one quarter wavelength long, at the frequency f_0 , the next larger tooth on the same side of the supporting boom will become resonant at the frequency τf_0 . The frequency range from τf_0 to f_0 thus defines one period of operation.

The test setup is shown in Fig. 2. Relative phases and amplitudes of the RF fields of the antenna were directly recorded on a Diagraph, type FT-ZDU. For measurement of the E field, a short dipole, 0.15 wavelength long, was used as a test probe as indicated in Fig. 2. For the current measurements in the teeth a small current loop was used.

Measurements of the electric field very near one of the half structures are presented first at a single frequency. An interpretation of these data in terms of two waves on the antenna is then substantiated by electric field measurements in the central or x - z plane of the antenna and by current measurements in the tooth elements.

Following this, the behavior of the field on the structure is shown as frequency is varied through one period of operation.

III. THE ELECTRIC FIELD AT A SINGLE FREQUENCY

A. Electric Field Measurements

The first E -field data are taken in a plane parallel to, and very near, one of the two half-sections of the antenna. It is found that two separate standing waves exist along the structure, one along the teeth on one

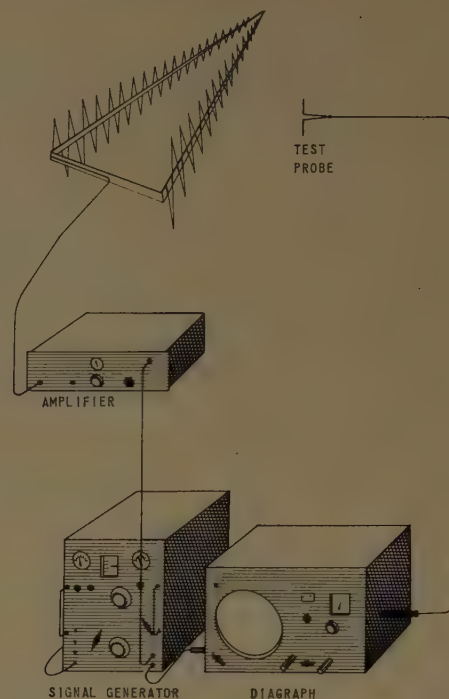


Fig. 2—Test setup for amplitude and phase measurements near the surface of a log periodic antenna.

side of the supporting boom, and another along the teeth on the other side of the boom. Relative phases and amplitudes of these standing waves are shown in Fig. 3. The positive direction of the electric field is away from the boom in a plane parallel to the teeth for both cases.

The figure reveals several interesting features of the E -field distribution on the structure. The two standing waves are 90° out of phase in time and are separated by approximately a quarter of a wavelength along the structure. The amplitudes of the standing wave patterns are relatively constant up to what is termed the active region, *i.e.*, the region surrounding the tooth that is nearest resonant length. The amplitude then decays very rapidly to negligible values beyond this region. The active region for this particular antenna includes five teeth on each boom and is approximately centered on the tooth nearest resonant length. This definition of the active region is based on significant current amplitudes and phases as shown in Section IV-B. The fact that the electromagnetic fields are negligible beyond the active region is, of course, the reason for the lack of "end effect" with this antenna, as has been previously reported.⁴

B. Electric Field Model

The E -field measurements above suggest a model of the RF field surrounding the structure. The standing waves in Fig. 3 are composed of two traveling waves which are partially indicated in Fig. 4. The first wave is the transverse electromagnetic (TEM) two-wire transmission line wave which originates at the apex of the structure and propagates toward the active re-

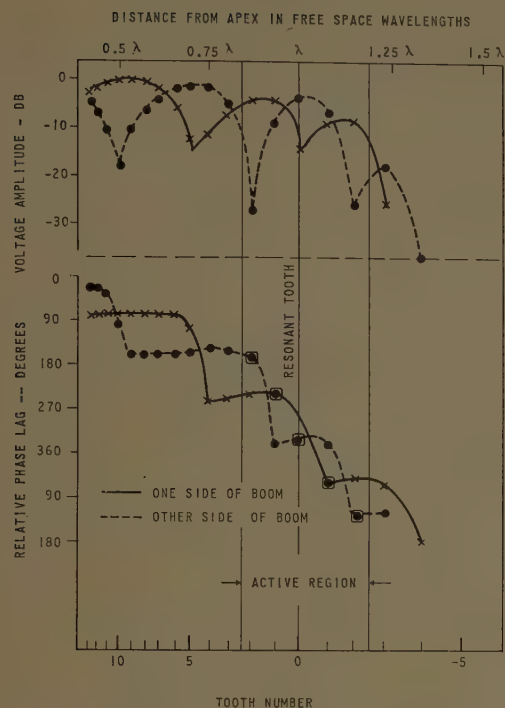


Fig. 3—E-field measurements along the antenna.

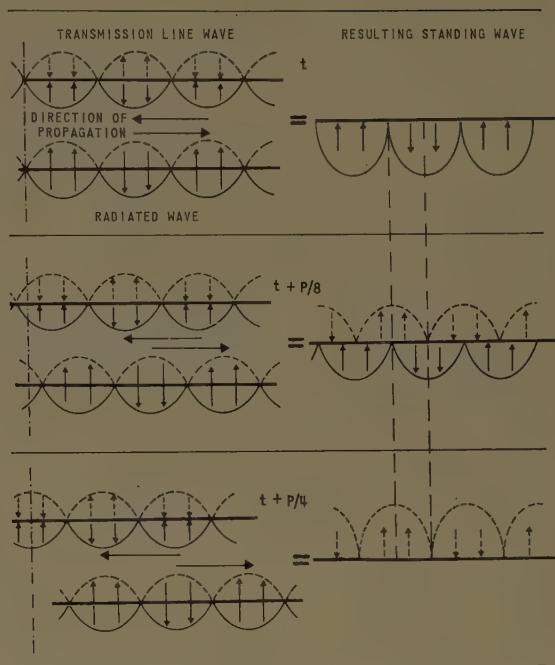


Fig. 5—Model of waves on the antenna giving rise to standing waves.

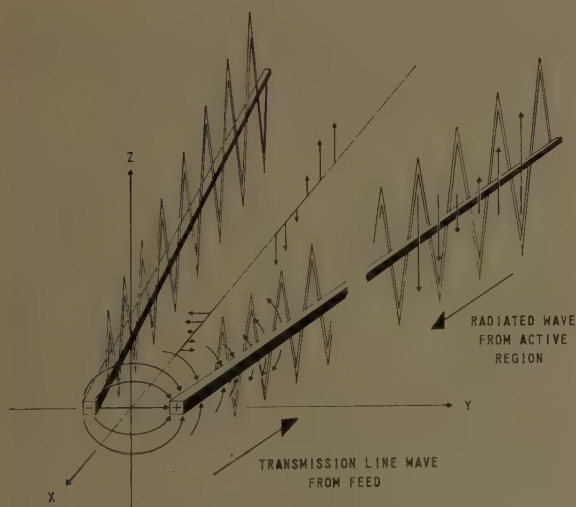


Fig. 4—The two waves on the antenna structure.

gion of the antenna. This wave decays rapidly in the active region of the antenna and has negligible amplitudes at distances beyond this region. The second wave is a radiated wave that originates in the active region and propagates toward the apex of the antenna and then into space beyond. This wave accounts for the far-field pattern characteristics of the antenna.

In the plane of either half of the antenna, the two waves contain parallel field components as shown in Fig. 4. In this plane, the combination of the instantaneous electric fields of the two waves is shown in Fig. 5 to add in such a manner as to produce two standing wave patterns similar to those of Fig. 3, 90° out of phase in time and physically spaced about a quarter wavelength apart.

C. Measurement of the Separate Traveling Wave Components

In order to verify the hypothesis described in the previous section, it is desirable to measure the two waves separately. As may be seen from Fig. 4, the two fields are orthogonally polarized at all points in the central or x - z plane. The electric field of the radiated wave is parallel to this plane, and the electric field of the transmission line wave is perpendicular to this plane. Hence, by measurements of the electric field in and orthogonal to this plane, the components of these waves can be determined independently of one another.

Fig. 6(a) shows the phase and amplitude of the electric field of the transmission line wave as measured along the x axis. The phase progression in either direction from the apex is linear except for distortion very near the apex caused by the finite size of the dipole probe. Some distance in front of the antenna the phase velocity is that of free space, while in the immediate vicinity of the antenna, between the apex and the active region, the phase velocity is approximately $\frac{2}{3}$ that of free space. This indicates that the portion of the antenna structure between the apex and the active region behaves as a slow wave transmission line. The structure is physically similar to a slow-wave helical wound conductor, so that it is plausible that the propagation characteristics should be that of a slow-wave structure.

The amplitudes in Fig. 6(a) are shown plotted on a logarithmic distance scale from the apex in Fig. 7. The field in front of the antenna falls off at a rate of 6 db for a two-to-one change of distance (one octave of distance) which indicates a $1/r$ field dependence. Inside

the antenna, between the apex and the active region, the average rate of field variation is also 6 db for a two-to-one change of distance; however, a standing wave pattern is imposed upon this average variation which agrees with the VSWR about the nominal impedance measured at the antenna feed. Since the expansion of the antenna at any point of the central or x axis is proportional to the distance from the apex, and a constant RF potential exists between the two halves of the structure for the TEM transmission line mode, it follows that the electric field of the transmission line wave should vary as $1/r$ along the central axis. In the active region the field decays at an extremely high rate, indicating that the field is essentially terminated in this region. The field beyond this region reverts to the 6-db slope, but the wave is attenuated greater than 20 db in the active region.

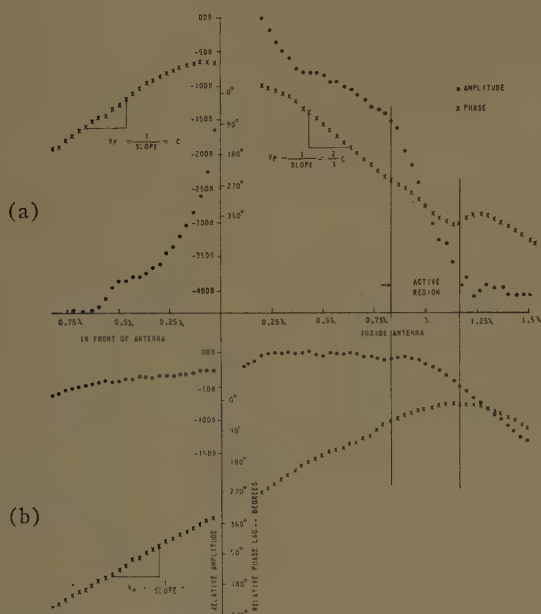


Fig. 6—Phases and amplitudes of the two waves measured along the center axis of the antenna (x axis). (a) Transmission line wave. (b) Radiated wave.

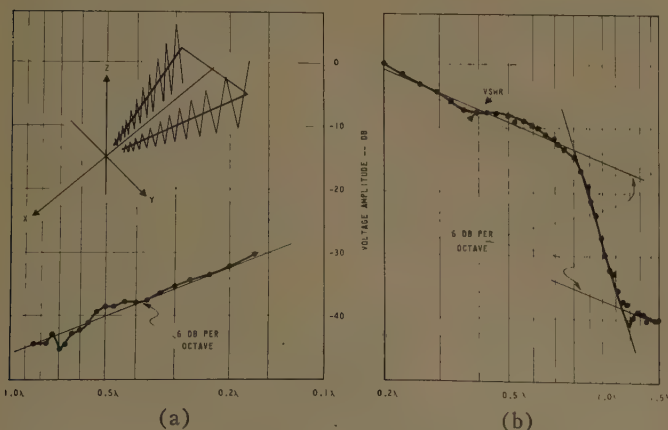


Fig. 7—Amplitude of the transmission line wave measured along the x axis. (a) Distance along x axis in front of antenna. (b) Distance along x axis inside of antenna.

Fig. 6(b) shows the amplitude and phase of the radiated field along the central axis of the structure. The phase progression is that of a wave originating in the active region and propagating at the velocity of free space outside this region. The amplitude of this field builds up in the active region with minor variations in the near field. At some distance in front of the antenna, the amplitude falls off in the manner of a diverging wave.

To give a more complete picture of these fields, contour plots for constant phase and amplitude of both fields in the central or x - z plane are shown in Fig. 8. Since the contour plots of both fields are symmetrical about the x axis, only half of each complete contour is shown in the figure for direct comparison of the two fields. The contour plot of the transmission line wave is shown in the upper portion of the figure. This wave originates at the apex of the antenna and is essentially terminated in the resonant region. The radiated wave as shown in the bottom of the figure propagates from the active region toward the apex and on into the far field. The contour plot shows an angular dependence similar to that of the far-field antenna pattern at some distance in front of the antenna.

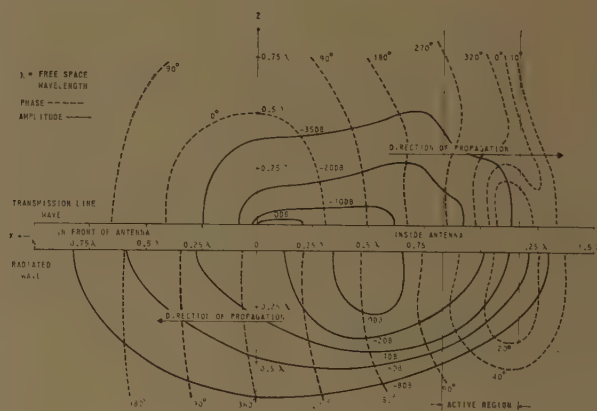


Fig. 8—Contours of the transmission line wave and the radiated wave.

IV. TOOTH CURRENTS IN THE ACTIVE REGION AT A SINGLE FREQUENCY

Since the transmission line wave terminates in the active region and the radiated wave originates in this region, the current distribution in this region serves as the common boundary for the two waves that allows energy to be transferred from one wave to the other. Tooth current measurements described in this section show the extent of the active region and give some insight into the nature of the coupling between the two waves.

Any contribution to the radiated field arising from currents in the boom is polarized orthogonal to the desired radiated field. This orthogonal polarization has been measured to be greater than 20 db below the de-

sired polarization, so it is concluded that the current distribution in the boom may be neglected when considering the far-field radiation of the antenna. Because of this, no measurements are shown of the currents in the antenna booms.

A. Measurement Techniques

Magnetic fields produced by the currents in the teeth were probed with a small current loop. Fig. 9 is a photograph of the probe installed in a tooth on the antenna. The transmission line leading to the probe is buried within the structure, and the probe is brought through the conductor surface at the point where the current measurement is to be made. The transmission line continues inside the tooth to the boom, and then inside the boom to the large end of the antenna. At this point, the line is led away from the antenna with negligible effect on the antenna fields. The tooth is slotted to permit current measurements at a number of points along the tooth. A similar loop is located at the apex of the antenna to serve as a reference.



Fig. 9—Current probe in tooth of antenna.

It is inconvenient to slot a large number of teeth to make current measurements over a larger part of the antenna, and fortunately it is not necessary to do so. With negligible end effects the current distribution on the antenna at any given frequency, f , is the same as the distribution at a frequency $\tau^{n/2}f$, except that the distribution at f is shifted n teeth along the structure toward the apex. This follows from the fact that the antenna structure "looks" the same to any two frequencies separated by an integral number of logarithmic half-periods.

If the current phase and amplitude distribution in one tooth is measured as the frequency is varied through n

half-period steps, the results may also be interpreted as the currents in n teeth along the antenna structure at one frequency.

B. Measured Tooth Currents

Data taken as described above is presented in Fig. 10. The relative amplitude and phase of current is indicated at five positions along each tube forming the teeth in the vicinity of the tooth that is of resonant length. The phase of the current is essentially constant along each tube, and the amplitude varies in a near-sinusoidal manner with a maximum value at the boom. This indicates a standing wave of current along each tube. It should be noted that the currents in successive teeth are approximately 90° out of phase.

Current amplitudes fall to negligible values in teeth longer than those in the active region. The current phases depart greatly from the 90° phase progression from tooth to tooth for teeth that are shorter than those in the active region. The bounds on the active region of the antenna are established using current phase progression as the criteria at the bound nearer the apex, and using current amplitude as the criteria at the farther bound.

That the current distribution in the active region satisfies the general requirement of orientation and phase progression for interaction with both of the travel-

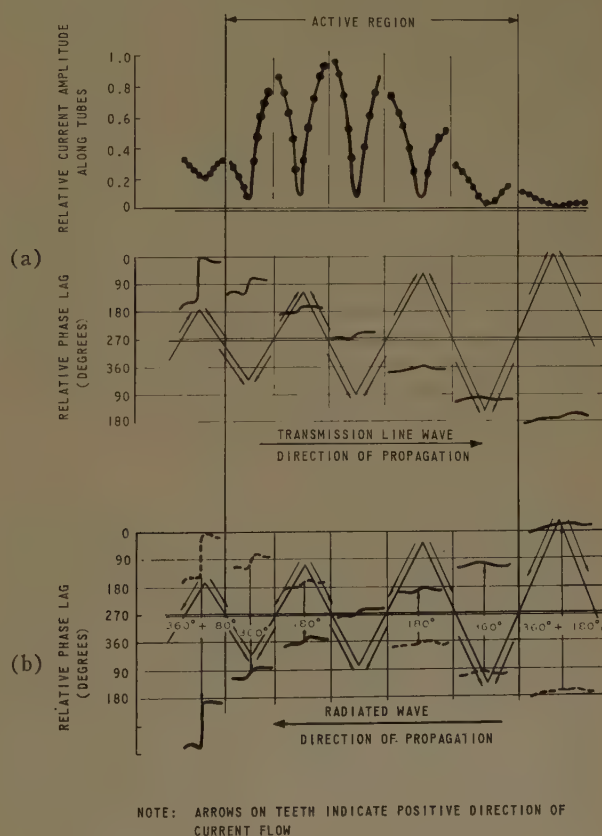


Fig. 10—Phase progression of currents in the teeth of the antenna.

ing waves is seen by a close examination of the phases of the currents in the teeth. For clarification, the tooth current phases are presented in Fig. 10 with two different references for the positive direction of current flow. The positive direction of currents in Fig. 10(a) is outward from the center boom for all tubes forming a tooth, and it is evident that the orientation and the direction of phase progression of these currents are the same as that of the electric field of the transmission line wave which is traveling from the apex to the active region of the structure. The phases of these same currents are shown again in Fig. 10(b), this time with the reference of current flow on one side of the boom rotated 180° . These currents now have the same orientation and direction of phase progression as the electric field of the radiated wave which is traveling toward the apex of the antenna.

The transmission line wave induces a current distribution on the teeth in the active region of the antenna. The currents vary in phase and amplitude from one tooth to the next. In turn, this array of current elements excites the wave radiated by the antenna.

C. Patterns Computed Using Measured Values of Current

E- and *H*-plane patterns are computed to verify that the far field radiation is essentially produced by the currents in the teeth in the active region of the antenna. An equivalent structure is devised for these calculations which simplifies the expression for the far electric field. Relative phases and amplitudes of the currents in the elements of the equivalent antenna are assigned from measured values of current in the teeth of the actual antenna.

The instantaneous values of current in the two tubes forming a tooth are shown in Fig. 11(a). The tube designated *A* is nearest the apex of the antenna. The currents I_A and I_B of Fig. 11(a) may be divided into their *x* and *z* components as shown. Since the currents I_A and I_B are separated by a small portion of a wavelength, the contributions of I_{Ax} and I_{Bx} to the far-field radiation tend to cancel. Also, radiations produced by I_{Az} and I_{Bz} are additive in the far field. This suggests representing both tubes, *A* and *B*, by a single thin linear element with a current equal to $I_{Az} + I_{Bz}$ as shown.

Fig. 11(b) shows the comparison of a sine wave with the current distribution that was measured on a tooth in the active region. The sum of the two currents I_A and I_B closely approximates a sine wave distribution.

Fig. 12 shows the antenna with the teeth replaced by equivalent linear elements. For convenience, the elements are designated by *n* where the $n=0$ element is in the center of the active region, *i.e.*, the element of resonant length. The elements numbered 1, 2, \dots are toward the apex while the elements numbered -1 , -2 , \dots are toward the rear of the antenna.

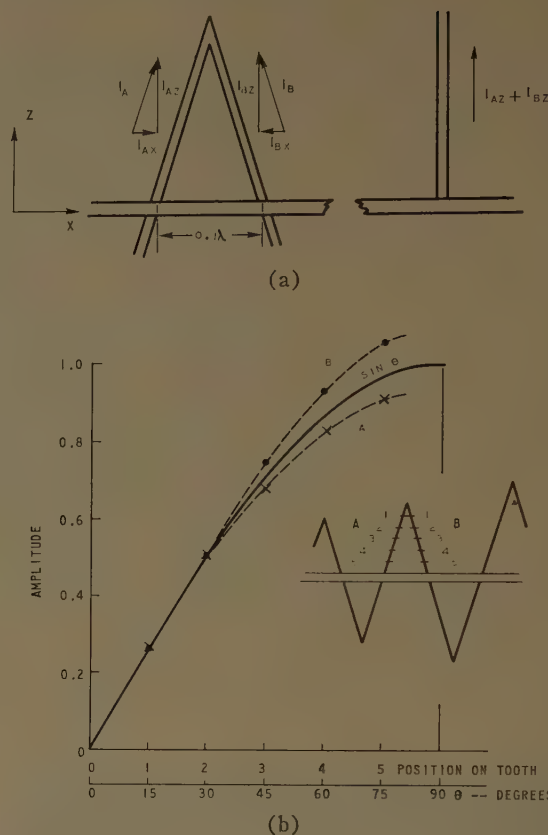


Fig. 11—Tooth approximations for pattern calculations.

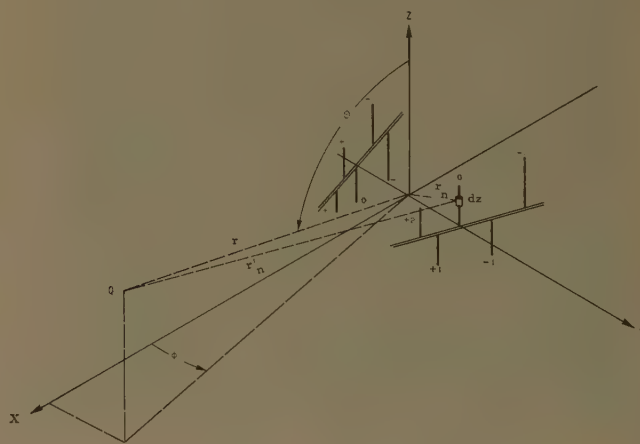


Fig. 12—Antenna configuration assumed for far field calculations.

Contributions to the far electric field by a differential segment of an element are given by¹⁰

$$dE_{\theta_n} = \frac{j\eta k I_n(z)}{4\pi r_n'} e^{-j(kr_n' - \gamma_n)} \sin \theta dz \quad (1)$$

¹⁰ S. Ramo and J. R. Whinnery, "Fields and Waves in Modern Radio," John Wiley and Sons, Inc., New York, N. Y., 2nd ed., p. 500; 1953.

where $e^{j\omega t}$ is understood. Here η is the impedance of free space, k is the wave number $2\pi/\lambda$, and γ_n is the relative phase of the current in tooth n . The tooth current $I(z)$, assumed sinusoidal with distance along the tooth, is approximated by

$$I_n(z) = I_{\max} \sin \frac{2\pi}{\lambda} (z_n - z), \quad (2)$$

where $z_n = L_0 \tau^{n/2} \tan \alpha/2$, and L_0 is the distance from the apex to the tooth of resonant length. For this antenna, $L_0 = \lambda$ and $z_n = (\lambda/4) \tau^{n/2}$. The measured value of current at the base of the tooth is expressed by

$$I_n = I_{\max} \sin \frac{2\pi}{\lambda} z_n. \quad (3)$$

After integrating (1) and simplifying, we obtain the following expression for the far zone electric field:

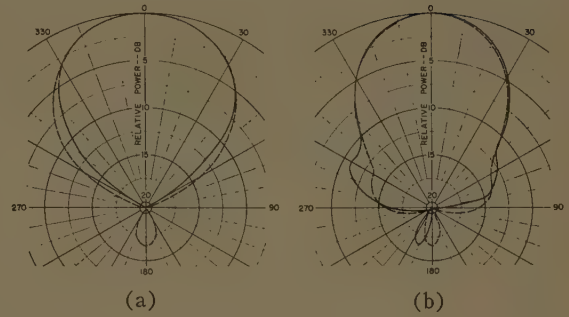
$$E_\theta = \frac{j\eta e^{-jk\tau}}{2\pi\tau} \sum_{n=-2}^2 \left(\frac{I_n e^{j\gamma_n}}{\sin kz_n} \right) \left(\frac{e^{jkx_n \sin \theta \cos \phi}}{\sin \theta} \right) \\ (-\cos kz_n \cos \{(-1)^n k y_n \sin \theta \sin \phi\} \\ - \cos \theta \sin kz_n \sin \{(-1)^n k y_n \sin \theta \sin \phi\} \\ + \cos \{(-1)^n k y_n \sin \theta \sin \phi - kz_n \cos \theta\}). \quad (4)$$

E - and H -plane patterns were computed from (4) and are shown in Fig. 13. Measured patterns are also shown in Fig. 13 for comparison.

D. Discussion of the Significance of the Measured Fields

The agreement between measured antenna patterns and the pattern calculated from the measured current distribution in the active region of the log periodic structure verifies that the active region is actually the radiating portion of the antenna at the operating frequency. The portion of the structure between the apex and the active region serves as a transmission line to excite the active region, and the portion of the antenna beyond the active region has negligible effect, as the transmission line wave is effectively terminated within this region. Thus, the transmission line wave may be considered as the input to the active region, and the radiated wave may be considered as the output from the active region of the antenna.

The physical distance along the structure containing these five elements is approximately one-third wavelength, or 120° in terms of phase shift. However, the phase difference between currents in the first and in the fifth elements is 360° . Thus, the phase shift along the structure exceeds the length of the active region by approximately 240° . This indicates that the structure exhibits increased directivity. In fact, the excess phase shift is greater than that of the conventional Hansen-



Values of Measured Current Used for Calculation

n	I_n	γ_n
-2	0.230	180
-1	0.675	90
0	1.000	0
1	0.965	-90
2	0.590	-180

— Typical measured pattern
 --- Calculated Pattern

Fig. 13—Calculated and measured radiation patterns of log periodic antenna. (a) E plane. (b) H plane.

Woodyard increased directivity condition, which is, of course, based on equal excitation amplitudes of each element.

V. MEASUREMENTS IN THE IMMEDIATE VICINITY OF THE STRUCTURE THROUGH ONE PERIOD OF OPERATION

The broad-band properties of these antennas have been explained by DuHamel in terms of their periodic performance with frequency. Essentially then, the analysis of these structures hinges on their operation over any other period of frequency (f to τf , where f may be any frequency in the operating range). To determine the manner of the variations within a period, near-electric field measurements were made at several frequencies within one period of operation. Also, the current was measured in one tooth over several periods of operation. Phase and amplitude data are with reference to the transmission line wave at the apex of the antenna.

A. Current Variations

Relative current amplitude and phase measured in one tooth is shown in Fig. 14 over a frequency range of several periods. Data were taken with a probe built into the antenna structure as described in Section IV-A. Current data are shown at five equidistant points located along each tube that forms the tooth. The figure clearly shows the frequency response of the tooth. The current amplitudes are significant and the phases vary smoothly over a frequency range of approximately two and one-half periods.

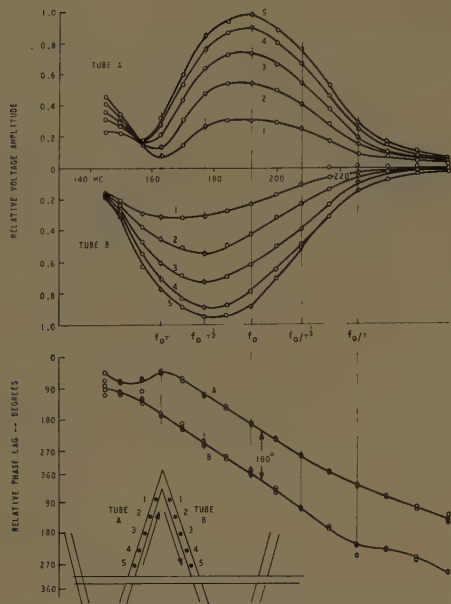


Fig. 14—Current variations with frequency at fixed positions along tubes forming a tooth.

These same basic data are presented again in Fig. 15 to show the manner of variation of current in a number of teeth in and near the active region as frequency is varied through one period of operation. The relative amplitude and phase of the current in each tube are determined from the frequency scaling technique given in Section IV-A. The average amplitude and phase values of current in the two tubes of each tooth are plotted as a function of frequency. The positive direction of current flow is taken toward the boom on one side and away from the boom on the other side, as in Fig. 10(b). This convention produces addition in the radiated far field. As expected, the amplitude of the current in the shorter or higher frequency teeth increases as the frequency is increased, while the amplitude in the longer or lower frequency teeth decreases.

The phase plots of Fig. 15 show that the current in each successive shorter tooth lags that of the previous tooth by approximately 90° in the active region of the antenna.

These plots also show that the phase of the current in each tooth in the active region lags as the frequency is increased. If the frequency is increased by one half period, then the current in each tooth is delayed by 90° . However, when the frequency is increased by one-half period, the next shorter tooth becomes the resonant tooth. Therefore, the phase of the currents in the teeth in the new active region lags those of corresponding teeth in the old active region by 180° when the frequency is increased by one half period. By continuing this same line of reasoning, it may be shown that the phase of the currents lags by 360° when the frequency is increased by a full period. Since these currents launch the radiated wave, the phase of the far-field radiation

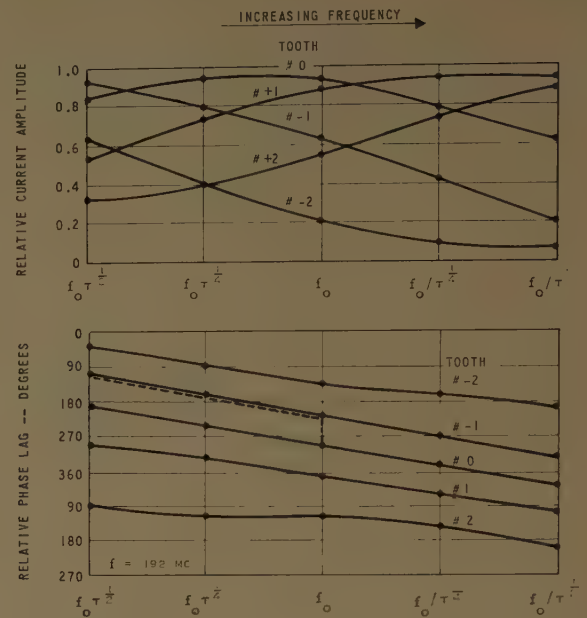


Fig. 15—Amplitudes and phases of current in teeth in active region of the antenna through one period of operation. Note: Positive direction of current flow is as shown in Fig. 10(b).

lags 360° with respect to the antenna feed point when the frequency is increased by a full period. This phenomenon was previously noticed in the far-field radiation phase and was reported by DuHamel and Ore.⁶

B. Electric Field Variations

The relative amplitudes and phases of the electric field on each side of the center boom are shown in Fig. 16 for four frequencies encompassing one period of operation. The tooth of resonant length at frequency f_0 is tooth number 0 as indicated. If the frequency is decreased to $f_0\tau^{1/2}$, or one-half a period from f_0 , the next larger tooth (tooth number -1) becomes resonant, and so on. The amplitude distribution extends farther along the structure toward the larger teeth as the frequency is lowered.

However, the motion of the maxima and the minima of the standing wave patterns on either side of the center boom is toward the apex of the structure as the frequency is lowered, as may be seen from the successive standing wave pictures presented in Fig. 16. This motion corresponds to the standing wave pattern that would be produced by the combination of a radiated wave which advances in phase as frequency is lowered and a transmission line wave of relatively constant phase. The phase variation with frequency of the radiated wave agrees with that deduced from the current measurements.

VI. CONCLUSIONS

Some insight into the basic operation of the logarithmically periodic antenna is gained from the meas-

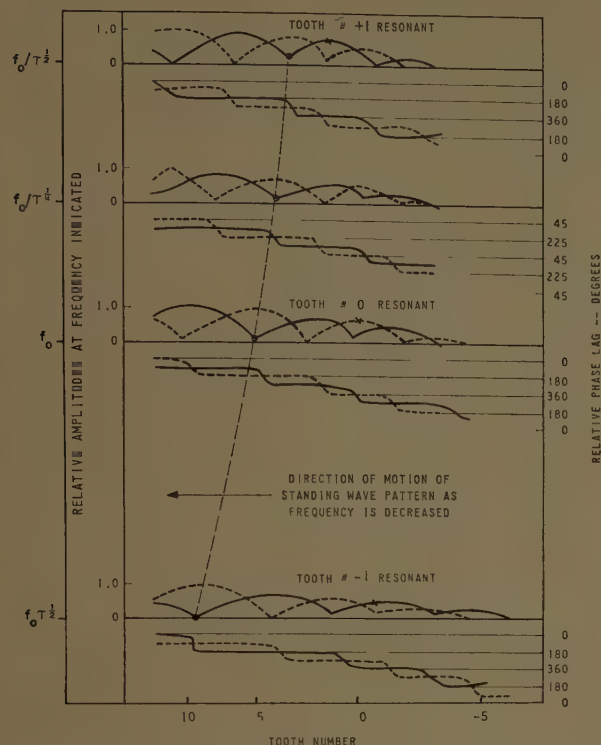


Fig. 16—*E*-field measurements along the antenna structure through one period of operation.

ured RF fields surrounding the structure. A TEM transmission line wave is launched from the apex and travels to the active region of the structure. This wave excites currents in the teeth and is effectively terminated within this region. These currents in the active region produce a radiated wave which accounts for the far-field pattern of the antenna. The two waves may be considered as the input to and the output from the active region of the antenna.

The active region for the log periodic antenna considered in this paper consists of five teeth centered on the tooth nearest resonant length. Close agreement between measured antenna patterns and patterns calculated from the currents measured in this region, as well as the measured attenuation of the transmission line wave in this region, indicates that these five teeth constitute the radiating portion of the antenna. A pronounced degree of increased directivity is indicated by the measured phase progression of the currents in the active region.

Near-field measurements within one period of operation show smooth variations of tooth currents and electric fields with frequency. The phase variations with frequency are in agreement with the far-field phase variations reported by DuHamel.

Distribution Functions for Monopulse Antenna Difference Patterns*

O. R. PRICE[†], SENIOR MEMBER, IRE, AND R. F. HYNEMAN[‡], MEMBER, IRE

Summary—Theoretical considerations of monopulse antisymmetrical or difference radiation patterns which have optimum properties in the Dolph-Tchebycheff sense are discussed. An approximate technique for synthesizing such patterns from linear arrays or continuous line sources is given. A highly desirable feature of the method is that the excitation function may be written as a simple modification of a (known) conventional Dolph-Tchebycheff excitation function. In addition, the method is also applicable to the synthesis of other specialized antisymmetrical patterns.

I. INTRODUCTION

DESIGN methods for the sum patterns of monopulse antennas (which are directly related to conventional antennas) are well established. If the ultimate in narrow beamwidth and low sidelobes

is desired, then a pattern with all sidelobes equal must be obtained. Application of the Tchebycheff polynomial [1]–[3] yields equal sidelobes provided one considers only the space factor of an antenna. However, operational requirements sometimes dictate that the designer sacrifice some beamwidth or sidelobe level near the main lobe in order to obtain very low sidelobes far from the main beam. Design criteria for the conventional (sum pattern) antenna have also been derived for this case [4].

Many monopulse antennas in operation are modifications of parabolic-dish-reflector antennas. Laboratory prototypes of two- and three-dimensional slotted waveguide antennas have been constructed and tested. In the near future monopulse antenna arrays with independent power sources, and accompanying independent phase and amplitude control for each radiating element, will be built. Especially in view of the last two

* Received by the PGAP, March 12, 1960.

[†] Res. Labs., Hughes Aircraft Co., Culver City, Calif.

[‡] Ground Systems Group, Hughes Aircraft Co., Fullerton, Calif.

developments it is apparent that there is a need for difference (antisymmetrical) pattern design methods.

In this paper, design methods for obtaining difference patterns satisfying various operational requirements will be derived. Because the element pattern in most antennas lacks much directivity, and in order to maintain wide applicability of the methods to be derived here, only the space factor will be considered.

II. REVIEW OF DOLPH-TCHEBYCHEFF OPTIMUM SUM PATTERNS

In preparation for later consideration it will be advantageous to review briefly methods for obtaining optimum patterns of arrays of isotropic sources. Considering a linear broadside array of equispaced, isotropic, in-phase sources, Dolph [1] has shown that a pattern with minimum main lobe beamwidth for a given ratio of main lobe amplitude to sidelobe amplitude will have sidelobes of equal amplitude.

Fig. 1 shows the configurations under consideration. Since the amplitude distribution is symmetrical ($A_r = A_{-r}$), the radiation pattern for an even number of elements, n_e , may be expressed as

$$\frac{1}{2} E_{S,2N} = \sum_{r=1}^N A_r \cos(2r-1) \frac{\psi}{2}, \quad (1a)$$

and for an odd number, n_o , as

$$\frac{1}{2} E_{S,2N+1} = \sum_{r=0}^N A_r \cos 2r \frac{\psi}{2}, \quad (1b)$$

where $n_e = 2N$, $n_o = 2N+1$, and where the excitation of the r th element is proportional to A_r for $r \neq 0$ and to $2A_0$ for $r=0$. In each case $\psi/2 = \psi d/\lambda \sin \theta = \psi du/\lambda$, where d/λ is the center-to-center element spacing in terms of free space wavelength, and $u = \sin \theta$, where θ is the angle measured from the broadside direction:

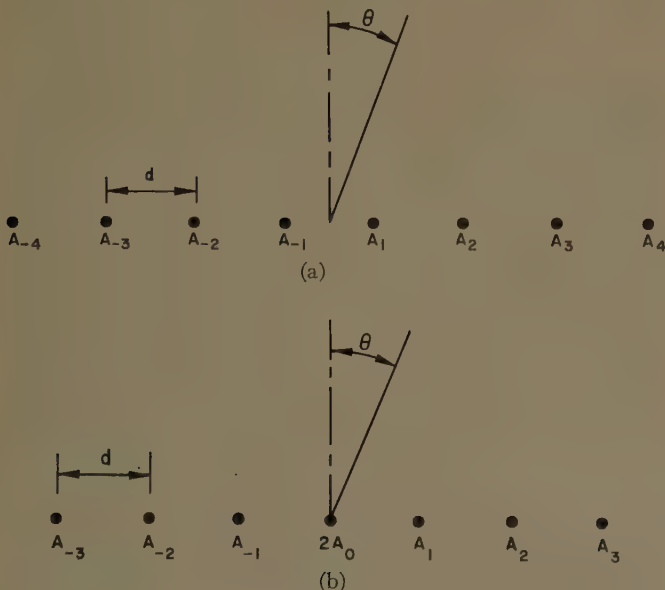


Fig. 1—Array of radiating elements.

Following Dolph, each amplitude pattern may also be represented by an appropriate Tchebycheff polynomial or by a single trigonometric term.

$$\frac{1}{2} E_{S,2N} = T_{2N-1}(x) = \cos [(2N-1) \arccos x] \quad (2a)$$

$$\frac{1}{2} E_{S,2N+1} = T_{2N}(x) = \cos (2N \arccos x), \quad (2b)$$

where $x = x_0 \cos \psi/2$, and x_0 is defined by

$$T(x) \big|_{x=x_0} = R_S, \quad (4)$$

where

$$R_S = \frac{\text{amplitude of main lobe of sum pattern}}{\text{amplitude of secondary lobes}}.$$

III. THEORETICAL CONSIDERATION OF THE DIFFERENCE PATTERN

The difference pattern is antisymmetric and, characteristically, for broadside operation, has a null at $\theta = 0^\circ$ with main lobes of equal magnitude on each side of 0° together with the usual secondary maxima or sidelobes.

Again consider the configurations shown in Fig. 1, except now we will use B_r to designate the feeding coefficient of the r th element. Since $B_r = -B_{-r}$, the difference patterns may be expressed as

$$\frac{E_{D,2N}}{2} = i \sum_{r=1}^N B_r \sin \left[(2r-1) \frac{\psi}{2} \right], \quad (6a)$$

and

$$\frac{E_{D,2N+1}}{2} = i \sum_{r=0}^N B_r \sin \left(2r \frac{\psi}{2} \right). \quad (6b)$$

With the substitution $y = \sin \psi/2$, (6a) may be written

$$\frac{E_{D,2N}}{2} = i \sum_{r=1}^N B_r' y^{2r-1},$$

which is a real polynomial of degree $2N-1$. In the case of an odd number of elements, a corresponding *real-polynomial* representation does not appear possible,¹ and therefore this case will not be treated from the theoretical standpoint. However, the excitation envelopes for the two cases differ insignificantly for arrays having a reasonably large number of elements, and so the approximate method outlined subsequently applies equally well to either case.

¹ Representations of the forms

$$\frac{E_{D,2N+1}}{2} = i \sqrt{1-y^2} \sum_{r=1}^N B_r' y^{2r-1}$$

or

$$\frac{E_{D,2N+1}}{2} = Z^{-N} \sum_{r=1}^N B_r' (Z^{N+r} - Z^{N-r})$$

where $Z = e^{i\psi}$ and $y = \sin \psi/2$, are of course possible.

By definition, the characteristics of the optimum difference patterns are essentially the same as for the conventional Dolph (sum) pattern, and the proof of the optimum property follows the same line of reasoning. For simplicity, the case of $d/\lambda = \frac{1}{2}$ is treated, which results in a range of y from -1 to 1 for θ over the visible region.

Theorem:

Consider a class of odd, real polynomials of degree n ,

$$F_n(y) = a_1y + a_3y^3 + \cdots + a_ny^n$$

which satisfy the following conditions:

- 1) All the roots of $F_n(y)$ are real and lie in the interval $(-1, 1)$.
- 2) The $F_n(y)$ are normalized so as to make the magnitude of the first left-hand and the first right-hand extrema from the origin (the two innermost extrema) equal to a given constant R (See Fig. 2).
- 3) All $F_n(y)$ have the same ratio R of the magnitudes of the innermost extrema to the magnitude of the largest other extremum for y in the range $(-1, 1)$.

Let the particular function $F_n^\circ(y)$ satisfy the above conditions and have the further property that all subsidiary extrema, *i.e.*, all extrema except the innermost pair in the interval $(-1, 1)$, are of magnitude unity. Then $F_n^\circ(y)$ has the smallest distance from the origin to the first nulls, $y_{\pm 1}$.

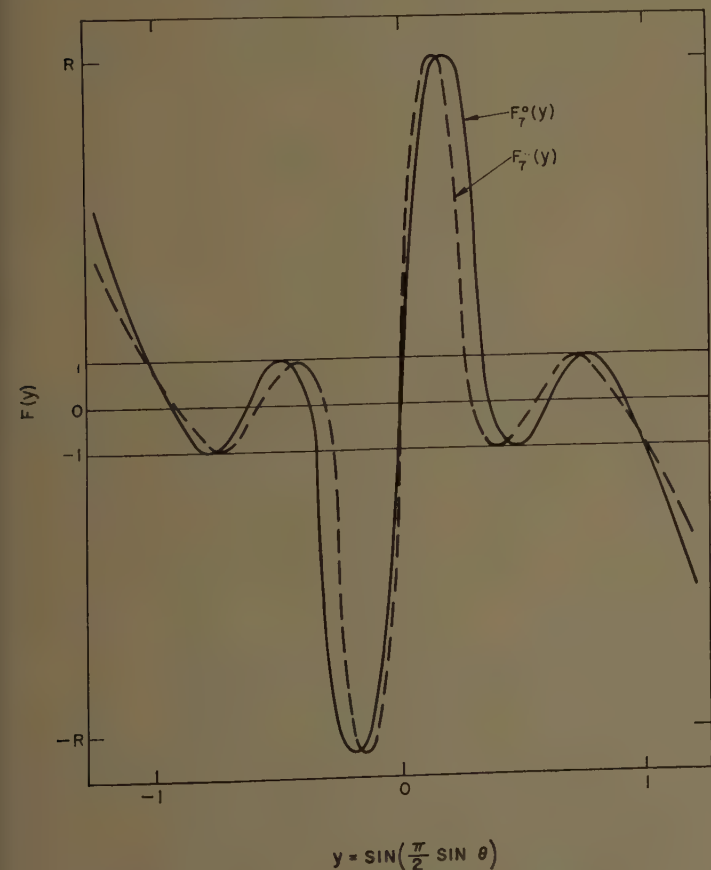


Fig. 2—Sketch of optimum and narrower-than-optimum polynomial.

The proof is equivalent to that given by Dolph [1] in his treatment of the Tchebycheff array. Let $D_n(y)$ be the difference between $F_n^\circ(y)$ and any other $F_n(y)$; then

$$D_n(y) = F_n^\circ(y) - F_n(y).$$

Hence $D_n(y)$ is a polynomial of degree not greater than n . Now assume that the above theorem is false, *i.e.*, that $|y_{\pm 1}| < |y_{\pm 1}^\circ|$, where $y_{\pm 1}$ and $y_{\pm 1}^\circ$ are first nonzero roots of $F_n(y)$ and $F_n^\circ(y)$, respectively. Since no subsidiary extrema of $F_n(y)$ may exceed unity in magnitude, and all subsidiary extrema of $F_n^\circ(y)$ must have that value, it follows that $F_n(y)$ and $F_n^\circ(y)$ must intersect in not less than $n+2$ points. Thus by counting the number of intersection points, $D_n(y)$ must have not less than $n+2$ zeros. Since $D_n(y)$ is a polynomial of degree not greater than n , it follows that $D_n(y) = 0$. As a result, if the function $F_n^\circ(y)$ exists, then it is optimum in the sense that it will have the least distance between first nulls for the given ratio R .

Corollary: One of the above class of functions, the function $F_n^\circ(y)$, has the (normalized) slope of greatest magnitude at the origin. The proof follows exactly as above and will not be repeated here.

Thus, it can be shown that the postulated function $F_n^\circ(y)$ is optimum from the standpoint of a monopulse application in that it displays *both* the lowest sidelobe ratio for a given beamwidth as well as the greatest rate of change in signal amplitude with angle about the boresight direction. This latter characteristic is of importance in obtaining good error sensitivity in the monopulse system.

Unfortunately, no known polynomial has the required characteristics; indeed the function is of the class considered by Sinclair and Cairns² in their treatment of the conventional optimum distribution for an even number of elements which are spaced less than one-half wavelength apart. Methods of solution involving trial and error, and analog techniques, as well as an iterative technique for improving the characteristics of a trial polynomial, are indicated in their paper. However, the operation must be carried out in entirety for each new attempted design. In the material below, a simple method for obtaining a close approximation to the optimum difference pattern from existing Dolph-Tchebycheff distribution tables is outlined. In addition, the method is applicable for obtaining difference patterns having the specialized sidelobe characteristics of other directive pattern distributions, *e.g.*, the Taylor distribution for continuous line sources [5] and the Taylor modified $\sin u/u$ distribution [4].

IV. AN APPROXIMATE METHOD FOR OBTAINING THE OPTIMUM DIFFERENCE PATTERN

Upon comparing (1) and (6) one observes, in particular, that the trigonometric factor in each term of

² See [3], discussion on p. 53, (18) through (26).

(6) is (Transmutation I) $f_1(r)$ times the derivative with respect to $\psi/2$ of the trigonometric factor of the corresponding term of (1), and (Transmutation II) $f_2(r)$ times the integral of the corresponding trigonometric term of (1). A brief consideration shows that application of Transmutation II (*i.e.*, an integrative technique), to a Dolph-Tchebycheff distribution generating function yields an aperture illumination even more highly peaked centrally. In turn, although such a distribution may be used to obtain an antisymmetrical pattern, the resulting pattern in general will not have the nulls required for an optimum antisymmetrical pattern as defined in Section III. However, a practical application of Transmutation II will be described subsequently. On the other hand Transmutation I (*i.e.*, a differentiative technique), results in a distribution less highly peaked than the generating function; the resulting pattern will be compared with the optimum pattern.

Transmutation I

The application of Transmutation I to (1) and (2) yields alternate expressions for the difference (odd) amplitude patterns which result from a Dolph-Tchebycheff pattern used as a generating function. Thus upon applying $d/d(\psi/2)$ to (1) and (2), and again letting $x = x_0 \cos \psi/2$, $y = \sin \psi/2$, we obtain

$$\frac{E_{D,2N}}{2} = -i \sum_{r=1}^N A_r (2r-1) \sin \left[(2r-1) \frac{\psi}{2} \right], \quad (7a)$$

$$\frac{E_{D,2N+1}}{2} = -i \sum_{r=0}^N A_r (2r) \sin \left(2r \frac{\psi}{2} \right); \quad (7b)$$

$$\begin{aligned} \frac{E_{D,2N}}{2} &= -i \sqrt{x_0^2 - x^2} \frac{d}{dx} T_{2N-1}(x) \\ &= -(2N-1) \sqrt{\frac{x_0^2 - x^2}{1 - x^2}} \sin [(2N-1) \arccos x] \\ &\equiv P(2N-1; x), \end{aligned} \quad (8a)$$

$$\begin{aligned} \frac{E_{D,2N+1}}{2i} &= -i \sqrt{x_0^2 - x^2} \frac{d}{dx} T_{2N}(x) \\ &= -2N \sqrt{\frac{x_0^2 - x^2}{1 - x^2}} \sin [2N \arccos x] \\ &\equiv P(2N; x). \end{aligned} \quad (8b)$$

Eqs. (8a) and (8b) are transcendental functions of x ; however, as indicated previously, (7a) may be expressed as an odd polynomial in y , where $y = \sin \psi/2$. In order to obtain the corresponding odd polynomial (in y) form of (8a), write

$$\sqrt{x_0^2 - x^2} = x_0 y, \quad x = x_0 \sqrt{1 - y^2}.$$

Since the associated Tchebycheff polynomial [6] of degree $2N-2$

$$S_{2N-2}(2x) = \frac{\sin [(2N-1) \arccos x]}{\sqrt{1 - x^2}}$$

is even in terms of

$$x = x_0 \sqrt{1 - y^2},$$

it is also even in terms of y . Then

$$P(2N-1; x) = -(2N-1)y S_{2N-2}(2x)$$

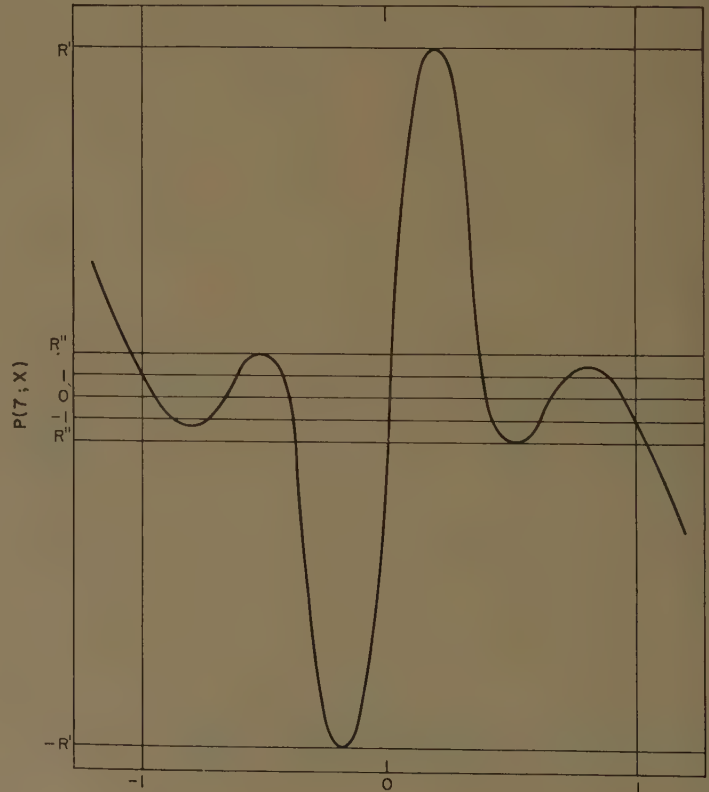
is an odd polynomial in y . In a similar manner it may be shown that (7b), and therefore (8b), are transcendental functions of y of the form

$$E_{D,2N+1}^{(1)} = \sqrt{1 - y^2} \sum_{r=0}^N a_r y^{2r-1}.$$

Although the polynomial representation is possible in the even cases, the behavior for both the even and odd cases is more clearly displayed by the transcendental representation in terms of x (8). Inspection of these equations shows that the sidelobe maxima differ in magnitude only through variation of the factor

$$\sqrt{\frac{x_0^2 - x^2}{1 - x^2}}.$$

This variation is small for the values of x_0 usually employed, whenever $|x| < 1 - \epsilon$, *i.e.*, in the sidelobe regions. For example, a plot of $P(7; x)$ against y is shown in Fig. 3, from which it is evident that the magnitudes of the subsidiary extrema decrease only slightly as $|y| \rightarrow 1$.



$$y = \sin \left(\frac{\pi}{2} \sin \theta \right) = \sqrt{1 - (x/x_0)^2}$$

Fig. 3—Plot of the approximately optimum transcendental $P(7, x)$.

The coefficients B_r are most easily obtained by equating the right side of (6) to the right side of (7). Thus,

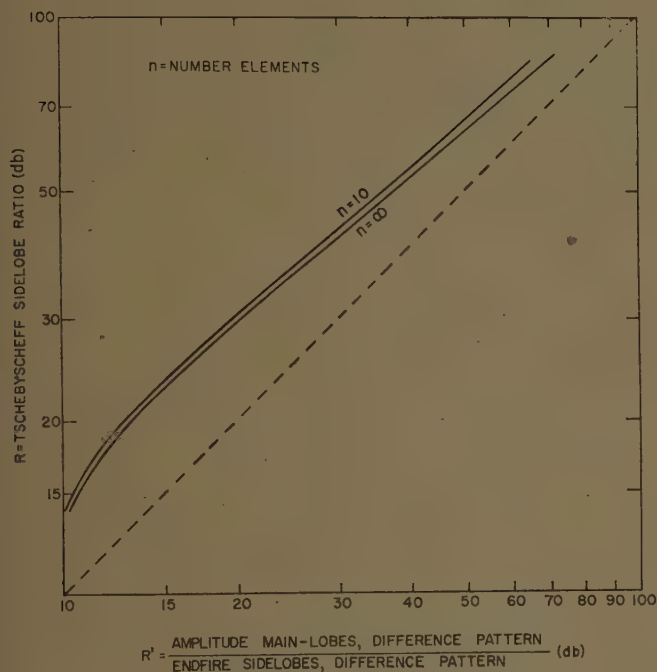
$$B_r = (2r - 1)A_r, \quad (9a)$$

for an even number of elements and

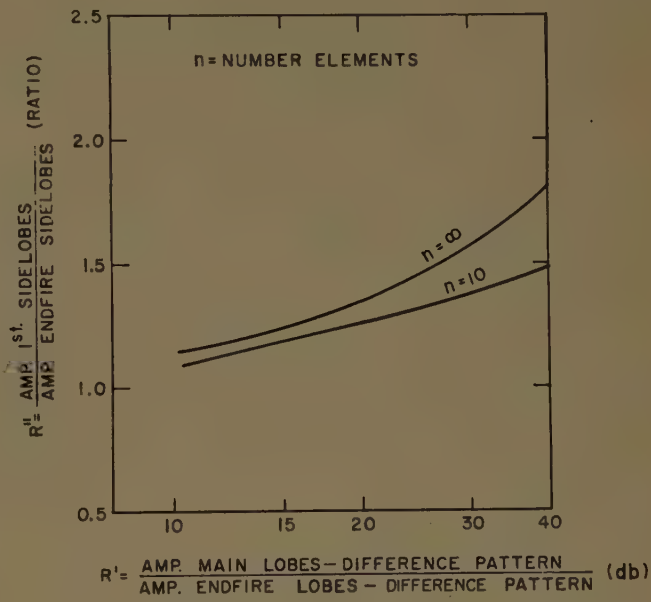
$$B_r = 2rA_r, \quad (9b)$$

for an odd number of elements. An extensive table [7] of values for A_r has been published.

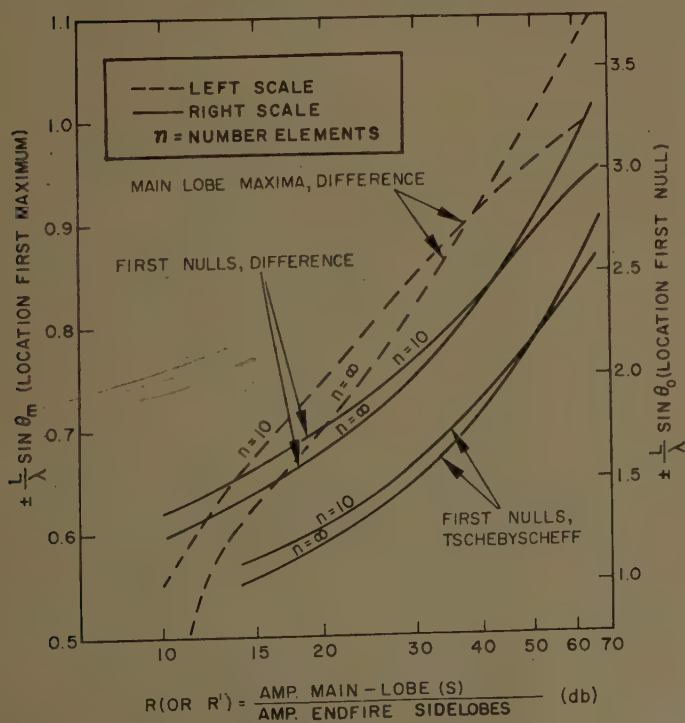
Characteristics of the near-optimum difference pattern, *e.g.*, beamwidth, sidelobe ratio, and location of the main lobes in terms of corresponding characteristics of the parent or generating Tchebycheff pattern are derived in Appendix I and plotted in Figs. 4(a) through 4(c). From these graphs, and using published results for the Tchebycheff pattern distribution function, a difference pattern having the desired sidelobe ratio may be determined.



(a)



(b)



(c)

Fig. 4—(a) Sidelobe relationship between parent and transmuted Tchebycheff patterns. (b) Sidelobe variation of transmuted pattern. (c) Directivity of Tchebycheff and difference pattern.

The patterns obtained by this transmutation method and represented by (8) are only *nearly* optimum. In principle, one could find a distribution which would yield a pattern slightly better in the sense that for a given value of R the beamwidth would be narrower than that represented by $P(x)$. From a practical standpoint, the pattern represented by $P(x)$ is more than an adequate approximation because of the very slight variation from equal sidelobe magnitudes as subsequently shown in Appendix I and plotted in Fig. 4(b). Indeed, for an actual antenna it is suggested that it would be more fruitful to optimize the complete difference pattern (*i.e.*, the array pattern times the element pattern), as has been done by Sinclair and Cairns [3] for the conventional Tchebycheff pattern.

Example 1—The Tchebycheff Generating Function

Consider the space factor of an eight-element, one-half wavelength spaced broadside array with real feeding coefficients B_r . Require the first sidelobe to be 17.5 db below the two main lobes. Fig. 4(a) gives the sidelobe level of the generating function vs sidelobe level obtained with the use of Transmutation I. The two curves shown indicate the slight variation in design sidelobe level with number of elements. From this figure a Dolph-Tchebycheff distribution for a 27-db sidelobe level ($R_S=22.2$) sum pattern must be used as a generating function.

For the sum pattern case one finds

$$\begin{aligned}x_0 &= 1.150, \\A_1 &= 8.25, \\A_2 &= 6.82, \\A_3 &= 4.56, \\A_4 &= 2.66.\end{aligned}$$

The coefficients B_r for the difference amplitude pattern are then found by use of (9) and, after normalization to $B_4=1.00$, are

$$\begin{aligned}B_1 &= 0.44, \\B_2 &= 1.10, \\B_3 &= 1.23, \\B_4 &= 1.00.\end{aligned}$$

The ratio of amplitudes of the first sidelobe (lobe nearest broadside) and the lobe at endfire is shown from Fig. 4(b) to be 1.45, or 3.2 db.

Table I gives information on this example and those to follow. Fig. 5 shows the theoretical pattern for this first example with $d=\lambda/2$. An array constructed by Tang [8] was used to obtain the experimental patterns for this example and the ones to follow. This array is a standing wave array with micrometer adjustable irises for controlling the slot coupling. The slots are longitudinal and are on the center line of the waveguide broad wall. For each case eight slots were used with a slot spacing $d=0.7\lambda$. In Fig. 6 the experimental pattern is shown, as well as the theoretical pattern of Fig. 5 adjusted for the slot spacing of 0.70λ and an assumed element factor (power) $=\cos^2\theta$.

Example 2

In order to see how theoretical values compare with experimental results for a more stringent sidelobe level, the case of a transmuted -35.5-db Dolph-Tchebycheff generating function is shown in Table I.

Example 3—The Binomial Generating Function

A familiar limiting application of the Dolph-Tchebycheff method to the sum pattern is to require that the ratio of the main lobe to the sidelobe amplitude level be infinite. The result, of course, is that the feeding coefficients are proportional to the coefficients of a binomial series. Application of Transmutation I to the binomial distribution generating function leads to a difference pattern with no sidelobes for a spacing $d=\lambda/2$; the theoretical and experimental patterns for $d=0.70\lambda$ are shown in Fig. 7.

V. EXTENSION TO OTHER PATTERN-GENERATING FUNCTIONS

The general procedure of transmuting a known conventional pattern distribution to obtain the difference pattern distribution which will produce approximately similar sidelobe characteristics, is, of course, not limited to the Tchebycheff case. In general, the success of the procedure is based on the fact that the spacing between zeros and the shapes of the sidelobes in all conventional

TABLE I
APPLICATIONS OF TRANSMUTATION No. I

Example Number	Width Between Nulls Each Main Lobe for $d=\lambda/2$	(Theoretical) First Sidelobe at	(Experimental) First Sidelobe at	(Theoretical) Width of Each Main Lobe for $d=0.70\lambda$	(Experimental) Full Width of Each Main Lobe for $d=0.70\lambda$	Generating Function Used
1	25°	-17.5 db	-16 db	17.5°	18°	-27 db Dolph-Tchebycheff
2	28.5	-24 db	-21 db	20°	20°	-35.5 db Dolph-Tchebycheff
3	—	—	—	—	—	-∞ db Dolph-Tchebycheff
4	25°	-15 db	-14 db	17.5°	18.5°	-23 db Taylor's Modified $\sin x$
						x

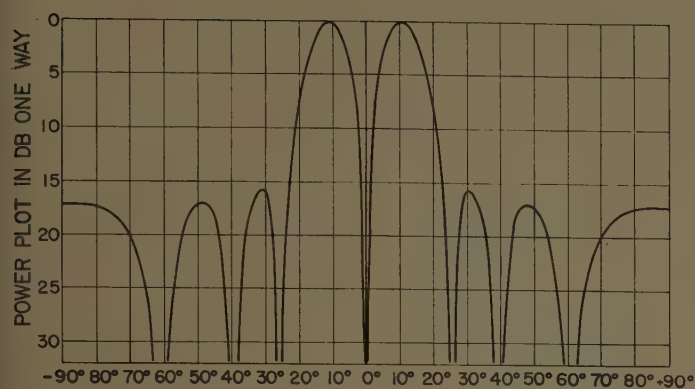


Fig. 5—Computed difference power pattern for eight-element array with spacing $d=\lambda/2$ and an isotropic element factor; differentiative technique applied to 27-db Dolph-Tchebycheff generating pattern.

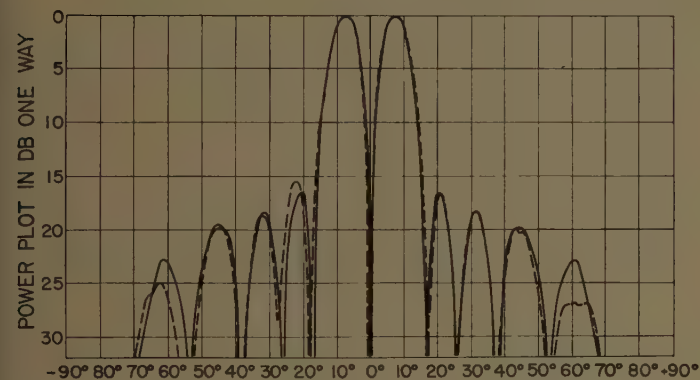


Fig. 6—Experimental and computed difference pattern for eight-element array with spacing $d=0.7\lambda$ and with an assumed element factor (power) $=\cos^2 \theta$; differentiative technique applied to 27-db Dolph-Tchebycheff generating pattern.

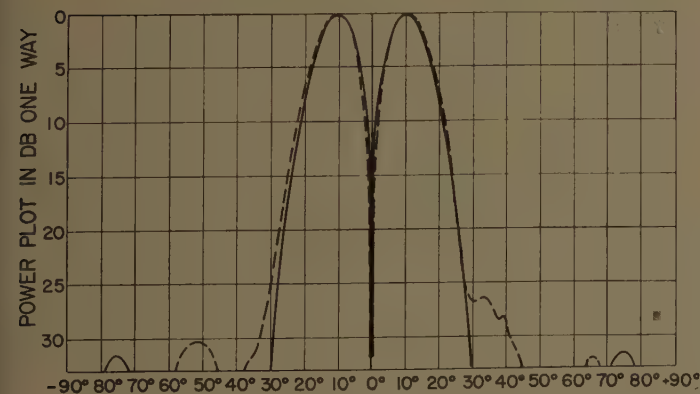


Fig. 7—Experimental and computed difference pattern for eight-element array with spacing $d=0.7\lambda$ and with assumed element factor (power) $=\cos^3 \theta$; differentiative technique applied to a binomial distribution generating pattern.

directive patterns is an almost uniform function of ψ , where $\psi = kd \sin \theta$. As a result, the maximum of a given sidelobe of a pattern obtained by the differentiative technique is centered approximately at a zero of the generating or parent function, and its amplitude tends to be proportional to the magnitudes of the maxima on either side of the corresponding zero in the parent function. Except for a second-order effect resulting from the nonuniform spacing of nulls in the parent pattern, the sidelobe decay characteristic of the difference pattern is essentially that of the parent pattern. However, since differentiation of the single main lobe in the parent pattern results in a pair of main lobes, each of lower amplitude, in the difference pattern, the latter pattern always has an over-all sidelobe level higher than the corresponding parent pattern.

The general procedure works equally well for continuous line-source distributions as for arrays of discrete elements. For a continuous distribution $g(z)$ and a line source of length L , the radiation pattern is given by

$$F(u) = \int_{-L/2}^{L/2} g(z) e^{-iku_z} dz, \quad (10)$$

where $u = \sin \theta$.

The corresponding difference pattern may be obtained from

$$F_D(u) = \frac{d}{du} F(u) = c \int_{-L/2}^{L/2} zg(z) e^{-iku_z} dz, \quad (11)$$

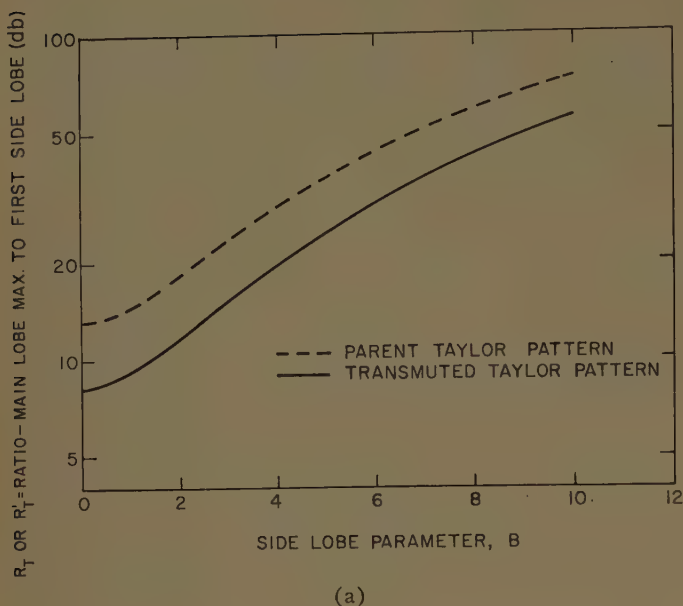
thus requiring the new aperture distribution $h(z)$ where

$$h(z) = zg(z). \quad (12)$$

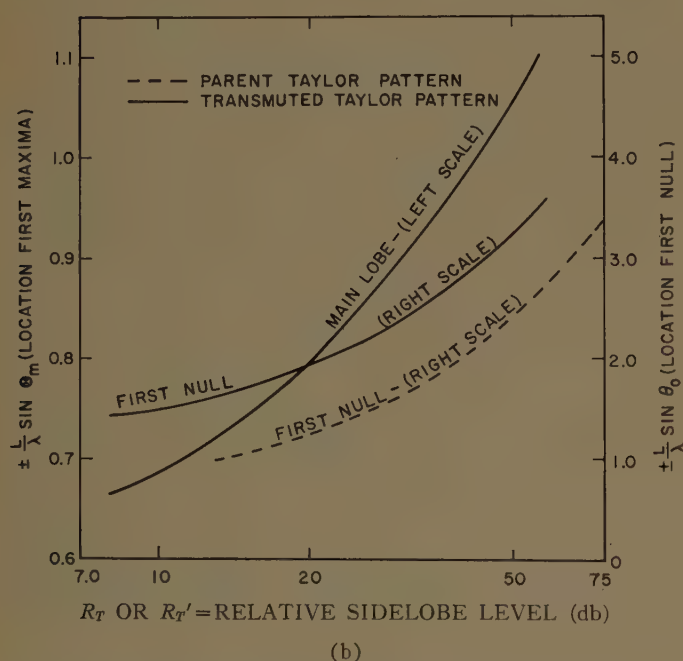
An example involving the Taylor modified $\sin \pi u / \pi u$ pattern [4] is given below.

Example 4—The Taylor Generating Function

In order to obtain a difference pattern with substantially lower sidelobes far from the two central beams, a Taylor modified $\sin \pi u / \pi u$ distribution may be used as a generating function. The corresponding sidelobe level and beamwidth characteristics of parent and transmuted Taylor patterns are obtained in Appendix II and plotted in Fig. 8. For an example, a Taylor generating pattern corresponding to a first sidelobe level of 23 db was used, resulting in a theoretical difference pattern first sidelobe at 15 db. Fig. 9 shows computed and experimental patterns for an array approximating the required line-source distribution with an element spacing of 0.7λ .



(a)



(b)

Fig. 8—(a) Parent and transmuted Taylor pattern sidelobe levels.
(b) Directivity of parent and transmuted Taylor patterns.

VI. THE INTEGRATIVE TRANSMUTATION³

Previously it was mentioned that the integrative method of Transmutation II results in an aperture distribution more highly peaked in magnitude than that of the generating function. Because the resulting aperture distribution is both sharply peaked in magnitude and antisymmetric in phase, there is a very sharp discontinuity in the aperture distribution at the center of the

³ A. Ksienski, Hughes Aircraft Co., private communication. Dr. Ksienski has independently utilized the integrative method in the synthesis of sector beams.

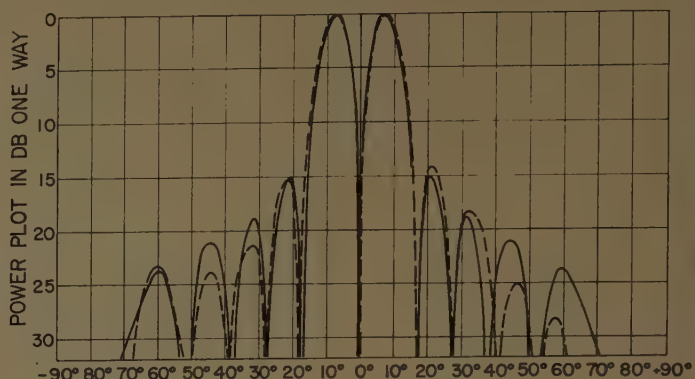


Fig. 9—Experimental and computed difference pattern for eight-element array with spacing $d=0.7\lambda$, with assumed element factor (power) $=\cos^2 \theta$; differentiative technique applied to a Taylor-modified $\sin \pi u/\pi u$ generating pattern.

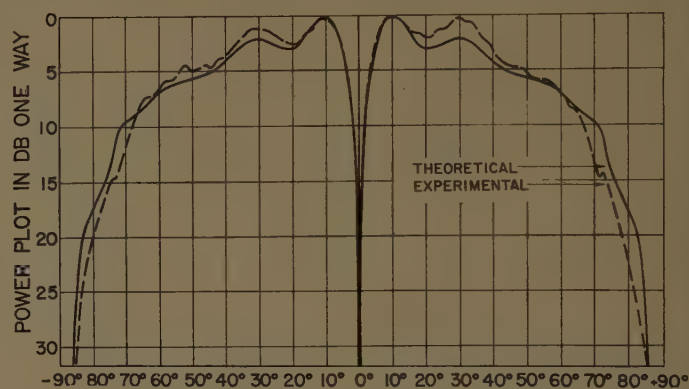


Fig. 10—Experimental and computed difference pattern for eight-element array with spacing $d=0.7\lambda$ and with assumed element (power) factor $=\cos^2 \theta$; integrative technique applied to a uniform distribution generating function.

array. The effect of the described distribution is to produce an antisymmetric radiation pattern with a high level of radiation everywhere except for a sharp null at broadside. This type of pattern would be desirable for those applications where the specifications require that the radiation level of the difference pattern be high compared with the sum pattern in every direction except near broadside.

Derivation of the expression which relates the feeding coefficients for Transmutation II to the feeding coefficients of the parent pattern is strictly analogous to the procedure used in (7) through (9). Thus

$$C_r = \frac{A_r}{2r-1} \quad \text{for } n = n_0, \quad (13a)$$

$$C_r = \frac{A_r}{2r} \quad \text{for } n = n_e, r \neq 0, \quad (13b)$$

and

$$C_0 = 0 \quad (13c)$$

where C_r = feeding coefficient for the r th element when Transmutation II is applied.

An example of this is given in Fig. 10.

VII. CONCLUSIONS

A synthesis method for antisymmetric (difference) patterns used in monopulse antennas has been presented. Linear arrays and line sources have been considered here, but the extension of the techniques to two-dimensional antennas is straightforward. The antisymmetric patterns resulting from the application of transmutation No. I to Dolph-Tchebycheff aperture distributions are nearly optimum in the Dolph-Tchebycheff sense. Application of the transmutation to other distributions used as generating functions yields antisymmetrical patterns which are analogous to the symmetrical patterns obtained from the generating functions. This was illustrated in the case of Taylor's $\sin \pi u / \pi u$ pattern. A special case of interest which utilizes Transmutation II was illustrated.

A highly desirable feature of the method is that the excitation coefficients for the difference patterns may be very simply obtained from tables of aperture coefficients applicable to the parent functions. Thus any necessary compromises in the design of a monopulse antenna can be made in a more direct manner.

APPENDIX I

DERIVATION OF TCHEBYCHEFF PARAMETERS

The sidelobe level of the derived near-optimum difference pattern may be determined as follows. From (2) and (8)

$$\frac{E_{S_n}}{2} = T_{n-1}(x) = \cos [(n-1) \arccos x] \quad (14)$$

$$\frac{E_{D_n}}{2} = -i(n-1) \sqrt{\frac{x_0^2 - x^2}{1 - x^2}} \sin [(n-1) \arccos x] \quad (15)$$

where n stands for either $n_e = 2N$ or $n_o = 2N+1$. The value of x_0 is given in terms of the sidelobe ratio, R , of the parent function (14),

$$x_0 = \cosh \left[\frac{\arccosh R}{n-1} \right] \quad (16)$$

or, for large R and n ,

$$x_0 \approx 1 + \frac{1}{2} \left[\frac{\ln 2R}{n-1} \right]^2 \quad (17)$$

For the maxima of the right side of (15) nearest endfire $u \approx 1$, $x \approx 0$,

$$\frac{E_D}{2i} \approx -(n-1)x_0 \quad (18)$$

where the expressions are exact for n even. The value of (15) for the principal maxima near $u=0$ is found by differentiating (15) and equating the result to zero. Let

$$x_0 = 1 + \alpha$$

$$x = 1 + \delta;$$

then for α and δ small (15) becomes

$$\frac{E_{D_n}}{2} \approx -(n-1) \frac{\sqrt{\alpha - \delta}}{\sqrt{\delta}} [\sinh \{(n-1)\sqrt{2\delta}\}]. \quad (19)$$

Differentiating (19) with respect to δ and equating the result to zero gives approximately

$$\tanh \beta \Delta_{\max} = \beta \Delta_{\max} (1 - \Delta_{\max}^2) \quad (20)$$

where

$$\beta = \ln 2R$$

$$\Delta_{\max} = \sqrt{\delta_{\max}/\alpha}.$$

For $R \geq 20$, it may be shown that, to a good approximation,

$$\tanh \beta \Delta_{\max} \approx 1$$

or

$$1 - \Delta_{\max}^2 \approx \frac{1}{\beta \Delta_{\max}} \quad (21)$$

The roots of this expression are given by

$$\Delta_{\max} = \mp 2 \left(\frac{1}{3} \right)^{1/2} \cos \left[\frac{\cos^{-1} \frac{2.6}{\beta} + 2p\pi}{3} \right] \quad (22)$$

where $\beta \geq 2.6$ and where $p=0, 1, 2$. The required root is that one in the range $0 < \Delta_{\max} < 1$ which is nearest to 1. Expanding the cosine term in (22) gives for this root

$$\begin{aligned} \Delta_{\max} &= \cos \left[\frac{1}{3} \sin^{-1} \frac{2.6}{\beta} \right] - \frac{1}{\sqrt{3}} \sin \left[\frac{1}{3} \sin^{-1} \frac{2.6}{\beta} \right] \\ &\approx 1 - \frac{0.644}{\beta} \end{aligned} \quad (23)$$

Substitution into (19) and comparison of the result with (18) gives for the ratio, R' , of the difference pattern main-beam amplitude to the endfire sidelobe amplitude

$$R' \approx \frac{1}{x_0} \frac{\sinh (\beta - 0.644)}{[\beta - 1.644]^{1/2}} \quad (24)$$

This expression is plotted in Fig. 4(a).

In a similar manner, the ratio, R'' , of the amplitude of the first sidelobe to that of the endfire sidelobe can be determined approximately as

$$R'' \approx \frac{1}{x_0} \sqrt{1 + \frac{(\beta)^2}{20}} \quad (25)$$

This expression is plotted in Fig. 4(b).

The locations of the first nulls in the difference pattern are given by

$$\sin \theta_{0D} \simeq + \frac{\lambda}{L} \frac{n}{n-1} \sqrt{\frac{1 + \left(\frac{\beta}{\pi}\right)^2}{1 + \frac{1}{2} \left(\frac{\beta}{n-1}\right)^2}} \quad (26)$$

and in the parent pattern by

$$\sin \theta_{0p} \simeq \pm \frac{1}{\sqrt{2}} \frac{\lambda}{L} \frac{n}{n-1} \sqrt{\frac{1 + 2 \left(\frac{\beta}{\pi}\right)^2}{1 + \frac{1}{2} \left(\frac{\beta}{n-1}\right)^2}} \quad (27)$$

The locations of the principal maxima for the difference pattern are given by

$$\sin \theta_{\max} \simeq \pm \frac{\lambda}{\pi L} \frac{n}{n-1} \sqrt{\frac{1.3\beta - 0.41}{1 + \frac{1}{2} \left(\frac{\beta}{n-1}\right)^2}} \quad (28)$$

These last three expressions are plotted in Fig. 4(c).

APPENDIX II

THE TAYLOR MODIFIED $\sin \pi u / \pi u$ PATTERN

The far-field Taylor or parent pattern is given by

$$F(u) = \frac{\sin \frac{\pi L}{\lambda} \sqrt{u^2 - B^2}}{\frac{\pi L}{\lambda} \sqrt{u^2 - B^2}} \quad B \leq |u|$$

$$= \frac{\sinh \frac{\pi L}{\lambda} \sqrt{B^2 - u^2}}{\frac{\pi L}{\lambda} \sqrt{B^2 - u^2}} \quad 0 \leq |u| \leq B \quad (29)$$

where L is the total aperture length, $u = \sin \theta$, and B is a parameter determining the ratio of amplitudes of main-beam to first sidelobe. As shown in Fig. 9 the sidelobe level decreases inversely with u . The aperture distribution required to produce this pattern is given by

$$g(z) = I_0 \left[\pi B \sqrt{1 - \left(\frac{2z}{L}\right)^2} \right], \quad (30)$$

where $I_0(\xi)$ is the modified Bessel function, and z is the distance along the aperture measured from the aperture center.

The derived difference pattern is given by

$$F_D(u) = \frac{d}{du} F(u)$$

$$= \frac{u}{(u^2 - B^2)} \left[\cos \frac{\pi L}{\lambda} \sqrt{u^2 - B^2} - \frac{\sin \frac{\pi L}{\lambda} \sqrt{u^2 - B^2}}{\frac{\pi L}{\lambda} \sqrt{u^2 - B^2}} \right] \quad |u| \geq B$$

$$= \frac{-u}{B^2 - u^2} \left[\cosh \frac{\pi L}{\lambda} \sqrt{B^2 - u^2} - \frac{\sinh \frac{\pi L}{\lambda} \sqrt{B^2 - u^2}}{\frac{\pi L}{\lambda} \sqrt{B^2 - u^2}} \right] \quad 0 \leq |u| \leq B. \quad (31)$$

Again, because of the more rapid decay of the $\sin \xi / \xi$ factor, as compared with that of the cosine term, the sidelobe level eventually decreases inversely with u , as u increases from B .

The aperture distribution required to produce the difference pattern, (31), is just

$$g_D(z) = z I_0 \left[\pi B \sqrt{1 - \left(\frac{2z}{L}\right)^2} \right]. \quad (32)$$

Characteristics of the Taylor pattern and the derived difference pattern are given in Fig. 8.

ACKNOWLEDGMENT

The authors wish to acknowledge the many hours of computation by Miss Carol Hasson, and the excellent experimental pattern work by C. H. Nonnemaker.

BIBLIOGRAPHY

- [1] C. L. Dolph, "A current distribution for broadside arrays which optimizes the relationship between beam width and sidelobe level," *Proc. IRE*, vol. 34, pp. 335-348; June, 1946.
- [2] H. J. Riblet, "Discussion on 'A current distribution for broadside arrays which optimizes the relationship between beam width and sidelobe level,'" *Proc. IRE*, vol. 35, pp. 489-492; May, 1947.
- [3] G. Sinclair and F. V. Cairns, "Optimum patterns for arrays of nonisotropic sources," *IRE TRANS. ON ANTENNAS AND PROPAGATION*, vol. AP-1, pp. 50-61; February, 1952.
- [4] T. T. Taylor, "One-Parameter Family of Line Sources Producing Modified ($\sin \pi u / \pi u$) Patterns," Hughes Aircraft Co., Culver City, Calif., Tech. Memo. No. 324; September, 1953.
- [5] T. T. Taylor, "Design of Line Sources for Narrow Beamwidth and Low Sidelobes," Hughes Aircraft Co., Culver City, Calif., Tech. Memo. No. 316; July, 1953.
- [6] NBS, *Appl. Math. Ser. 9*, "Tables of Chebyshev Polynomials $S_n(x)$ and $C_n(x)$," U. S. Government Printing Office, Washington, D. C.; December, 1952.
- [7] "Tschebyscheff Antenna Distribution, Beamwidth, and Gain Tables," Navord Rept. 4629; 1958.
- [8] R. Tang, "A Slot with Variable Coupling and Its Application to a Linear Array," Hughes Aircraft Co., Culver City, Calif., RLM(M) 56-15; July, 1956.

Radiation from a Tapered Surface Wave Antenna*

LEOPOLD B. FELSEN†, SENIOR MEMBER, IRE

Summary—Utilizing results obtained previously for the propagation of electromagnetic waves along a plane surface having a linear spatial variation of surface admittance, an approximate analysis of the radiation properties of a certain two-dimensional tapered surface wave antenna is carried out. The radiating structure consists of a surface waveguide of finite length having a linear susceptance variation, inserted between a feeding surface waveguide with constant susceptance, and a perfectly conducting plane. The separate junction effects at the input and output ends of the taper are evaluated approximately for the case where the taper susceptance variation is gradual, and their combined influence on the radiation pattern is discussed.

I. INTRODUCTION

IN A previous publication,¹ formal solutions have been obtained for the electromagnetic fields radiated by line and ring sources in the presence of a semi-infinite wedge and cone, respectively, having a linearly varying surface impedance (or admittance, depending on polarization). In this paper, some of the above-mentioned results are utilized for the analysis of a tapered surface wave antenna along which the surface susceptance increases linearly.

A tapered reactive surface plays an important role in surface wave antenna applications. A conventional plane surface wave structure with constant surface reactance guides energy along its surface but does not radiate. To induce radiation, the surface impedance must be varied: either abruptly, as in the case of a sudden termination of the guiding structure or an abrupt junction with a different reactive surface, or gradually, as in a taper. Concerning abrupt transitions in surface reactance, these are accompanied not only by radiation but also by reflection. To minimize reflections, the changes in reactance at a junction must be kept small, leading also to a small amount of radiated energy; to obtain substantial radiation, a series of junctions is usually required. A tapered reactive surface constitutes the more desirable smooth equivalent of a sequence of small abrupt transitions. The use of tapers also arises in passing from surfaces supporting strongly bound surface waves to surfaces supporting weakly bound surface waves. The relatively pure excitation of a surface wave is most easily accomplished on the former, while radiation proceeds most readily from the latter.

Surface wave antennas are commonly used to yield high-gain endfire radiation patterns. The radiation from any very long taper, over which the reactance changes slowly and monotonically from a fixed value to zero,² is expected to be high-gain endfire; *i.e.*, the pattern has a sharp maximum in the direction along the surface. However, the manner of decrease of the field intensity in the angular direction away from the surface depends on the functional variation of the surface reactance in the taper. Tapers having a susceptance which increases linearly with distance along the surface, as considered herein, can support a "surface wave" whose field intensity decreases exponentially away from the surface in an angular direction. However, this exponential pattern is maintained only if the taper is infinite in length. To aid in the evaluation of the radiation from a finite taper, we consider below two junction effects which arise in practice: 1) the junction between a surface having a constant reactance $X_0 < 0$ and the infinite taper having a variable reactance $X(x)$ [Fig. 1(a)], and 2) the junction between the taper and a surface of zero reactance [Fig. 1(b)]. In both cases, a surface wave is assumed incident from the left.³ A practical arrangement comprising a combination of these two effects is also discussed (see Fig. 9). The surface reactance in Fig. 1(a) is seen to be continuous at the junction point $x=a$, while that in Fig. 1(b) is discontinuous at the junction point $x=b$. An approximate analysis of these junctions is carried out below. As a preliminary we first recall some of the properties of the infinitely long taper.

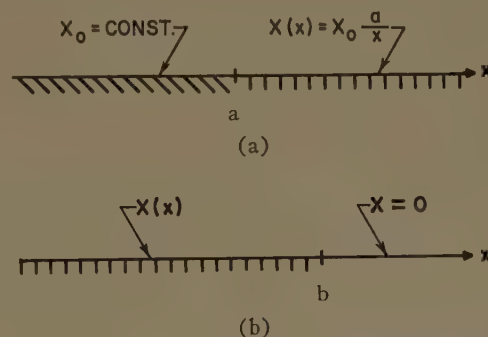


Fig. 1—(a) Junction between constant and tapered reactive surfaces; (b) junction between tapered reactive surface and perfect conductor.

* Received by the PGAP, March 15, 1960.

† Office of Naval Res., London, Eng. On leave of absence from Microwave Res. Inst., Polytechnic Inst. of Bklyn., N. Y., where this work was performed under AF Cambridge Res. Cntr. Contract No. AF-19 (604)-4143.

¹ L. B. Felsen, "Electromagnetic properties of wedge and cone surfaces with a linearly varying surface impedance," IRE TRANS. ON ANTENNAS AND PROPAGATION, vol. AP-7, pp. S231-S243; December, 1959.

² This variation is appropriate to surface waves whose only magnetic field component is parallel to the surface. Only this polarization is considered henceforth.

³ For effects of radiation from the feed, not considered herein, see F. J. Zucker, "A surface wave antenna paradox," presented at URSI Fall Meeting, Pennsylvania State University, Pa.; 1958.

II. THE INFINITE TAPER

Consider the plane surface shown in Fig. 2, along which the surface impedance z (normalized to the impedance of free space) varies like $z = -i/kcx$, where k is the free-space wave number, c is a constant with $\text{Im } c \leq 0$, $\text{Re } c > 0$, and x is the rectilinear variable along the surface. The origin $x=0$ is assumed to be situated somewhere to the left. In view of the assumed time dependence $\exp(-i\omega t)$, the reactive part of the surface impedance is inductive; if $\text{Im } c = 0$, the surface impedance is purely inductive. (Such a reactive surface can be realized approximately by closely spaced metallic corrugations whose depth is chosen so as to produce the desired reactance variation). It was shown in (4) and (20) of the previous paper¹ that the variable impedance surface in Fig. 2 can support a "radiating surface wave" whose only magnetic vector field component H is directed parallel to the z axis and varies like

$$H(\rho) \propto e^{-\phi/c} H_{-\frac{1}{2}}^{(1)}(k\rho), \quad \rho = (\rho, \phi), \quad (1)$$

where ρ and ϕ are cylindrical polar coordinates measured from the origin $x=y=0$ and $H_{\nu}^{(1)}(x)$ is the Hankel function of the first kind of order ν and argument x . In this expression, it is assumed that $\text{Re } (1/c)$ is large enough so that terms of $O[\exp(-2\pi/c)]$ are negligible (this corresponds to an assumed wedge angle $\alpha = \pi$ in (18) of the earlier work¹), and that all sources are situated to the left of the observation point; i.e., the wave is propagating to the right. It was noted previously [discussion following (20)]¹ that the above surface wave can be excited in pure form by a source distribution having a dependence $\exp(-\phi/c)$ over any cylindrical surface surrounding the origin. Once excited, the surface wave will maintain its form indefinitely; if the taper is infinitely long, the variation of the far magnetic field is obtained from (1) by employing the asymptotic form of the Hankel function:

$$H(\rho) \propto \frac{e^{ik\rho}}{\sqrt{k\rho}} e^{-\phi/c}, \quad \rho \rightarrow \infty, \quad (2)$$

so that $\exp(-\phi/c)$ constitutes the angular radiation pattern of the infinite taper when excited in the surface wave mode only. We note that the field decays the more rapidly away from the surface the smaller the value of c , i.e., the more slowly the surface admittance $1/z$ increases.

III. JUNCTION BETWEEN CONSTANT AND TAPERED REACTIVE SURFACES

A. Formulation and Assumptions

We proceed now to an approximate analysis of the radiating properties of the configuration shown in Fig. 1(a), when excited by a surface wave incident from the left. The magnetic field of this incident wave has only

a z component and is assumed to be given by:

$$H_0(\rho) = e^{ik_0 x} e^{-\eta_0 y}, \quad \eta_0 = ikz_0 = -kX_0, \quad \kappa_0 = \sqrt{k^2 + \eta_0^2} \quad (3)$$

where y is the direction perpendicular to the surface, and $z_0 = iX_0$ is the constant (purely reactive) surface impedance normalized to that of free space. [A constant factor A_0 denoting the strength of the incident magnetic field in amperes per meter (MKS units) has been omitted from (3) for the sake of simplicity.] Since the surface is inductive, $X_0 < 0$ and $\eta_0 > 0$. It is well known that (3) constitutes a solution of the Maxwell field equations in the presence of a surface with constant reactance X_0 . [As noted previously, a time dependence $\exp(-i\omega t)$ is implied throughout.] Because of the symmetry of the incident field with respect to the configuration in Fig. 1(a), the problem is independent of the z coordinate and can be described everywhere in terms of the single (z) component of magnetic field.

To evaluate the magnetic field $H(\rho)$ to the right of the junction, we construct the auxiliary region S depicted in Fig. 3, bounded by the curves s_1 , s_2 , s_3 , and s_4 , for a subsequent application of Green's theorem. s_1 is the semi-infinite segment of the x axis occupied by the tapered reactive surface. s_2 is a quarter circle of radius a centered at the origin $x=y=0$. s_3 is the segment of the positive y axis lying between $y=a$ and $y=\infty$. s_4 is a quarter circle of infinite radius centered at the origin. It is to be noted that the choice of the origin in Fig. 3 is dictated by the value of a , which in turn is specified at the outset as part of the boundary conditions on the tapered reactive surface. The choice of a determines the rate of impedance variation along the

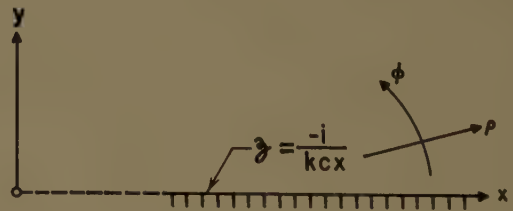


Fig. 2—Variable impedance surface.

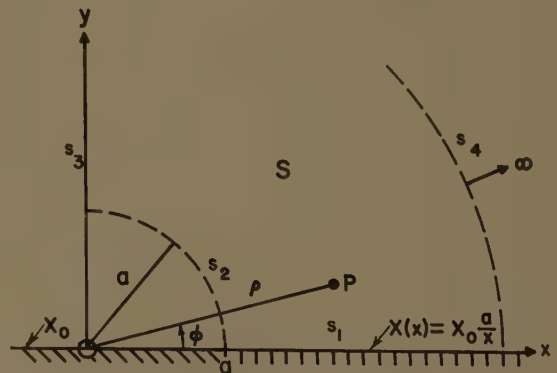


Fig. 3—Auxiliary regions for use in Green's theorem.

taper as evident from the equation

$$X(x) = X_0 \frac{a}{x}. \quad (4a)$$

In terms of the parameters employed previously¹ and shown on Fig. 2, we note that for a purely reactive surface,

$$X(x) = -iz(x) = \frac{-1}{kc x}, \quad c > 0, \quad (4b)$$

whence the relation between the taper parameters a and c is

$$a = \frac{-1}{kc X_0}. \quad (4c)$$

Green's theorem, as applied to the magnetic field $H(\rho)$ and a Green's function $G(\rho, \rho')$, is as follows:

$$\begin{aligned} \int_S [H(\rho')(\nabla'^2 + k^2)G(\rho, \rho') - G(\rho, \rho')(\nabla'^2 + k^2)H(\rho')] dS' \\ = \oint_S \left[H(\rho') \frac{\partial}{\partial n'} G(\rho, \rho') - G(\rho, \rho') \frac{\partial}{\partial n'} H(\rho') \right] ds' \end{aligned} \quad (5)$$

where $s = s_1 + s_2 + s_3 + s_4$ and n denotes the outward normal. Now H satisfies the wave equation

$$(\nabla^2 + k^2)H = 0 \text{ in } S, \quad (6a)$$

the radiation condition

$$\sqrt{\rho} \left(\frac{\partial H}{\partial \rho} - ikH \right) \rightarrow 0 \text{ as } \rho \rightarrow \infty \text{ on } s_4 \quad (6b)$$

and the impedance boundary condition

$$E_\rho ik \sqrt{\frac{\epsilon}{\mu}} = \frac{\partial H}{\partial n} = ikz(\rho)H \text{ on } s_1. \quad (6c)$$

The first equality in (6c) is a consequence of the Maxwell field equations. $\sqrt{\epsilon/\mu}$ represents the admittance of free space. It is convenient to choose a Green's function G which satisfies the inhomogeneous wave equation

$$(\nabla^2 + k^2)G(\rho, \rho') = -\delta(\rho - \rho') \text{ in } S, \quad (7a)$$

the radiation condition

$$\sqrt{\rho} \left(\frac{\partial G}{\partial \rho} - ikG \right) \rightarrow 0 \text{ as } \rho \rightarrow \infty \text{ on } s_4, \quad (7b)$$

the impedance condition

$$\frac{\partial G}{\partial n} = ikz(\rho)G \text{ on } s_1 \quad (7c)$$

and the Dirichlet condition

$$G = 0 \text{ on } s_2. \quad (7d)$$

The behavior of G on s_3 is left unspecified for the moment. Upon taking account of (6) and (7), (5) reduces to:

$$\begin{aligned} -H(\rho) &= \int_{s_2+s_3} H(\rho') \frac{\partial}{\partial n'} G(\rho, \rho') ds' \\ &\quad - \int_{s_3} G(\rho, \rho') \frac{\partial}{\partial n'} H(\rho') ds'. \end{aligned} \quad (8)$$

We now make the following assumptions in the formulation:

- 1) The actual magnetic field $H(\rho)$ on s_2 and s_3 is approximated by the incident magnetic field $H_0(\rho)$ given in (3).
- 2) Terms of $O(e^{kaX_0})$, $X_0 < 0$, are negligible as compared with terms of $O(1)$.

The first assumption is based on the known fact that the reflection from a small discontinuity in surface impedance is very small.⁴ In the junction problem considered here, the surface impedance is actually continuous at $x=a$ and the discontinuities occur only in the derivatives of the surface impedance. By choice of the parameter a in (4a) reasonably large to assure a gradual taper (this is the only type of taper to be considered), the discontinuities in the derivatives of $z(x)$ at $x=a$ can be made small so that the reflection from the junction produces a negligible effect. Thus, the actual field in, and to the left of, the junction plane is well approximated by the incident field as stated in assumption 1). The second assumption is consistent with the first in that it also applies for large enough values of a . For example, if we employ the criterion that values of $(-kX_0a) > 7$ are satisfactory [$\exp(-7) = 0.00091$], we require $a > 3.5\lambda/(-X_0\pi)$, where $\lambda = 2\pi/k$ is the free-space wavelength.

Since $y \geq a$ on s_3 in Fig. 3, and since H_0 in (3) varies like $\exp(-\eta_0 y)$, $\eta_0 = -kX_0$, we note that the integrals over s_3 are 0 [$\exp(-\eta_0 a)$] and therefore negligible under assumption 2). Thus, we obtain the approximate expression:

$$H(\rho) \cong a \int_0^{\pi/2} e^{i\eta_0 a \cos \phi' - \eta_0 a \sin \phi'} \left(\frac{\partial}{\partial \rho'} G(\rho, \rho') \right)_{\rho'=a} d\phi'. \quad (9)$$

The specification of the Green's function G as in (7) is not unique since no statement was made as yet about its behavior on s_3 . However, from the above considerations, the contribution from the integrals taken over s_3 in (8) is neglected, and we now choose that Green's function G defined in S which satisfies conditions (7a)–(7d) and simplifies as much as possible the evaluation of the integral in (9). The most suitable choice appears

⁴ A. F. Kay, "Scattering of a surface wave by a discontinuity in reactance," IRE TRANS. ON ANTENNAS AND PROPAGATION, vol. AP-7, pp. 22–31, (66)–(69); January, 1959.

to be that appropriate to an infinitely extended angular domain, *i.e.*, one in which the ϕ variable is defined in the interval $0 \leq \phi < \infty$. For the case where the radial domain extends from $\rho=0$ to $\rho=\infty$, such a Green's function (remaining finite at $\rho=0$) has been given (in (21) of the earlier work)¹. The present problem requires instead the boundary condition (7d) at $\rho=a$. By an obvious modification of the radial Green's function g_ρ in (21)¹ to meet condition (7d), we obtain:

$$G(\rho, \rho') = 2\eta e^{-\eta(\phi+\phi')} \hat{g}_\rho(\rho, \rho'; -i\eta) + \frac{1}{2\pi} \int_0^\infty \left[e^{i\mu(\phi-\phi')} + e^{-i\mu(\phi-\phi')} + \frac{\mu+i\eta}{\mu-i\eta} e^{i\mu(\phi+\phi')} + \frac{\mu-i\eta}{\mu+i\eta} e^{-i\mu(\phi+\phi')} \right] \hat{g}_\rho(\rho, \rho'; \mu) d\mu, \quad (10)$$

where $\eta = 1/c = -ka X_0$ and

$$\hat{g}_\rho(\rho, \rho'; \mu) = \frac{\pi i}{2} \left[J_\mu(k\rho') - \frac{J_\mu(ka)}{H_\mu^{(1)}(ka)} H_\mu^{(1)}(k\rho') \right] H_\mu^{(1)}(k\rho), \quad \rho > \rho'. \quad (10a)$$

For $\rho' > \rho$, ρ and ρ' in (10a) are interchanged.

We note from (10a) and the value of the Wronskian for the cylinder functions that

$$\frac{\partial \hat{g}_\rho}{\partial \rho'} \bigg|_{\rho'=a} = \frac{1}{a} \frac{H_\mu^{(1)}(k\rho)}{H_\mu^{(1)}(ka)} = \frac{1}{a} \frac{H_{-\mu}^{(1)}(k\rho)}{H_{-\mu}^{(1)}(ka)}. \quad (11)$$

The second equation in (11) follows from the first in view of the property $H_{-\mu}^{(1)}(z) = e^{i\mu\pi} H_\mu^{(1)}(z)$. Upon substituting (11) into (10) and introducing the change of variable $\mu \rightarrow -\mu$ in part of the integrand, we obtain

$$\frac{\partial}{\partial \rho'} G(\rho, \rho') \bigg|_{\rho'=a} = \frac{2\eta}{a} e^{-\eta(\phi+\phi')} \frac{H_{-i\eta}^{(1)}(k\rho)}{H_{-i\eta}^{(1)}(ka)} + \frac{1}{2\pi a} \int_{-\infty}^\infty \left[e^{i\mu(\phi-\phi')} + \frac{\mu+i\eta}{\mu-i\eta} e^{i\mu(\phi+\phi')} \right] \frac{H_\mu^{(1)}(k\rho)}{H_\mu^{(1)}(ka)} d\mu. \quad (12)$$

Substitution of (12) into (9) and a permissible interchange of the orders of integration leads to the desired formulation:

$$H(\rho) \cong e^{-\eta\phi} \frac{H_{-i\eta}^{(1)}(k\rho)}{H_{-i\eta}^{(1)}(ka)} e^{i\kappa_0 a} 2\eta Q(\eta, \eta) + \frac{e^{i\kappa_0 a}}{2\pi} \int_{-\infty}^\infty e^{i\mu\phi} \left[Q(\eta, i\mu) + \frac{\mu+i\eta}{\mu-i\eta} Q(\eta, -i\mu) \right] \frac{H_\mu^{(1)}(k\rho)}{H_\mu^{(1)}(ka)} d\mu, \quad (13)$$

where

$$Q(\eta, w) = \int_0^{\pi/2} e^{-i2\kappa_0 a \sin^2(\phi'/2) - \eta \sin \phi' - w \phi'} d\phi', \quad (13a)$$

and $\kappa_0 a = ka(1+X_0^2)^{1/2}$, $\eta = -kaX_0$. The first term on the right-hand side of (13) represents the surface wave guided by the taper [see (1)], into which mode we seek to convert as much of the incident energy as possible. The integral represents the additional contribution which arises because the incident field over the surface s_2 in Fig. 3 departs from the $\exp(-\eta\phi)$ dependence required for the establishment of a pure surface wave along the taper.

B. Approximate Field Evaluation

It does not seem possible to evaluate the integral in (13a) exactly in terms of known functions. However, an approximate evaluation can be carried out based on the assumption that η is large. As ϕ' increases away from zero, the integrand is both exponentially damped and rapidly oscillating (*note*: w is either positive real or imaginary); therefore, its maximum contribution arises from the vicinity of $\phi'=0$. An asymptotic evaluation of the integral in (13a) for large values of η can be carried out by various means. By what appears to be the most direct approach, we approximate $\sin^2(\phi'/2)$ and $\sin \phi'$ by $(\phi'/2)^2$ and ϕ' , respectively. The resulting integrand then contains the factor $\exp(-\eta\phi')$. If the upper limit on the integral is now taken as ∞ instead of $\pi/2$, the error is $0[\exp(-\eta\pi/2)]$, which is neglected in view of the assumption made in the preceding section. Thus, we obtain the approximate expression

$$Q(\eta, w) \cong \int_0^\infty e^{-i\kappa_0 a \phi'^2/2 - (\eta+w)\phi'} d\phi'. \quad (14)$$

Upon completion of the square in the exponent of (14), the integral can be written in the form

$$Q(\eta, w) \cong e^{\gamma^2} \int_0^\infty e^{-(\xi\phi'+\gamma)^2} d\phi', \quad \gamma = \frac{\eta+w}{\sqrt{2i\kappa_0 a}}, \quad \xi = \sqrt{\frac{i\kappa_0 a}{2}}, \quad (14a)$$

which in turn can be expressed in terms of the error function complement

$$Q(\eta, w) \cong \sqrt{\frac{2}{i\kappa_0 a}} e^{\gamma^2} \int_\gamma^\infty e^{-y^2} dy. \quad (14b)$$

For large values of γ , $Q(\eta, w)$ in (14b) can be represented via the asymptotic expansion for the error function complement as⁵

$$Q(\eta, w) \sim \frac{1}{\eta+w} \left[1 - \frac{1}{2\gamma^2} + \frac{3}{4\gamma^4} + 0\left(\frac{1}{\gamma^6}\right) \right]. \quad (15)$$

⁵ W. Magnus and F. Oberhettinger, "Special Functions of Mathematical Physics," Chelsea Publishing Co., New York, N. Y., p. 96; 1949.

Thus, the amplitude factor appearing in the surface-wave term in (13) is given for large values of η approximately by:

$$2\eta Q(\eta, \eta) \sim 1 - \frac{i\kappa_0 a}{4\eta^2} - \frac{3(\kappa_0 a)^2}{16\eta^4} + \dots \quad (16a)$$

$$= 1 - \frac{iv}{4kaX_0^2} - \frac{3v^2}{16(ka)^2X_0^4} + \dots,$$

$$v = \sqrt{1 + X_0^2}. \quad (16b)$$

We note that the criterion for the validity of the asymptotic expansion in (16b) is not merely that η is large, but more precisely that $kaX_0^2 = -\eta X_0$ is large.

Since ka is large and $k\rho > ka$, we will have occasion to employ the Debye asymptotic formula for the Hankel function⁶

$$H_\nu^{(1)}(y) \sim \sqrt{\frac{2}{\pi y \cos \psi}} e^{i\psi [\cos \psi + (\psi - \pi/2) \sin \psi] - i\pi/4},$$

$$\sin \psi = \frac{\nu}{y}, \quad (17)$$

valid for large y with $(y - \nu) > 0(y^{-2/3})$ when $y > \nu$ and y, ν are positive, and valid for all imaginary values of ν when y is positive. Thus, we find that

$$\frac{H_{-i\eta}^{(1)}(k\rho)}{H_{-i\eta}^{(1)}(ka)} \sim \sqrt{\frac{av}{\rho\bar{v}}} \exp ik \left\{ \rho\bar{v} - av + iaX_0 \left[\sin^{-1} \left(\frac{iaX_0}{\rho} \right) - \sin^{-1}(iX_0) \right] \right\}, \quad (18)$$

where $\bar{v} = [1 + (aX_0/\rho)^2]^{1/2}$. For far field observations, $\rho \rightarrow \infty$, the above expression reduces to

$$\frac{H_{-i\eta}^{(1)}(k\rho)}{H_{-i\eta}^{(1)}(ka)} \sim \sqrt{\frac{av}{\rho}} e^{ik\rho} e^{-ika[v + iX_0 \sin^{-1}(iX_0)]}$$

$$v = (1 + X_0^2)^{1/2}. \quad (18a)$$

We verify first that, for the limiting case $a \rightarrow \infty$, the result in (13) reduces to that for a constant reactive surface as given in (3). This transition is achieved by moving the origin in Fig. 3 toward $-\infty$ and leaving the points $x=a$ and P fixed. Thus, $a/\rho \rightarrow 1$, $\phi \rightarrow 0$, $a\phi \rightarrow y$, $\rho \rightarrow x$. From (18) we find that

$$\frac{H_{-i\eta}^{(1)}(k\rho)}{H_{-i\eta}^{(1)}(ka)} \sim e^{ik(x-a)v}, \quad a \rightarrow \infty, \rho > a, \quad (19)$$

while from (16b), $2\eta Q(\eta, \eta) \rightarrow 1$. Thus, the surface-wave term in (13) reduces to that in (3). The contribution from the integral in (13) tends to zero as $a \rightarrow \infty$ because of the vanishing of the terms inside the square brackets in the integrand.

Concerning the integral in (13) we ascertain its behavior for large values of ka from a stationary phase evaluation.⁷ For simplicity, only the far field at $\rho \rightarrow \infty$ will be considered. From (14) and (15), one notes that $Q(\eta, \pm i\mu)$ is a slowly varying function of μ which has no singularities on or near the path of integration (at least, for large η). Thus, the possible saddle points of the integrand are those arising from $A = \exp(i\mu\phi) H_\mu^{(1)}(k\rho)/H_\mu^{(1)}(ka)$. In the range $|\mu| < ka$, the ratio of Hankel functions can be approximated using (17); a saddle point of A is found to exist at $\mu_s = ka \sin \phi$. In the range $|\mu| > ka$, the appropriate Debye representation for $H_\mu^{(1)}(ka)$ is employed and reveals no saddle point. Thus, we obtain for the first-order asymptotic representation of the integral

$$I = \int_{-\infty}^{\infty} e^{i\mu\phi} \frac{H_\mu^{(1)}(k\rho)}{H_\mu^{(1)}(ka)} f(\mu) d\mu, \quad (20a)$$

as $\rho \rightarrow \infty$ and for large values of ka , the result

$$I \sim \frac{e^{ik\rho}}{\sqrt{k\rho}} \sqrt{2\pi} ka \cos \phi e^{-ika \cos \phi - i\pi/4} f(ka \sin \phi). \quad (20b)$$

The magnetic field in (13) can now be expressed approximately via (16b), (18a) and (20b) for $\rho \rightarrow \infty$ as:

$$H(\rho) \sim \frac{e^{ik\rho}}{\sqrt{k\rho}} [H_s(\phi) + H_c(\phi)], \quad (21)$$

where $H_s(\phi)$ denotes the surface-wave contribution

$$H_s(\phi) \cong \sqrt{kav} e^{-i\eta \sinh^{-1} X_0} e^{-\eta\phi}$$

$$\cdot \left[1 + \frac{iv}{4\eta X_0} - \frac{3v^2}{16\eta^2 X_0^2} + \dots \right], \quad (21a)$$

while $H_c(\phi)$ represents the contribution from the continuous spectrum

$$H_c(\phi) \cong -\frac{2X_0 v}{\sqrt{2\pi} ka} e^{ika(v - \cos \phi) - i\pi/4}$$

$$\cdot \left[\frac{(\sin 2\phi)(X_0 + i \sin \phi)}{(X_0^2 + \sin^2 \phi)^3} \right]. \quad (21b)$$

It is recalled that $\eta = -kaX_0$, $X_0 < 0$, and $v = (1 + X_0^2)^{1/2}$. Eq. (21) applies for large values of ka , with $-kaX_0$ also large. Concerning the dependence on ka , we note that $H_c(\phi)$ is $O[(ka)^{-3/2}]$ as compared with $H_s(\phi)$. The magnitudes of H_s and H_c are given by:

$$|H_s| \cong \sqrt{kav} e^{-\eta\phi} \left[1 - \frac{5v^2}{32(\eta X_0)^2} + \dots \right], \quad (22a)$$

$$|H_c| \cong \frac{-2X_0 v}{\sqrt{2\pi} ka} \frac{\sin 2\phi}{(X_0^2 + \sin^2 \phi)^{5/2}}. \quad (22b)$$

⁷ See, for example, N. G. de Bruijn, "Asymptotic Methods in Analysis," Interscience Publishers, New York, N. Y., sec. 5.7; 1958.

⁶ *Ibid.*, p. 23.

Viewed as a function of ϕ , $H_s(\phi)$ has its maximum value in the endfire direction $\phi=0$, while $H_c(\phi)$ contributes side-lobes which have a maximum for some finite value of ϕ . We note from (22a) that $|H_s|_{\max} = \sqrt{ka}v\{1-5v^2[32(\eta X_0)^2]^{-1}\}$, while for $-X_0 > 1$, a crude estimate yields from (22b):

$$|H_c|_{\max} < \sqrt{2/\pi} v/(kaX_0^4).$$

Plots of (22) as a function of ϕ , for various values of ka and X_0 , are shown in Figs. 4 and 5. In Fig. 4, a fixed value $ka=20$ is assumed and $(-X_0)$ ranges from 0.3 to 2 ($ka=20$ implies that $a=10\lambda/\pi \approx 3.2\lambda$, *i.e.*, the surface reactance in the taper decreases in absolute value by a factor of $(1/2)$ over an interval of 3.2λ). For $(-X_0)=0.3$, 0.5, 1, the relative side-lobe level $|H_c|_{\max}^2/|H_s|_{\max}^2$ is, respectively, 0.04, 0.0015, 0.00003. This decrease in the side-lobe level with increasing $(-X_0)$ is to be expected since the larger $(-X_0)$, the more tightly bound is the incident surface wave and the less is the radiation due to the junction discontinuity. Similarly, we note from Fig. 5 that, for fixed X_0 , the side-lobe level decreases with increasing ka , *i.e.*, for more gradual tapers. It is also evident that the surface-wave pattern becomes sharper when either ka or $(-X_0)$ (*i.e.*, η) is increased.

C. Radiated Power

It is also of interest to evaluate the fractions of incident power carried by the surface wave and the continuous spectrum. We recall first the relation between E_ϕ and H :

$$E_\phi = \frac{1}{ik} \sqrt{\frac{\mu}{\epsilon}} \frac{\partial H}{\partial \rho}. \quad (23)$$

The power per unit length along the z direction (see Fig. 2) radiated through a quarter circle of infinite radius is given by

$$P = \text{Re} \int_0^{\pi/2} E_\phi H^* \rho d\phi, \quad \rho \rightarrow \infty, \quad (24)$$

where the asterisk denotes the complex conjugate. Upon inserting the expressions for E_ϕ and H [see (23)] from (13) into (24) and carrying out the ϕ integration, we find, upon neglecting terms of $O(e^{-\eta})$, that P can be written as

$$P = P_s + P_c, \quad (25)$$

where P_s is the power carried by the surface wave and P_c is the power in the continuous spectrum. This observation could have been anticipated from the results of (21) in the previous paper,¹ where it was shown that the surface wave mode is orthogonal to the continuous

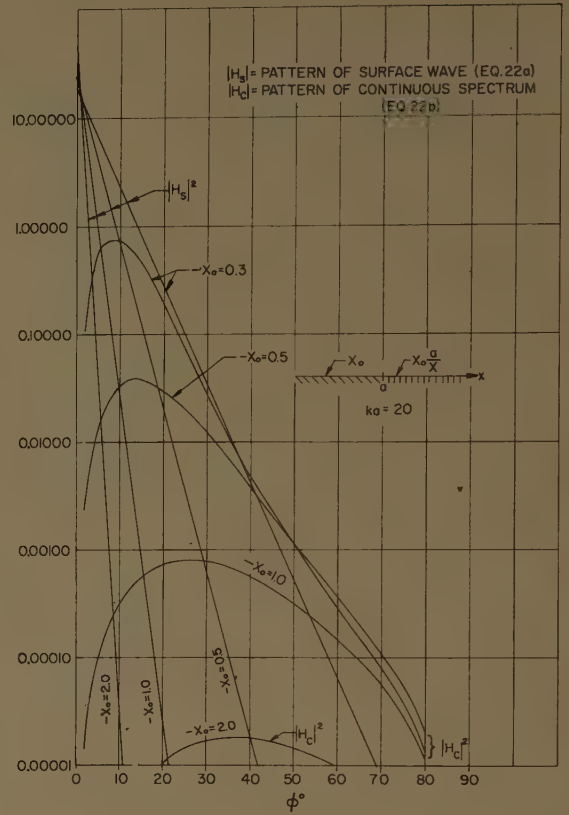


Fig. 4—Radiation from junction between constant and tapered reactive surfaces.

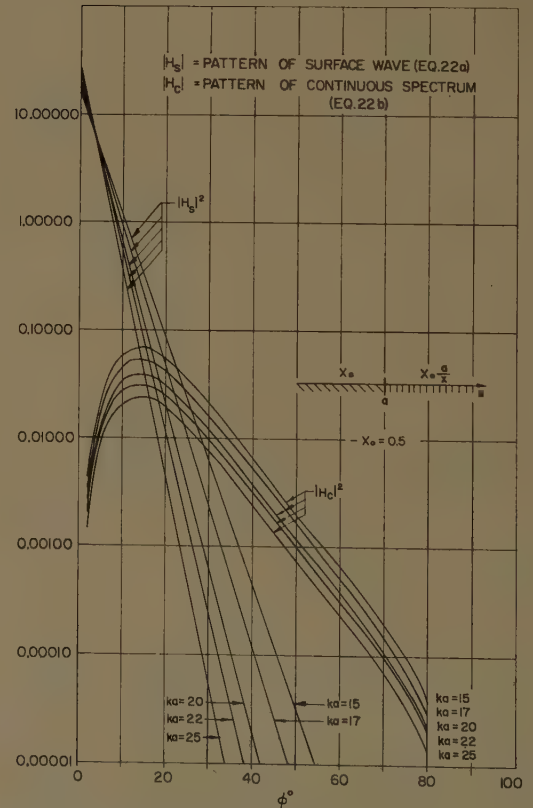


Fig. 5—Radiation from junction between constant and tapered reactive surfaces.

spectrum.⁸ P_s is evaluated readily upon substituting from (21) and (21a) into (24):

$$P_s \cong \sqrt{\frac{\mu}{\epsilon}} \frac{v}{-2kX_0} \left[1 - \frac{5}{16} \left(\frac{v}{\eta X_0} \right)^2 + \dots \right], \quad X_0 < 0, \quad (26)$$

where terms of $O(e^{-v})$ have been neglected.

To calculate the incident power P_i (per unit length in the z direction), we note that E_y is given in terms of H_0 in (3) by:

$$E_y = \sqrt{\frac{\mu}{\epsilon}} \frac{1}{ik} \frac{\partial H_0}{\partial x} = \sqrt{\frac{\mu}{\epsilon}} v H_0, \quad (27)$$

so that

$$P_i = \text{Re} \int_0^\infty E_y H_0^* dy = \sqrt{\frac{\mu}{\epsilon}} \frac{v}{-2kX_0}. \quad (28)$$

(Concerning dimensional units, it is recalled from the comment following (3) that (28) should actually be multiplied by A_0^2 (amp²/meter²), yielding for P_i the dimensions watts per meter.) The fraction of incident power carried by the taper surface wave is therefore seen to be

$$\frac{P_s}{P_i} \cong 1 - \frac{5}{16} \left(\frac{v}{\eta X_0} \right)^2 + \left(\text{higher-order terms in} \left(\frac{v}{\eta X_0} \right) \right). \quad (29)$$

Since $(P_s + P_c)$ must be approximately equal to P_i (note: the reflected power has been neglected), one obtains directly the relative power in the continuous spectrum

$$\frac{P_c}{P_i} \cong \frac{5}{16} \left(\frac{v}{\eta X_0} \right)^2 + \dots \quad (30)$$

A plot of $(P_c/v^2 P_i)$ vs (ηX_0) is shown in Fig. 6. For $(-X_0) \leq 1$, i.e., $v^2 \leq 2$, the relative power carried by the continuous spectrum is seen to be less than 1 per cent when $(-\eta X_0) > 8$.

IV. JUNCTION BETWEEN TAPERED REACTIVE SURFACE AND PERFECTLY CONDUCTING PLANE

This junction, depicted in Fig. 1(b), arises when the tapered reactive surface is terminated in a perfectly

⁸ For a lossless surface (η positive real), orthogonality between mode functions implies power orthogonality as well. This statement does not apply for lossy surfaces, although other considerations in this paper hold also for lossy structures, i.e., complex η .

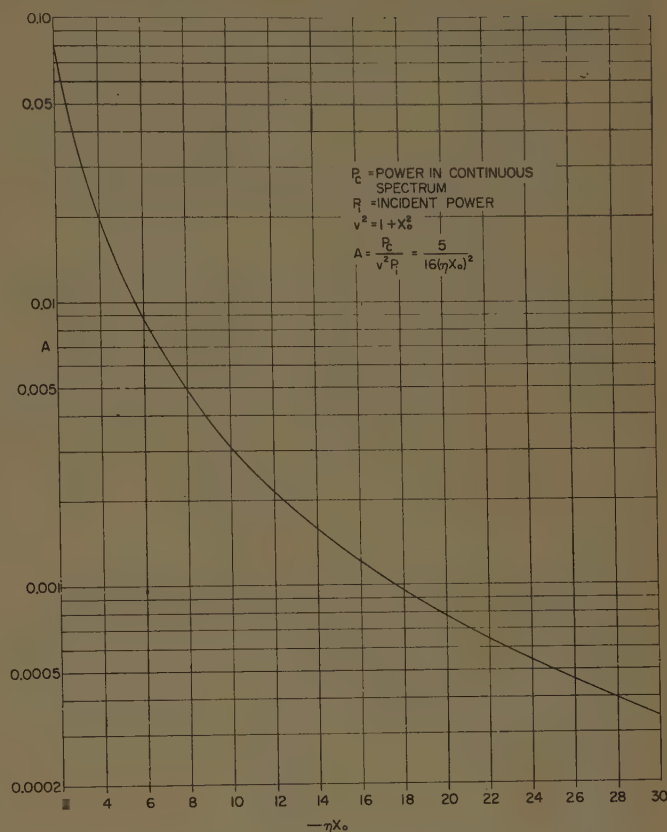


Fig. 6—Relative power radiated in the continuous spectrum.

conducting plane. If the variable reactance along the taper is given by $X(x) = X_0 a/x$,⁹ the reactance at the junction point $x=b$ is $X(b) = X_0 a/b$. [See (4c) for the relation between the taper parameter $(X_0 a)$ and that for the infinite taper, c , as in Fig. 2.] For use as an effective endfire antenna, the taper should be long enough to permit almost all of the energy to be radiated off before it reaches the termination. Thus, $X(b)$ is assumed to be very small so that the discontinuity in reactance at the junction point is likewise small. Consequently, we assume as in Section III. A that the field to the left of the junction in Fig. 1(b) can be approximated by the incident field only.

An approximate formulation for the field to the right of the junction plane in Fig. 1(b) can be carried out by applying Green's theorem in (5) to the region shown in Fig. 3, provided that a is replaced by b , X_0 by $X(x)$, and $X(x)$ by $X=0$. H satisfies (6) except that $\partial H/\partial n = 0$ on s_1 . Upon choosing a Green's function G as in (7), but satisfying on s_1 the condition $\partial G/\partial n = 0$, we find that the magnetic field H in S is still given by (8). If we now assume, as mentioned above, that the magnetic field on s_2 and s_3 is approximated by the incident magnetic

⁹ In the present discussion, X_0 represents the surface reactance at any selected point $x=a$ on the taper.

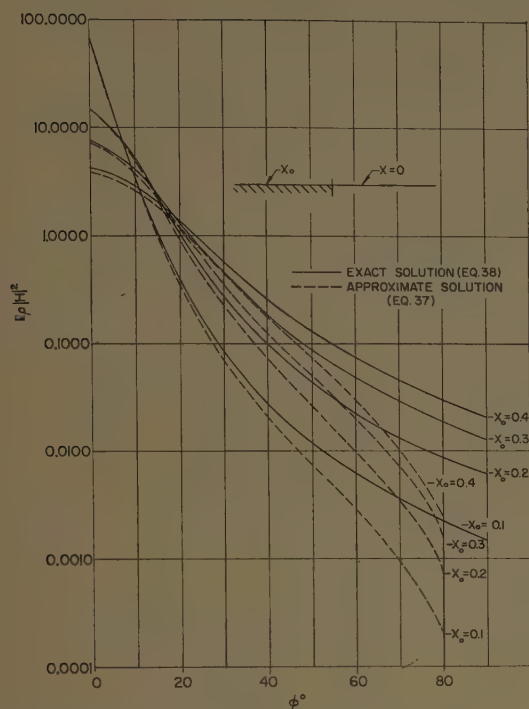


Fig. 8—Radiation from junction between constant reactive surface and perfect conductor; comparison of approximate and exact results.

with the incident power in (28).¹⁰ The two results agree very closely for small values of X_0 , thus verifying that the reflected wave contribution in Fig. 4 is indeed negligible. The same statement then applies to the junction in Fig. 1(b) if $(-\alpha X_0)$ is small.

V. FINITE TAPER

The preceding considerations permit us to make a few remarks about a taper of finite length as in Fig. 9. The taper (region II) is situated between a surface with constant reactance (region I) and zero reactance (region III). A surface wave is assumed incident from the left. If the taper is gradual (ka large) and long enough to make $X_0 a/b = \alpha X_0$ small, the following observations can be made:

1) Because of the junction at $x=a$, the incident surface wave excites in region II the taper surface wave mode plus a continuous spectrum [see (13) and (21)]; reflection back into region I is expected to be negligible since the surface reactance is continuous at $x=a$ and

¹⁰ The integration in (39), with (37), is performed readily by changing to the complex variable z via $z = e^{i\phi}$. (See A. F. Kay, *op. cit.*) Then,

$$\int_{-\pi/2}^{\pi/2} \frac{\cos^2 \phi}{(\sin^2 \phi + X_0^2)^2} d\phi = \frac{4}{i} \int_C \frac{(1+z^2)^2}{[(z^2-1)^2 - 4X_0^2 z^2]} dz,$$

where the closed contour C consists of the segment of the imaginary axis lying between $z = -i$ and $z = i$ and the semicircle of unit radius passing through $z = 1$. The integral is then evaluated in terms of the residue at the double pole $z = v - X_0$.

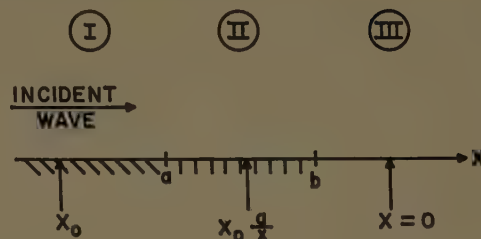


Fig. 9—Finite taper.

the discontinuity in its rate of change per wavelength is small

$$\left[(1/k) dX(x)/dx \right]_{x=a} = \frac{-X_0}{ka}.$$

2) Since the continuous spectrum in region II vanishes on the reactive surface [see (21b)], it will be affected negligibly by the junction at $x=b$; thus, the discontinuity in reactance at $x=b$ is excited only by the taper surface wave. The reflection from this junction is negligible since αX_0 is assumed small.

3) The radiation field in region III consists of the continuous spectrum excited by the incident taper surface wave [see (34) and (35)] plus the continuous spectrum resulting from the junction at $x=a$.¹¹ The former yields an endfire pattern, while the latter contributes sidelobes at some finite elevation from the surface.

Upon combining the results in (21) and (34), we then obtain the following approximate expression for the far field in region III due to the surface wave (3) incident in region I:

$$H(\phi) \sim \frac{e^{i(k\rho - \pi/4)}}{\sqrt{k\rho}} [H_1(\phi) + H_2(\phi)], \quad \rho \rightarrow \infty, \quad (40)$$

where $H_1(\phi)$ is the primary pattern function

$$H_1 \cong \sqrt{\frac{2\alpha v}{\pi v'}} \left[1 + \frac{iv}{\eta X_0} - \frac{3v^2}{16\eta^2 X_0^2} \right] \frac{(-\alpha X_0) \cos \phi}{(\alpha X_0)^2 + \sin^2 \phi} \cdot e^{ikb[v' - i\alpha X_0 \{\sin^{-1}(\alpha X_0) - \sin^{-1}(iX_0)\} - \cos \phi]} \quad (40a)$$

while $H_2(\phi)$ represents the sidelobe pattern

$$H_2 \cong \sqrt{\frac{2}{\pi}} \frac{(-X_0 v)}{ka} \frac{(\sin 2\phi)(X_0 + i \sin \phi)}{(X_0^2 + \sin^2 \phi)^3} \cdot e^{ika(v - \cos \phi)}. \quad (40b)$$

We have defined

$$v = \sqrt{1 + X_0^2}, \quad v' = \sqrt{1 + (\alpha X_0)^2}, \quad \eta = -kaX_0 > 0, \quad \alpha = \frac{a}{b}. \quad (40c)$$

¹¹ As pointed out previously, the feed radiation pattern is not considered herein.

In obtaining (40a) from (34), we have approximated the ratio of the Hankel functions by its asymptotic form as in (18), and the factor $2\eta Q(\eta, \eta)$ from (16b) as well as the factor $\exp(ikva)$ has been included to make the taper surface wave in (31) correspond with that in (13), as appropriate to the excitation in (3). The magnitude of H_1 is evidently given by (35) provided that we multiply that equation by

$$\sqrt{k\rho} \left(1 - \frac{5v^2}{32\eta^2 X_0^2} \right);$$

the magnitude of H_2 is given in (22b).

The above considerations concerning radiation from the finite taper shown in Fig. 9 can be summarized as follows:

1) The primary radiation pattern is approximately the same as that arising from a terminated surface with constant reactance αX_0 , where αX_0 is the surface reactance at the endpoint of the taper. The smaller αX_0 , the sharper the pattern.

2) Sidelobes are caused by the junction effect at $x=a$ in Fig. 9. If $-X_0 > 1$, a crude estimate yields for the maximum sidelobe level:

$$|H_2|_{\max} < \sqrt{\frac{2}{\pi}} \frac{v}{kaX_0^4} [\text{see (22b)}].$$

The maximum main lobe level (at $\phi=0$) is obtained from (40a). Thus, for $-X_0 > 1$, the relative sidelobe level

$$\frac{|H_2|_{\max}}{|H_1|_{\max}} < \sqrt{v\alpha} \frac{-1}{kaX_0^3} \left(1 + \frac{5}{32} \frac{v^2}{(ka)^2 X_0^4} \right). \quad (41)$$

3) The required minimum physical length of the taper is a function of both α and X_0 . Suppose that we specify $(-\alpha X_0)$ at some small value (say, less than 0.1) in order to obtain a sufficiently sharp pattern. Suppose also that X_0 is given (e.g., $-X_0 > 0.5$); the value of α is thereby determined. We now choose $ka = 2\pi a/\lambda$ such that the sidelobe level is below some specified maximum value. Then the length of the taper in wavelengths is $(b-a)/\lambda = (a/\lambda) [1/\alpha - 1]$. If $(-X_0)$ is large, (a/λ) can be relatively small; but α must then be correspondingly small to yield the desired terminal reactance $(-\alpha X_0)$. Conversely, if $(-X_0)$ is small, i.e., α is relatively large, the taper must be made more gradual and requires a larger value of (a/λ) . There appears to be no obvious combination of α and X_0 which minimizes the taper length.

Near-Field Gain of Aperture Antennas*

ALAN F. KAY†, MEMBER, IRE

Summary—Formulas for the ratio η of received to transmitted power are examined for microwave aperture antennas at any range.

It is shown that with optimum aperture illuminations the far-field range equation continues to hold fairly well in the near field down to a distance at which it implies that nearly all the transmitted power is received! However, the aperture illuminations with maximum η (nearly 100 per cent) are different from the uniform, constant phase illumination which is optimum in the far-field case. The optimum near-field illuminations not only have the phase variation associated with elliptic rather than parabolic reflectors but they also have some amplitude variations. Some simple illuminations which can be realized practically by lenses and dishes are shown to be sufficiently close to the optimum cases for most practical purposes.

A formula for the power density in the near field of a transmitting aperture is also derived and it is shown how to maximize the power flow through any given area of space by design of the transmitting aperture illumination.

I. INTRODUCTION

LET η be the ratio of received to transmitted power in a one-way system. We refer to η as the path efficiency and $-10 \log_{10} \eta$ as the path loss in db. If the transmitting and receiving antennas have aperture areas A_T and A_R , aperture efficiencies η_T and η_R , and are separated by a distance R_0 at a wavelength λ , then in the far field

$$\eta = \frac{P_R}{P_T} = \eta_T \eta_R \frac{A_T A_R}{\lambda^2 R_0^2}. \quad (1)$$

This is the far-field range equation.

Several forms of a near-field range equation are available in the literature [1]–[4]. The report [5], on which this paper is based, has shown the equivalence of some of these expressions and has derived some new forms. It also considers the effect on these formulas of permitting supergain antennas. The question of super-

* Received by the PGAP, April 21, 1960; revised manuscript received, June 27, 1960. The work reported here was sponsored by the AF Cambridge Res. Center under Contract AF19(604)-5532.

† Technical Research Group, Inc., Somerville, Mass.

gaining is related to the validity of the far-field range equation (1). This fact may be seen from a consideration of two antennas of fixed aperture size, one transmitting, the other receiving, placed so far from each other that the far-field range equation (1) would ordinarily be presumed to hold. Now if the aperture illuminations of either (or both) antennas are changed so that, by means of supergain distributions, the gain or gains of the antennas increase indefinitely, (1) must ultimately fail, for not to do so would violate conservation of energy. Therefore as the gain of an antenna increases without limit in the supergain region, the far field must recede to infinity. Formulas for η , such as (22) or (25) of [5], valid in either the near or far field, continue to hold. But if supergaining is ruled out (which is equivalent to assuming that (6) is valid [5]), then a simplified formula for near-field gain, sufficient for most practical applications, results. This formula is derived heuristically in the next section and is given by (8). One principal purpose of this paper is to examine this formula in the Fresnel zone in regard to the design of aperture illuminations for maximizing η .

Another important quantity considered, η_1 , is defined as the ratio of the power transmitted through a given area A of space to the total power radiated by an aperture antenna. This is the key quantity if power is beamed not to a nearby receiving antenna but to any absorbing, reflecting, or scattering body which is characterized as absorbing, reflecting, or scattering a certain ratio of the total power incident on it regardless of the phase or amplitude distribution of the field over the body. Without supergaining, it is shown that

$$\eta \leq \eta_1$$

if the body is the same size as the receiving antenna ($A_R = A$). That is, an aperture antenna can not receive at its terminals more than 100 per cent of the energy which falls on its aperture without supergaining. A formula is obtained for the receiving antenna illumination so that it *can* receive all of the energy which falls on it from a given transmitter. If the transmitting antenna also satisfies this formula, it will focus as much as possible of its energy on the receiving reflector. If both formulas are satisfied simultaneously, then the path loss will be minimized and the efficiency will be close to the maximum possible, namely $\min\{1, A_T A_R / \lambda^2 R_0^2\}$. The meaning of "close to" is made clear in the sequel.

All of the considerations in this paper neglect multiple scattering between the antennas. In the case of principal interest where nearly all of the power transmitted is received on a direct path, there is necessarily little multiple scattering.

In this paper an aperture antenna is defined as one which radiates only into a half space, say $z > 0$, and has a bounded aperture. The plane $z = 0$ is then called the

aperture plane, and an area A' in this plane is called the aperture if it is the smallest area in $z = 0$ such that the tangential E field of the antenna vanishes in $z = 0$ outside of A' . For example, a small slot in an infinite ground screen satisfies this definition. However, the small slot is not an antenna for which supergain can be neglected.

The results in Sections V and VI and many of the results mentioned in this introduction are valid only in the Fresnel zone and the far field. The Fresnel zone is defined in Section V, and it is shown there that it includes most of the region of interest outside the far field. It includes, for example, all of the ranges to which a paraboloid may be defocussed to obtain close to the maximum possible energy transfer.

II. NEAR-FIELD RANGE EQUATIONS

In this section we give a heuristic derivation of the desired near-field range equation.

Let P and P' be general points in the receiving and transmitting apertures A and A' respectively and let $f_R(P)$ and $f_T(P')$ be the corresponding aperture illuminations. The field at P will be [6]

$$f(P) = c_0 \int_{A'} f_T(P') \frac{e^{ikR}}{R} dP' \quad (2)$$

where R is the distance from P to P' and c_0 is a proportionality constant. The received voltage V due to this field will be proportional to this field times the receiving illumination at P and will be the integral of contributions from all points P . Thus if c_0' is another constant,

$$V = c_0' \int_A f_R(P) dP \int_{A'} f_T(P') \frac{e^{ikR}}{R} dP'. \quad (3)$$

The ratio of received to transmitted power is then, for some constant c_0'' ,

$$\eta = c_0'' \left| \int_A f_R(P) dP \int_{A'} f_T(P') \frac{e^{ikR}}{R} dP' \right|^2. \quad (4)$$

We may evaluate c_0'' by allowing R to approach infinity. For sufficiently large R we know that the far-field range equation (1) can be written in the form

$$\eta = \frac{G_T G_R \lambda^2}{16\pi^2 R_0^2} \quad (5)$$

where G_T and G_R are the transmitting and receiving antenna gains given by

$$G_T = \frac{4\pi \left| \int_{A'} f_T(P') dP' \right|^2}{\lambda^2 \int_{A'} |f_T(P')|^2 dP'}$$

$$G_R = \frac{4\pi \left| \int_A f_R(P) dP \right|^2}{\lambda^2 \int_A |f_R(P)|^2 dP} \quad (6)$$

For large R , (4) becomes

$$\eta = \frac{c_0''}{R_0^2} \left| \int_A f_R(P) dP \right|^2 \left| \int_{A'} f_T(P') dP' \right|^2 \quad (7)$$

We may evaluate c_0'' by equating (5) and (7). Making use of (6) we obtain an expression for c_0'' which, when substituted in (4), yields

$$\eta = \frac{\left| \int_A f_R(P) dP \int_{A'} f_T(P') \frac{e^{ikR}}{R} dP' \right|^2}{\lambda^2 \int_A |f_R(P)|^2 dP \int_{A'} |f_T(P')|^2 dP'} \quad (8)$$

which is the result that we desire. In [5] this equation is shown to be rigorously correct in the general case if the illuminations are properly interpreted as vector functions and if supergain is neglected.

III. ENERGY FOCUSED ON AN AREA AT ANY DISTANCE FROM AN APERTURE ANTENNA

We derive a formula for the fraction η_1 of the total power radiated by an antenna with aperture A' , which flows through a fixed plane area A of space, lying in the near (or far) field, parallel to the aperture plane of the transmitter a distance R_0 from it.

The power transmitted per unit area at a point P is

$$T_P = c_1 \left| \int_{A'} f_T(P') \frac{e^{ikR}}{R} dP' \right|^2 \quad (9)$$

where c_1 is a proportionality constant which will be determined by allowing R to approach infinity. In the far field, we know that

$$T_P = \frac{G_T}{4\pi R_0^2} = \frac{\left| \int_{A'} f_T(P') dP' \right|^2}{\lambda^2 R_0^2 \int_{A'} |f_T(P')|^2 dP'} \quad (10)$$

where G_T is the gain of the antenna. Comparing (10) with the asymptotic form of (9) we find that

$$T_P = \frac{\left| \int_{A'} f_T(P') \frac{e^{ikR}}{R} dP' \right|^2}{\lambda^2 \int_{A'} |f_T(P')|^2 dP'} \quad (11)$$

The total power flow through the area A is thus

$$\eta_1 = \frac{\int_A dP \left| \int_{A'} f_T(P') \frac{e^{ikR}}{R} dP' \right|^2}{\lambda^2 \int_{A'} |f_T(P')|^2 dP'} \quad (12)$$

IV. MINIMIZING PATH LOSS (GENERAL APPROACH)

When the phase variation of e^{ikR} can be neglected in the integrand of (8), in view of (6), the far-field formula (5) will continue to hold. Insofar as phase variations can be introduced in the distributions $f_T(P')$, $f_R(P)$ to compensate for the variation in e^{ikR} , the path efficiency will also be increased. A simple picture shows approximately what the optimum phase corrections in the apertures are and also points out that complete correction is not possible.

Fig. 1 shows in section the two planar apertures with general points P' and P in each, respectively, and distance $R = R(P, P')$ between them. Associated with the phase of $f_T(P')$ and $f_R(P)$ are the equiphase fronts shown schematically. The length of the line joining P to P' which lies between the phase fronts is (apart from a constant) the electrical distance $R_E(P, P')$ given by

$$R_E = R(P, P') + \frac{\arg f_R(P) + \arg f_T(P')}{k} \quad (13)$$

for slightly curved phase fronts.

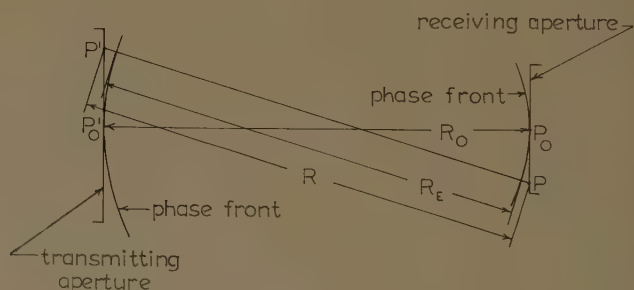


Fig. 1.

From (8) it is clear that with any given $|f_T(P')|$ and $|f_R(P)|$ the path efficiency will be increased if R_E is made constant with respect to P and P' rather than variable. Thus ideally every point in the receiving phase front should be the same distance from every point in the transmitting phase front. This condition can be satisfied only for one point P_0 in the receiving aperture and one point P'_0 in the transmitting aperture, and this comes about if the transmitting wave front is a sphere centered on P'_0 and the receiving wave front is a sphere centered on P_0 . Then

$$R_E(P_0, P') = R_E(P, P'_0) = \text{constant with respect to } P \text{ and } P'. \quad (14)$$

Since only one point can be equidistant from all the points on a surface (which situation occurs only for a sphere where the point is at the center), $R_E(P, P')$ will not equal this constant for all P and P' . Thus a residual phase variation must remain.

In the next two sections we shall examine the path efficiency formula in the Fresnel zone and determine mathematically how path loss can be minimized. It will be determined that (13) and (14) are generally, but not always, the conditions which optimize the phase of $f_R(P)$ and $f_T(P')$ for minimum path loss.

V. THE FRESNEL ZONE

Let (r, θ) and (r', θ') be polar coordinates in the receiving and transmitting apertures, respectively. The Fresnel zone approximation is obtained from setting

$$\frac{e^{ikR}}{R} \simeq \frac{e^{ikR_0}}{R_0} e^{ik[r^2 + r'^2 - 2rr' \cos(\theta - \theta')]/2R_0} \quad (15)$$

which is a second order approximation in the phase and a first order approximation in the amplitude of e^{ikR}/R . The region of validity of this approximation may be estimated by requiring that the relative difference between the exact and approximate values of e^{ikR}/R never exceeds a certain amount. The usual criterion is that no phase error greater than $\pi/8$ be permitted. For gain, this is equivalent to a fractional amplitude error of 0.077 (Fig. 2).

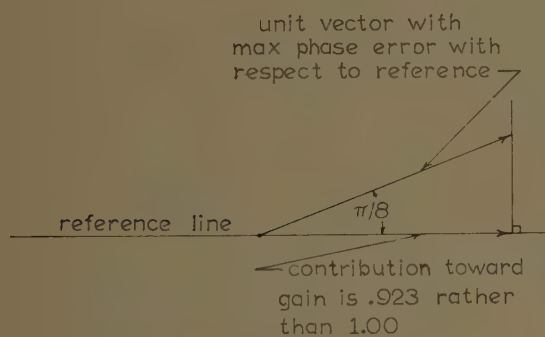


Fig. 2.

We shall assume that the $\pi/8$ phase criterion and the equally significant amplitude criterion define the limits of the Fresnel zone. We shall now find these limits.

For the present discussion we shall assume that the apertures A and A' can be inscribed in circles of minimum radii r_0 and r'_0 and that the origins of the polar coordinates in these apertures are taken at the centers of these circles. We further assume that the line joining two centers is perpendicular to both aperture planes. In this case the phase error is maximized if $\theta = \theta' + \pi$, $r = r_0$, and $r' = r'_0$. The phase error is then

$$\Delta \simeq R_0 \left(\sqrt{1 + b^2} - 1 - \frac{b^2}{2} \right) \quad (16)$$

where

$$b = \frac{r_0 + r'_0}{R_0} \quad (17)$$

We require

$$\Delta < \frac{\lambda}{16} \quad (\text{phase criterion}). \quad (18)$$

Similarly the amplitude criterion of Fig. 2 implies that

$$R_0 \geq 0.923 \sqrt{R_0^2 + (r + r')^2} \quad (\text{amplitude criterion}). \quad (19)$$

In Fig. 3 we have plotted the curves defined by equality in (18) and (19) vs D/λ and $R_0/D^2/\lambda$, where $D = r_0 + r'_0$ is the "average diameter." Together with the curve $R_0 = 2D^2/\lambda$, which is, by the same criterion, the boundary between the far zone and the Fresnel zone, we obtain the complete boundary of the Fresnel zone. Below $D/\lambda \simeq 9$, the amplitude criterion is more severe than the phase criterion and it defines the lower boundary. The reverse is true for D/λ above this value. For further comparison, the Fresnel zone region for a phase error of $\lambda/32$ and a comparable amplitude error is also shown. Polk's criterion [8] for the Fresnel zone, a $\lambda/4$ phase error but no amplitude criterion, is also shown and seems quite optimistic. Finally in order to give some further significance to these results the distance of one aperture diameter is indicated. We can make Table I from these results.

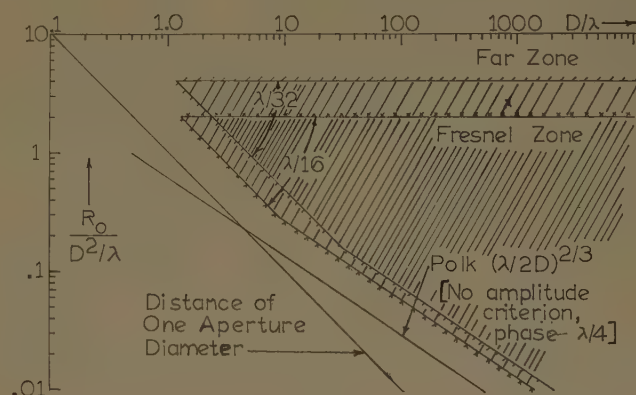


Fig. 3.

TABLE I
SMALLEST R_0 (IN APERTURE DIAMETERS) IN FRESNEL ZONE

D/λ	Polk's Criterion	$\lambda/16$	$\lambda/32$
10	1.5	2.6	4.7
100	2.9	5.7	7.2
500	5.0	10.0	12.5

We see that only a few aperture diameters separation between antennas puts them in the Fresnel zone. Closer distances, besides requiring more difficult expansions for approximations, imply more serious multi-

ple scattering effects and are fortunately not generally as important as the Fresnel zone.

In the Fresnel zone it is convenient to make the following change of variables.

$$\sqrt{\frac{k}{R_0}} r = \rho \quad \sqrt{\frac{k}{R_0}} r' = \rho'. \quad (20)$$

The angles θ and θ' remain unchanged, so that this transformation represents simply a change of scale. If a and a' are the images of A and A' under this change of scale and if p and p' are points (ρ, θ) and (ρ', θ') in the transformed planes, we set

$$\begin{aligned} f_T(P') e^{ikr'^2/2R_0} &= f(p') \\ f_R(P) e^{ikr^2/2R_0} &= g(p). \end{aligned} \quad (21)$$

Then using (15), (20), and (21) in (8), we find

$$\eta = \frac{\left| \int_{a'} f(p') dp' \int_a g(p) e^{ip\rho' \cos(\theta-\theta')} dp \right|^2}{4\pi^2 \int_{a'} |f(p')|^2 dp' \int_a |g(p)|^2 dp}. \quad (22)$$

Similarly from (12), in the Fresnel zone

$$\eta_1 = \frac{\int_a dp \left| \int_{a'} f(p') e^{ip\rho' \cos(\theta-\theta')} dp' \right|^2}{4\pi^2 \int_{a'} |f(p')|^2 dp'}. \quad (23)$$

Within the accuracy of the Fresnel approximation, if $f(p')$ is real, the transmitting antenna aperture phase front is a zone of the sphere centered on the receiving antenna, and if $g(p)$ is real, the receiving antenna aperture phase front is a zone of a sphere centered on the transmitting antenna. We saw in Section III that this situation is generally the near-field phase error correction which we desire for optimum efficiency. It turns out that in this case, η may be explicitly evaluated in terms of Bessel functions for a set of aperture illuminations which can usually approximate all commonly used tapers for circular apertures. Such illuminations are, namely,

$$\begin{aligned} f_T(r') &= e^{-ikr'^2/2R_0} \left[\left(1 - \left(\frac{r'}{r_0'} \right)^2 \right)^m + c_m \right] \\ f_R(r) &= e^{-ikr^2/2R_0} \left[\left(1 - \left(\frac{r}{r_0} \right)^2 \right)^n + c_n \right] \end{aligned} \quad (24)$$

for any integers m and n and arbitrary constants c_m and c_n . Using (24) in (21) and (22), we find that (22) reduces to

$$\eta = \frac{\sigma^2 |I(m, n) + c_n I(m, 0) + c_m I(0, n) + c_m c_n I(0, 0)|^2}{\left(\frac{c_m^2}{2} + \frac{c_m}{m+1} + \frac{1}{4m+2} \right) \left(\frac{c_n^2}{2} + \frac{c_n}{n+1} + \frac{1}{4n+2} \right)} \quad (25)$$

where

$$I(m, n) = \int_0^1 y(1-y^2)^m dy \int_0^1 x(1-x^2)^n J_0(\sigma xy) dx \quad (26)$$

and

$$\sigma = kr_0 r_0' / R_0. \quad (27)$$

It is shown in [6] that

$$\begin{aligned} I(m, n) &= \frac{m!n!}{\sigma^2} \left[\sum_{j=0}^{\min\{m,n\}} \frac{(-1)^j 4^j}{\sigma^{2j} (n-j)!(m-j)!} \right. \\ &\quad \left. + (-1)^{m+1} J_{n-m}(\sigma) \left(\frac{2}{\sigma} \right)^{n+m} \right] \\ &= n!m! \sum_{j=0}^{\infty} \frac{(-1)^j (\sigma/2)^{2j}}{(j+m+1)!(n+j+1)!}. \end{aligned} \quad (28)$$

The cases $m=n=0, 1, 2$, and 3 and $m=n=1$, $c_m=c_n=0.462$ (10-db taper) and $c_m=c_n=0.111$ (20-db taper) have been calculated, and η vs σ is shown for these cases in Fig. 4. We find that in each case there is an optimum value of σ for minimum path loss and that these minimum path losses are surprisingly small. A summary of the optimum values is given in Table II.

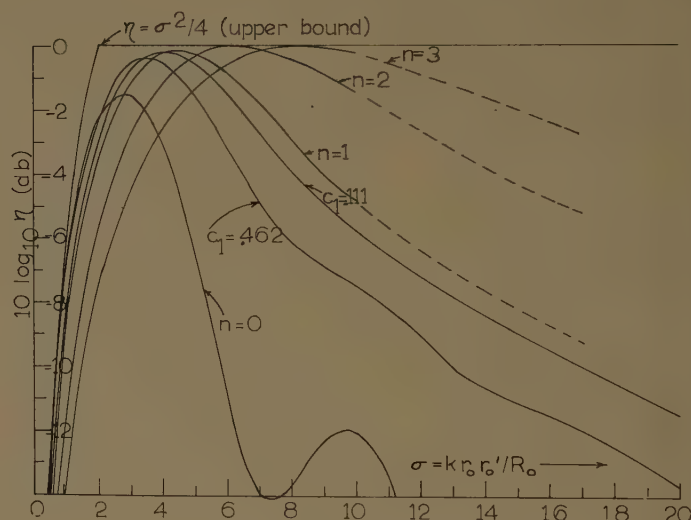


Fig. 4.

TABLE II

Case $m=n$	$c_m=c_n$	Optimum σ	Minimum Path Loss (db)
0	0	2.75	1.46
1	0.462	3.3	0.38
1	0.111	4.0	0.16
1	0	4.5	0.16
2	0	6.3	0.03
3	0	8.3	0.01

This table indicates the relationship that the more severe the taper, the larger the optimum σ and the smaller the optimum path loss. This is reasonable since

greater tapers are somewhat equivalent to smaller dish sizes and also imply less importance for the aperture extremities where the phase errors are greatest.

The existence of an optimum σ is perhaps somewhat surprising. This suggests that the simple phase correction given in Section IV, which is nearly optimum for small values of σ , may no longer be optimum in the nearer part of the Fresnel zone. Such a conclusion will be verified in the next section.

VI. A. OPTIMUM ILLUMINATIONS FOR MINIMUM PATH LOSS BETWEEN TWO ANTENNAS IN THE FRESNEL ZONE WITHOUT SUPERGAIN

B. OPTIMUM ILLUMINATION OF A SINGLE TRANSMITTING ANTENNA FOR MAXIMUM ENERGY RADIATED TO A FIXED AREA IN THE FRESNEL ZONE WITHOUT SUPERGAIN

Let us define the two-dimensional Fourier transforms in cylindrical coordinates as

$$G(p') = \frac{1}{2\pi} \int_a g(p) e^{i p \rho' \cos(\theta - \theta')} dp$$

$$F(p) = \frac{1}{2\pi} \int_{a'} f(p') e^{i p \rho' \cos(\theta - \theta')} dp' \quad (29)$$

Then (22) may be written in either of two forms as

$$\eta = \frac{\left| \int_a g(p) F(p) dp \right|^2}{\int_{a'} |f(p')|^2 dp' \int_a |g(p)|^2 dp}$$

$$= \frac{\left| \int_a f(p') G(p') dp' \right|^2}{\int_a |f(p')|^2 dp' \int_a |g(p)|^2 dp} \quad (30)$$

Schwartz's inequality yields immediately that

$$\eta \leq \eta_1, \quad (31)$$

$$\eta \leq \eta_2, \quad (32)$$

where

$$\eta_1 = \frac{\int_a |F(p)|^2 dp}{\int_{a'} |f(p')|^2 dp'}, \quad \eta_2 = \frac{\int_{a'} |G(p')|^2 dp'}{\int_a |g(p)|^2 dp} \quad (33)$$

As already observed in (23), η_1 is the ratio of power radiated through the area A to the total power radiated by the aperture A' , and η_2 , the dual of η_1 , is the ratio of power which the aperture A , if transmitting, would radiate through the area A' , to the total power radiated by A . Eqs. (31) and (32) merely state that, without

supergaining, the receiving antenna can absorb no more than all of the energy which falls on its area.

We also find from the precise statement of Schwartz's inequality, the condition under which equality holds in (31) and (32). If and only if for some constant c_0

$$f(p') = c_0 \overline{G(p')}, \text{ if } p' \text{ is in } a' \quad (34)$$

where the bar means the complex conjugate, then

$$\eta = \eta_2. \quad (35)$$

Also, if and only if for some constant c_1 ,

$$g(p) = c_1 \overline{F(p)}, \text{ if } p \text{ is in } a \quad (36)$$

then

$$\eta = \eta_1. \quad (37)$$

Thus (34) and (36) give the ideal distributions which, without supergaining, will enable the receiving antenna to receive all the energy which falls upon it and the transmitting antenna to transmit all the energy it possibly can onto the receiving aperture. From Parseval's equality we find that

$$\eta_1 = \frac{\int_a |F(p)|^2 dp}{\int_{\infty} |F(p)|^2 dp}, \quad \eta_2 = \frac{\int_{a'} |G(p')|^2 dp'}{\int_{\infty} |G(p')|^2 dp'} \quad (38)$$

where the integrals " \int_{∞} " are taken over the whole (ρ, θ) and (ρ', θ') planes. Applying the elementary properties of integrals of positive functions to (38), we find that

$$\eta_1 \leq 1, \quad \eta_2 \leq 1, \quad (39)$$

which is a restatement of conservation of energy.

On the other hand, from (29) we may write (33) as

$$\eta_1 = \frac{\int_a dp \left| \int_{a'} f(p') e^{i p \rho' \cos(\theta - \theta')} dp' \right|^2}{4\pi^2 \int_{a'} |f(p')|^2 dp'} \quad (40)$$

Again applying Schwartz's inequality we find

$$\eta_1 \leq \frac{\int_a dp \int_{a'} dp'}{4\pi^2} = \frac{aa'}{4\pi^2} \quad (41)$$

so that, finally, from (20), (31), (32), (39), and (41)

$$\eta \leq \min(\eta_1, \eta_2) \leq \min \left\{ 1, \frac{AA'}{\lambda^2 R_0^2} \right\}. \quad (42)$$

If the areas A, A' are inscribed in circles of radii r_0 and r_0' from (27) and (42)

$$\eta \leq \min \left\{ 1, \frac{\sigma^2}{4} \right\}. \quad (43)$$

The upper bound (43) to the path efficiency is plotted on Fig. 4 and indicates that the envelope of the cases previously computed falls surprisingly close to the upper bound. The greatest difference, about 2 db, occurs at $\sigma = 2$.

If the actual optimum illuminations are desired, a Fredholm equation must be solved. The optimum occurs when both (34) and (36) are satisfied. Then

$$\eta = \eta_1 = \eta_2 = \eta_{\max}. \quad (44)$$

Use of (33)–(37) shows that

$$\eta_{\max} = \eta_1 = \frac{s}{|c_1^2 c_0^2|} = \eta_2 = \frac{1}{s} \quad (45)$$

where

$$s = \frac{\int_a |g(\rho)|^2 d\rho}{\int_{a'} |G(\rho')|^2 d\rho'} \quad (46)$$

and hence

$$\eta_{\max} = \frac{1}{|c_0 c_1|}. \quad (47)$$

From (29), (34), and (36), the optimum illumination $f(\rho')$ satisfies

$$f(\rho') = \frac{c_0 c_1}{4\pi^2} \int_{a'} f(\rho'') d\rho'' \int_a e^{i[-\rho\rho' \cos(\theta-\theta') + \rho\rho'' \cos(\theta-\theta'')]} d\rho \quad (48)$$

which is a homogeneous Fredholm equation with symmetric kernel and hence is guaranteed solutions for a set of eigenvalues [9]. From (47) the magnitude of this eigenvalue is inversely proportional to the path loss, and hence the solution of (48) for the eigenvalue of least magnitude is the desired optimum.

In the special case where a and a' are circles, $f(\rho')$ and $f(\rho'')$ must be independent of θ and θ'' respectively. The angle integrations may then be explicitly performed to yield

$$f(\rho') = c_0 c_1 \int_0^{\rho''} \rho'' f(\rho'') d\rho'' \int_0^{\rho_0} J_0(\rho\rho') J_0(\rho\rho'') \rho d\rho \quad (49)$$

where

$$\rho_0' = \sqrt{\frac{k}{R_0}} r_0', \quad \rho_0 = \sqrt{\frac{k}{R_0}} r_0. \quad (50)$$

This in turn can be reduced to

$$f(\rho') = c_0 c_1 \rho_0 \int_0^{\rho''} f(\rho'') \frac{\rho'' d\rho''}{\rho'^2 - \rho''^2} [\rho' J_0(\rho'' \rho_0) J_1(\rho' \rho_0) - \rho'' J_1(\rho'' \rho_0) \cdot J_0(\rho' \rho_0)]. \quad (51)$$

One would now have to obtain the eigenvalue and eigensolution by numerical methods. This process hardly seems justified, since our "trial" solutions (Fig. 4) are close enough to the optimum for most purposes.

Although the optimum pair of illuminations is difficult to determine, it is fairly simple in certain cases to find the optimum illumination of one antenna given the illumination of the other. For example, if we assume that

$$f(\rho') = 1 \quad (52)$$

and let $g(\rho)$ be defined by (36), then

$$g(\rho) = c_1 \rho_0 J_1(\rho \rho_0') / \rho \quad (53)$$

or from (20), (21), and (50)

$$f_R(P) = \frac{c_1 r_0' e^{-ikr^2/2R_0}}{r} J_1\left(\frac{kr_0' r}{R_0}\right) \quad (54)$$

which is essentially constant only for large R_0 . For smaller R_0 there are oscillations in the illumination which show that the optimum receiver illumination phase is not always that of $e^{-ikr^2/2R_0}$ but departs from this value by 180° in certain rings defined by the zeros of the Bessel function.

From (36), (38), (52), and (53)

$$\eta = \eta_1 = \frac{\int_a \left| \frac{J_1(\rho \rho_0')}{\rho} \right|^2 d\rho}{\int_\infty \left| \frac{J_1(\rho \rho_0')}{\rho} \right|^2 d\rho} = \frac{\int_0^\sigma \frac{J_1^2(x) dx}{x}}{\int_0^\infty \frac{J_1^2(x) dx}{x}} \quad (55)$$

which is plotted vs σ in Fig. 5. This efficiency everywhere exceeds that of the case where $f(\rho')$ and $g(\rho')$ are both constant ($n=0$ in Fig. 4), as the theory says it must, but the improvement is negligible below a value of σ about equal to three. It should be pointed out, however, that unlike the illuminations of Fig. 4, the illumination (53) depends on R_0 .

VII. EXAMPLES

1) A recent paper [11] has described a proposed radio powered unmanned helicopter. The energy to support the helicopter would be beamed through space from the ground to the helicopter above. According to the description, the ratio of received to transmitted antenna power is to be

$$\eta = (0.65)(0.75)(0.65) = 0.317 = 5 \text{ db}. \quad (56)$$

The frequency is 3000 mc ($\lambda = 0.327$ feet), and the proposed aperture areas are

$$A = 2500\pi \text{ square feet} \quad A' = 400 \text{ square feet}. \quad (57)$$

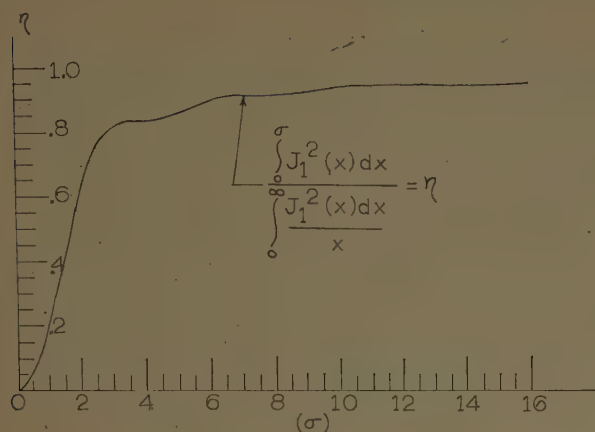


Fig. 5.

From (42), we find the maximum altitude at which this helicopter could hover and maintain the desired path efficiency is

$$R_0 \leq \frac{1}{\lambda} \sqrt{\frac{AA'}{\eta}} = 9640 \text{ feet.}^1 \quad (58)$$

If the apertures are uniformly illuminated in amplitude and have the correct "defocused" phase, from Fig. 4, at this distance the efficiency would be about 28.2 per cent instead of the desired 31.7 per cent, a small difference. If, however, the apertures had a fairly severe amplitude taper, such as the case $n=2$ of Fig. 4, the range at which the desired path efficiency would hold would be 5040 feet maximum.

2) *Minimum Spot Size: Into how small an area can the power flow from a transmitter be concentrated?* Our investigations shed the following light on this question.

In order for substantially all the energy to be focussed

¹ It has been alleged that $A'=400$ square feet was a misprint for 400 feet square, in which case R_0 would increase by a factor of 20.

we have seen (Fig. 4) that

$$\frac{k r_0 r_0'}{R_0} = \sigma \geq 2. \quad (59)$$

In order for our results to apply, moreover, we must be in the Fresnel zone. For present purposes, we optimistically use a " $\lambda/4$ " phase criterion for the Fresnel zone which implies (see Fig. 3)

$$\left(\frac{\lambda}{4r_0'}\right)^{1/3} \geq \frac{r_0'}{R_0}. \quad (60)$$

As long as the transmitting antenna radius r_0' is greater than a wavelength, both (59) and (60) can not hold unless

$$r_0 \geq \frac{4^{1/3}\lambda}{\pi} = 0.507\lambda. \quad (61)$$

So the "minimum spot size" in the Fresnel zone is about one wavelength.

BIBLIOGRAPHY

- [1] A. F. Kay, "Far-Field Data at Close Distances," Technical Research Group, Inc., New York, N. Y., Contract No. AF19(604)-1126; October, 1956.
- [2] J. Robieux, "Near-zone power transmission formulas," *PROC. IRE*, vol. 47, pp. 1161-1163; June, 1959.
- [3] V. Rumsey, "Reaction concept in electromagnetic theory," *Phys. Rev.*, vol. 94, pp. 1483-1491; June, 1954.
- [4] M. K. Hu, Syracuse University, Contract No. AF30(602)-928, AD131190; also 1958 IRE NATIONAL CONVENTION RECORD, vol. 6, pt. 8, pp. 128-135.
- [5] A. F. Kay, "Near Field Gain," Rept. No. SR 131-1, AF19(604)-5532; August, 1959.
- [6] *Ibid.*, p. 33.
- [7] P. Morse and H. Feshbach, "Methods of Theoretical Physics," McGraw-Hill Book Co., Inc., New York, N. Y., pp. 812-816; 1953.
- [8] C. Polk, "Optical Fresnel-zone gain of a rectangular aperture," *IRE TRANS. ON ANTENNAS AND PROPAGATION*, vol. AP-4, pp. 65-69, January, 1956; also M.S. Thesis, University of Pennsylvania, Philadelphia, Pa., 1956.
- [9] S. G. Mikhlin, "Integral Equations," Pergamon Press, Inc., New York, N. Y., ch. 3; 1957.
- [10] H. T. Friis, "A note on a simple transmission formula," *PROC. IRE*, vol. 34, pp. 254-256; May, 1946.
- [11] "Raytheon Wins Platform Contract," *Aviation Week*, pp. 34-39; August 17, 1959.

Measured Distribution of the Duration of Fades in Tropospheric Scatter Transmissions*

K. F. WRIGHT†, MEMBER, IRE, AND J. E. COLE†, MEMBER, IRE

Summary—Results of experimental measurements of fade durations at the output of tropospheric scatter receivers operating at a frequency of 950 Mc are presented. The special test equipment and the test procedures required to perform the measurements are described. The accumulated time the fades are below a reference level is shown. A family of curves representing the number of fades per hour which equal or exceed a given duration, and a family of curves representing the percentage of the total fades that equal or exceed different fade durations are presented. All the data are referenced to fade margin, which is defined as the difference between the received median level and the reference level. This enables the information given in this paper to be readily applied to other systems. A method for computing circuit reliability, based on the results of this paper, is suggested.

INTRODUCTION

THE amplitude distribution characteristics of a tropospheric scatter signal are well known; however, little experimental information exists regarding the number and duration of fades below a specified level. Knowledge of this distribution is needed to expand the present information on scatter signal characteristics, and to provide a more accurate basis for estimating data transmission performance of a tropospheric scatter system.

Normally, scatter circuit reliability is based upon the percentage of time the received signal level is above a specified reference level. For example, in the case of an FM system, this reference level is usually the threshold level of the receivers, which is the signal level required for a 10-db signal-to-noise ratio in the IF output. This method of computing reliability implies that data outage time consists simply of the total time the received signal level is below the reference level. This is not necessarily true for all types of data transmission because the rapid and continuous variations in received level of a scatter signal may not deteriorate the intelligence. The period during which the signal is below the reference level may not be long enough to affect the transmitted information.

The analysis of the fine structure of a scatter signal is difficult. This becomes evident by referring to Fig. 1, which is a typical recording of a scatter signal. The fact that the short-term variations of a tropospheric scatter signal are Rayleigh distributed makes it possible to obtain the total duration, at selected fade margins, from the probability density function. This method fails, however, to give the number and duration of fades at these fade margins. An accurate way to determine this

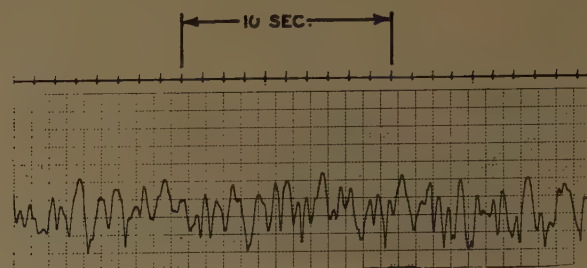


Fig. 1—Recording of typical tropospheric scatter signal.

information is by experimental means, consisting of actually counting the number and duration of the times the signal dropped below a reference level.

In these tests, FM threshold was found to be a convenient reference level for the fade duration measurements. This point provides a positive means for triggering counter circuits because, at this level, the signal-to-noise ratio changes rapidly with a change in received signal level. In order to obtain measurements at various fade depths, the signal median level was changed, and the reference level was held constant.

Since the data in this paper are presented on the basis of fade margin, it is applicable to other systems which may use different reference levels.

CIRCUIT DESCRIPTION AND TEST EQUIPMENT

The fade duration measurements were made using the Collins TST-101 Transhorizon UHF Communications System at a frequency of 950 Mc. This is a full-duplex system using a 1-kw FM transmitter, dual-diversity reception, and 15-foot parabolic antennas which have a beamwidth of 4.9° at 950 Mc. The antenna horizontal spacing was 100 feet. Fig. 2 is a path profile of the transmission path from Eloy, Ariz., to Fort Huachuca, Ariz., a distance of 103.2 statute miles. The sum of the horizon angles was $+0.0117^\circ$.

Signal correlation measurements taken on the two diversity receivers indicated that the correlation coefficient of this circuit was approximately zero with an extreme of 0.1.

The number and duration of the fades were measured by test equipment specifically designed for this purpose. Fig. 3 is a block diagram of the fade duration analyzer. Output from one channel of a 12-channel multiplex system is applied to the analyzer. As the received signal level drops below the receiver threshold, the resulting channel noise closes an electronic gate, allowing a 1000-cps signal to be applied to a preset counter and a standard frequency counter. A preset frequency counter is a precision electronic counter which produces an output

* Received by the PGAP, December 12, 1959; revised manuscript received, June 8, 1960.

† Collins Radio Co., Tucson, Ariz.

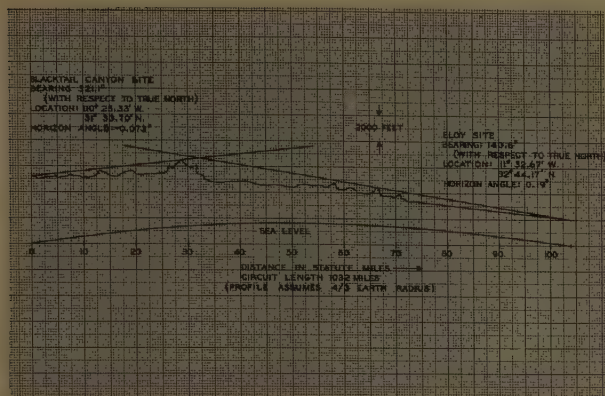


Fig. 2—Great circle path profile for Blacktail Canyon-to-Eloy circuit.

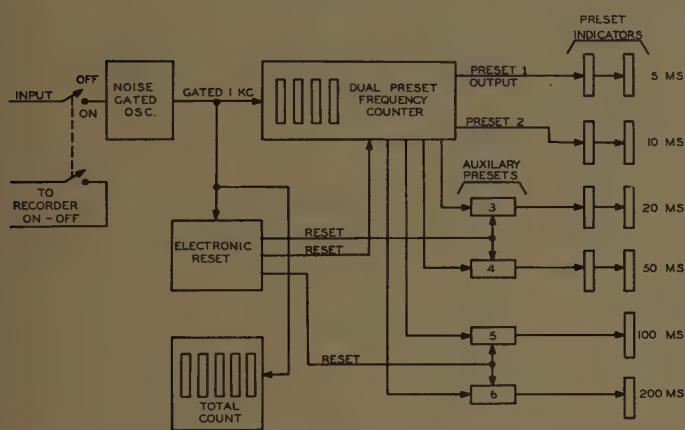


Fig. 3—Fade duration analyzer.

signal when the number being counted equals or exceeds the preset number. The preset counter contains six presets. Each preset indicates a count if the time duration of the fade exceeds or equals the value of the preset. Since $t = 1/f$ and the frequency being counted is 1000 cps, each cycle represents a millisecond duration. Preset times of 5, 10, 20, 100, and 200 msec were used. Selection of these durations was based upon previous experimental work.¹ The counting circuits were automatically reset within $\frac{1}{4}$ of a millisecond after the end of each fade.

The standard frequency counter indicated the total count for a given period of time and, therefore, represented the total outage time or total time the received signal was below the reference level.

The accuracy of the analyzer was verified by applying the output of a square-wave generator to the noise-gated oscillator. The frequency was changed in steps from 2.5 to 100 cps. This corresponded to fade durations from 200 to 5 msec, since the noise-gated oscillator uses only the positive half of the wave. The analyzer was checked at each of the input frequencies to insure

that the preset indicators only registered a count when the duration of the frequency being counted equalled or exceeded the preset numbers. For example, when a frequency of 25 cps was used, only the 5-, 10-, and 20-msec indicators registered counts. The number of counts equalled the product of the input frequency and the time interval of the test.

The shortest time duration measured was limited by the low-frequency end of the pass band, since noise peaks of these frequencies caused triggering of the analyzer. Therefore, the minimum fade duration measured was 5 msec. The longest time duration measured was limited only by the choice of the time durations that resulted in a good fade duration distribution.

TEST PROCEDURES

The maximum time possible for each fade duration test was limited by the counting capacity of the preset indicators. However, each test was restricted to a maximum time of ten minutes to limit the change in median received signal level during the test period. The start and stop time of the tests was measured by a digital timer. The following data were recorded for each test.

- 1) Start and stop time.
- 2) Number of counts on each preset indicator.
- 3) Count on the outage time counter.
- 4) Type of reception (dual or nondiversity).

In addition, a Sanborn paper recorder and magnetic tape recorder, both time-synchronized with the fade duration analyzer, monitored the signal level at the last IF stage of each receiver. The time constant of the signal level detector circuit was 0.22 msec. The Sanborn paper recording was used to check the characteristics of the signal, and to determine the presence and approximate time of airplane flutter. The magnetic tape recordings were used in conjunction with a Collins 478M-3 Amplitude Distribution Analyzer and an IBM 526 Summary Punch to analyze the received signal distribution for determining the received signal median level.

The transmitter power at the other terminal was changed as necessary to obtain the desired distribution in received median levels or fade margins. Continuous analysis was made of the received signal to insure that the measurements were made during periods of a good representative scatter signal. This was checked by monitoring the instantaneous signal variations on the Sanborn recorder for changes in signal characteristics resulting from ducting, multipath effects, or aircraft in the propagation path.

DATA ANALYSIS

After the median levels were obtained from the magnetic tape recordings, and the Sanborn recordings were analyzed, the data were classified according to fade margin. No attempt was made to analyze the data obtained during periods when aircraft were in the propaga-

¹ K. F. Wright and J. E. Cole, "Operational Evaluation of Tropospheric Scatter Techniques," Collins Radio Co., Cedar Rapids, Iowa, Rept. on Signal Corps Contract DA 36-039-ac-67491; July 5-October 5, 1958.

tion path, because of the complexity of the fade distribution during these times.

The experimental and theoretical short-term fading characteristics for nondiversity reception are shown in Fig. 4. The circled points are plotted from experimental data on the basis of fade margin and percentage of total outage time. It can be seen that the points approximate a theoretical Rayleigh distribution. The data taken during periods of low fade margins were compiled from short test durations of 30 to 120 seconds. The test durations at low fade margins were, in part, limited by the storage capacity of the decade indicators. The test duration at higher fade margins was increased to a maximum of ten minutes to provide an adequate number of fades. The median test duration was approximately three minutes. Other authors² indicate that a sampling period of one minute results in an almost perfect Rayleigh distribution. The problem encountered, when using a test duration of one minute at high fade margins, is that a very low number of fades and, in many cases, no fades are recorded. This necessitates taking a great number of tests at the higher fade margins to provide an adequate sample.

Fig. 5 is a plot of fade margin vs per cent of total outage time for nondiversity and dual-diversity reception. The known advantages of diversity reception are further demonstrated by these curves. For example, a fade margin of 18 db in a diversity system results in one-tenth per cent outage time, while a fade margin of approximately 26 db in a nondiversity system results in the same percentage outage time. Note that approximately 50 per cent outage time occurs at zero fade margin with nondiversity operation. This is as expected,

² L. P. Yeh, "Basic analysis on controlled carrier operation of tropospheric scatter communications systems," 1958 IRE NATIONAL CONVENTION RECORD, pt. 8, pp. 261-283.

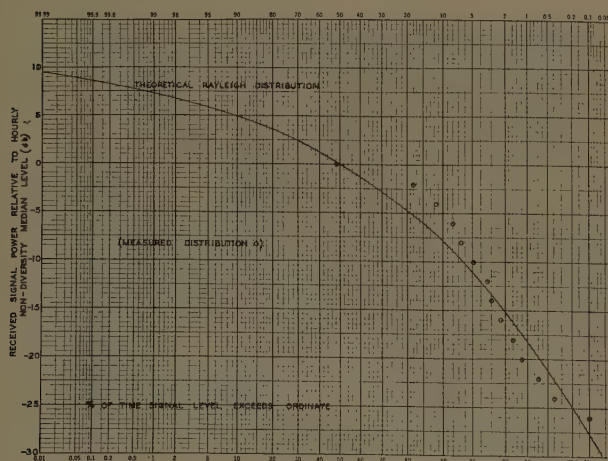


Fig. 4—Short term fading characteristic for a nondiversity circuit.

since, at zero fade margin, the signal level is below the reference level 50 per cent of the time. The two curves should diverge progressively at the low percentage end of the scale, if the distributions were Rayleigh.

Fig. 6 is a family of curves which shows fade per hour vs fade duration for selected fade margins using non-diversity reception. The number of fades per hour for a particular fade margin equals or exceeds the given fade duration. For example, the curve for a fade margin of 20 db indicates that there are 590 fades per hour which have a fade duration of 20 msec or longer. Since a 5-msec fade was the shortest duration measured, the curves were extrapolated to a fade duration of 1 msec, to remove some of the uncertainty regarding the number of fades with a duration less than 5 msec.

The total number of fades per hour at 0 fade margin, based upon a lower limit of one millisecond, is 13,500. This corresponds to approximately 3.75 fades per second.

Fig. 7 is a family of curves which shows fades per hour vs fade duration for several selected fade margins using dual-diversity reception. The number of fades per hour for dual-diversity reception are, as expected, considerably less than that for nondiversity reception. Table I compares the data shown in Figs. 6 and 7, and shows the number of fades per hour for both non-diversity and dual-diversity reception for fade durations which are equal to, or greater than, 1, 10, and 50 msec. The diversity improvement, based upon the number of fades per hour, increases rapidly as the fade margin is increased.

Curves showing the fade duration distribution for selected fade margins for nondiversity and dual-diversity reception are shown in Figs. 8 and 9, respectively. These curves are plotted using a log-normal coordinate system. Since the curves are linear over much of their length, extrapolation of the curves in Figs. 6 and 7 for durations less than 5 msec can be used. The median fade duration, or the fade duration exceeded 50 per cent

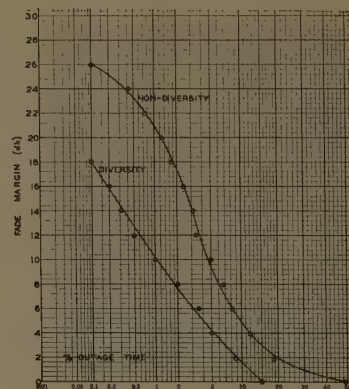


Fig. 5—Percentage outage time as a function of fade margin.

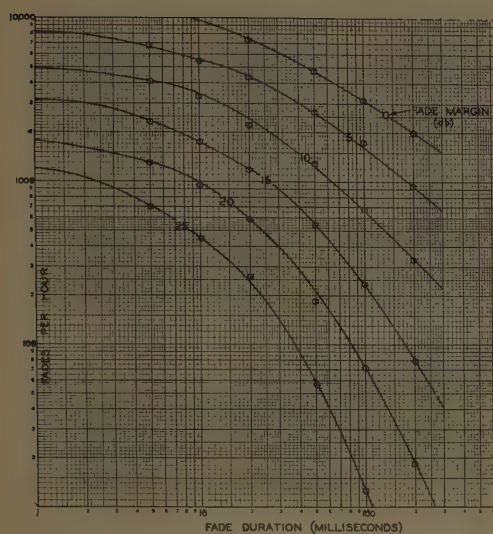


Fig. 6—Nondiversity fade duration distribution.

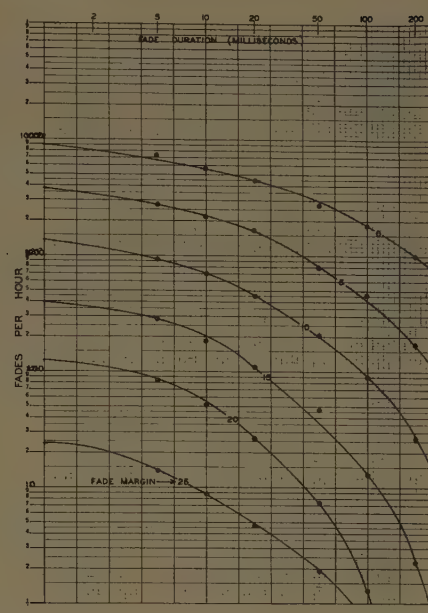


Fig. 7—Dual-diversity fade duration distribution.

TABLE I
NONDIVERSITY FOR DUAL-DIVERSITY FADES PER HOUR FOR SELECTED FADE MARGINS
FOR DURATIONS WHICH EXCEED 1, 10, AND 50 MSEC

Fade Margin	Fades/Hour ≥ 1 Msec		Diversity Improvement Percentage $(100 - \frac{DD}{ND} \cdot 100)$	Fades/Hour ≥ 10 Msec		Diversity Improvement Percentage $(100 - \frac{DD}{ND} \cdot 100)$	Fades/Hour ≥ 50 Msec		Diversity Improvement Percentage $(100 - \frac{DD}{ND} \cdot 100)$
	ND	DD		ND	DD		ND	DD	
0	13500	9000	33.3	9700	5600	42.3	4700	2750	41.5
5	8250	3750	54.6	5500	2200	60.0	2650	800	69.8
10	4950	1350	72.7	3300	700	78.8	1300	205	84.2
15	3150	390	87.6	1750	180	89.7	540	47	91.3
20	1780	125	93.0	950	52	94.5	185	7	96.2
25	1200	24	98.0	450	9	98.0	57	2	96.5

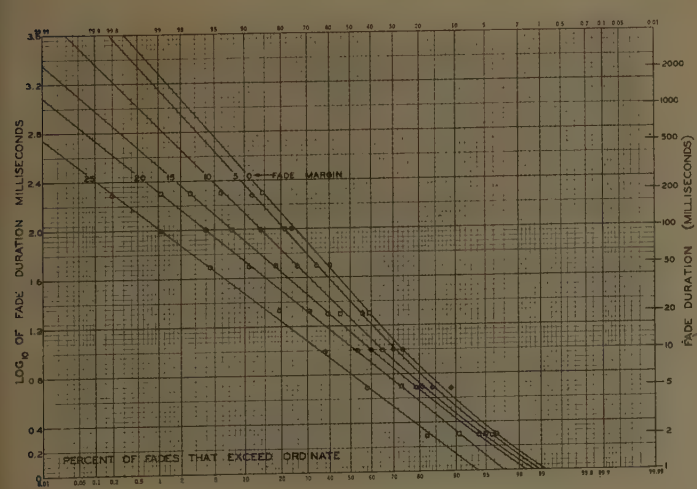


Fig. 8—Nondiversity fade distribution.

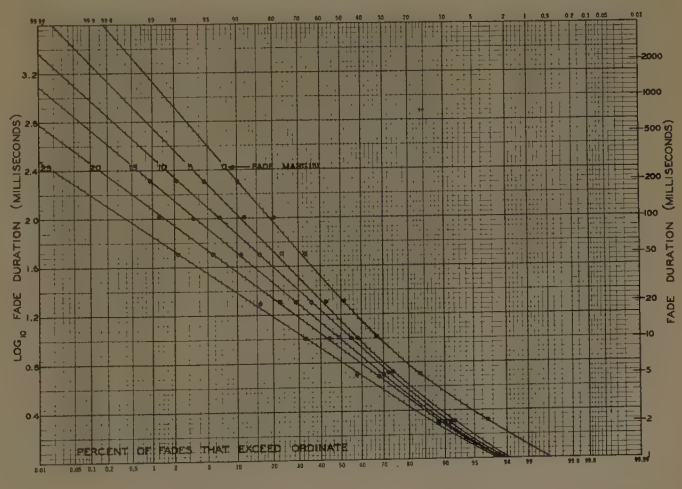


Fig. 9—Dual-diversity fade duration distribution.

of the time, for nondiversity reception ranges from 6.5 to 30.2 msec. The median fade duration for dual-diversity reception ranges from 6.5 to 21.4 msec in length. Table II shows the median fade durations for the fade margins shown in Figs. 8 and 9.

It is interesting to note that, although the diversity improvement based upon the number of fades per hour *increases* as the fade margin is increased, the diversity improvement based upon median fade duration actually *decreases* for fade margins greater than 5 db.

CONCLUSIONS

The results of the fade duration distribution measurements have shown that a large percentage of the fades measured were of very short duration. For example, for the fade margins selected, between 33 to 77 per cent of the total number of fades had a duration less than, or equal to, 15 msec. Two conclusions can be drawn from these data showing a large percentage of short-duration fades. First, the time constant of the detector circuit, from which the instantaneous signal levels are recorded, and the recording circuit itself, must be in the order of one millisecond to follow properly the fast fading of the scatter signal. Second, because of the number of short fades, it is apparent that a certain amount of intelligibility of data systems using tropospheric scatter as the propagation medium can be retained, during periods of fading below a reference level normally used as the reliability criterion. This would be especially true when the data system used has an information bit length considerably greater than the length of the fade. For the foregoing reason, it is suggested that data system reliability be based upon the number and duration of fades rather than on outage time.

In order to predict data system reliability, it is not only necessary to know the nature of the signal fades, but the data system characteristics must also be taken

TABLE II
MEDIAN FADE DURATION FOR SELECTED FADE MARGINS FOR
NONDIVERSITY AND DUAL-DIVERSITY RECEPTION

Fade Margin	Median Fades Duration		Diversity Improvement Percentage ($100 - \frac{DD}{ND} 100$)
	ND	DD	
0	30.2	21.4	29.1
5	25.2	14.1	44.1
10	18.2	12.0	34.1
15	14.1	9.8	30.5
20	10.7	8.3	22.4
25	6.5	6.5	0

into consideration. With this information, a statistical analysis must be made to determine the probability of a fade occurring during an information bit, and also the probability of the data converter responding properly in the absence of an information bit.

Although the fade duration tests described in this paper were run each day for a period of several months, there is still a great deal of additional knowledge to be gained from future tests of this nature. Further study should be made to increase the confidence factor of the curves presented here, and to relate the effects of: 1) transmitter frequency, 2) antenna beamwidth, 3) transmission path length, 4) path terrain, and 5) meteorological factors, to fade duration distributions.

ACKNOWLEDGMENT

The authors wish to thank their associates at Collins Radio Company for their many helpful suggestions, and to acknowledge gratefully the permission to release the information contained in this paper by the Army Electronic Proving Ground, Fort Huachuca, Ariz.

An Experimental Investigation of the Fock Approximation for Conducting Cylinders*

L. WETZEL†, MEMBER, IRE, AND D. B. BRICK‡, SENIOR MEMBER, IRE

Summary—The high-frequency current distributions over several conducting elliptic cylinders for normal, plane-wave excitation are measured at a wavelength of 3.2 cm using image-plane techniques. The experimental distributions are compared with the Fock approximation, verifying its validity over a wide range of kR_0 in the neighborhood of the shadow boundary.

INTRODUCTION

IN THE PAST, measurements have been made of the current distributions on conducting cylinders of circular cross section for both polarizations of plane-wave excitation [1, 2]. Measured currents on cylinders of more complex cross section are needed, however, to determine the validity of approximations devised for more general geometries. The purpose of this paper is to describe a series of such measurements and to compare the experimental currents with those predicted by the well-known Fock approximation [3]. The use of these results in the verification of improved approximations derived on a different theoretical basis may be found elsewhere [4–6].

A useful group of test obstacles, each with a continuously varying radius of curvature, is a sequence of elliptic cylinders having the same major axis, but different eccentricities. For the incident wave polarized with the magnetic vector parallel to the cylinder axis, and the electric field parallel to the major axis, image-plane techniques [1] make possible a relatively simple experimental arrangement by which the currents over cylinders of this shape can be measured.

Half-cylinders, cut along the minor axis, were formed of thin sheet brass and mounted on an image plane with the cylinder axis normal to the direction of the incident radiation. The source of illumination was a horn mounted flush with the image plane. A small shielded half-loop fixed on a flexible metallic strap fitting flush into a slot on the cylinder was used to probe the tangential magnetic field at the surface of the cylinder. Since the electric surface current is proportional to the tangential magnetic field, the output of this probe measured the current distribution as the probe was moved over the surface of the cylinder.

This method was used to investigate the current distributions over elliptic cylinders of eccentricities 0, 0.552, 0.780 and 0.910, each having a semimajor axis of 6.1 cm. The results for the circular cylinder were

compared with the theoretically exact current calculated from the eigenfunction expansion, thus permitting an initial appraisal of the accuracy of the experiment and a demonstration of whatever shortcomings may be inherent in it. The results for the remaining cylinders were compared with the theoretical predictions of Fock [3] for the current in the so-called "penumbra" region.

A brief description of the apparatus and a discussion of the measurements and their comparison with the theoretical currents appear in the following sections.

DESCRIPTION OF THE APPARATUS

The image-plane method and the general instrumentation of this experiment have been described in detail elsewhere [1, 7]; therefore, only a brief description of these aspects of the arrangement will be included. The duraluminum image-plane used was located on the roof of the Gordon McKay Laboratory. It measures 24 by 48 feet, or 230λ by 460λ at $\lambda = 3.19$ cm. Near the center of the plane is a circular hole beneath which is a well for the measuring and positioning apparatus. An aluminum plug with the probe-positioning mechanism mounted below it fits this circular hole, flush with the image-plane. Each cylinder was mounted on a rectangular aluminum plate which was bolted into a rectangular recess in the top of the plug. The flush copper strip, which carried the probe over the cylinder, emerged through a slot in the plug and was weighted at one end to keep it securely against the shoulder on the cylinder; the other end was attached to a geared probe-positioning mechanism.

Plane-wave excitation was approximated by using a simple horn clamped to the image plane at a distance of about 48 wavelengths from the center of the cylinder and directed perpendicular to the axis of the cylinder, as illustrated in Fig. 1. The vertical pattern follows roughly the cosine of the angle between the image-plane and the direction of observation; thus, the incident field was substantially uniform from the plane to the top of the cylinder (from 0 to 2.3 degrees). Horizontally, the half-power points lie about 28 cm (9 wavelengths) from the center of the cylinder.

The RF equipment consisted of an X-band klystron feeding the transmitting horn through a ferrite rotator which was sinusoidally modulated by a 1-kc signal. A sample of the modulated signal for use in phase measurements and spectrum analyses was obtained via a directional coupler. With the system tuned for a minimum number of spurious sidebands, the free space

* Received by the PGAP, January 27, 1960; revised manuscript received, May 23, 1960. This research was made possible by support extended by Cruft Lab., Harvard University, under Contract No. AF19(604)-786.

† Brown University, Providence, R. I.

‡ Appl. Res. Lab., Sylvania Electric Products, Inc., Waltham, Mass.

wavelength was 3.192 cm. The detection system was almost identical to that described by Row [7].

The cylinders were constructed of sheet brass sweated to accurately-machined steel elliptical templates. A gap, to permit passage of the probe cable, and shoulders, to support the copper strip carrying the current probe, were left between the two center templates. These were adjusted so that with the strip pulled taut by the probe-positioning mechanism at one end and a weight at the other, a smooth surface was maintained. A mounted cylinder can be seen in the right of the illustration, Fig. 1.

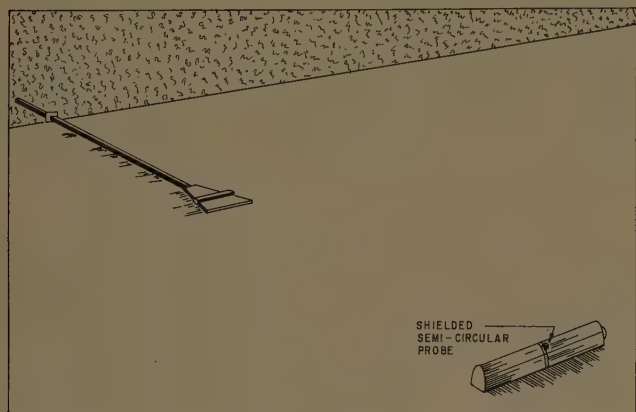


Fig. 1—View of the horn and a mounted cylinder.

The probe used to explore the tangential magnetic field over the cylinder was a shielded half-loop [8]. Since the probe must pass over a wide range of curvatures in this experiment, the shielding gap at the center of the loop arc helped prevent distortion of the copper strip, to which it is attached. The half-loop was made from the center conductor and Teflon insulation of a piece of 50-ohm Microdot cable bent into the tightest semicircle allowed by the rigidity of the Teflon and shielded with two small arcs of thin-walled copper tubing. The radius of the loop to the center conductor is about 0.2 cm and the length of the gap is about 0.015 cm when the strip is flat.

DISCUSSION OF THE MEASUREMENTS AND COMPARISON WITH THEORY

The Circular Cylinder

For the circular cylinder, the theoretical current distribution is given rigorously in the form of the usual series expansion involving cylindrical eigenfunctions. For an infinite, perfectly conducting cylinder illuminated by a source of plane waves of unit amplitude directed normally to the cylinder axis and polarized with the magnetic vector parallel to the cylinder axis, the total magnetic field at the cylinder is given by

$$H_z(\theta) = \frac{2i}{\pi ka} \sum_{n=0}^{\infty} \epsilon_n i^n \frac{\cos n\theta}{H_n^{(1)'}(ka)}$$

where $k=2\pi/\lambda$, λ being the wavelength of the incident wave, and a the radius of the cylinder. The surface electric current is just $c/4\pi$ times the tangential magnetic field.

The circular cylinder in this experiment was constructed so that $ka=kR_0=12$, thus permitting the use of the current distributions already calculated by Riblet [2] from the expression above for this value of kR_0 . Unfortunately, the angles at which the series was evaluated in Riblet's report were at 10° intervals, as a result of which the important oscillating character of the current in the extreme shadow region of the cylinder did not appear. In order to display in more detail the structure of the current amplitude in the range of angles from 140 to 180° , the series was evaluated for intermediate points. It is sufficient to include only terms out to $n=19$ when $ka=12$. The exact current in Fig. 2 is different from that appearing in Riblet's report only for angles between 140 and 180° . From the point of view of Franz's "Creeping Waves" [9], these oscillations appear as a result of the interference of waves traveling around the back of the cylinder from either side.

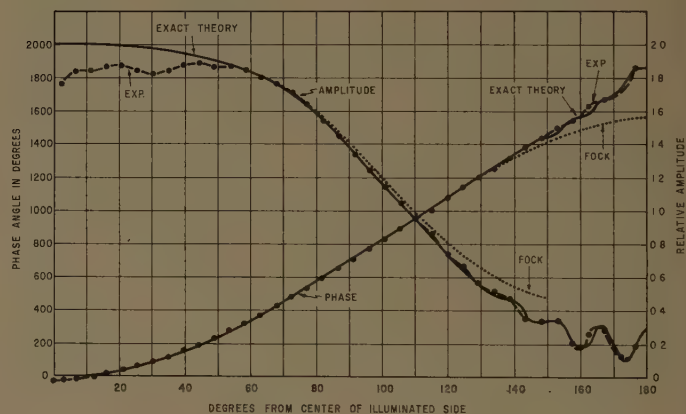


Fig. 2—Current amplitude and phase angle on circular cylinder ($kR_0=12$).

The experimental data were normalized to coincide with the exact theoretical results for $\theta=90^\circ$, i.e., at the "shadow boundary." The current amplitudes for all cylinders were obtained by taking the square root of the average of the results obtained from three consecutive runs, the detector being a square-law device. The phase of the current was obtained from a single set of measurements over each cylinder. The experimental and theoretical distributions are compared in Fig. 2. It is evident that there is good agreement between theory and experiment except over the first 50 or 60° of the cylinder.

The depression of these readings can be ascribed to the large variation of the electric field across the loop in the illuminated region; while the oscillatory behavior may be explained by the coupling between the

loop and its image in the image plane. (See the discussion in [5] and the additional sources cited there.) An unshielded loop used in the preliminary stages of this experiment introduced much larger errors over the illuminated face of the cylinder. The shielded loop described in the last section reduced this error by about 80 per cent. Presumably, then, the residual discrepancy can be ascribed to effects inherent in the loop system as constructed. Since it is difficult to isolate the sources of these perturbations and to correct for them theoretically in a convincing way, no attempt was made to do so. The "inherent error" of the loop system appears to be negligible in the region of the shadow boundary, and it is just here that the currents are of greatest importance for the purpose of this experiment. (It may be noted in passing that the use of even smaller loops would appear to be worth trying. The simple fact is that, at the time this experiment was carried out, the smallest loop it was possible to construct was used.)

Finally, the circular cylinder was used to determine the effect due to the finite length of the cylinder. Since the primary lobe of the horn pattern does not quite fall to half-power at the ends of the cylinder, a run was made, with hemicylindrical end-pieces attached, which doubled the length of the cylinder. The data taken with and without the end-pieces showed no greater variation than between two successive runs on the cylinder without the end-pieces. It appears, then, that the currents being measured closely approximate those for an infinite cylinder.

The Elliptic Cylinders

Since the wave equation is separable in elliptic-cylindrical coordinates, it is possible to construct a series expansion (in this case in odd and even Mathieu functions) for the current over elliptic cylinders [10]. As might be expected, the resultant series is too unwieldy to justify an attempt to evaluate current distributions from it numerically.

The experimental results obtained here are to be used in exploring the range of validity of the Fock approximation for currents induced by plane waves on perfect conductors. In the case of large kR_0 , Fock has expressed current in the penumbra region (*i.e.*, in the neighborhood of the shadow boundary) in the form,

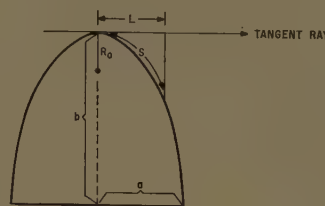
$$j = j^{ex} G(\xi),$$

where j^{ex} is the current associated with the incident wave $(c/4\pi)H_z^{ex}$ and $G(\xi)$ is a complex function of the variable

$$\xi = \sqrt[3]{\frac{kR_0}{2}} \frac{L}{R_0}.$$

R_0 is the radius of curvature of the diffracting obstacle at the point where an incident ray is tangent to the

obstacle (the shadow boundary); L is the distance measured along the tangent ray. $G(\xi)$ is tabulated in Fock's paper. Fig. 3 shows the correspondence between the distance L and the arc length, and the values of R_0 and kR_0 for the various cylinders.



$$S = b[E(\alpha, \pi/2) - E(\alpha, \phi)]$$

where:

$$\begin{aligned} b &= 6.1 \text{ cm} \\ \sin \alpha &= e \\ \cos \phi &= L/\alpha \\ E(\alpha, \phi) &= \text{incomplete elliptic integral [10]} \end{aligned}$$

R_0 and kR_0 for the cylinders used:

θ	$R_0 = \alpha^2/b$	kR_0
0	6.1 cm	12
0.552	4.2 cm	8.3
0.780	2.4 cm	4.7
0.910	1.1 cm	2.2

Fig. 3—Elliptic cylinder dimensions.

It can be seen from Fig. 2 that, although the Fock current amplitude is slightly larger than the exact current in the penumbra region, the slope is in close agreement. The results of the amplitude measurements on the first two elliptic cylinders were normalized to coincide with the Fock currents at the shadow boundary. The results for the third elliptic cylinder ($e=0.910$) were normalized for consistency with the other cylinders at the extremes of the curve. (The peculiar behavior over the illuminated face of this cylinder is due to a small mechanical irregularity which slightly distorted the probe strip in this region.) It is clear from Figs. 4–6 that the slope of both the amplitude and phase of the Fock current in the penumbra region is in excellent agreement with the experimental results for all three cylinders.

CONCLUSIONS

Since the Fock approximation was derived under the condition that kR_0 be large, the accuracy of the predicted penumbral currents demonstrated by this experiment for radii of curvature down to $kR_0=2.2$ was quite unexpected. Although the approximation is much less satisfactory in the extreme shadow region, the currents here are beyond the range over which the assumptions of the Fock approximation are valid.

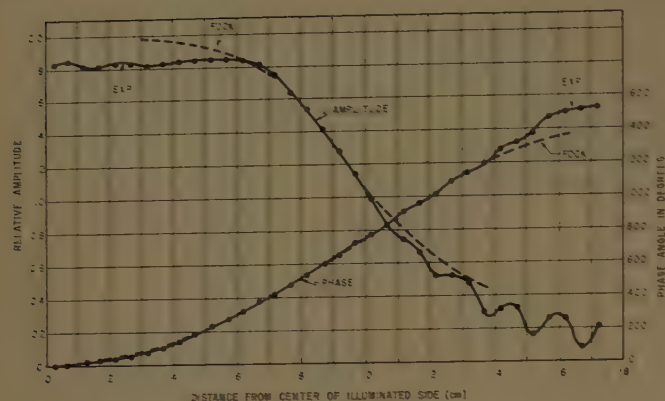


Fig. 4—Current amplitude and phase angle on elliptic cylinder; $e=0.552$ ($kR_0=8.3$).

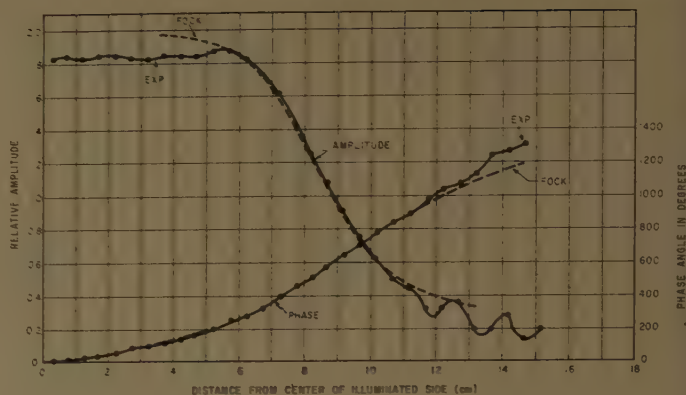


Fig. 5—Current amplitude and phase angle on elliptic cylinder; $e=0.780$ ($kR_0=4.7$).

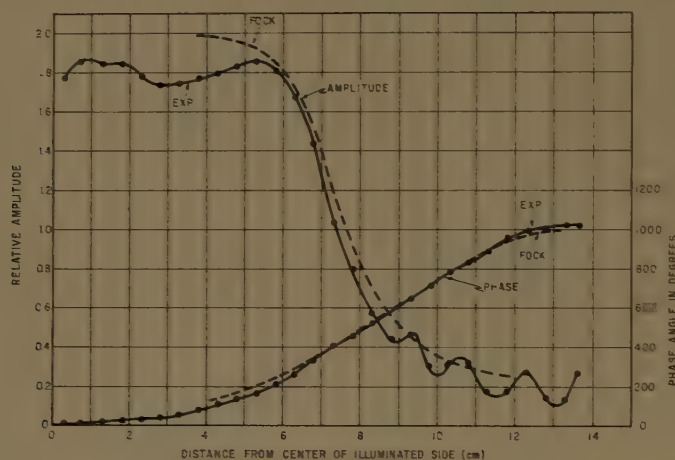


Fig. 6—Current amplitude and phase angle on elliptic cylinder; $e=0.910$ ($kR_0=2.2$).

ACKNOWLEDGMENT

We wish to thank Prof. R. V. Row for his interest and generous assistance and A. Vobach for his help in translating Fock's data into a form applicable to the elliptic cylinders. A. DesJardins did the exacting work required in building the cylinders used.

VI. BIBLIOGRAPHY

- [1] R. D. Kodis, "Diffraction measurements at 1.25 centimeters," *J. Appl. Phys.*, vol. 23, pp. 249-255; February, 1952. (See also Cruft Lab., Harvard University, Cambridge, Mass., Rept. No. 105; 1950.)
- [2] H. J. Riblet, "Geometric-Optical Currents," Microwave Development Labs., Brooklyn, N. Y., Contract AF19(122)-167; 1952.
- [3] V. Fock, "The distribution of currents induced by a plane wave on the surface of a conductor," *J. Phys. (USSR)*, vol. 10, pp. 130-140; February, 1946.
- [4] L. Wetzel, "High Frequency Current Distributions on Conducting Obstacles," Cruft Lab., Harvard University, Cambridge, Mass., Rept. No. 10; May, 1957.
- [5] R. W. P. King and T. T. Wu, "The Scattering Diffraction of Waves," Harvard University Press, Cambridge, Mass.; 1959.
- [6] R. F. Goodrich, "Studies in Radar Cross Section XXVI, Fock Theory," Univ. of Michigan Res. Inst., Ann Arbor, Mich., Scientific Rept. No. 3; July, 1958.
- [7] R. V. Row, "Microwave diffraction measurements in a parallel-plate region," *J. Appl. Phys.*, vol. 24, pp. 1448-1452; December, 1953.
- [8] D. K. Reynolds, "Surface-Current and Charge Measurements on Flat Metal Sheets," Cruft Lab., Harvard University, Cambridge, Mass., Tech. Rept. No. 53, p. 22 ff.; August 1, 1948.
- [9] W. Franz and K. Deppermann, "Theorie der Beugung am Zylinder unter Berücksichtigung der Kriechwelle," *Ann. Phys.*, vol. 10, pp. 361-373; June, 1952.
- [10] G. Sinclair, "Patterns of antennas located near cylinders of elliptical cross section," *Proc. IRE*, vol. 39, pp. 660-668; June, 1951.
- [11] E. Jahnke and F. Emde, "Tables of Functions," Dover Publications, Inc., New York, N. Y.; 1945.

Frequency Spectra of Transient Electromagnetic Pulses in a Conducting Medium*

W. L. ANDERSON†, MEMBER, IRE, AND R. K. MOORE†, SENIOR MEMBER, IRE

Summary—The energy density spectra of transient electromagnetic fields generated by a pulsed ideal dipole source in an infinite conducting medium have been investigated for various distances from the source. A characteristic frequency ω_c , corresponding either to the peak of the spectrum or to its half-width, is defined and shown to vary inversely as the square of distance at large distances. The behavior of ω_c with distance is a measure of the behavior of the pulse energy. Thus, at large distances it appears that the attenuation factor associated with ω_c , $\exp\{-r\sqrt{\omega_c\mu\sigma}/2\}$, is independent of r , due to the constancy of the product $r\sqrt{\omega_c}$. From this point of view, the transient fields do not decrease exponentially as r , but as inverse powers of r .

This should not be construed as meaning that the transient possesses an advantage over CW. The attenuation for monochromatic components of the pulse is the same as for continuous waves of the same frequency and at large distances the energy put into the high frequency components is wasted.

The phenomenon is illustrated by calculations that have been carried out for the case of pulses in sea water.

INTRODUCTION

It has been shown by Richards¹ that at large distances in an infinite conducting medium the variation of the peak transient electromagnetic fields generated by a pulsed dipole source takes place as r^{-3} or r^{-4} . This rather unexpected situation is not clarified by the work of other authors²⁻⁶ on the subject. Consequently, this study was undertaken in order to relate this phenomenon to the exponential attenuation which is known to apply to the monochromatic components of the pulse and to determine whether the apparent advantage of transients over pulse-modulated carriers might, in fact, be illusory. The results show that a pulse spectrum with appreciable high-frequency content wastes energy.

In this development, the displacement current term of the wave equation has been dropped, since the main interest is in the fields at considerable distances. At these distances the practical aspect of the problem is chiefly concerned with that part of the frequency

spectrum containing the major portion of the pulse energy, and for these frequencies displacement currents are negligible.

For purposes of investigation the source has been taken as a magnetic dipole and some numerical results are developed for the case where the medium is sea water. Using triangular and rectangular pulses, expressions are derived for the relationship between pulse width, distance from source, and frequency ω_c at which either the peak or the half-width of the energy density spectrum occurs. It is shown that at large distances an approximation can be made which results in a simple inverse relation between ω_c and r^2 . The product $r\sqrt{\omega_c}$ then appears constant whenever it occurs, including the exponential term, and, in the sense described, exponential attenuation does not occur. Any given spectral component of the pulse is attenuated exponentially with distance, however, and it therefore follows that energy should not be wasted on high frequencies which will be effectively filtered out at long distances.

DEVELOPMENT OF EQUATIONS

The fields from an idealized magnetic dipole in a conducting medium can be derived from the Hertz vector

$$\Pi^*(\omega) = \frac{e^{-r\sqrt{i\omega\mu\sigma}}}{4\pi r} \mathbf{m}(\omega), \quad (1)$$

where Fourier transform quantities are used exclusively. The displacement current term is not included. The parameters are defined as follows:

μ = permeability of the medium,

σ = conductivity of the medium,

r = distance from source,

$\mathbf{m}(\omega)$ = magnetic moment (transform) of the dipole.

When $\mathbf{m}(\omega)$ is assumed to be along the polar axis and the medium is assumed infinite, the fields derived from (1) are given by:

$$E_\phi(\omega) = \frac{-\mu |\mathbf{m}(\omega)| \sin \theta}{4\pi r^2} (1 + r\sqrt{i\omega\mu\sigma}) i\omega e^{-\sqrt{i\omega\mu\sigma} r} \quad (2)$$

$$H_\theta(\omega) = \frac{|\mathbf{m}(\omega)| \sin \theta}{2\pi r^3} (1 + r\sqrt{i\omega\mu\sigma} + i\omega\mu\sigma r^2) e^{-\sqrt{i\omega\mu\sigma} r} \quad (3)$$

$$H_r(\omega) = \frac{|\mathbf{m}(\omega)| \cos \theta}{2\pi r^3} (1 + r\sqrt{i\omega\mu\sigma}) e^{-\sqrt{i\omega\mu\sigma} r}. \quad (4)$$

* Received by the PGAP, February 29, 1960; revised manuscript received, June 25, 1960.

† Elec. Engrg. Dept., University of New Mexico, Albuquerque, N. M.

¹ P. I. Richards, "Transients in conducting media," IRE TRANS. ON ANTENNAS AND PROPAGATION, vol. AP-6, pp. 178-182; April, 1958.

² J. R. Wait, "Transient electromagnetic propagation in a conducting medium," *Geophysics*, vol. 16, pp. 213-221; April, 1951.

³ W. J. Yost, "The interpretation of electromagnetic reflection data in geophysical exploration—Part I, general theory," *Geophysics*, vol. 17, pp. 89-106; January, 1952.

⁴ J. R. Wait, "A transient magnetic dipole source in a dissipative medium," *J. Appl. Phys.*, vol. 24, pp. 341-343; March, 1953.

⁵ J. Keilson and R. V. Row, "Transfer of transient electromagnetic surface waves into a lossy medium," *J. Appl. Phys.*, vol. 30, pp. 1595-1598; October, 1959.

⁶ A. Grumet, "Penetration of transient electromagnetic fields into a conductor," *J. Appl. Phys.*, vol. 30, pp. 682-686; May, 1959.

The variation of the transient current in the loop constituting the dipole is now taken to be as shown in Fig. 1. The Fourier transform of this current is

$$I(\omega) = \frac{-I_m}{W} \left[\frac{1}{\omega^2} (1 - 2e^{-i\omega W} + e^{-i2\omega W}) \right] \quad (5)$$

and from this we obtain

$$|m(\omega)|^2 = |I(\omega)|^2 dA^2 = \frac{4I_m^2}{W^2} \left[\frac{1}{\omega^4} (1 - \cos \omega W)^2 dA^2 \right] \quad (6)$$

where dA is the area of the loop.

Lumping together factors not involving frequency into the term L , and making the abbreviation $a = r\sqrt{2\sigma\mu}$, we find

$$|E_\phi(\omega)|^2 = L_1^2 \frac{e^{-a\sqrt{\omega}}}{\omega^2} \left(1 + a\sqrt{\omega} + \frac{a^2\omega}{2} \right) (1 - \cos \omega W)^2 \quad (7)$$

$$|H_\theta(\omega)|^2 = L_2^2 \frac{e^{-a\sqrt{\omega}}}{\omega^4} \left(1 + a\sqrt{\omega} + \frac{a^2\omega}{2} + \frac{a^3\omega^{3/2}}{2} + \frac{a^4\omega^2}{4} \right) (1 - \cos \omega W)^2 \quad (8)$$

$$|H_r(\omega)|^2 = L_3^2 \frac{e^{-a\sqrt{\omega}}}{\omega^4} \left(1 + a\sqrt{\omega} + \frac{a^2\omega}{2} \right) (1 - \cos \omega W)^2 \quad (9)$$

Differentiating with respect to ω and setting the results equal to zero gives the following expressions, wherein ω_p denotes a frequency to be associated with the peak of

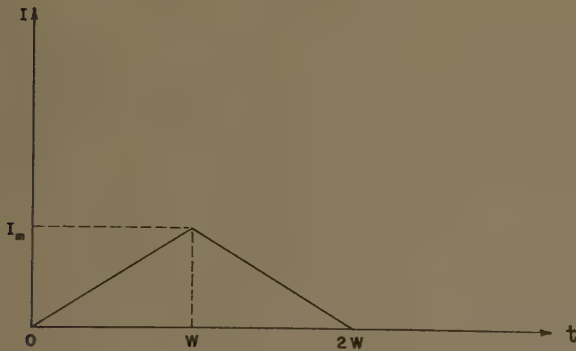


Fig. 1—Dipole current.

the spectral density, and the abbreviation $p = a\sqrt{\omega_p}$ is made:

For $|E_\phi(\omega)|^2$:

$$\frac{2}{\omega_p W} \tan \frac{\omega_p W}{2} (p^3 + 4p^2 + 8p + 8) = 8p^2 + 16p + 16. \quad (10)$$

For $|H_\theta(\omega)|^2$:

$$\frac{2}{\omega_p W} \tan \frac{\omega_p W}{2} (p^5 + 6p^4 + 12p^3 + 16p^2 + 32p + 32) = 8p^4 + 16p^3 + 16p^2 + 32p + 32. \quad (11)$$

For $|H_r(\omega)|^2$:

$$\frac{2}{\omega_p W} \tan \frac{\omega_p W}{2} (p^3 + 8p^2 + 16p + 16) = 8p^2 + 16p + 16. \quad (12)$$

For arbitrary W , it is obviously difficult to deal with these equations. However, if trial values are assumed, it can be ascertained that for $W \ll a^2$, the value of ω_p satisfying (10) and (11) will be sufficiently small so that the approximation

$$\tan \frac{\omega_p W}{2} \approx \frac{\omega_p W}{2} \quad (13)$$

can be made. Under this condition the equations become independent of W , and a solution for p is readily obtained in each case. Eq. (12) is not satisfied for $\omega_p W/2$ in the first quadrant except for $p=0$. Hence, in this range of frequency the energy spectral density for $H_r(\omega)$ is monotonically decreasing from its value at $\omega=0$, and some quantity other than peak value must be used as a measure of spectrum behavior. One possibility, denoted by $\omega_{1/2}$, is the value of ω for which $|H_r(\omega)|^2 = \frac{1}{2} |H_r(0)|^2$. It can be shown that this latter quantity is $\frac{1}{2}(L_3^2(W^4/4))$. Assuming distances sufficiently great so that $\omega_{1/2}W$ is small, we approximate $(1 - \cos \omega W)^2$ by $(\omega W)^4/4$. The relation to be satisfied becomes

$$e^{-p'} \left(1 + p' + \frac{p'^2}{2} \right) = 1/2 \quad (14)$$

where p' is defined as $a\sqrt{\omega_{1/2}}$.

Eqs. (10), (11), and (14) can now be solved for p or p' under the given assumptions. Table I presents the values obtained for p and p' , together with the values

TABLE I

$ E_\phi(\omega) ^2$	$ H_\theta(\omega) ^2$	$ H_r(\omega) ^2$
$p = 5.662$	$p = 3.236$	$p' = 2.674$
$\frac{(5.662)^2}{a^2}$	$\frac{(3.236)^2}{a^2}$	$\frac{(2.674)^2}{a^2}$
$\omega_p(\text{sea water}) = \frac{3.19 \times 10^6}{r^2} \text{ rad/sec}$	$\omega_p(\text{sea water}) = \frac{1.04 \times 10^6}{r^2} \text{ rad/sec}$	$\omega_{1/2}(\text{sea water}) = \frac{7.11 \times 10^6}{r^2} \text{ rad/sec}$

of ω_c (ω_p or $\omega_{1/2}$) both for an arbitrary medium and for sea water ($\sigma = 4$ mho/meter, $\mu = 4\pi \times 10^{-7}$ henry/meter).

To determine more specifically the limits within which the assumption (13) is valid, we may note that when $\omega_p W/2 = \frac{1}{2}$ radian, the tangent differs from its argument by about 10 per cent. Since $\omega_p = p^2/a^2$, we require

$$p^2 W \leq a^2 \quad (15)$$

$$a \geq p\sqrt{W} \quad (16)$$

for the assumption to be reasonably good. This condition, with p replaced by p' , applies also in obtaining (14). For a particular field component, p or p' assumes its appropriate numerical value from Table I.

At lesser distances the trigonometric term in the spectral density equations plays a more important role. By assuming specific values of W , the problem can be attacked on a point-by-point basis, and the results plotted as in Fig. 2. Although only the electric field situation is shown, a similar analysis can be made for H_θ and H_r .

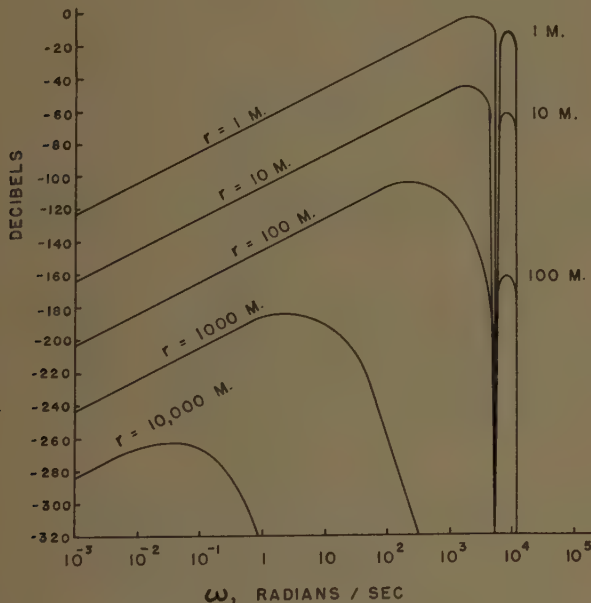


Fig. 2—Energy density spectrum for E_ϕ , triangular pulse, at various distances. ($\omega < 4000\pi$.)

The steeply sloping line of Fig. 2 represents the energy spectral peak behavior under the conditions defined by (15). It is therefore an absolute upper limit on the spectral peak regardless of the value of W . The gently sloping lines are the result of the point by point calculations, and show that the peak frequency decreases relatively slowly until the critical distance is reached. Beyond the critical distance, the product $a\sqrt{\omega_p}$ is constant; that is, ω_p varies as r^{-2} .

In order to determine the attenuation with distance of the main energy of the pulse, an evaluation can now

be made of $|E_\phi(\omega)|$ and $|H_\theta(\omega)|$ at $\omega = \omega_p$. $|H_r(\omega)|$ at $\omega = \omega_{1/2}$ is probably of less interest and is therefore not calculated. Using the relations given by Table I, writing

$$(1 - \cos \omega_p W) \approx \frac{(\omega_p W)^2}{2}, \quad (17)$$

and reintroducing factors not involving frequency into (7) and (8), it is found that:

$$|E_\phi(\omega)|_{\omega_p} = \frac{0.358}{\sigma} \frac{W I_m d A \sin \theta}{r^4},$$

(under condition $a \geq 5.662\sqrt{W}$) (18)

$$|H_\theta(\omega)|_{\omega_p} = 0.116 \frac{W I_m d A \sin \theta}{r^3}$$

(under condition $a \geq 3.236\sqrt{W}$). (19)

For the pulse considered, these equations are applicable to any highly conducting medium ($\sigma \gg \omega\epsilon$), provided the restriction as to distance of (16) is satisfied. The electric field magnitude for sea water is obtained immediately by substituting $\sigma = 4$ in (18). The magnetic fields do not depend on the parameters of the medium. An interesting point is that varying widths of the transmitted pulse are converted into proportionally varying amplitudes at large distances.

It should be noted that a physical measurement of the field quantities expressed as transforms necessarily involves an integration over the bandwidth of the measuring device. This multiplies the units of (18) and (19) by (sec^{-1}) .

The variation of electric field associated with the spectrum peak at distances for which a is less than $p\sqrt{W}$ seems to be rather difficult to formulate analytically. An approximate expression can be obtained by examining

$$|E_\phi(\omega)| = \frac{\mu I_m d A \sin \theta}{2\pi r^2 \omega W} (1 - \cos \omega W) e^{-a\sqrt{\omega}/2} \cdot \left(1 + a\sqrt{\omega} + \frac{a^2 \omega}{2}\right)^{1/2}. \quad (20)$$

It can easily be verified that the product

$$e^{-a\sqrt{\omega}/2} \left(1 + a\sqrt{\omega} + \frac{a^2 \omega}{2}\right)^{1/2}$$

does not differ greatly from unity until $a\sqrt{\omega}$ becomes larger than about 3. From Fig. 2 it can be seen that this condition holds for a major part of the small slope linear variation of $\sqrt{\omega_p}$. The product $1/\omega W (1 - \cos \omega W)$ is also nearly constant when evaluated at ω_p in this region. Consequently, the electric field as defined by the above equation varies approximately as $1/r^2$ for $a \leq 3\sqrt{W}$ and as $1/r^4$ for $a \geq 5.662\sqrt{W}$. It is apparent from (2) that the transition from $1/r^2$ to $1/r^4$ behavior is due to the presence of the multiplicative factor ω_p

and to the fact that it begins to vary as $1/r^2$ after the critical distance has been reached. The absence of this ω factor in (3) and (4) assures us that a $1/r^3$ behavior will obtain for both "near" and "far" situations for the magnetic field.

The above considerations can be clarified by reference to Fig. 3, where the energy spectral density for E_ϕ of a pulse with $W=0.001$ second is plotted for various distances from the source in sea water. The spectrum is, of course, continuous from zero to infinity, with nulls in this case separated by 2000π . The plot is carried out only up to the second null. The first spectral peaks for $r=1$ meter and $r=10$ meters differ by 40 db, whereas those for $r=100$, 1000, and 10,000 meters differ by 80 db.

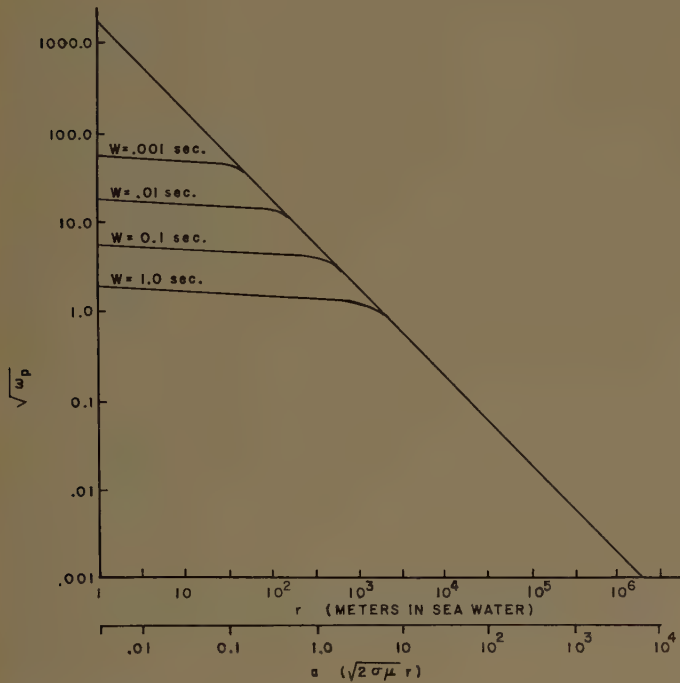


Fig. 3—Behavior of electric field energy spectral peak with distance.

Alternatively, the figure can be used to compare the attenuation of monochromatic waves of different frequencies. For example, if we wished to transmit a single frequency with minimum attenuation for a distance of 10,000 meters, entirely through water, we would be required to select a frequency of around 10^{-2} radian/second or less. If the maximum distance were only 300 meters, a frequency of around 30 radian/second could be used.

Likewise, if transient propagation with minimum attenuation is desired, the duration of the transient should be chosen so that the ω_c of its predominant energy spectral peak undergoes the minimum attenuation of 40 db per decade of distance over the range required.

RECTANGULAR PULSE

To demonstrate that the spectrum for a different type of transient will behave in essentially the same way, a development for the rectangular pulse can be carried out along exactly the same lines. In this case the transform current is

$$I(\omega) = \frac{I_m}{i\omega} (1 - e^{-i\omega W}). \quad (21)$$

The energy spectral density for the electric field is as follows:

$$|E_\phi(\omega)|^2 = L_4^2 \frac{e^{-a\sqrt{\omega}}}{\omega^2} \left(1 + a\sqrt{\omega} + \frac{a^2\omega}{2}\right) (1 - \cos \omega W). \quad (22)$$

Since this density is monotonically decreasing for $\omega W < \pi$, as in the case of H_r for the triangular pulse, we find it necessary to investigate $\omega_{1/2}$. It can be shown that

$$|E_\phi(0)|^2 = L_4^2 W^2 / 2, \quad (23)$$

so that for distances such that ωW is small,

$$L_4^2 \frac{e^{-a\sqrt{\omega}}}{\omega^2} (1 + a\sqrt{\omega} + a^2\omega/2) \frac{(\omega W)^2}{2} = \frac{1}{2} L_4^2 W^2 / 2 \quad (24)$$

is the determining equation for $\omega^{1/2}$. This gives

$$e^{-p'} (1 + p' + p'^2) = 1/2, \quad (25)$$

with the result $p' = 2.674$ or

$$\omega_{1/2} = \frac{(2.674)^2}{a^2}. \quad (26)$$

Evidently the loss of high frequencies occurs in a manner similar to that of the triangular pulse; i.e., either ω_p or $\omega_{1/2}$ decreases with distance as $1/r^2$.

PHASE VELOCITY

In a highly conducting medium ($\sigma \gg \omega\epsilon$) the phase velocity for a monochromatic wave is known to be

$$v = \sqrt{\frac{2\omega}{\mu\sigma}}. \quad (27)$$

It has been shown that ω_c for a transient pulse at large distances varies continuously as r^{-2} . By substituting $\omega = \omega_p$ in the above equation, we define a velocity v_p which is associated with the peak of the energy spectrum. Taking ω_p for the electric field (triangular pulse), $\sigma = 4$ mho per meter, and $\mu = 4\pi \times 10^{-7}$ henry per meter, we find:

$$v_p = \frac{1.143 \times 10^6}{r} \text{ meters/second.} \quad (28)$$

At 1 kilometer in sea water, v_p is thus seen to be 1143 meters/sec. Since ω_p at 1 kilometer is 3.28 radians/sec ($W < 0.1$ sec) and since a monochromatic wave of frequency 3.28 radians/sec propagates at a constant phase velocity of 1143 meters/sec, it is evident that the action of the medium on the spectrum of the pulse is simply that of low-pass filtering.

GENERAL CONSIDERATIONS

Although the foregoing calculations have been carried out for only two particular types of transient, it is obvious that the same procedure is applicable in any case. When computational difficulties arise, the information of interest can always be obtained from point-by-point graphical plots, numerical calculations, etc.

The most obvious and the most important factor in an analysis of this kind is the assumed linearity of the medium. After a transient has traveled an arbitrary distance, its spectrum can be considered to consist of a superposition of monochromatic components, each of which has been acted upon as if it alone existed. In any particular situation, knowledge of the general attenuation vs the frequency-distance characteristics of the medium enables one to make an educated guess as to how a spectrum will appear at various distances from the source. Guesswork on such a basis should tell us that the generation of high-frequency components is quite undesirable for communication over appreciable distances. It is this point that has been demonstrated by a specific analysis for triangular and rectangular pulses.

Propagation in a conducting medium is analogous to propagation along a transmission line under two different situations. This analogy can be seen by inspection of the general equation for voltage on a line with distributed parameters R , L (in series) and C , G (in shunt):

$$\frac{\partial^2 v}{\partial x^2} = RGv + (RC + LG) \frac{\partial v}{\partial t} + LC \frac{\partial^2 v}{\partial t^2}. \quad (29)$$

Setting L and G or R and C equal to zero gives an equation corresponding to that obtained by omission of the displacement current term from the wave equation:

$$\nabla^2 \mathbf{E} = \sigma \mu \frac{\partial \mathbf{E}}{\partial t} + \mu \epsilon \frac{\partial^2 \mathbf{E}}{\partial t^2}. \quad (30)$$

The result is the diffusion equation in each case. Physically, it is somewhat more satisfactory to use the analog obtained when R and C are zero, since the units then correspond more directly.

This well-known analogy is mentioned here because the RC transmission line was originally investigated

more than 100 years ago,⁷ and, as would be expected, some important conclusions as to its performance have long been known.⁸ These results are immediately applicable to the situation that is the topic of this paper. Some of the major conclusions are as follows:

- 1) Signal velocity is inversely dependent on distance.
- 2) The pulse shape is "smeared out" in time.
- 3) Consequently, there is a limitation on signaling rate.

CONCLUSIONS⁹

After a fairly small distance of travel in an infinite conducting medium, most of the energy in a transient pulse is contained in a frequency range around its lowest spectral peak. An analysis of the behavior of this peak or its half width, therefore, gives a good description of what is happening to the major portion of the energy in the pulse. Under the conditions assumed, it has been shown in the case of triangular and rectangular pulses generated by a magnetic dipole that the energy spectrum displays the following characteristics:

- 1) As distance increases up to a critical value which can be determined in terms of pulse width, there is a slow shift downward in the frequency ω_c at which the spectrum peak or its half width occurs. In this range, the electric field associated with ω_c decreases approximately as r^{-2} , while magnetic fields decrease as r^{-3} .
- 2) After the critical distance is reached, ω_c shifts downward proportionally as r^{-2} . Then the electric field associated with ω_c decreases as r^{-4} . In this "far" range an r^{-3} behavior continues to obtain for the magnetic fields.
- 3) The same considerations apply to propagation of transients as to propagation of continuous waves; namely, the range of transmission sets an upper limit to the frequencies which can be sent with minimum attenuation. Energy put into frequencies above this limit is essentially wasted.

⁷ W. Thompson (Lord Kelvin), "On the theory of the electric telegraph," *Proc. Roy. Soc.*, vol. 7, pp. 382 ff; 1856.

⁸ The authors of some recent papers on electromagnetic transients in a lossy medium have apparently been unaware of these transmission line investigations. A very good discussion of the RC transmission line is contained in the book by E. Weber, "Linear Transient Analysis," John Wiley and Sons, Inc., New York, N. Y., vol. II, ch. 7; 1956. Another briefer discussion of this subject is in R. K. Moore's "Traveling Wave Engineering," McGraw-Hill Book Co., Inc., New York, N. Y.; 1960.

⁹ Since this paper was first submitted, a communication has appeared by S. H. Zisk, "Electromagnetic transients in a conducting medium," *IRE TRANS. ON ANTENNAS AND PROPAGATION*, vol. AP-6, pp. 229-230; March, 1960. Zisk uses an integration, by means of the saddle-point method, to obtain a time-domain result from which he concludes, as in this paper, that Richards' results arise because of dispersion in the conducting medium.

Reflection Factor of Gradual-Transition Absorbers for Electromagnetic and Acoustic Waves*

KLAUS WALTHER†

Summary—Absorbers for electromagnetic or acoustic waves are described, for which a good impedance match and low reflection factor can be achieved by providing a gradual transition of material constants into the lossy medium. The reflection factor can be calculated by means of a Riccati-differential equation. General conclusions from the WKB-perturbation method can be drawn for absorbers, the layer thickness of which is either very small or very large in comparison to the wavelength. For "thin" layers, wave energy penetrates the whole thickness of the absorber. Suitable average values of the material constants are derived to describe the performance of the panel in this case. For "thick" layers only the initial part of the panel is energized. The asymptotic expressions contain only the material constants of this part. The results are interpreted physically. Numerical solutions of the reflection factor for highly refractive panels with exponentially varying material constants are reported.

I. INTRODUCTION

THE PROBLEM of absorbing electromagnetic and acoustic waves is important for many applications in measuring techniques, for the construction of anechoic chambers, and for camouflaging targets in radar and sonar detection. Only plane waves, which propagate in a direction perpendicular to a plane absorbing surface, shall be considered here. The cases of electromagnetic and acoustic waves can be treated in complete analogy. Assuming normal incidence and isotropic media, the differential equations become identical in both cases. Various basic principles can be utilized in constructing absorbers. A good summary of these can be found in a paper by Meyer and Severin.¹

One objective in absorber design is to achieve a low reflection factor over a frequency range as large as possible and simultaneously to keep the thickness l of the absorbing layer very small in comparison to the free field wavelength λ . This paper considers the principle of the gradual-transition absorber: A layer of lossy material covers a perfectly reflecting plane surface. By varying the material constants within the lossy panel, a good impedance match between the free propagation medium and the absorbing structure can be achieved. Such a gradual transition can be realized either by arranging a homogeneous lossy material in the form of wedges and pyramids or by using layers of varying material constants.

If the absolute amount r of the amplitude reflection factor for a gradual-transition absorber is plotted as a function of the ratio l/λ , the reflection decreases with

some oscillations as l/λ increases. A satisfactory performance of absorbers can be specified by the requirement $r \leq 10$ per cent. For well designed sound and microwave absorbers this condition can be realized in the range $l/\lambda \gtrsim 0.2$. For low frequencies a large layer thickness l would thus be required. One idea for the reduction of the l/λ -cutoff value is to apply lossy materials with a high index of refraction. Thus, the wavelength within the material can be reduced far below the free-field value. Artificially refractive media for microwaves and sound waves are well known.^{2,3}

This paper derives the differential equations for the electromagnetic and acoustic inhomogeneous absorber. Some general conclusions for absorbers, which are either very thin or very thick in comparison to λ , are drawn. The performance of gradual-transition absorbers is then illustrated by several numerical solutions for highly refractive panels, in which the material constants vary according to exponential functions.

II. THE RICCATI-DIFFERENTIAL EQUATION FOR THE GRADUAL-TRANSITION ABSORBER

A. Electromagnetic Waves

The theory of electromagnetic wave propagation in an inhomogeneous dielectric medium can be found in a paper by Barrar and Redheffer.⁴ Consider a medium in which the material constants $\epsilon(x) = \epsilon'(x) - j\epsilon''(x)$ and $\mu(x) = \mu'(x) - j\mu''(x)$ depend on one coordinate x only. $\epsilon(x)$ and $\mu(x)$ are, respectively, the relative dielectric constant and permeability referred to the free-space values ϵ_0 and μ_0 . A linearly polarized plane wave of time dependence $\exp(j\omega t)$ is assumed to propagate in parallel to the x axis. Then Maxwellian equations read

$$\left. \begin{aligned} \frac{dH_z(x)}{dx} &= -j\omega\epsilon_0\epsilon(x)E_y(x) \\ \frac{dE_y(x)}{dx} &= -j\omega\mu_0\mu(x)H_z(x) \end{aligned} \right\}, \quad (1)$$

where

$E_y(x)$ = electric field strength

$H_z(x)$ = magnetic field strength.

* Received by the PGAP, April 14, 1960; revised manuscript received, June 16, 1960.

† Research Labs. Division, Bendix Corp., Southfield, Mich.

¹ E. Meyer and H. Severin, "Absorptionsanordnungen für elektromagnetische Zentimeterwellen und ihre akustischen Analogien," *Z. angew. Phys.*, vol. 8, pp. 105-114; March, 1956.

² W. E. Kock, "Metallic delay lenses," *Bell Sys. Tech. J.*, vol. 27, pp. 58-82; January, 1948.

³ W. E. Kock and F. K. Harvey, "Refracting sound waves," *J. Acoust. Soc. Am.*, vol. 21, pp. 471-481; September, 1949.

⁴ R. B. Barrar and R. M. Redheffer, "On nonuniform dielectric media," *IRE TRANS. ON ANTENNAS AND PROPAGATION*, vol. AP-3, pp. 101-107; July, 1955.

An electric wave impedance $Z_e(x)$ can be defined for every position x within the layer:

$$Z_e(x) = -\frac{E_y(x)}{H_z(x)}. \quad (2)$$

The minus sign in this definition is necessary because of the choice of the coordinate system in Fig. 1. A differential equation satisfied by $Z_e(x)$ can be derived by means of (1):

$$\begin{aligned} \frac{dZ_e}{dx} &= -\frac{1}{H_z} \frac{dE_y}{dx} + \left(\frac{E_y}{H_z}\right)^2 \frac{1}{E_y} \frac{dH_z}{dx} \\ &= j\omega\mu_0\mu(x) - j\omega\epsilon_0\epsilon(x)Z_e^2(x). \end{aligned} \quad (3)$$

The amplitude reflection factor $R_e(x)$ is defined

$$R_e(x) = \frac{Z_e(x) - Z_0}{Z_e(x) + Z_0}, \quad (4)$$

where $Z_0 = \sqrt{\mu_0/\epsilon_0} = 377\Omega$ = wave impedance of free space. Eq. (3) may be transformed into a Riccati-differential equation for $R_e(x)$:⁵⁻⁷

$$\frac{dR_e}{dx} = -j\frac{\pi}{\lambda_e} [\epsilon(x)(1 + R_e)^2 - \mu(x)(1 - R_e)^2] \quad (5)$$

where $\lambda_e = 2\pi/\omega(\epsilon_0\mu_0)^{-1/2}$ is the electric free space wavelength.

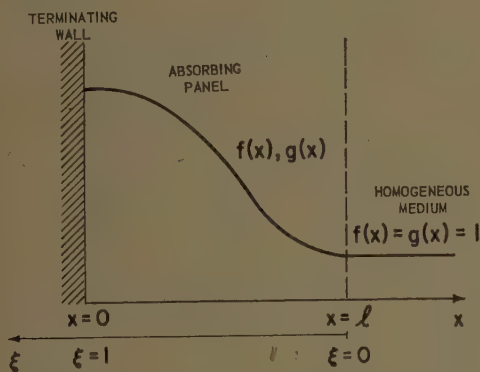


Fig. 1—Inhomogeneous absorbing panel of thickness l .

B. Acoustic Waves

The theory of acoustic wave propagation in an inhomogeneous medium can be found in a paper by Bergman.⁸ The material constants $\kappa(x) = \kappa'(x) - j\kappa''(x)$ and $\rho(x) = \rho'(x) - j\rho''(x)$ of the acoustic medium are assumed to depend on one coordinate x only. $\kappa(x)$ and $\rho(x)$ are, respectively, the relative compressibility and

density, referred to the values κ_0 and ρ_0 for the homogeneous medium in front of the absorber. A plane sound wave of time dependence $\exp(j\omega t)$ shall propagate in parallel to the x axis. Then the sound field equations for small amplitudes can be written

$$\left. \begin{aligned} \frac{dV(x)}{dx} &= -j\omega\kappa_0\kappa(x)P(x) \\ \frac{dP(x)}{dx} &= -j\omega\rho_0\rho(x)V(x) \end{aligned} \right\} \quad (6)$$

where $P(x)$ = sound pressure and $V(x)$ = particle velocity.

The acoustic wave impedance $Z_a(x)$ is defined

$$Z_a(x) = -\frac{P(x)}{V(x)}. \quad (7)$$

A differential equation for $Z_a(x)$ can be derived from (6):

$$\begin{aligned} \frac{dZ_a}{dx} &= -\frac{1}{V} \frac{dP}{dx} + \left(\frac{P}{V}\right)^2 \frac{1}{P} \frac{dV}{dx} \\ &= j\omega\rho_0\rho(x) - j\omega\kappa_0\kappa(x)Z_a^2(x). \end{aligned} \quad (8)$$

The acoustic amplitude reflection factor $R_a(x)$ is given by

$$R_a(x) = \frac{Z_a(x) - Z}{Z_a(x) + Z}, \quad (9)$$

where $Z = \sqrt{\rho_0/\kappa_0}$ is the wave impedance of the homogeneous medium in front of the absorber. Eq. (8) may be transformed into a Riccati-differential equation for $R_a(x)$:

$$\frac{dR_a}{dx} = -j\frac{\pi}{\lambda_a} [\kappa(x)(1 + R_a)^2 - \rho(x)(1 - R_a)^2], \quad (10)$$

where $\lambda_a = 2\pi/\omega(\kappa_0\rho_0)^{-1/2}$ is the acoustic wavelength in the homogeneous medium in front of the absorber.

C. The Analogy

Since (5) and (10) are identical in form, the reflection factor R for the electromagnetic and acoustic cases can be evaluated by the same differential equation:

$$\frac{dR}{dx} = -j\frac{\pi}{\lambda} [g(x)(1 + R)^2 - f(x)(1 - R)^2], \quad (11)$$

where the analogy

$$f(x) = u(x) - jv(x) = \mu(x) \triangleq \rho(x) \quad (12)$$

$$g(x) = s(x) - jt(x) = \epsilon(x) \triangleq \kappa(x) \quad (13)$$

between electric and acoustic quantities is used.

According to (4) and (9) a boundary condition $R = +1$ corresponds to a "magnetic" wall (surface of zero magnetic field strength) in the electromagnetic case and to a rigid wall in the acoustic case. The condition $R = -1$ requires an "electric" wall (metal plate) or a pressure

⁵ R. M. Redheffer, "Reflection and transmission equivalences of dielectric media," *Proc. IRE*, vol. 39, p. 503; May, 1951.

⁶ R. M. Redheffer, "Novel uses of functional equations," *J. Rat. Mech. Anal.*, vol. 3, pp. 271-279; March, 1954.

⁷ R. M. Redheffer, "Limit-periodic dielectric media," *J. Appl. Phys.*, vol. 27, pp. 1136-1140; October, 1956.

⁸ P. G. Bergman, "The wave equation in a medium with a variable index of refraction," *J. Acoust. Soc. Am.*, vol. 17, pp. 329-333; April, 1946.

release surface in the two cases, respectively. Interchanging $f(x)$ and $g(x)$ in (11) is equivalent to changing the sign of $R(x)$. According to (4) and (9) this corresponds to replacing impedance by admittance and vice versa. This is the well-known principle of duality.

III. SOME GENERAL PROPERTIES OF THE REFLECTION FACTOR FOR THE GRADUAL-TRANSITION ABSORBER

A. Interpretation of the Reflection Factor for an Inhomogeneous Medium

The geometry of the problem under consideration is shown in Fig. 1. An absorbing panel is terminated at $x=0$ by a totally reflecting wall. At the front surface $x=l$ the material constants shall be the same as for the homogeneous propagation medium, $f(x)=g(x)=1$ for $x \geq l$. The gradual transition of material constants is represented schematically by the functions $f(x)$ and $g(x)$. A solution $R(x)$ can be computed from (11) with the proper initial condition at $x=0$. The point $R(l)$ is the reflection factor of the total layer. A physical interpretation of the solution $R(x)$ is possible also for a point $x_0 \neq l$. The definition of $R(x)$ in (4) is due to Redheffer.⁵ The Redheffer-reflection factor $R(x_0)$ represents the reflection from an inhomogeneous panel, in which the region $x_0 \leq x \leq l$ has been replaced by a homogeneous medium of material constants $f(x)=g(x)=1$ (Fig. 2).

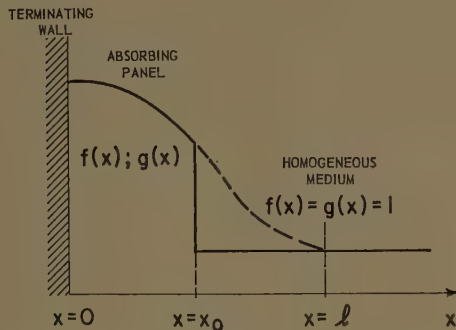


Fig. 2—Interpretation of the Redheffer reflection factor at $x=x_0$.

A different approach to the problem of wave propagation in an inhomogeneous medium may be found by defining the reflection factor $R_s(x)$:

$$R_s(x) = \frac{Z_e(x) - \sqrt{\mu(x)/\epsilon(x)}}{Z_e(x) + \sqrt{\mu(x)/\epsilon(x)}}, \quad (14)$$

instead of using (4). Kay⁹ associates this approach with the name of Schelkunoff (see additional references in his paper⁹) and compares several aspects of the "Redheffer" and "Schelkunoff" methods. The definition in (14) leads to a different Riccati equation for $R_s(x)$, requiring $f(x)$ and $g(x)$ to be differentiable. A solution

$R_s(x)$ at $x=x_0 \neq l$ corresponds to the reflection from an inhomogeneous layer, in which the whole region $x \geq x_0$ has been replaced by a homogeneous medium of material constants $f(x_0)$ and $g(x_0)$ (Fig. 3). Since in general $f(x_0)$ and $g(x_0) \neq 1$, the intermediate points $R_s(x_0)$ according to the Schelkunoff method do not represent physically interesting solutions for the absorber problem. On the other hand, the intermediate points of the Redheffer solution (Fig. 2) may give useful information on the effect of cutting away part of the panel (reduction of layer thickness, effect of an initial step). For the point $x=l$ the results of both methods are identical, if layers with no initial step are considered. An example of the Schelkunoff method for calculating the reflection factor of gradual-transition sound absorbers can be found in a paper by Miller.¹⁰ We prefer to use the Redheffer method in this paper.

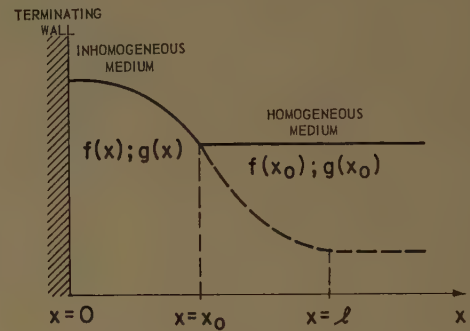


Fig. 3—Interpretation of the Schelkunoff reflection factor at $x=x_0$.

B. Behavior of Panels, Thin Compared to Wavelength

Integration of the Riccati equation (11) normally leads to nonelementary functions and has to be accomplished numerically; such results are reported in Section IV. Some general conclusions can be drawn, however, for the limiting cases of a layer thickness l which is either very small or very large in comparison to the wavelength λ .

1) *Taylor-Series Solution of the Riccati Equation:* For the case $l/\lambda \ll 1$ the quantity $r(x) = |R(x)|$ may be calculated from (11) in the form of a Taylor series, starting at the point $x=0$:

$$r(x) = \sum_{v=0}^{\infty} \left(\frac{d^{(v)}r}{dx^v} \right)_0 \frac{x^v}{v!}. \quad (15)$$

A similar method has been applied by Sampson.¹¹ Results shall be given here only for two simple cases (Table I). These can be characterized physically by the facts: Case 1 shows *high* energy dissipation near the terminating surface $x=0$. In Case 2 a *low* energy dissipa-

¹⁰ N. B. Miller, "Reflections from gradual transition sound absorbers," *J. Acoust. Soc. Am.*, vol. 30, pp. 967-973; October, 1958.

⁹ A. F. Kay, "Reflection of a Plane Wave by a Stratified Medium," McMillan Lab., Inc., Ipswich, Mass. Tech. Rept., Contract AF18(600)-1044; November 22, 1954.

¹¹ J. H. Sampson, "Some Absorbing Panels with Variable Dielectric Composition," McMillan Lab., Inc., Ipswich, Mass., Tech. Rept., Contract AF18(600)-1044; December 20, 1954.

TABLE I

Case 1: High Energy Dissipation Near $x=0$		Case 2: Low Energy Dissipation Near $x=0$	
Electromagnetic Waves			
a) Electric losses—Magnetic wall		a) Electric losses—Electric wall	
b) Magnetic losses—Electric wall		b) Magnetic losses—Magnetic wall	
Acoustic Waves			
a) Compressibility losses—Rigid wall		a) Compressibility losses—Pressure release wall	
b) Density (friction) losses—Pressure release wall		b) Density (friction) losses—Rigid wall	

tion near the terminating surface $x=0$ prevails. The energy N dissipated per unit volume is proportional to:

for electromagnetic waves:

$$N_e \sim \epsilon'' \cdot E^2 + \mu'' \cdot H^2$$

for acoustic waves:

$$N_a \sim \kappa'' \cdot P^2 + \rho'' \cdot V^2.$$

In the following cases we assume that only one type of loss mechanism is present, putting either $f(x)$ or $g(x) = 1$ in (11). The possible "simple" cases are summarized in Table I.

The cases that can be realized most easily in absorber design are Case 2a) for microwaves, Case 1a) for waterborne sound, and Case 2b) for airborne sound. The Taylor-series expansion of (15) shall be given for Cases 1a) and 2a) as examples: $t(x) = \epsilon''(x)$,

Case 1a):

$$r(x) \simeq 1 - \frac{4\pi}{\lambda} \epsilon''(0)x + \left[\frac{8\pi^2}{\lambda^2} \epsilon''^2(0) - \frac{2\pi}{\lambda} \left(\frac{d\epsilon''}{dx} \right)_0 \right] x^2 + \dots \quad (16)$$

Case 2a):

$$r(x) \simeq 1 - \frac{16\pi^3}{3\lambda^3} \epsilon''(0)x^3 - \frac{4\pi^3}{\lambda^3} \left(\frac{d\epsilon''}{dx} \right)_0 x^4 + \dots \quad (17)$$

These curves are shown in Fig. 4. For the case of high energy dissipation a sharp drop of $r(x)$ near $x=0$ can be observed. In the case of low energy dissipation the curve $r(x)$ starts from the point, $r=1$, with a horizontal slope, the deviation being given by a third-order term.

It should be emphasized that the convergence of the series (15) is very poor. Moreover, this approach is not very satisfactory for a physical interpretation, since only functional values and derivatives at $x=0$ are speci-

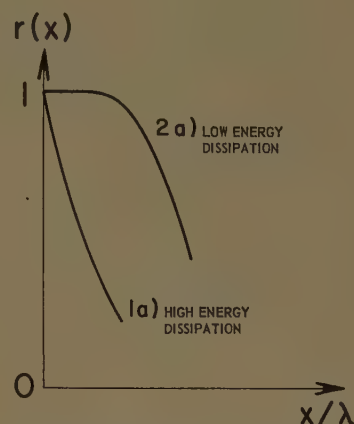


Fig. 4—Initial behavior of the reflection factor $r(x)$ for "thin" absorbers: $x/\lambda \ll 1$.

fied. For very "thin" layers energy is penetrating the full thickness l of the absorber. Therefore, it can be expected physically that certain average values of the material constants $f(x)$ and $g(x)$ in the form of integrals $\int_0^l f(x) \cdot w_1(x) dx$ and $\int_0^l g(x) \cdot w_2(x) dx$ are more appropriate for the description of very "thin" layers. These relations will now be derived.

2) *WKB Solution of the Wave Equation:* The WKB perturbation method for obtaining approximate solutions of the inhomogeneous wave equation has proved useful in many problems of quantum mechanics and wave propagation.¹² We follow a treatise by Zharkovskii and Todes,¹³ but we consider a more general case. Similar approximation methods can be found in a paper by Pipes.¹⁴

The wave equation for the electric field strength $E(\xi)$ can be derived from (1), where the coordinate transformation $\xi = 1 - x/l$ has been used (see Fig. 1):

$$\frac{d^2 E}{d\xi^2} - \frac{d(\ln \mu(\xi))}{d\xi} \cdot \frac{dE}{d\xi} + (kl)^2 \epsilon(\xi) \mu(\xi) E(\xi) = 0, \quad (18)$$

¹² See, e.g., references in C. O. Hines, "Reflection of waves from varying media," *Quart. J. Appl. Math.*, vol. 11, pp. 9-31; April, 1953.

¹³ A. G. Zharkovskii and O. M. Todes, "Reflection of waves from an isotropic inhomogeneous layer," *Soviet Phys. JETP*, vol. 4, pp. 701-703; June, 1957.

¹⁴ L. A. Pipes, "Computation of the impedances of nonuniform lines by a direct method," *Trans. AIEE*, vol. 75, pp. 551-554; November, 1956.

where $kl = 2\pi l/\lambda$. A solution of this equation is sought in the form:

$$E(\xi) = E^+ \cdot \exp\left(jkl \cdot \int_1^\xi f_s(\xi) d\xi\right) + E^- \cdot \exp\left(-jkl \cdot \int_1^\xi F_s(\xi) d\xi\right). \quad (19)$$

The functions $f_s(\xi)$ and $F_s(\xi)$ satisfy the following first-order differential equations:

$$-jkl[\epsilon\mu - f_s^2] + \left[\frac{df_s}{d\xi} - \frac{d(\ln \mu)}{d\xi} f_s\right] = 0 \quad (20)$$

and

$$+jkl[\epsilon\mu - F_s^2] + \left[\frac{dF_s}{d\xi} - \frac{d(\ln \mu)}{d\xi} F_s\right] = 0. \quad (21)$$

For the case of very thin layers $kl \ll 1$ we use asymptotic expansions of the form:

$$f_s(\xi) = \sum_{m=0}^{\infty} k^m f_{s,m}(\xi) \quad (22)$$

and

$$F_s(\xi) = \sum_{m=0}^{\infty} k^m F_{s,m}(\xi). \quad (23)$$

Eqs. (20) and (21) are solved by a perturbation method. An approximate solution $E(\xi)$ satisfying the short-circuit boundary condition at $\xi=1$ can thus be derived:

$$E(\xi) = A \cdot \exp\left[-(kl)^3 \cdot \int_1^\xi \mu(\xi') \int_1^{\xi'} (\epsilon - \mu) d\xi'' d\xi'\right] \sin \phi(\xi), \quad (24)$$

where

$$\phi(\xi) = kl \cdot \int_1^\xi \mu(\xi') d\xi' + 2(kl)^3 \cdot \int_1^\xi \mu(\xi') \int_1^{\xi'} \mu(\xi'') \int_1^{\xi''} (\epsilon - \mu) d\xi''' d\xi'' d\xi'.$$

This expansion is correct including terms of order $(kl)^3$. By application of Maxwell's equations (1) the normalized input admittance for the front surface $\xi=0$ of the layer may be derived:

$$\frac{Y_i}{Y_o} = jkl \cdot \int_0^1 (\epsilon - \mu) d\xi' - j[1 + 2(kl)^2 \cdot \int_0^1 \mu(\xi') \int_{\xi'}^1 (\epsilon - \mu) d\xi'' d\xi'] \cotan \phi(\xi). \quad (25)$$

After some mathematical manipulations, including removal of multiple integrations, (25) can be rewritten for the normalized input impedance and may be interpreted physically for simple cases.

Assuming $\mu(\xi) \equiv 1$, the result, including terms of order $(kl)^3$, reads

$$\frac{Z_i}{Z_o} = jkl + j \frac{(kl)^3}{3} \int_0^1 \epsilon(\xi) w_1(\xi) d\xi, \quad (26)$$

where the weighting function

$$w_1(\xi) = 3(1 - \xi)^2; \quad \int_0^1 w_1(\xi) d\xi = 1 \quad (27)$$

has been introduced. If this result is written in the form

$$\frac{Z_i}{Z_o} = jkl + j \frac{(kl)^3}{3} \cdot \bar{\epsilon} = jkl + j \frac{(kl)^3}{3} \cdot \bar{\epsilon}' + \frac{(kl)^3}{3} \cdot \bar{\epsilon}'', \quad (28)$$

it is equivalent to the input impedance of a homogeneous layer with average dielectric constant.

$$\bar{\epsilon} = \int_0^1 \epsilon(\xi) w_1(\xi) d\xi. \quad (29)$$

In the case $\epsilon(\xi) \equiv 1$, the expansion of the normalized input impedance may be written.

$$\frac{Z_i}{Z_o} = jkl \int_0^1 \mu(\xi) d\xi + j(kl)^3 \cdot 2 \int_0^1 \xi \mu(\xi) \int_{\xi}^1 \mu(\xi') d\xi' d\xi. \quad (30)$$

In order to show the physical significance of this result more clearly, we consider a layer in which the permeability $\mu(\xi)$ differs by only a small amount $\nu(\xi)$ from the homogeneous value μ : $\mu(\xi) = \mu + \nu(\xi)$. For this case we can rewrite (30) in the form

$$\frac{Z_i}{Z_o} = jkl \cdot \int_0^1 \mu(\xi) w_2(\xi) d\xi + j \frac{(kl)^3}{3} \left[\left(\int_0^1 \mu(\xi) w_3(\xi) d\xi \right)^2 + \Delta \right], \quad (31)$$

where the error Δ

$$\Delta = 6 \int_0^1 \xi \nu(\xi) \int_{\xi}^1 \nu(\xi') d\xi' d\xi - \left[\int_0^1 \nu(\xi) w_3(\xi) d\xi \right]^2 \quad (32)$$

is a second-order term in $\nu(\xi)$ and can be neglected, whenever $|\nu(\xi)| \ll \mu$. Thus, the almost homogeneous layer can be represented within a good approximation by means of two weighting functions:

$$w_2(\xi) \equiv 1 \quad (33)$$

$$w_3(\xi) = 3\xi - \frac{3}{2} \xi^2; \quad \int_0^1 w_3(\xi) d\xi = 1 \quad (34)$$

which are different for the two degrees of expansion in (kl) .

These analogies with the homogeneous case suggest the definition of two average values of the permeability:

$$\bar{\mu} = \int_0^1 \mu(\xi) d\xi \quad (35)$$

$$(\bar{\mu})^2 = 6 \int_0^1 \xi \mu(\xi) \int_{\xi}^1 \mu(\xi') d\xi' d\xi. \quad (36)$$

Using these values, (30) may be rewritten

$$\frac{Z_i}{Z_e} = jkl\bar{\mu} + j \cdot \frac{(kl)^3}{3} \cdot (\bar{\mu})^2 \simeq jkl \cdot \bar{\mu}' + kl \cdot \bar{\mu}'' + \dots \quad (37)$$

This is a well-known result for the homogeneous case, where $\bar{\mu} = \mu = \mu_0$.

The weighting functions $w_1(\xi)$ through $w_3(\xi)$ for a short-circuit termination at $\xi=1$ are plotted in Fig. 5. A physical interpretation suggests that $w_1(\xi)$ has to be zero near $\xi=1$, because in a region of low electric field strength a dielectric constant of the material cannot be effective. From (27) it could be concluded that a variation of dielectric constant

$$\epsilon(\xi) \sim (1 - \xi)^{-2} \quad (38)$$

would result in a constant value of the weighted dielectric constant $\epsilon(\xi) \cdot w_1(\xi)$ throughout the layer and should have favorable applications in absorber design. Such a function (38) was considered by Jacobs.¹⁵ This author arrives at (38) by attempting to find a function $\epsilon(\xi)$, for which the fractional change $1/\epsilon \cdot d\epsilon/d\xi$ referred to the "local" wavelength $\lambda(\xi) = \lambda/\sqrt{\epsilon(\xi)}$ is the same small constant a for all positions ξ within the layer:

$$\frac{1}{2\pi\epsilon(\xi)} \cdot \frac{d\epsilon}{d\xi} = \frac{\lambda}{2\pi} \cdot \frac{1}{\epsilon^{3/2}} \cdot \frac{d\epsilon}{d\xi} = a \ll 1.$$

This statement may be similar to our interpretation of (38). Because of the singularity of (38) at $\xi=1$ we have to be cautious, however, in drawing too many conclusions from perturbation theory.

From a similar physical reasoning the weighting function $w_2(\xi)$ should be unity near the short circuit $\xi=1$, since in a region of maximum magnetic field strength the permeability can be fully effective. The higher order weighting function $w_3(\xi)$ should decrease with the distance from the terminating wall, since the magnetic field strength decreases. The functions $w_1(\xi)$ and $w_3(\xi)$ should thus have an opposite trend.

Assuming frequency independent material constants ϵ and μ , the impedance curves corresponding to (28) and (37) are shown schematically in Fig. 6. For the case of electric losses (curve 1), the deviation from the imaginary axis is given by a third-order term in ω . In the case of magnetic losses (curve 2), the impedance

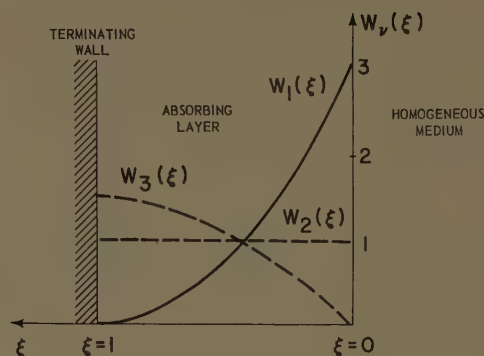


Fig. 5—Weighting functions $w_v(\xi)$ for "thin" absorbers:

$$w_1(\xi) = 3(1 - \xi)^2,$$

$$w_2(\xi) = 1,$$

$$w_3(\xi) = 3\xi - \frac{3}{2}\xi^2$$

$$\int_0^1 w_v(\xi) d\xi = 1.$$

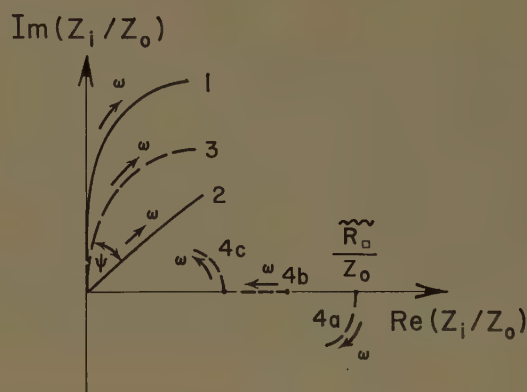


Fig. 6—Impedance curves for "thin" absorbers.

$$(a) \tilde{Y}_{\square} < Y_c, \quad (b) \tilde{Y}_{\square} = Y_c, \quad (c) \tilde{Y}_{\square} > Y_c.$$

Curve 1: electric losses, short-circuit termination.
Curve 2: magnetic losses, short-circuit termination; $\tan \psi = \bar{\mu}''/\bar{\mu}'$.
Curve 3: conductivity losses, short-circuit termination.
Curve 4: conductivity losses, open-circuit termination.
 \tilde{Y}_{\square} = averaged value of the "area-conductance."
 Y_c = critical value of the "area-conductance."

curve starts at an angle ψ off the imaginary axis, where $\tan \psi = \bar{\mu}''/\bar{\mu}'$.

The reflection factors corresponding to (28) and (37) are

$$|R| \simeq 1 - \frac{16\pi^3}{3\lambda^3} l^3 \bar{\epsilon}'' + \dots \text{ for electric losses} \quad (39)$$

and

$$|R| \simeq 1 - \frac{4\pi}{\lambda} l \bar{\mu}'' + \dots \text{ for magnetic losses.} \quad (40)$$

These functions are shown in Fig. 7, curves 1 and 2. A comparison with the initial parts of (16) and (17) shows that the averaged values of ϵ'' and μ'' have been substituted for the initial values at $\xi=1$. [Instead of (16) the dual case has to be considered.]

¹⁵ I. Jacobs, "The nonuniform transmission line as a broadband termination," *Bell Sys. Tech. J.*, vol. 37, pp. 913-924; July, 1958.

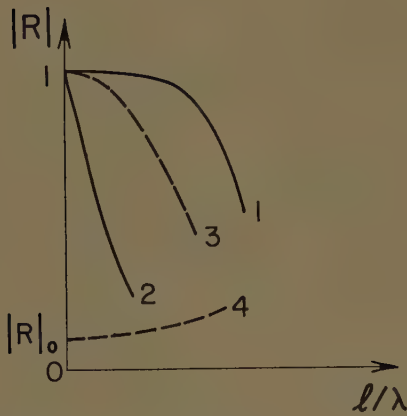


Fig. 7—Initial behavior of the reflection factor $|R|$ for "thin" absorbers: $l/\lambda \ll 1$.

Curve 1: electric losses, short-circuit termination.
Curve 2: magnetic losses, short-circuit termination.
Curve 3: conductivity losses, short-circuit termination.
Curve 4: conductivity losses, open-circuit termination.

$$|R|_0 = \left| \frac{R_\square - Z_0}{R_\square + Z_0} \right|$$

A different result is obtained if frequency dependent losses are taken into account. A loss mechanism, in which the loss factor is proportional to ω^{-1} , has special interest for very thin panels at low frequencies. Examples of such loss mechanisms are: 1) ohmic conductivity σ in the case of electromagnetic waves and 2) viscous friction in the case of acoustic waves (porous absorbers). Only the first case shall be considered here.

Substituting the expression for $\bar{\epsilon}' = \bar{\sigma}/\omega\epsilon_0$ into (28) gives the following result for the short-circuit case:

$$\frac{Z_i}{Z_0} = j\Omega + \frac{1}{3} \cdot \Omega^2 \cdot \frac{Z_0}{\bar{R}_\square} + j \cdot \frac{\Omega^3}{3} \cdot \bar{\epsilon}' + \dots \quad (41)$$

Here the normalized frequency $\Omega = (\omega/c)l$ and the averaged "area-resistance" $\bar{R}_\square = 1/\bar{\sigma}l$ of the layer have been introduced, where $\bar{\sigma} = \int_0^1 \sigma(\xi) \cdot w_1(\xi) d\xi$ is the averaged conductivity. The reflection factor corresponding to (41) reads

$$|R| \simeq 1 - \frac{8\pi^2}{3\lambda^2} \cdot l^2 \cdot \frac{Z_0}{\bar{R}_\square} + \dots \quad (42)$$

These relations are shown graphically as curve 3 in both Fig. 6 and Fig. 7. The deviation of the impedance curve 3 (Fig. 6) from the imaginary axis is given by a second-order term in ω and thus is much more effective than in the case of curve 1. Fig. 7 shows that the reflection factor for curve 3 drops much faster with increasing l/λ as compared to curve 1. The low-frequency properties of a "thin" conductive layer with short-circuit termination can be described qualitatively by the equivalent circuit of Fig. 8.¹⁶

The case of a conductive layer with open-circuit termination at $\xi = 1$ gives considerably different results. If $\epsilon(\xi)$ is substituted instead of $\mu(\xi)$ and the normalized

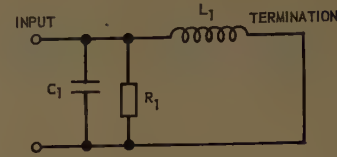


Fig. 8—Approximate equivalent circuit for the "thin" conductive layer with short-circuit termination.

input admittance Y_i/Y_0 is written instead of Z_i/Z_0 the following result can be obtained directly from (37):

$$\frac{Y_i}{Y_0} = jk\bar{\epsilon}' + j \cdot \frac{(kl)^3}{3} \cdot (\bar{\epsilon})^2. \quad (43)$$

By inserting the value $\epsilon = \epsilon' - j(\sigma/\omega\epsilon_0)$ the expansion including linear terms in frequency can be written.

$$\frac{Y_i}{Y_0} = \frac{\tilde{Y}_\square}{Y_0} - j\Omega \left[\frac{1}{3} \cdot \left(\frac{\tilde{Y}_\square}{Y_0} \right)^2 - \tilde{\epsilon}' \right], \quad (44)$$

where $\Omega = (\omega/c)l$ is the normalized frequency and $\tilde{\epsilon}' = \int_0^1 \epsilon'(\xi) d\xi$. Two averaged values for the "area-conductance" of the layer have been introduced:

$$\tilde{Y}_\square = \tilde{\sigma}l, \quad \text{where} \quad \tilde{\sigma} = \int_0^1 \sigma(\xi) d\xi \quad (45)$$

$$\tilde{Y}_\square = \tilde{\sigma}l, \quad \text{where} \quad (\tilde{\sigma})^2 = 6 \int_0^1 \xi \sigma(\xi) \int_\xi^1 \sigma(\xi') d\xi' d\xi. \quad (46)$$

The normalized input impedance Z_i/Z_0 corresponding to (44) is plotted as curves 4a through 4c in Fig. 6. All these curves start with a finite real value of the input impedance $Z_i = \tilde{R}_\square = 1/\tilde{Y}_\square$. The reactive behavior depends on the value of the average area-conductance \tilde{Y}_\square with respect to a critical value

$$Y_c = Y_0 \cdot \sqrt{3\tilde{\epsilon}'}. \quad (47)$$

Low conductive layers with $\tilde{Y}_\square > Y_c$ show a capacitive component; highly conductive layers with $\tilde{Y}_\square \leq Y_c$ are inductive. In the case $\tilde{Y}_\square = Y_c$, the first-order reactive component is zero. From higher-order approximations the frequency dependence of curves 4a through 4c in Fig. 6 can be derived. The equivalent circuit of Fig. 9 qualitatively shows the same behavior if the resistance R_2 is varied with respect to the wave impedance $\sqrt{L_2/C_2}$. The reflection factor corresponding to (44) starts with a finite value

$$|R|_0 = \left| \frac{\tilde{R}_\square - Z_0}{\tilde{R}_\square + Z_0} \right|$$

These facts are familiar from the theory of the Salisbury screen, for which the area-resistance is chosen to be $R_\square = 377 \Omega$ in order to match the absorber. The open-circuit termination in the case of electromagnetic waves can be realized in a resonance condition by placing a resistive foil at a distance of $\lambda/4$ in front of a metal plate. A "magnetic" wall can only be approximated

¹⁶ *Ibid.*, p. 916.

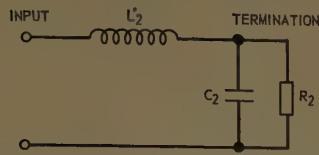


Fig. 9—Approximate equivalent circuit for the "thin" conductive layer with open-circuit termination.

roughly over a limited frequency band below the microwave range by using media with $|\mu| \gg |\epsilon|$ (for instance, ferrites).

The analogous acoustic case would be a porous absorber in water near a pressure release surface. Such porous materials (for instance fiberglass) are very effective as absorbers for airborne sound. However, the achievable friction losses with porous frameworks or similar structures for waterborne sound are much more limited.^{17,18} The reason for this is partly that a motion of the absorbing structure cannot be avoided at low frequencies, thus the achievable friction is limited. Although the acoustic analog of a "magnetic" wall can be realized easily, for the reasons mentioned, the required layer thickness of the absorber would be rather large. Therefore the analysis for the "thin" layer cannot be applied in this case.

C. Behavior of Panels, Thick Compared to Wavelength

Section III-B dealt with the theory of the "thin" layer. The analysis and interpretation have to be rather detailed, because energy penetrates the full layer thickness l . If the other limiting case of panels, thick compared to wavelength, is considered, we should expect physically a simpler situation. In this case only the initial part of the layer near the front surface $\xi=0$ is energized. The multiple reflections from the terminating wall $\xi=1$ become more and more insignificant as the frequency increases.

The analysis of the "thick" layer starts in a way that is analogous to the derivations in Section III-B, 2).¹³ A solution of the wave equation (18) is sought in the form of (19), with (20) and (21) being the same. Instead of the asymptotic expansions (22) and (23) we use

$$f_s(\xi) = \sum_{m=0}^{\infty} \left(\frac{1}{k} \right)^m f_{s,m}(\xi) \quad (48)$$

$$F_s(\xi) = \sum_{m=0}^{\infty} \left(\frac{1}{k} \right)^m F_{s,m}(\xi), \quad (49)$$

for the case $kl \gg 1$. The differential equations (20) and (21) are solved by a perturbation method. A solution $E(\xi)$ satisfying the short-circuit boundary condition at

the terminating wall $\xi=1$ can thus be derived:

$$E(\xi) = A \exp \left[\frac{1}{2} \int_1^{\xi} \frac{d}{d\xi} \left(\ln \sqrt{\frac{\mu}{\epsilon}} \right) d\xi \right] \sin \left(kl \int_1^{\xi} \sqrt{\epsilon\mu} d\xi \right). \quad (50)$$

The normalized input admittance for the front surface $\xi=0$ can be computed by means of Maxwell's equations (1):

$$\frac{Y_i}{Y_o} = \frac{-j}{4kl\mu(0)} \left[\frac{d \ln \epsilon}{d\xi} - \frac{d \ln \mu}{d\xi} \right]_{\xi=0} - j \sqrt{\frac{\epsilon(0)}{\mu(0)}} \cotan \left(kl \int_0^1 \sqrt{\epsilon\mu} d\xi \right). \quad (51)$$

Considering a layer without an initial discontinuity, $\epsilon=\mu=1$ for $\xi=0$, (51) can be simplified:

$$\left. \begin{aligned} \frac{Y_i}{Y_o} &= \frac{-j}{4kl} \left[\left(\frac{d\epsilon}{d\xi} \right)_0 - \left(\frac{d\mu}{d\xi} \right)_0 \right] \\ &\quad - j \cotan \left(kl \int_0^1 \sqrt{\epsilon\mu} d\xi \right) \\ &= \frac{j(\dot{u} - \dot{s})_0 + (\dot{v} - \dot{i})_0}{4kl} \\ &\quad - j \cotan \left(kl \int_0^1 \sqrt{\epsilon\mu} d\xi \right) \end{aligned} \right\}, \quad (52)$$

where

$$(\dot{u})_0 = \left(\frac{du}{d\xi} \right)_{\xi=0}, \text{ etc.}$$

The real and imaginary parts of $\mu(\xi)$ and $\epsilon(\xi)$ have been substituted from (12) and (13).

Consider the case of frequency independent material constants $\epsilon(\xi)$ and $\mu(\xi)$ first. Then the impedance curve corresponding to the first term in (52) runs to zero along a straight line in the complex plane as $\omega \rightarrow \infty$. The second term in (52) represents the short-circuit input admittance of a transmission line with an averaged refraction index:

$$\bar{n} = \int_0^1 \sqrt{\epsilon(\xi)\mu(\xi)} d\xi \quad (53)$$

According to our assumptions, no initial discontinuity of wave impedance for this equivalent transmission line is present at $\xi=0$. From transmission line theory it is well known that the corresponding impedance plot is a spiral in the complex plane, approaching the point $Y_i/Y_o = +1$ in a clockwise sense as $\omega \rightarrow \infty$. In (52) both the real and imaginary part of the argument for the cotan function increase proportional to frequency. Therefore, the distance between any point of the spiral $Y_i/Y_o = -j \cotan(kl \cdot \int_0^1 \sqrt{\epsilon\mu} d\xi)$ and the limiting point $Y_i/Y_o = +1$ vanishes according to an exponential function of general form $\exp(-\text{const } l/\lambda)$. Since the first

¹⁷ E. Meyer and K. Tamm, "Breitbandabsorber für Flüssigkeits-schall," *Acustica*, vol. 2, Beiheft 2, pp. AB 91-AB 104; 1952.

¹⁸ K. Tamm, "Broad-band absorbers for water-borne sound," in E. G. Richardson, "Technical Aspects of Sound," Elsevier Publishing Co., New York, N. Y., vol. 2, ch. 6, pp. 240-286; 1957.

term in (52) only vanishes like an inverse power in (l/λ) , this is the significant part for the calculation of the reflection factor $|R|$ in the limiting case $\omega \rightarrow \infty$. Thus the following result can be obtained:

$$|R|_{l/\lambda \rightarrow \infty} = \frac{\sqrt{(\dot{u} - \dot{s})_0^2 + (\dot{v} - \dot{t})_0^2}}{\frac{16\pi}{\lambda} l} \quad (54)$$

The reflection factor vanishes like $(l/\lambda)^{-1}$ for $l/\lambda \rightarrow \infty$. The only quantities of the layer which appear in this equation are the first order derivatives of the material constants at the front surface $\xi=0$. Reflections from the terminating wall can be neglected completely, since no energy enters this part of the absorber. By application of Schwarz's inequality, Kay⁹ has shown, generally, that the Schelkunoff-reflection factor R_s (14) cannot vanish as a weaker power than $\lambda^{1/2}$ for the limit $\lambda \rightarrow 0$.

Eq. (54) breaks down for the case

$$\epsilon(\xi) \equiv \mu(\xi), \quad (55)$$

because then the first term in (52) vanishes. However, in this case it is easy to derive an exact solution for R from (11):

$$|R| = \exp\left(-\frac{4\pi}{\lambda} l \int_0^1 v(\xi) d\xi\right). \quad (56)$$

Thus, an exponential decay of $|R|$ for all values l/λ should be expected.

Eq. (52) shows that, in the general case, both effects are present simultaneously. The qualitative course of $|R|$ with increasing l/λ can thus be described as follows. The reflection factor $|R|$ shows damped oscillations around a decreasing average value. The decrease of the average level is determined by the combination of an inverse power term and an exponential term in l/λ . This also can be seen by plotting some of the numerical curves of Section IV on a double or semi-logarithmic scale. In neither of the two cases straight lines are obtained. Moreover, (52) shows that by increasing one type of material losses the oscillatory term can be damped out faster with increasing l/λ . However, at the same time the average level represented by the inverse power term is raised. Therefore, a compromise in choosing material losses is necessary according to the selected performance criterion for the absorber. The numerical solutions in Section IV shall illustrate these statements.

In the case of ohmic conductivity losses (54) is not valid either. This can be seen from (52). Assuming $\mu(\xi) = 1$, the argument of the cotan-function can be approximated for very high frequencies:

$$kl \cdot \int_0^1 \sqrt{\epsilon'(\xi) - j \frac{\sigma(\xi)}{\omega \epsilon_0}} d\xi \simeq \frac{\omega}{c} l \cdot \int_0^1 \sqrt{\epsilon'(\xi)} d\xi - j \frac{l}{2c\epsilon_0} \int_0^1 \frac{\sigma(\xi)}{\sqrt{\epsilon'(\xi)}} d\xi. \quad (57)$$

The impedance values of the function $-j \cdot \cotan(kl \int_0^1 \sqrt{\epsilon} d\xi)$ are located on a closed limit-curve ($\omega \rightarrow \infty$) around the point $+1$, which is determined by the finite imaginary part in (57). Since the real part in (57) increases with ω , rotations along this limiting curve continue with increasing l/λ . The reflection factor, according to the cotan-term in (52), does not approach zero, but shows fluctuations between two finite values which are determined by the distance from the limiting-curve to the point $+1$. For these considerations see also the papers of Lenz and Zinke.^{19,20}

IV. NUMERICAL SOLUTIONS OF $|R|$ FOR ABSORBERS WITH EXPONENTIALLY VARYING MATERIAL CONSTANTS

In this section some numerical solutions for the absolute amount r of the reflection factor of gradual-transition absorbers shall be reported. These solutions have been calculated from the differential equation (11) by means of a Bendix analog computer. Some check solutions on an IBM 650 digital computer have been computed also. The accuracy of the calculations is estimated to be $\Delta r = \pm 1$ per cent.

Lenz²⁰ carried out many analog measurements on electrical models of gradual-transition absorbers, in order to determine optimum functions for the variation of the material constants within the layer. In these measurements ohmic conductivity losses were studied, the real part of the dielectric constant being unity. A short circuit termination of the layer was assumed. In the investigations of Lenz, layers with exponentially varying conductivity losses show a favorable result. The condition $r < 10$ per cent can be satisfied for all $l/\lambda \geq 0.35$. Layers with three sections of piece-wise constant conductivity even show a slightly better result: $r \leq 10$ per cent for all $l/\lambda \geq 0.33$. Numerical calculations of Sampson¹¹ on some highly refractive dielectric panels also show some advantages for exponentially varying material constants.

For these reasons we choose exponential functions to describe the variations of material constants in the numerical solutions. For the first part of the calculations [Figs. 10 through 18(b), pp. 618–619] we consider "simple" cases according to Table I, for which either $f(x) = 1$ or $g(x) = 1$ in (11). As an example the functions $s(x)$ and $t(x)$ and the boundary conditions for $R(x)$ at $x=0$ are specified in Figs. 10 through 18(b). The physical interpretation of the results for either electromagnetic or acoustic waves can be accomplished easily by means of Table I and the analogy given in Section II-C, including the principle of duality. We consider the general form of

¹⁹ K. L. Lenz and O. Zinke, "Die Absorption elektromagnetischer Wellen in Absorbern und Leitungen mit abschnittsweise homogenem Leitwertbelag," *Z. angew. Phys.*, vol. 9, pp. 481–489; October, 1957.

²⁰ K. L. Lenz, "Leitungen mit ortsabhängiger Dämpfung zur reflexionsarmen Absorption elektromagnetischer Wellen," *Z. angew. Phys.*, vol. 10, pp. 17–25; January, 1958.

functions $g(x) = s(x) - j \cdot t(x)$:

$$s(x) = a^{(1-x/l)} \quad (58)$$

$$t(x) = b^{(1-x/l)} - d. \quad (59)$$

A more special form of equation (59) is also used throughout the computations:

$$t(x) = c[a^{(1-x/l)} - 1] = c[s(x) - 1]. \quad (60)$$

The coordinate system of Fig. 1 is used here. The real part of $g(x)$ increases from a value $s(l) = 1$ at the front surface $x = l$ to a maximum value $s(0) = a$ at the terminating wall $x = 0$. The loss part $t(x)$ may have an initial step at $x = l$, if $d \neq 1$ in (59).

In Fig. 10 two solutions are plotted for comparison. The solid line represents the electromagnetic case of conductivity losses ($t \sim 1/\omega$) with a short-circuit termination. The dashed line corresponds to frequency independent losses. The differences between the two cases for small l/λ have been discussed in Section III-B, 2); also compare Fig. 7. The solid curve in Fig. 10 is very close to an example given by Lenz.²⁰ The l/λ cutoff values for $r \leq 10$ per cent are located between 0.35 and 0.40.

The solutions in Fig. 11 are to illustrate the electromagnetic case of a conductive layer with an open-circuit termination; compare Fig. 7, curve 4. The difficulties in realizing this case physically have been mentioned in Section III-B, 2). The curves in Fig. 11 start with finite r values for $l/\lambda = 0$. Reflection factors below 10 per cent are not accomplished over a wide l/λ range for low frequencies. For low conductivities (solid line in Fig. 11), a fairly good impedance match can be achieved for $l/\lambda = 0$; however, the attenuation for higher frequencies is insufficient (57). Therefore, the reflection factor increases with l/λ . Increasing the conductivity (dotted line in Fig. 11) lowers the reflection factor for higher frequencies; however, a severe mismatch is caused for small l/λ values.

Another interesting possibility of combining the principles of the Salisbury screen and the gradual-transition absorber has been pointed out by Deutsch and Thust.²¹ These authors suggest placing a resistive foil in front of a gradual-transition absorber in order to extend the low-frequency absorption range by means of a resonance effect. Kurtze²² was able to improve the low-frequency response of porous sound absorbers (wedge-type) by providing an air space between the wedges and the terminating wall.

In order to study the effect of highly refractive panels for the construction of gradual-transition absorbers, several numerical solutions of r have been calculated. These are shown as a function of the ratio l/λ in Figs. 12(a) through 18(b). Frequency independent material

constants are assumed. The maximum values of $s(x)$ vary from 1 in Fig. 12 to 100 in Fig. 18. The parts (a) of Figs. 12 through 18 satisfy the boundary condition $R(0) = -1$. This case can be realized with electric losses and a short-circuit termination for electromagnetic waves. For parts (b) of Figs. 12 through 18 the boundary condition reads $R(0) = +1$. An example for waterborne sound waves can be realized with compressibility losses in front of a rigid wall. Some numerical solutions for this case have been reported by Miller,¹⁰ describing linear transitions in material constants and other functions.

The results in Figs. 12(a) through 18(b) show that the smallest l/λ value for which $r \leq 10$ per cent is accomplished for the optimum case of Fig. 12(a) with $s(x) = 1$ (see also Lenz²⁰). For highly refractive panels (Figs. 16 through 18) oscillations due to multiple reflections are observed. The "wavelength" of these oscillations decreases with increasing $s(x)$, as we would expect. Narrow-band resonance absorption for some points can be accomplished. However, judged from the $r \leq 10$ per cent criterion, these curves look inferior to the result of Fig. 12(a). The general behavior of these curves has been discussed in detail in Section III-C of this paper. If only one loss mechanism is present [$f(x) = 1$ in Figs. 12(a) through 18(b)], increasing the losses does not improve the performance of the absorber. The oscillations are damped out by this method, but the "average" level is raised at the same time (52).

An improvement in the performance of highly refractive panels can be achieved if two types of losses are present simultaneously (for instance, electric and magnetic losses). The difficulties for realizing the desired condition $f(x) = g(x)$ in absorber design for electromagnetic and acoustic waves are mentioned in the literature.^{1,23} Pottel²³ points out some possibilities of realizing the condition $\epsilon = \mu$ for some anisotropic media in the microwave range. In artificial dielectric media both electric and magnetic losses are present simultaneously, although generally $|\epsilon| \gg |\mu|$ in the microwave range.^{1,23-25} Porous materials for absorption of sound waves in air (for instance fiberglass) show high friction losses and a small component of compressibility losses.²⁶ Plastic materials are used in underwater sound absorption. Complex compressibilities and densities of the materials can be adjusted in wide ranges by either introducing cavities filled with different lossy materials or by loading the material with heavy, rigid obstacles, for instance metal disks, etc.^{1,3,10,17,18}

²³ R. Pottel, "Absorption elektromagnetischer Zentimeterwellen in künstlich anisotropen Medien," *Z. angew. Phys.*, vol. 10, pp. 8-16; January, 1958.

²⁴ J. M. Kelly, J. O. Stenoi, and D. E. Isbell, "Waveguide measurements in the microwave region on metal powders suspended in paraffin wax," *J. Appl. Phys.*, vol. 24, pp. 258-261; March, 1953.

²⁵ E. Meyer, H. J. Schmitt, and H. Severin, "Dielektrizitätskonstante und Permeabilität künstlicher Dielektrika bei 3 cm Wellenlänge," *Z. angew. Phys.*, vol. 8, pp. 257-263; June, 1956.

²⁶ C. W. Kosten, "Behaviour of absorbing materials," in "Technical Aspects of Sound," E. G. Richardson, ed., Elsevier Publishing Co., New York, N. Y., vol. 1, ch. 4, pp. 49-104; 1953.

²¹ J. Deutsch and P. Thust, "Breitbandabsorber für elektromagnetische Wellen," *Z. angew. Phys.*, vol. 11, pp. 453-455; December, 1959.

²² G. Kurtze, "Untersuchungen zur Verbesserung der Auskleidung schallgedämpfter Räume," *Acustica*, vol. 2, Beiheft 2, pp. AB 104-AB 107; 1952.

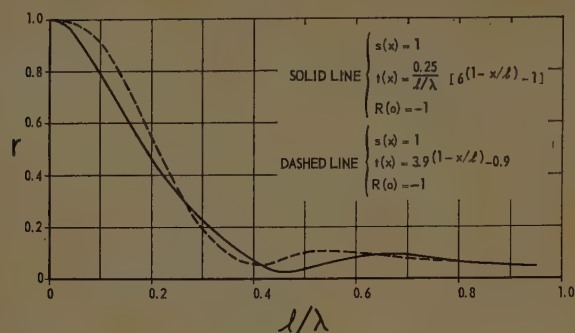


Fig. 10—Reflection factor r for layers with electric losses and short-circuit termination.

Solid line: ohmic conductivity losses with $t \sim \omega^{-1}$.
Dashed line: frequency independent electric losses.

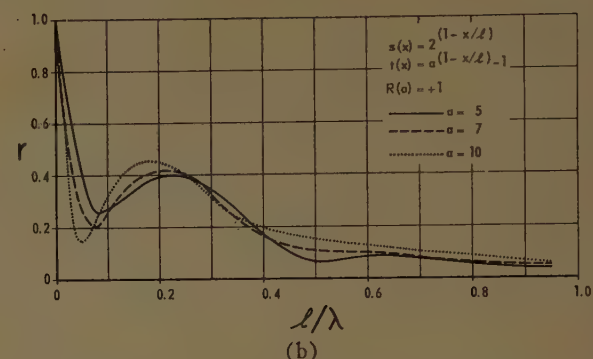
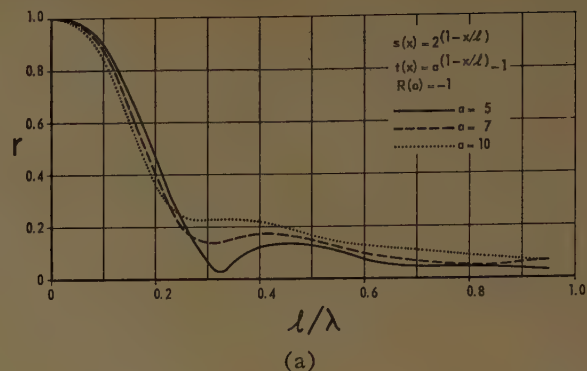


Fig. 13—Reflection factor r for layers with one type of frequency independent losses: $g(x) = s(x) - j \cdot t(x)$; $f(x) \equiv 1$. (a) Boundary condition $R(0) = -1$. (b) Boundary condition $R(0) = +1$.

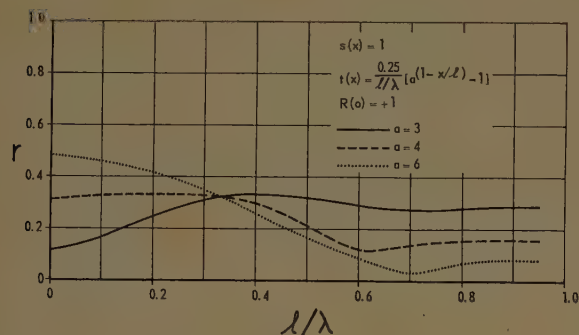


Fig. 11—Reflection factor r for layers with ohmic conductivity losses and open circuit termination.

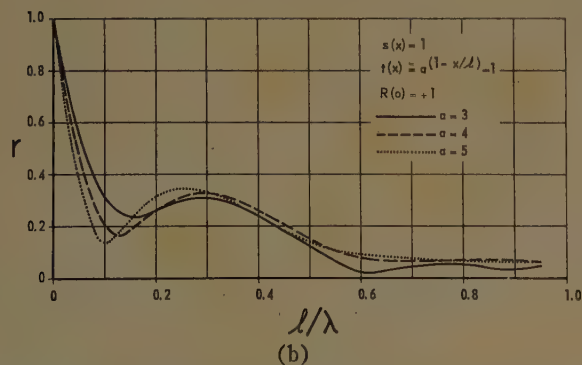
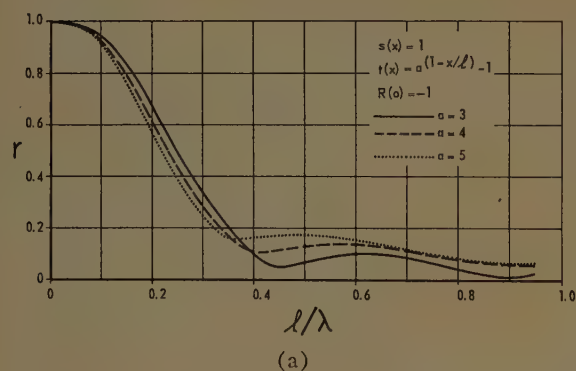


Fig. 12—Reflection factor r for layers with one type of frequency independent losses: $g(x) = s(x) - j \cdot t(x)$; $f(x) \equiv 1$. (a) Boundary condition $R(0) = -1$. (b) Boundary condition $R(0) = +1$.

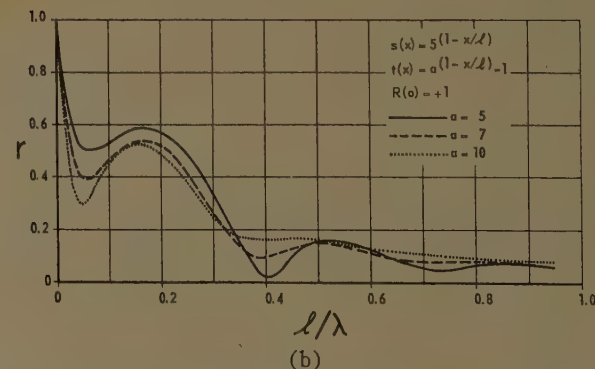
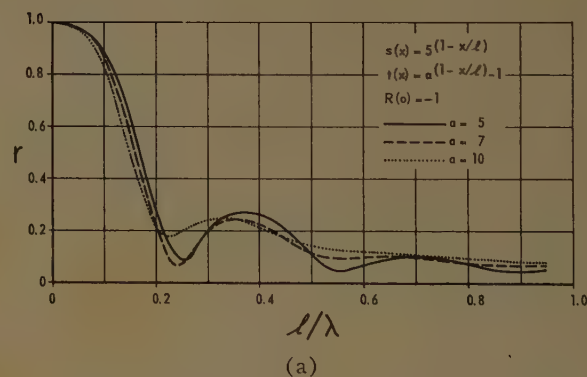


Fig. 14—Reflection factor r for layers with one type of frequency independent losses: $g(x) = s(x) - j \cdot t(x)$; $f(x) \equiv 1$. (a) Boundary condition $R(0) = -1$. (b) Boundary condition $R(0) = +1$.

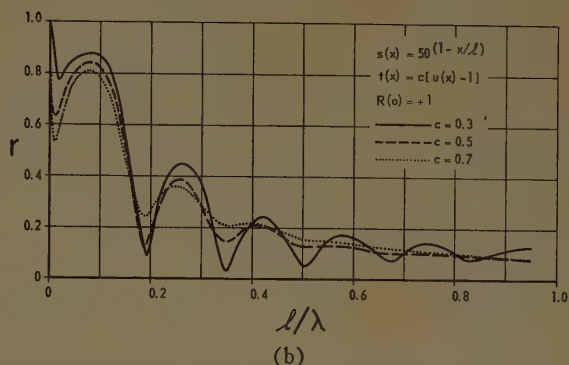
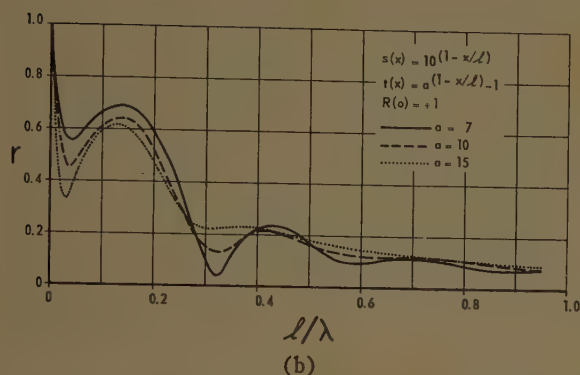
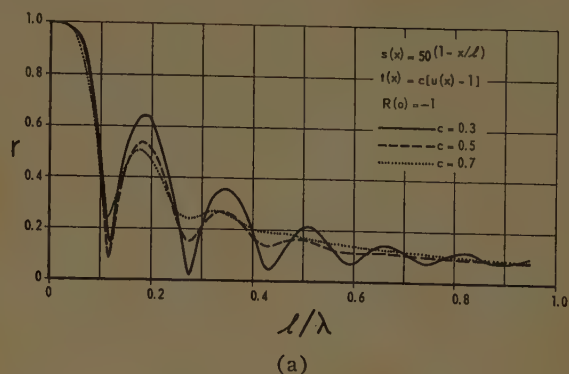
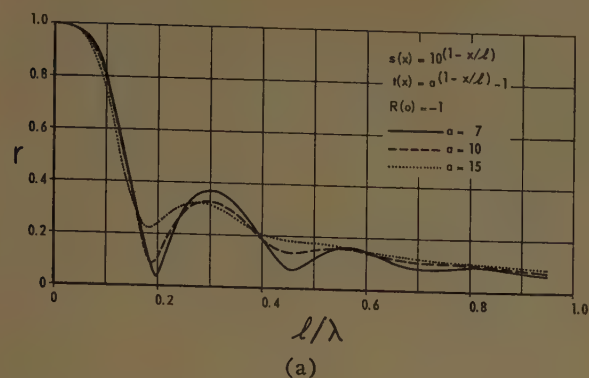


Fig. 15—Reflection factor r for layers with *one* type of frequency independent losses: $g(x) = s(x) - j \cdot t(x)$; $f(x) \equiv 1$. (a) Boundary condition $R(0) = -1$. (b) Boundary condition $R(0) = +1$.

Fig. 17—Reflection factor r for layers with *one* type of frequency independent losses: $g(x) = s(x) - j \cdot t(x)$; $f(x) \equiv 1$. (a) Boundary condition $R(0) = -1$. (b) Boundary condition $R(0) = +1$.

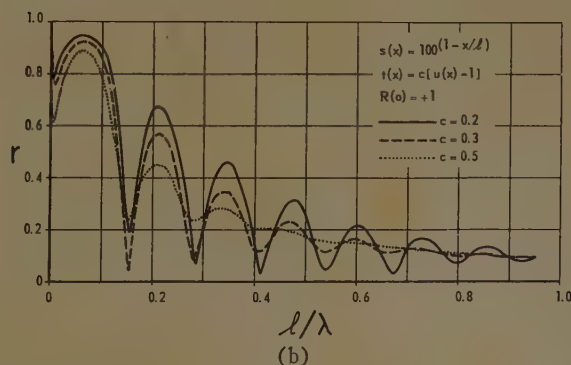
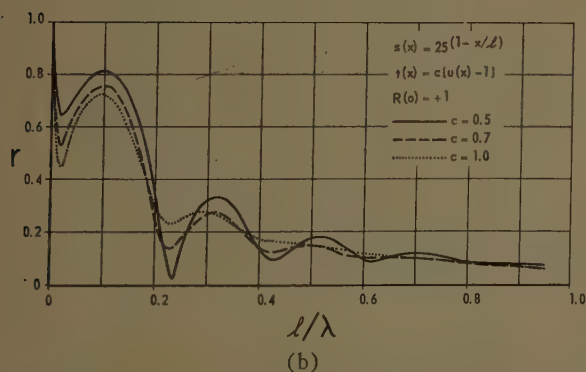
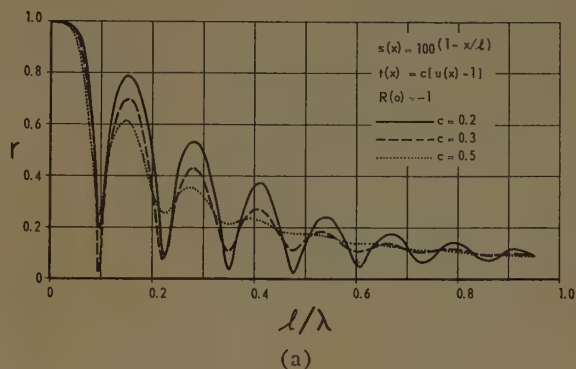
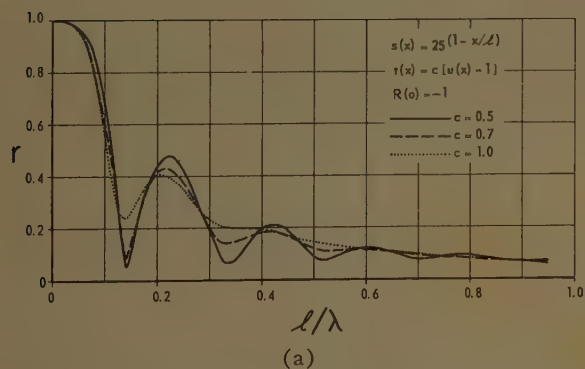


Fig. 16—Reflection factor r for layers with *one* type of frequency independent losses: $g(x) = s(x) - j \cdot t(x)$; $f(x) \equiv 1$. (a) Boundary condition $R(0) = -1$. (b) Boundary condition $R(0) = +1$.

Fig. 18—Reflection factor r for layers with *one* type of frequency independent losses: $g(x) = s(x) - j \cdot t(x)$; $f(x) \equiv 1$. (a) Boundary condition $R(0) = -1$. (b) Boundary condition $R(0) = +1$.

These examples illustrate that generally two types of losses can be realized simultaneously. However, either a condition $|f| \gg |g|$ or $|f| \ll |g|$ may prevail. Figs. 19(a) and 19(b) show that even under such conditions a considerable improvement in the performance of highly refractive panels can be achieved. For the microwave case, Fig. 19(a) may represent a panel with high real part of dielectric constant $s(0) = \epsilon'(0) = 50$ and a small real part $u(0) = \mu'(0) = 3.3$ in permeability. It can be seen that for increasing magnetic losses $v(x)$ the typical oscillations of Fig. 18 are damped out very rapidly. At the same time, the "average" level is lowered, since the tendency is to approach the condition $f(x) = g(x)$ in this case. Measurements of Pottel²³ on mixtures of paraffin and carbonyl iron powder at frequencies around 4 kmc show that the material constants of Fig. 19(a) can be realized approximately. It should be mentioned that for the calculations in Figs. 19(a) and 19(b) the material constants are assumed to be independent of frequency. In such artificial dielectrics, however, the magnetic losses vary with frequency according to a magnetic relaxation process.²⁷

According to the criterion $r \leq 10$ per cent, the curves in Figs. 19(a) and 19(b) do not show advantages as compared to the results of Lenz²⁰ (see Fig. 10). If, however, somewhat higher reflection factors can be tolerated, for instance $r \leq 20$ per cent, the case of highly refractive panels in Fig. 19 shows a definite improvement over the case $s(x) = 1$ (Fig. 10).

Experimental results for the reflection factor of gradual-transition absorbers show that, in practice, smaller l/λ cutoff values for $r \leq 10$ per cent can be obtained than those predicted from theory. For wedge-type porous sound absorbers the condition $r \leq 10$ per cent can be realized for $l/\lambda \gtrsim 0.2$ or even slightly smaller values.^{22, 28} For commercially available microwave absorbers a similar situation prevails. Measurements by Haddenhorst²⁹ on dielectric wedge structures show that for lossless dielectrics with moderate ϵ' values a wedge structure can be adequately described by the theory of an equivalent inhomogeneous layer. We feel, however, that the one-dimensional theory of inhomogeneous layers is not completely satisfactory for describing the performance of highly absorbent wedge or pyramid structures. For these cases the exact two- or three-dimensional boundary value problems have to be solved in order to get a better agreement with the experimental results.

²⁷ L. Lewin, "The electrical constants of a material loaded with spherical particles," *J. IEE*, pt. III, vol. 94, pp. 65-68; January, 1947.

²⁸ L. Z. Pronenko and A. N. Rivin, "Absorbent linings of glass staple fibre for an acoustic test chamber," *Soviet Phys. Acoustics*, vol. 5, pp. 387-388; February, 1960.

²⁹ H. G. Haddenhorst, "Durchgang von elektromagnetischen Wellen durch inhomogene Schichten," *Z. angew. Phys.*, vol. 7, pp. 487-496; October, 1955.

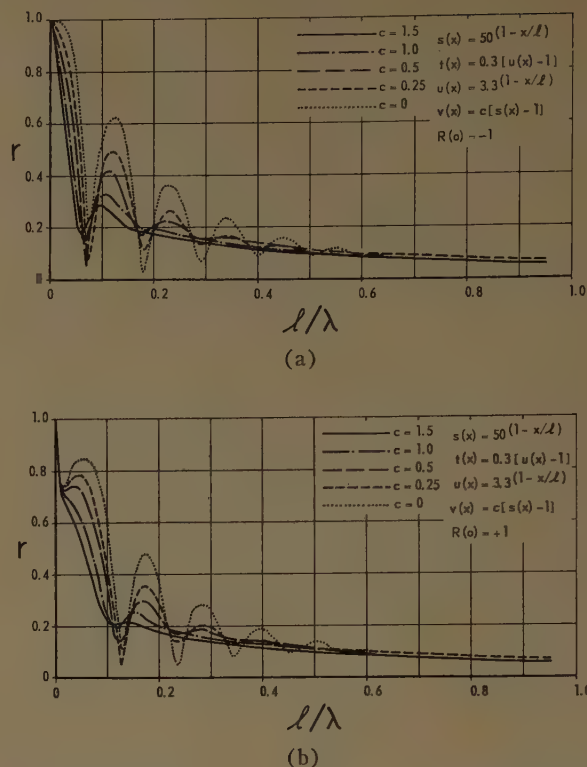


Fig. 19—Reflection factor r for layers with two types of frequency independent losses: $g(x) = s(x) - j \cdot t(x)$; $f(x) = u(x) - j \cdot v(x)$; $|f(x)| \ll |g(x)|$. (a) Boundary condition $R(0) = -1$. (b) Boundary condition $R(0) = +1$.

LIST OF SYMBOLS³⁰

- l = thickness of absorbing layer.
- x, y, z = rectangular coordinates.
- ξ = normalized length coordinate.
- λ = wavelength in free propagation medium.
- $k = 2\pi/\lambda$ = wave number.
- ω = angular frequency.
- $\Omega = (\omega/c)l$ = normalized frequency.
- $c = \omega/k$ = phase velocity in free propagation medium.
- $w_v(\xi) (v = 1, 2, 3)$ = weighting functions for thin absorbers.
- $E(x)$ = electric field strength.
- $H(x)$ = magnetic field strength.
- $\epsilon(x) = \epsilon'(x) - j\epsilon''(x)$ = relative dielectric constant.
- $\mu(x) = \mu'(x) - j\mu''(x)$ = relative permeability.
- ϵ_0 = absolute dielectric constant of free space.
- μ_0 = absolute permeability of free space.
- $Z_0 = \sqrt{\mu_0/\epsilon_0}$ = electric wave impedance of free space.

³⁰ Further symbols, which are used less frequently, are explained in the text.

$P(x)$ = sound pressure.

$V(x)$ = particle velocity.

$\kappa(x) = \kappa'(x) - j\kappa''(x)$ = relative compressibility.

$\rho(x) = \rho'(x) - j\rho''(x)$ = relative density.

κ_0 = absolute compressibility
 ρ_0 = absolute density

} of homogeneous medium.

$Z = \sqrt{\rho_0/\kappa_0}$ = acoustic wave impedance of homogeneous medium.

$Z(x)$ = general wave impedance.

$R(x)$ = "Redheffer"-reflection factor.

$R_s(x)$ = "Schelkunoff"-reflection factor.

$r(x) = |R(x)|$ = absolute amount of reflection factor.

$f(x) = u(x) - jv(x)$
 $g(x) = s(x) - jt(x)$

} loss functions in absorbing material.

Y_i/Y_o = normalized input admittance.

Z_i/Z_o = normalized input impedance.

σ = ohmic conductivity.

R_{\square} = area-resistance.

$Y_{\square} = R_{\square}^{-1}$ = area-conductance.

"e" as a subscript = refers to the electromagnetic case.

"a" as a subscript = refers to the acoustic case.

ACKNOWLEDGMENT

Stimulating discussions with Dr. W. E. Kock and E. J. McGlinn on the general subject are appreciated. Assistance in numerical calculations was given by R. E. Lord and J. M. Patterson, supervisors of the Bendix Analog and Digital Computer Facility. The author especially wishes to acknowledge the cooperation of Mrs. P. A. Jacoby, who carried out most of the numerical runs on the Bendix analog computer.

A New Sporadic Layer Providing VLF Propagation*

J. ORTNER, A. EGELAND, AND B. HULTQVIST†

Summary—During two periods in May and July, 1959, following strong solar flares, the signal strength of receptions at Kiruna of VLF transmissions from Rugby (16 kc) showed no or only slight diurnal variation. It is proposed that the change of the diurnal variation is due to the production by solar protons of an ionized layer very deep in the atmosphere, the electron density of which is sufficient for reflection of very long waves but too low to cause measurable nondeviative absorption in the HF band at geomagnetic latitudes lower than approximately 60° .

INTRODUCTION

SOLAR flares are known to influence VLF propagation in several ways. One of the most spectacular effects of the ultraviolet radiation emitted by such flares is the "sudden phase anomaly" of VLF transmissions, first reported by Budden and Ratcliffe [12], which permits good timing of the arrival of the electromagnetic radiation upon the day side of the earth. The sudden ionospheric disturbance usually does not produce any appreciable change of amplitude on very low frequencies, at least over distances shorter than 1000 km [10], but there are indications that for waves reflected at oblique incidence, the reflection coefficient of the ionosphere is reduced during an SID for frequencies less than 10 kc [17], [9], and increased for frequencies greater than 10 kc [13].

Some of the evidence as to the effect on VLF propagation of the beams of corpuscular radiation emitted by solar flares, which produce magnetic storms, is inconclusive and in certain cases contradictory [24]. However, several workers agree that over transatlantic paths, the effect of a magnetic storm on VLF propagation is to reduce field strength at night and to increase it by day [16], [3], [4], [7]. In any case, the magnetic storm effect is not a spectacular one.

A very great effect on VLF propagation, of a kind never before observed [18], [15], was produced by the solar eruption of February 23, 1956.

Coinciding with the increase of cosmic ray intensity at about 0345 UT, a rapid diminution of the signal strength of atmospherics in the VLF and lower LF bands was observed by Aarons and Barron [1] (49 kc), Belrose, *et al.* [8] (22 kc), Ellison and Reid [15] (24 kc), Gold and Palmer [18] (27 kc), Ehmert and Revellio [14] (27 kc), and Lauter, *et al.* [25] (25, 35, and 40 kc). A similarly rapid and substantial decrease of the field strength of transmissions from Rugby (GBR, 16 kc) was found by Stoffregen [37] at Uppsala, Sweden; and an analogous phenomenon was recorded at Munich, Germany, by Schumann [34] for signals from the U. S. transmitter NSS (17.7 kc). At the same time, a sudden phase anomaly occurred in the receptions of GBR at Cambridge, England [8]. Allan, *et al.* [2] in New Zea-

* Received by the PGAP, June 30, 1960.

† Kiruna Geophys. Observatory of the Royal Swedish Academy of Science, Kiruna, Sweden.

land, and Pierce and Moritz [29] at Cambridge, Mass., observed a frequency increase of 16-kc transmissions from Rugby (GBR).

As far as we are aware, the solar eruption of February 23, 1956, is the only one for which a world-wide diminution of VLF field strengths as described above has been reported. Most of the aforementioned observers state that the anomalous propagation conditions were detectable only for a few hours, but in some cases abnormal conditions persisted throughout February 23 [8].

OBSERVATIONS AT KIRUNA, SWEDEN, OF UNUSUAL VLF PROPAGATION IN MAY AND JULY, 1959

The 16-kc transmissions from Rugby (GBR) have been monitored at Kiruna Geophysical Observatory since September, 1958, with only a few short interruptions. The geographical situation of the propagation path is shown in Fig. 1.

An American "Radio Test Set AN/URM-6B," covering the frequency range 14–250 kc, was used for the receptions. The bandwidth was about 100 cps and the sensitivity of the equipment about $1 \mu\text{v}/\text{m}$. The accuracy of the field strength measurements was 10 per cent or better at signal levels above $10 \mu\text{v}/\text{m}$. The antenna was a shielded loop, consisting of 11 turns solenoid and having a mean diameter of 75 cm. It was mounted on a tripod approximately 6 feet in height. The signal was recorded by an Esterline-Angus milliamperemeter with a paper speed of 5 inches per hour.



Fig. 1—A map of North Europe showing the VLF-propagation path between Rugby and Kiruna.

At the high northern latitude of Kiruna Geophysical Observatory (geographic coordinates, 67.8°N , 20.4°E ; geomagnetic coordinates, 65.3°N , 115.5°E), the diurnal variation curves for the various seasons have some special features which will be seen from Fig. 2, where some typical curves are reproduced. Thus, the well-known minima at sunrise and sunset overlap during the summer months (there are two months of midnight sun at Kiruna), resulting in a pronounced minimum around midnight in that season. The gradual changeover from two minima to one is illustrated in Fig. 3, where the average normal curves for the periods May 1–9, May 18–31, and July 1–9, 1959, are given, together with the disturbed condition curves.

No evident effects of magnetic storms have been found, and it should be mentioned that the morning and evening minima (night minimum during the summer) have been observed daily except for the few days that will be referred to below.

Following four solar flares of importance 3+, which occurred on May 10 and July 10, 14, and 16, 1959, respectively, diurnal curves quite different from the common type described above were observed. These

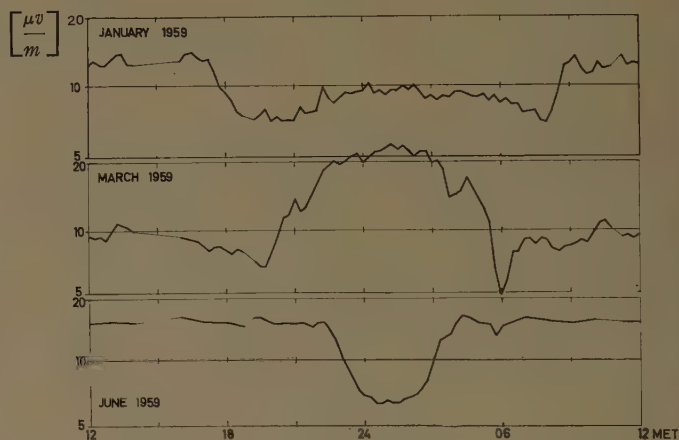


Fig. 2—Diurnal variation curves of VLF field strength for the various seasons.

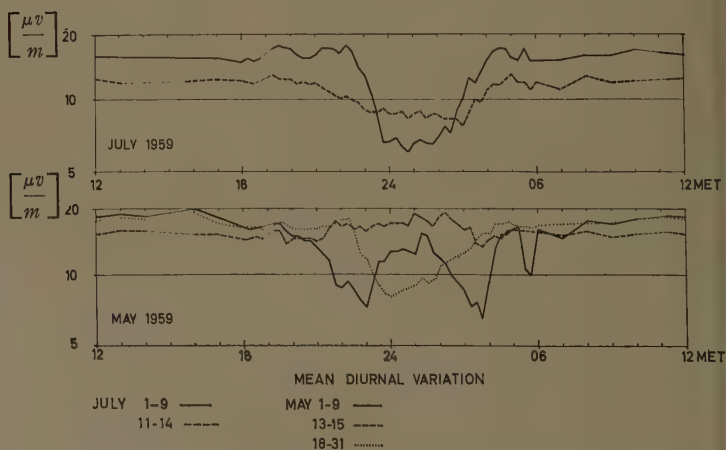


Fig. 3—Average signal-strength curves for the quiet periods May 1–9, 18–31, and July 1–9, 1959, and for the disturbed periods May 11–14 and July 13–15, 1959.

curves are reproduced in Figs. 4-6 (pp. 623-624) and should be compared with Figs. 2 and 3, showing the ordinary diurnal variation for the same periods of the year.

No sudden diminution of the field strength received within the first few hours after a solar flare outbreak, like that observed by other groups after the flare of February 23, 1956, was detected at Kiruna following the four solar eruptions that occurred in May and July, 1959. On the contrary, a very constant signal level was recorded for several days after the flares; diurnal variation was virtually absent in May and only slight in July. In particular, no minima were found at sunrise and sunset. That effect was strongest in the May period. It was already perceptible in the morning minimum of May 11, only a few hours after the flare outbreak (May 10 at 2202 MET). A morning minimum occurred on May 12, but otherwise there was no appreciable diurnal variation for the whole period May 11-17, which is the longest duration of any of the various solar flare effects observable on that occasion. The daytime signal strength was some 10 to 15 per cent lower than during the rest of the month (Fig. 3), but that level was maintained also at night. In the July period, the signal was some 20 per cent lower than normally by day. For this period a nocturnal decrease can be seen in Figs. 3 and 6, but it is much less than that for undisturbed summer conditions (Figs. 2 and 3).

The solar flare effect described here has never been reported before, as far as we are aware. A possible explanation of the absence of diurnal variation in the May period is that the propagation occurred via an ionized layer not controlled by the sun. However, some solar control must be assumed to exist in any layer in or below the lowest ionosphere, due to the occurrence of

the photo detachment reaction when the atmosphere is sunlit but not by night. The absence of diurnal variation in May and the existence of a small variation in July indicates that the electron density in the hypothetical layer was so high in May that even the lower night density—due to the lower elevation of the sun in the upper atmosphere around local midnight as compared to local noon—sufficed for total reflection; while in July, the minor nocturnal decrease of the electron density reduced the reflection coefficient slightly. It will be shown below that this hypothesis fits very well into the total picture of these solar flare effects.

SOLAR FLARES PRODUCING POLAR CAP ABSORPTION

The four flares referred to above are special not only because of their influence on the VLF propagation but also in several other respects. They belong to a category of flares which at high latitudes produce very heavy absorption of HF and VHF radio waves of very long duration, starting within a few hours after the solar flare outbreak and affecting both the day and the night side of the earth (so-called polar cap absorption).

Such absorption was first reported after the solar eruption of February 23, 1956, by several ionospheric observatories located north of 60° geomagnetic latitude [35]. An important characteristic of the phenomenon is that it is not associated with any appreciable magnetic disturbance. The polar cap absorption and related phenomena have been studied most intensively at the Radio Physics Laboratory, Defence Research Board, Ottawa, Canada [31], at the Geophysical Institute, College, Alaska [26], [32], and at Kiruna Geophysical Observatory, Sweden [19]–[23].

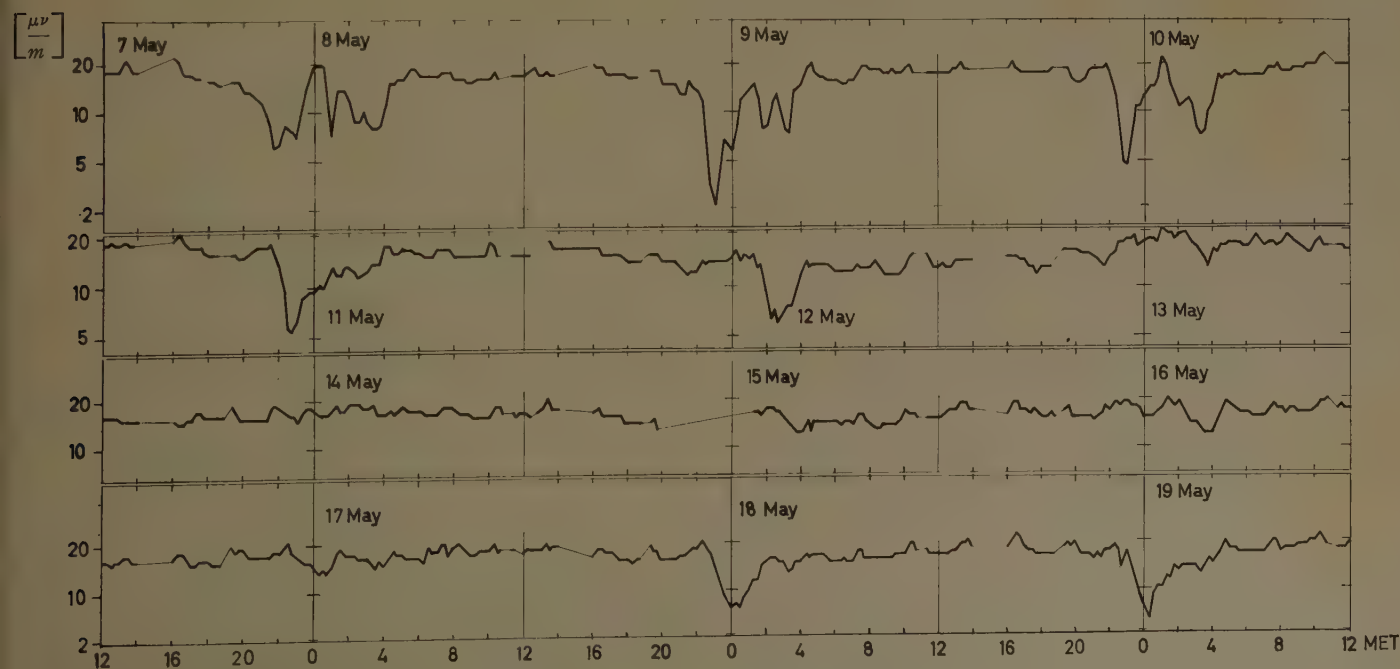


Fig. 4—Day to day variation curves of the VLF signal strength May 7-19, 1959, showing the lack of the normal morning and evening minima. The transmitter has been off between 14 and 16 MET every day.

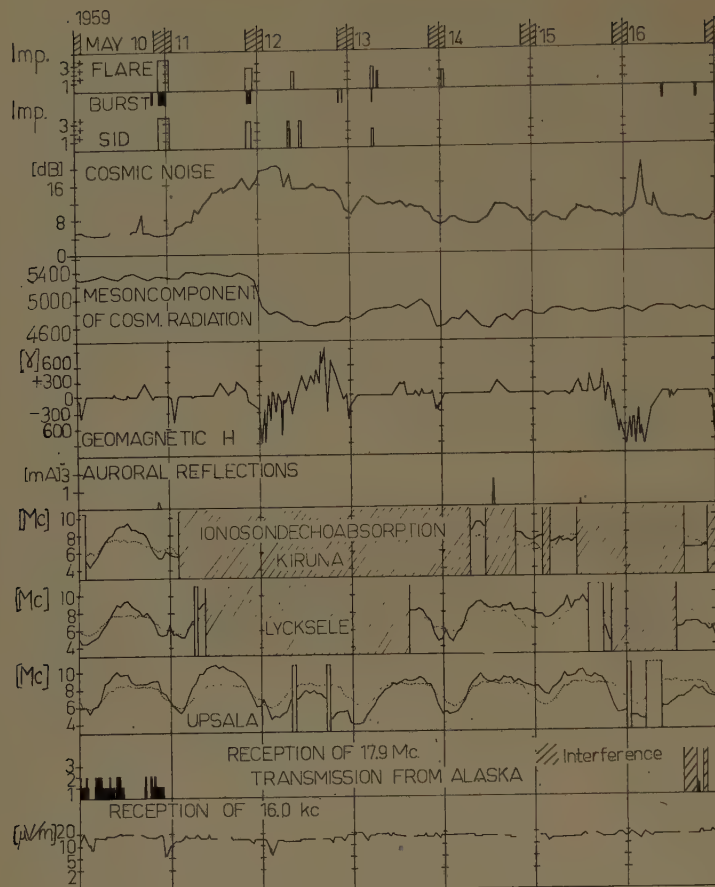


Fig. 5—Collocation of information on solar flares, SID's, and major radio bursts and of records of nine parameters, geomagnetic horizontal component at Kiruna, the critical frequencies of F_2 at Uppsala, Lycksele, and Kiruna, 27.6-Mc cosmic noise power at Kiruna, oblique auroral reflections on 92.8 Mc at Kiruna, reception of 17.9-Mc transmissions from Alaska at Kiruna, the neutron monitor component of cosmic radiation at Uppsala, and reception of 16-kc transmissions from Rugby at Kiruna.

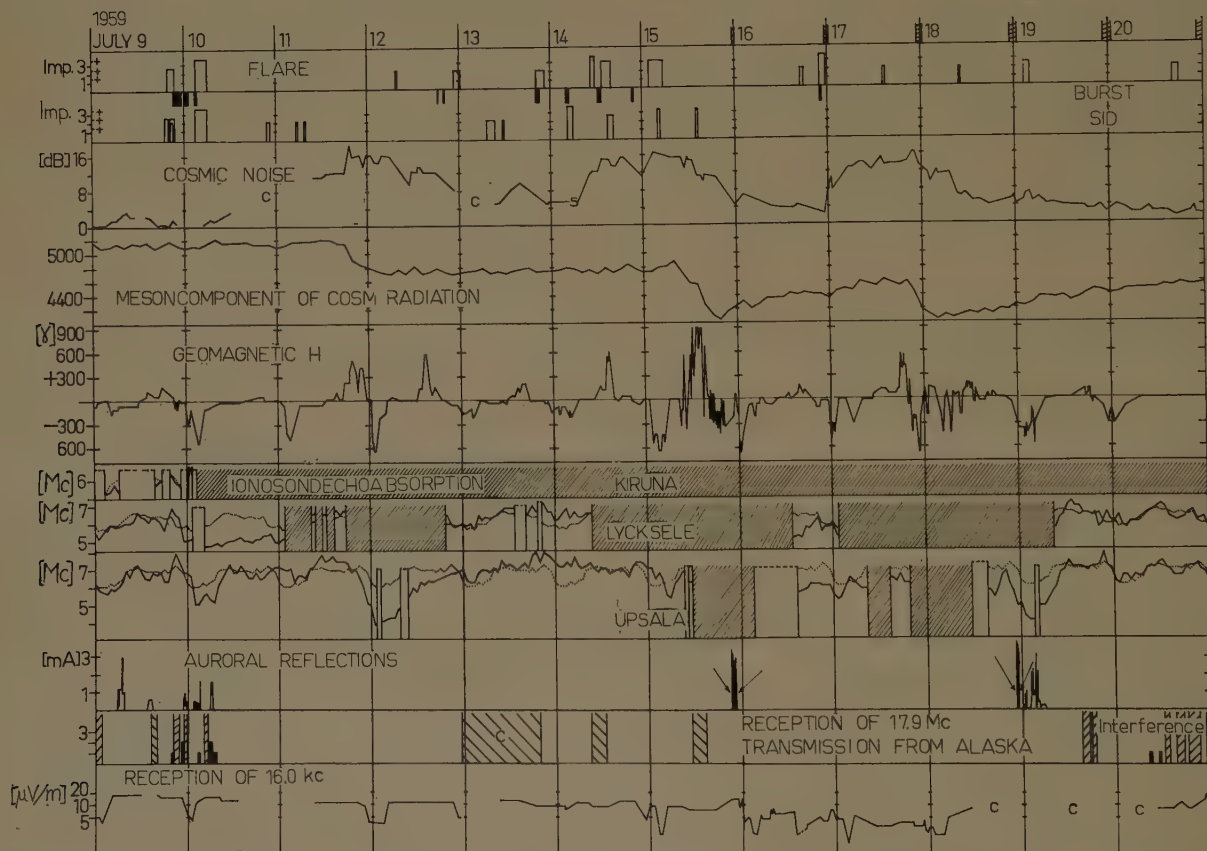


Fig. 6—Collocation of information on solar flares, SID's, and major radio bursts and of records of nine parameters, geomagnetic horizontal component at Kiruna, the critical frequencies of F_2 at Uppsala, Lycksele, and Kiruna, 27.6-Mc cosmic noise power at Kiruna, oblique auroral reflections on 92.8-Mc at Kiruna, reception of 17.9-Mc transmissions from Alaska at Kiruna, the neutron monitor component of cosmic radiation at Uppsala, and reception of 16-kc transmissions from Rugby at Kiruna. C=Instrument troubles. The arrows under "auroral reflections" indicate unusual receptions of sporadic E propagated signals. (For more details see Ortner and Egeland, *Arch. elekt. Übertragung*, pp. 420-428; October, 1959.)

From 1957 to date, some two dozen instances of polar cap absorption have been observed [32]. Continuous recording of the nondeviative ionospheric absorption at a frequency of 27.6 Mc—by means of a so-called Riometer [27]—was instituted at Kiruna Observatory in April, 1958, and during the 20 months of measurements eight definite polar cap events have occurred, on which some data are set forth in Table I.

to a number density in the proton beam of the order of 10^{-6} per cm^3 , which means that the conditions for the pure Störmer case of interaction between the proton beam and the earth's magnetic field are well fulfilled. The great depth in the atmosphere at which the protons give off most of their energy accounts for the observed absence of geomagnetic effects of the ionization [23]. The simplest way to explain the very long duration of

TABLE I
POLAR CAP ABSORPTION EVENTS AND THEIR EFFECTS ON UPPER ATMOSPHERE PARAMETERS
OBSERVED AT KIRUNA (ALL TIMES IN MET)

Date	Solar Flare					Riometer Absorption			Ionospheric Fadeout		Magnetic Storm and SC Effect on Riometer Absorption		Cosmic Ray Decrease	Unusual VHF Propagation Condition
	Imp.	Beg.	Max.	End.	Location	Approx. Start	Hours After Flare	Durat. Hours	Approx. Start	Durat. Hours	SC	+Incr. -Decr.	Start	Periods
July 7, 1958	3+	0139	0203	0424	24N 09W	0330	2	86	0800	73	8/7 0849	—	8/7 0900	8/7 1827–1934
August 16	3+	0532	0539	0710	14S 53W	0930	4	48	1400	42	17/8 0722	—	1	—
August 22	3+	1517	1606	1817	21N 08W	1730	2	74	1800	61	24/8 0240	+		—
August 26	3	0105	0127	0224	20N 54W	0300	2	65	0400	40	27/8 03xx	—		—
May 10, 1959	3+	2202	2248	0300	17N 50E	2400	2	221	11/5 0230	101.5	12/5 0018	+	11/5 2100	—
July 10	3+	0310	0340	0610	22N 70E	0500	2	504	10/7 ² 0200	270	11/7 1723	+	11/7 1600	—
July 14	3+	0442	0449	0534	16N 07E	0800	3		³		15/7 0902	no change	15/7 0900	15/7 2015–2235
July 16	3+	2218 2215	2225 2245	0020 2330	17N 30W	2300	1		³		17/7 1738	+	17/7 1700	18/7 2234–2301

¹ Cosmic ray meson telescope failures.

² Absorption due to auroral ionization accompanying geomagnetic disturbances being present already before the start of the solar flare.

³ The absorption event had not finished, when the following solar flare occurred.

Figs. 5 and 6 show records of a number of interconnected parameters taken at Kiruna Geophysical Observatory in the periods May 10–16, and July 9–20, 1959, respectively. It has been found that at Kiruna's geomagnetic latitude the absorbing layer is situated very deep in the atmosphere, with its upper boundary at a height of about 50 km [23].

All of the characteristics mentioned can be accounted for by assuming that the effects are caused by protons emitted from the sun during the solar eruption and that most of the protons have energies close to the Störmer energy for the latitude (97 mev at Kiruna). It can be shown that the necessary proton flux is a few thousand protons/ cm^2sec at Kiruna if reasonable values of the recombination coefficients are assumed, corresponding

the absorption—several days—would be to assume that a great deal of the protons in the beam become trapped in the vicinity of the earth, then leak out to the upper atmosphere over the course of a few days.

The assumption that protons of solar origin constitute the ionizing agent is supported by a few results of balloon measurements of protons at high latitudes during solar flare events producing polar cap absorption [5], [6], [28], [11].

IONIZATION SOUTH OF 60° GEOMAGNETIC LATITUDE

All determinations hitherto made by means of absorption measuring equipment indicate that the polar cap absorption is restricted to geomagnetic latitudes greater than approximately 60°. Rugby is situated,

however, at a geomagnetic latitude of 54.8°N , *i.e.*, far to the south of the layer producing appreciable absorption. At least one, and probably more, reflections must occur south of the boundary of the absorbing layer determined from absorption measurements. This conclusion is in conflict with the observed fact that no diurnal variation occurs while the absorbing layer is present. It will be shown here, however, that protons of a Störmer energy corresponding to the latitude of the transmitter can ionize the stratosphere sufficiently for reflection of VLF radiation without producing any measurable absorption.

A simplified height distribution of the absorption produced by Störmer energy protons has been calculated by Hultqvist and Ortner [23] for four different latitudes. The geomagnetic latitude nearest that of Rugby for which calculations have been made is 59.7°N . The calculations below refer to that latitude. The results differ only by some 10 or 20 per cent from those valid for Rugby's latitude, and this is of no importance here since we are interested in orders of magnitude.

For vertical radiation of 27.6 Mc at Kiruna's latitude the absorption A , measured in db, can be written

$$A = N \int_0^\infty \frac{0.459\nu N/N_0}{3.32 \cdot 10^{16} + \nu^2} dh,$$

where

$N = N(h)$ is the electron density at height h ,
 N_0 = electron density at the peak height, and
 ν = collision frequency.

In Fig. 7 of Hultqvist and Ortner [23], the integrand is given as a function of height for a proton energy of 360 mev (Störmer energy corresponding to the geomagnetic latitude 59.7°N). Electrons of the energy stated have been found to penetrate to a height of approximately 18 km if they move vertically and the effect of the geomagnetic field is ignored. In the investigation referred to above, the electron distribution produced by 360 mev protons was also calculated. Using this distribution, the following expression for the absorption can be evaluated: $A = 4.2 \cdot 10^{-4} N_0$.

For 16-kc propagation in the lower parts of the atmosphere, where the collision frequency is greater than the critical frequency—a condition that is very well fulfilled in the present case—Ratcliffe [30] has estimated the electron density necessary for reflection at 300 electrons per cm^3 . With this value for N_0 , a total absorption of 0.13 db is obtained which is not even measurable with a Riometer. The N_0 value can be increased to 2300 electrons/ cm^3 without the absorption value exceeding 1 db at 27.6 Mc.

To maintain a peak electron density of 300 per cm^3 —constant height distribution being assumed—a proton flux of only some hundred protons per cm^2 per second is required, using reasonable values of recombination coefficients in the lowest ionosphere for the estimation. This is about 1/200 of the figure necessary for production of the observed absorption at Kiruna's latitude. Such a proton flux is equivalent with a beam density of protons having the energy in question of the order of 10^{-8} protons/ cm^3 . This figure refers to a small energy interval and the total density is certainly several orders of magnitude higher, but in any case the conditions required for the existence of the pure Störmer case seem to be fulfilled as the margins are very wide [19].

The values given are valid for a geomagnetic latitude of 59.7° . The necessary proton flux and density of the proton beam will be approximately the same for 54.8° (Rugby's latitude) as can be seen from Fig. 8 of Hultqvist and Ortner [23]. At 54.8° the height of the lower boundary of the layer will be about 10 km and the minimum proton energy some 850 mev for the simple dipole approximation and a very steep energy spectrum if the particles come in vertically and the influence of the spiralling is neglected.

DISCUSSION

It is evident from the foregoing that the described change in VLF propagation is a far more sensitive indicator of low-altitude ionization than are absorption measurements.

It is interesting to note that the VLF propagation conditions are, on the average, better rather than worse during the existence of the heavily absorbing ionized layer, which interrupts radio communication over almost the whole frequency range up into the VHF band.

The VLF propagation conditions reported above lend further support to the whole picture of the effects caused by solar flare protons, as presented earlier. If, in the vicinity of Rugby, the anomalous VLF propagation is to exist without any appreciable absorption in the HF band, then the layer will have to be situated in the lower stratosphere. If the height of the point of gravity of the electron distribution were 55 km instead of, say, 15–20 km, the absorption caused by the same amount of electrons would be a factor of 50 to 100 greater, which would mean an absorption of the order of 10 db at 27.6 Mc.

All numerical values given above are based on the rough assumptions that the real lower energy limit of the protons entering a specific latitude is the Störmer energy for an undisturbed dipole field, that the radiation is virtually monochromatic and that it enters the atmosphere along vertical straight trajectories. Observations indicate that disturbances of the geomagnetic field occur [28] which permit lower energy protons to reach

the specific latitude. This certainly means that the real layers are situated somewhat higher in the atmosphere than was reported by Hultqvist and Ortner [23], although it will not influence the argumentation significantly. It should be borne in mind that the balloon observations were made after the start of the magnetic storms, *i.e.*, after the arrival of the slow dense beams, which may have a profound effect on the cutoff energies [33]. It seems highly improbable that similar effects could be caused by the high energy beams of extremely low density that produce polar cap absorption.

Balloon measurements during several of the exceptional flares in Table I have shown steep energy spectra. On August 22, 1958, Anderson, *et al.* [5], [6] found a spectrum of the form E^{-5} in northern Canada. Ney, *et al.* [28] reported an exponent of -4.8 for the event of May 12 1959, observed at Minneapolis, and Brown and d'Arcy [11] found the corresponding value to be -4.5 in July, 1959, over College, Alaska. As mentioned earlier, the observations reported in this paper indicate that the proton flux at a geomagnetic latitude of 59.7° is $1/200$ of the flux at Kiruna's latitude (65.3°) or more. This means that the energy spectrum of the proton beam before its interaction with the earth's magnetic field is less steep than has been observed at a place on the earth; the above-mentioned exponential spectra with exponents -5.0 and -4.5 would give corresponding ratios of about $1/600$ and $1/330$, respectively, for the proton flux of Störmer energy at the two latitudes. This conclusion seems plausible.

An attractive feature of the total picture of solar flare effects of the type dealt with here is that the layer produced by the protons is very sharp (see Fig. 4 of Hultqvist and Ortner [23]). Although the real layer is certainly not as distinct as that calculated by Hultqvist and Ortner [23], the height gradient of the electron density is probably very high, which is advantageous for VLF propagation. A possible explanation of the fact that propagation phenomena similar to the above were not reported in connection with the flare event of February 23, 1956, may be that the energy distribution of the incoming protons was such that the ionization produced reached down to the earth's surface, with a slight or even negative height gradient. A substantial increase of the cosmic ray intensity at the earth's surface was observed on that occasion but not in the summer of 1959. Available estimates of the energy spectrum after February 23, 1956 [36] do not support the hypothesis of a different type of spectrum at that time, but the maximal energy of the spectrum may have been higher. Only more detailed measurements when similar phenomena occur in the future can solve the problem.

Recording at a high-latitude station of the transmissions from several VLF transmitters located at dif-

ferent geomagnetic latitudes may yield valuable information as to how high up in energy the proton flux emitted by the special type of solar eruptions dealt with here exceeds some hundred 0.3 protons/cm²sec. This method of observing solar protons in an energy range not observable from the earth's surface by means of particle detectors seems to be more sensitive than any other earth surface method.

ACKNOWLEDGMENT

The authors are greatly indebted to Tage Mäkitalo and Björn Eriksson for operation of the measuring equipment, to Miss Elsy Olofsson and Miss Elisabeth Morell for assistance in reduction of the observational material and figure drawing, and to Mrs. Gunvor Wirtala for secretarial help.

BIBLIOGRAPHY

- [1] J. Aarons and W. R. Barron, "Sudden absorption of atmospherics due to increase in cosmic ray intensity," *Nature*, vol. 178, pp. 277-278; August, 1956.
- [2] A. H. Allan, D. D. Crombie, and W. A. Penton, "Long-path VLF-frequency variations associated with the solar flare of 23 February 1956," *J. Atmos. Terr. Phys.*, vol. 10, pp. 110-113; February, 1956.
- [3] C. N. Anderson, "Correlation of long wave transatlantic radio with other factors affected by solar activity," *Proc. IRE*, vol. 16, pp. 297-347; March, 1928.
- [4] C. N. Anderson, "Notes on radio transmission," *Proc. IRE*, vol. 19, pp. 1150-1165; July, 1931.
- [5] K. A. Anderson, "Ionizing radiation associated with solar radio noise storm," *Phys. Rev. Letters*, vol. 1, pp. 335-338; November, 1958.
- [6] K. A. Anderson, R. Arnoldy, R. Hoffman, L. Peterson, and I. R. Winckler, "Observations of low energy solar cosmic rays from the flare of 22 August 1958," *J. Geophys. Res.*, vol. 64, pp. 1133-1147; September, 1959.
- [7] L. W. Austin, "Solar activity and radio telegraphy," *Proc. IRE*, vol. 20, pp. 280-285; February, 1932.
- [8] J. S. Belrose, M. H. Davenport, and K. Weekes, "Some unusual radio observations made on 23 February 1956," *J. Atmos. Terr. Phys.*, vol. 8, pp. 281-286; May, 1956.
- [9] P. W. A. Bowe, "The waveforms of atmospherics and the propagation of very low frequency radio waves," *Phil. Mag.*, vol. 42, pp. 121-138; February, 1951.
- [10] R. N. Bracewell, K. G. Budden, J. A. Ratcliffe, T. W. Strickett, and M. A. Weeks, "The ionospheric propagation of low and very low frequency radio waves over distances less than 1000 km," *Proc. IEE*, pt. 3, vol. 98, pp. 221-236; May, 1951.
- [11] R. R. Brown and R. G. D'Arcy, "Observations of solar flare radiation at high latitude during the period July 10-17, 1959," *Phys. Rev. Letters*, vol. 3, pp. 390-392; October, 1959.
- [12] K. G. Budden and J. A. Ratcliffe, "An effect of catastrophic ionospheric disturbances on low frequency radio waves," *Nature*, vol. 140, pp. 1060-1061; December, 1937.
- [13] R. Bureau, "Les éruptions de la chromosphère solaire et leurs répercussions sur l'ionosphère et sur la propagation des ondes," *Onde élect.*, vol. 27, pp. 45-56; February, 1947.
- [14] A. Ehmert and K. Revellio, "Solare Ultrastrahlung und ionosphärische D-Schicht am 23 Februar 1956," *Z. Geophys.*, vol. 23, no. 3, pp. 113-134; 1957.
- [15] M. A. Ellison and J. H. Reid, "A long-wave anomaly associated with the arrival of cosmic-ray particles of solar origin on 23 February 1956," *J. Atmos. Terr. Phys.*, vol. 8, pp. 291-293; May, 1956.
- [16] L. Espenschied, C. N. Anderson, and A. Bailey, "Transatlantic radio telephone transmission," *Proc. IRE*, vol. 14, pp. 7-56; February, 1926.
- [17] F. F. Gardner, "The use of atmospherics to study the propagation of very long radio waves," *Phil. Mag.*, vol. 41, pp. 1259-1269; December, 1950.
- [18] T. Gold and D. R. Palmer, "The solar outburst, 23 February 1956," *J. Atmos. Terr. Phys.*, vol. 8, pp. 287-291; May, 1956.

- [19] B. Hultqvist, "On the interpretation of ionization in the lower ionosphere occurring on both day and night side of the earth within a few hours after some solar flares," *Tellus*, vol. 11, no. 3, pp. 332-343; 1959.
- [20] B. Hultqvist, "On lower ionosphere electron detachment- and recombination coefficients obtained from measurements of non-deviative ionospheric absorption," *Ark. Geofys.*, vol. 3, pp. 97-101; June, 1959.
- [21] B. Hultqvist, J. Aarons, and J. Ortner, "Effects of the solar flares of 7 July 1958 observed at Kiruna Geophysical Observatory, Sweden," *Tellus*, vol. 11, no. 3, pp. 319-331; 1959.
- [22] B. Hultqvist and J. Ortner, "Observations of intense ionization of long duration below 50 km altitude after some strong solar flares," *Nature*, vol. 183, pp. 1179-1180; April, 1959.
- [23] B. Hultqvist and J. Ortner, "Strongly absorbing layers below 50 km," *Planet Space Sci.*, vol. 1, pp. 193-204; August, 1959.
- [24] F. A. Kitchen, B. G. Pressey, and K. W. Tremellen, "A review of present knowledge of the ionospheric propagation of very low-, low- and medium-frequency waves," *Proc. IEE*, pt. 3, vol. 100, pp. 100-107; 1953.
- [25] E. A. Lauter, G. Bartels, K. Sprunger, and G. Skeib, "Solare Ultrastrahlung und ionosphärische D-Schicht am 23 Februar 1956," *Z. Geophys.*, vol. 23, no. 3, pp. 113-134; 1957.
- [26] H. Leinbach and G. C. Reid, "Ionization of the upper atmosphere by low energy charged particles from a solar flare," *Phys. Rev. Letters*, vol. 2, pp. 61-63; January, 1959.
- [27] C. G. Little and H. Leinbach, "The Riometer—a device for the continuous measurement of ionospheric absorption," *Proc. IRE*, vol. 47, pp. 315-319; February, 1959.
- [28] E. P. Ney, J. R. Winckler, and P. S. Freier, "Protons from the sun on May 12, 1959," *Phys. Rev. Letters*, vol. 3, pp. 183-185; August, 1959.
- [29] I. A. Pierce and E. M. Moritz, "Report on VLF Propagation Studies," Cruft Lab., Harvard University, Cambridge, Mass., Prog. Rept. 39; 1956.
- [30] J. A. Ratcliffe, "The Magneto-Ionic Theory and Its Application to the Ionosphere," Cambridge University Press, Cambridge, Eng., p. 162; 1959.
- [31] G. C. Reid and C. Collins, "Observations of abnormal VHF radio wave absorption at medium and high latitudes," *J. Atmos. Terr. Phys.*, vol. 14, pp. 63-81; April, 1959.
- [32] G. C. Reid and H. Leinbach, "Low energy cosmic ray events associated with solar flares," *J. Geophys. Res.*, vol. 64, pp. 1801-1087; November, 1959.
- [33] P. Rothwell, "Magnetic cutoff rigidities of charged particles in the earth's field at times of magnetic storms," *J. Geophys. Res.*, vol. 64, pp. 2026-2029; November, 1959.
- [34] W. O. Schumann, "Solare Ultrastrahlung und ionosphärische D-Schicht am Februar 1956," *Z. Geophys.*, vol. 23, pp. 113-134; February, 1957. See [14], p. 117.
- [35] A. H. Shapley and W. O. Roberts, "The Great Solar Regions of 9-24 February 1956 and Their Terrestrial Effects," Natl. Bur. of Standards, Washington, D. C., Rept. 5062; 1957.
- [36] J. A. Simpson, "Solar origin of changes in the primary cosmic radiation," *Proc. Natl. Acad. Sciences*, vol. 43, pp. 42-46; January, 1957.
- [37] W. Stoffregen, "Some unusual radio observations made on 23 February 1956," *J. Atmos. Terr. Phys.*, vol. 8, pp. 287-291; May, 1956. Also see [8], p. 283.

CORRECTION

J. R. Wait and A. M. Conda, whose paper, "Pattern of an Antenna on a Curved Lossy Surface," appeared on pages 348-359 in the October, 1958, issue of these TRANSACTIONS, have informed the Editor of the following corrections.

In column 2, p. 358, $(2/x)^{1/3}$ in (48) should read $(2/x)^{2/3}$, $e^{ix(\beta+2\pi m)}$ in (51) should read $e^{-ix(\beta+2\pi m)}$, and $\phi - \pi/2 + 2\pi m$ and $3\pi/2 - \phi + 2\pi m$ in (53) should read $[\phi - \pi/2 + 2\pi m]$ and $[3\pi/2 - \phi + 2\pi m]$, respectively.

communications

Gain of Tchebycheff Arrays*

ROBERT J. STEGEN†, SENIOR MEMBER, IRE

Summary—Exact expressions have been developed for the gain of a Tchebycheff array as a function of the number of elements and the sidelobe level.

A set of curves is presented showing gain as a function of the number of elements for various sidelobe levels.

INTRODUCTION

MUCH has been written to analyze Tchebycheff arrays.¹⁻³ Practically no analyses, however, have been performed to show how their gain depends upon the number of elements or sidelobe level. Brown and Sharp⁴ have computed a very comprehensive set of tables on Tchebycheff arrays. These list beamwidths, gain, current distributions and power distributions for linear broadside arrays of 3 to 40 isotropic elements and 0 thru 40 db sidelobe level. They also present an expression for the gain of a linear array having a spacing of an integral number of half wave-

lengths which may be rewritten as

$$G = \frac{\left(\sum_{k=1}^{M+1} I_k \right)^2}{\sum_{k=1}^{M+1} (I_k)^2} \quad (1)$$

where I_k = the current in the k th element from one end of the array, and $M+1$ = the number of elements.

EVALUATION OF NUMERATOR OF GAIN EXPRESSION

The following expressions for the radiated field of a Tchebycheff array are obtained from Barbieri² or Stegen³:

$$T_M(Z) = \sum_{m=1}^{(M/2)+1} I_m \cos 2(m-1)\mu \quad (2N+1 \text{ elements}) \quad (2)$$

and

$$T_M(Z) = \sum_{m=1}^{(M+1)/2} I_m \cos (2m-1)\mu, \quad (2N \text{ elements}) \quad (3)$$

where the currents I_m are numbered from the center of the array, the center current for $2N+1$ elements being $2I_1$,

$$Z = Z_0 \cos \mu, \quad (4)$$

* Received by the PGAP, June 16, 1960.

† Canoga Div., Underwood Corp., Van Nuys, Calif.

¹ C. L. Dolph, "A current distribution which optimizes the relationship between beamwidth and sidelobe level," *PROC. IRE*, vol. 34, pp. 335-348; June, 1946.

² D. Barbieri, "A method for calculating the current distribution of Tchebycheff arrays," *PROC. IRE*, vol. 40, pp. 78-82; January, 1952.

³ R. J. Stegen, "Excitation coefficients and beamwidths of Tchebycheff arrays," *PROC. IRE*, vol. 41, pp. 1671-1674; November, 1953.

⁴ L. B. Brown and G. A. Sharp, "Tchebycheff Antenna Distribution, Beamwidth and Gain Tables," Naval Ordnance Lab., Corona, Calif., Rept. No. 383; February, 1958.

and

$$\mu = \frac{\pi d}{\lambda} \sin \theta. \quad (5)$$

At the peak of the beam, $\theta=0$ and therefore, $\mu=0$, $Z=Z_0$,

$$T_M(Z_0) = \sum_{m=1}^{(M/2)+1} I_m, \quad (2N+1 \text{ elements}) \quad (6)$$

and

$$T_M(Z_0) = \sum_{m=1}^{(M+1)/2} I_m. \quad (2N \text{ elements}) \quad (7)$$

It has been shown¹ that

$$T_M(Z_0) = r = \text{the main beam to sidelobe voltage ratio.} \quad (8)$$

By inspection

$$\sum_{k=1}^{M+1} I_k = 2 \sum_{m=1}^{(M/2)+1} I_m \quad (2N+1 \text{ elements}) \quad (9)$$

$$= 2 \sum_{m=1}^{(M+1)/2} I_m. \quad (2N \text{ elements}) \quad (10)$$

Substituting (6)–(8) into (9) and (10) results in the numerator of the gain expression (1) being

$$\left(\sum_{k=1}^{M+1} I_k \right)^2 = 4r^2. \quad (11)$$

This expression is true independent of the number of elements in the array.

EVALUATION OF THE DENOMINATOR OF THE GAIN EXPRESSION

Assume an even number ($2N$) of elements. By modifying the current expression in Stegen³ we have

$$I_m = \frac{1}{N} \left[r + 2 \sum_{s=1}^{N-1} T_{2N-1} \left(Z_0 \cos \frac{s\pi}{2N} \right) \cdot \cos \frac{s\pi(2m-1)}{2N} \right], \quad (12)$$

where

$$m = 1, 2, 3, \dots, N.$$

Then

$$I_m^2 = \frac{1}{N^2} \left[r^2 + 4r \sum_{s=1}^{N-1} + 4 \left(\sum_{s=1}^{N-1} \right)^2 \right], \quad (13)$$

where the terms to be summed are obvious, and are left out for brevity.

Since there are two currents for each value of m , the sum of the squares of the currents is

$$\sum_{k=1}^{M+1} I_k^2 = \sum_{m=1}^N 2I_m^2 = \frac{2}{N^2} \left[Nr^2 + 4r \sum_{m=1}^N \left(\sum_{s=1}^{N-1} \right) + 4 \sum_{m=1}^N \left(\sum_{s=1}^{N-1} \right)^2 \right]. \quad (14)$$

The middle term in (14) contains the term

$$\sum_{m=1}^N \cos \frac{s\pi(2m-1)}{2N}, \quad (15)$$

which is identically zero, and therefore, the middle term in (14) disappears.

The third term of (14) may be written as

$$4 \sum_{s=1}^{N-1} \left[T_{2N-1} \left(Z_0 \cos \frac{s\pi}{2N} \right)^2 \sum_{m=1}^N \left[\cos \frac{s\pi(2m-1)}{2N} \right]^2 + 8 \sum_{s=1}^{N-1} T_{2N-1} \left(Z_0 \cos \frac{s\pi}{2N} \right) \times \sum_{r=s+1}^{N-1} T_{2N-1} \left(Z_0 \cos \frac{r\pi}{2N} \right) \sum_{m=1}^N \cos \frac{s\pi(2m-1)}{2N} \cos \frac{r\pi(2m-1)}{2N} \right]. \quad (16)$$

The second factor of the first term in (16) may be shown to have the value $N/2$.

The summed cosine product of the last term of (16) is zero. This third term of (14) then becomes

$$4 \sum_{s=1}^{N-1} \frac{N}{2} \left[T_{2N-1} \left(Z_0 \cos \frac{s\pi}{2N} \right) \right]^2 = 2N \sum_{s=1}^{N-1} \left[T_{2N-1} \left(Z_0 \cos \frac{s\pi}{2N} \right) \right]^2. \quad (17)$$

Substituting (17) into (14), deleting the middle term and simplifying gives the following expression for the denominator of (1):

$$\sum_{k=1}^{M+1} (I_k)^2 = \frac{2}{N} \left[r^2 + 2 \sum_{s=1}^{N-1} \left[T_{2N-1} \left(Z_0 \cos \frac{s\pi}{2N} \right) \right]^2 \right]. \quad (18)$$

RESULTANT GAIN EXPRESSIONS

Substituting (11) and (18) into (1) gives the gain of a linear Tchebycheff array of an even number of elements as

$$G = \frac{2N}{1 + \frac{2}{r^2} \sum_{s=1}^{N-1} \left[T_{2N-1} \left(Z_0 \cos \frac{s\pi}{2N} \right) \right]^2}. \quad (19)$$

A similar analysis for a Tchebycheff linear array of an odd number ($2N+1$) elements results in the following expression for the gain:

$$G = \frac{2N+1}{1 + \frac{2}{r^2} \sum_{s=1}^N \left[T_{2N} \left(Z_0 \cos \frac{2\pi}{2N+1} \right) \right]^2}. \quad (20)$$

GENERAL GAIN EXPRESSION

A general expression for the gain of an array of any number of elements ($M+1$) is, therefore,

$$G = \frac{M+1}{1 + \frac{2}{r^2} \sum_{s=1}^W \left[T_M \left(Z_0 \cos \frac{s\pi}{M+1} \right) \right]^2} \quad (21)$$

where

$$W = N \text{ for } 2N + 1 \text{ elements,}$$

and

$$W = N - 1 \text{ for } 2N \text{ elements.}$$

The calculation of the gain by this expression is as readily performed as the calculation of any one of the excitation coefficients of a Tchebycheff array.

COMPARISON TO UNIFORM LINEAR ARRAY

The gain of a linear array⁵ of $2N$ isotropic point sources equispaced, equiphased, and having a uniform current distribution, can be written as

$$G = \frac{1}{\frac{1}{2N} + \frac{1}{2N^2} \sum_{m=1}^{2N-1} (2N-m) \frac{\sin 2m \frac{\pi d}{\lambda}}{2m \frac{\pi d}{\lambda}}} \quad (22)$$

where d = spacing of the point sources.

⁵ R. M. Foster, "Directive diagrams of antennas arrays," *Bell Sys. Tech. J.*, vol. 5, pp. 292-307; April, 1926.

For $d = \lambda/2$ this expression reduces to

$$G = 2N. \quad (23)$$

Eqs. (19)–(21), therefore, show that the gain of a Tchebycheff array is less than that of a uniform array by the factor shown in their denominators which is always greater than unity.

GAIN CURVES

A plot of the gain as a function of the number of elements for Tchebycheff arrays having various sidelobe levels is shown in Fig. 1. It should be noted that this graph may also be used to determine the optimum gain to sidelobe level criterion for a given number of elements.

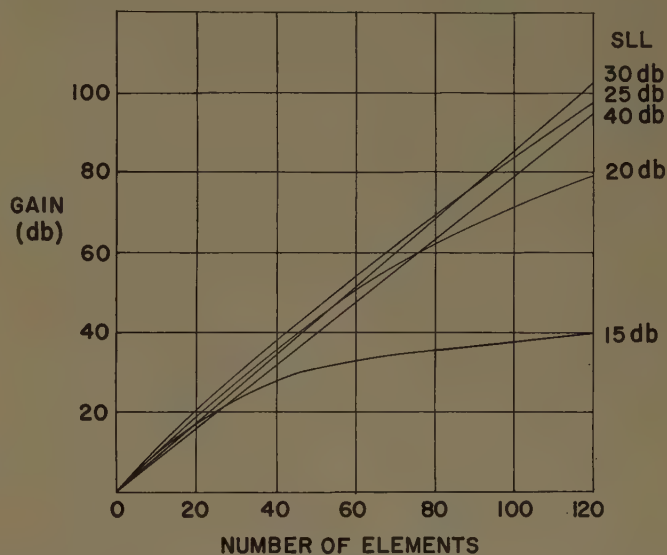


Fig. 1—Gain of $\lambda/2$ spaced linear arrays as a function of sidelobe level.

Comment on "Maximum Angular Accuracy of Tracking a Radio Star by Lobe Comparison"*

NICHOLAS GEORGE†

I HAVE READ the above timely paper by Manasse¹ with interest. It seems to me worthwhile to point out an important consequence of his equation for the optimum angular accuracy,

$$\delta_\theta = \frac{\lambda}{d_o P_s / P_n} \left(\frac{1 + P_s / P_n}{2TW} \right)^{1/2}. \quad (29)$$

While there is some discussion of the case for which $P_s/P_n > 1$, a case of more practical interest is that for which $P_s/P_n < 1$.² Furthermore, it is interesting to consider the frequency dependence of the flux from these weak sources. For nonthermal sources of cosmic radio waves, it is well known that the flux density of power displays an inverse power law; *i.e.*,

$$P_s = I_{s0} A \left(\frac{100 \times 10^6}{f} \right)^\mu, \quad (1)$$

where

A = effective area of the receiving aperture,

f = operating frequency in cps,

I_{s0} = intensity of the source in watts/m²(cps) at 100 Mc,

P_s = signal power received from the source in watts/cps,

P_n = noise power in watts/cps.

Whitfield³ has gathered data from several independent

observers and he presents plots of flux density vs frequency for several sources. He reports that a good compromise fit is obtained with this simple power law using the value $\mu = 0.8$. However, departures do exist; the mean spectrum is steeper for extragalactic sources (1.05) than for galactic ones (0.74), while that of some unidentified sources is steeper still (1.21). For this range in μ , it is seen by (29) and (1) that the angular pointing accuracy is nearly independent of the frequency, *i.e.*,

$$\delta_\theta = \frac{c P_n}{10^{8\mu} f^{1-\mu} I_{s0} A d_o \sqrt{2TW}}, \quad (2)$$

and for $\mu = 0.8$ and $c = 3 \times 10^8$ meters per second, this reduces to

$$\delta_\theta = \frac{120 P_n}{f^{0.2} I_{s0} A d_o \sqrt{2TW}}. \quad (3)$$

From (3) it is clear that the angular pointing accuracy, for the case of the weak, nonthermal source, is determined mainly by the background noise P_n , the size of the aperture as characterized by the product term $A d_o$, the observation time T , the bandwidth W , and the intensity of the source (normalized to 100 Mc). Since the pointing accuracy is nearly independent of the frequency, varying only as $1/f^{0.2}$, one is able to select an operating frequency based mainly on factors other than the desired angular accuracy, *e.g.*, the convenience of implementation, the sensitivity of P_n with frequency, etc.

The author is pleased to acknowledge a helpful discussion on this subject with G. J. Stanley of the California Institute of Technology.

* Received by the PGAP, May 19, 1960.

† Elec. Engrg. Dept., California Inst. Tech., Pasadena, Calif.

¹ R. Manasse, "Maximum angular accuracy of tracking a radio star by lobe comparison," IRE TRANS. ON ANTENNAS AND PROPAGATION, vol. AP-8, pp. 50-56; January, 1960.

² N. George, "Fundamental Limitation in the Pointing Accuracy of a Radio Telescope," Hughes Res. Labs., Malibu, Calif., SR 2, AF19(604)-5725; April, 1960.

³ G. R. Whitfield, "The spectra of radio stars," *Monthly Not. Roy. Astron. Soc.*, vol. 117, pp. 680-691; 1957.

Some Remarks on "Diffraction of Scalar Waves by a Circular Aperture"*

ALBERT E. HEINS†

THE above paper¹ requires some comment, if the earlier work upon which this paper is based is to be put in proper perspective. These authors state:

Our integral equations are most closely related to one first obtained by D. S. Jones. Although the general form of our inhomogeneous term is simpler, the kernels have fundamentally the same form. Mainly because of the simple form of the initial integral representations, our derivations of the Fredholm equations are shorter and more elementary than those of the authors mentioned above. In each of our representations, the field is related to the solution of the associated Fredholm equation by means of a single integral, and the derivation of the Fredholm equation involves only the inversion of a single convolution of the solution. In the work of Jones and of MacCamy and Heins, for example, double integrals replace the single integrals and successive convolutions replace the single convolutions. . . .

It is true that our approach depends essentially on guessing the proper form of the solution, whereas the several approaches mentioned above employ relatively familiar points of departure. It is our belief that the transparent nature of the representations and the elementary character of the subsequent analysis more than make up for this seeming defect. . . .

The situation is the following. In 1955, Jones² started with a Helmholtz representation and converted the angular integration into an integration of the convolution type with the aid of a number of integral identities involving Bessel functions. As a result of this fact, Jones produced the Fredholm integral equation which corresponds to Neumann boundary conditions on the disk. This derivation of Jones was long and required two convolutions, as Bazer and Brown state, but the fact remains that the paper of Jones indicated the integral equations and the representations some five years before Bazer and Brown.

In 1958, MacCamy and Heins,³ noting the effort of Jones to get these basic facts, re-examined the derivation and observed that there is a representation which goes back to Poisson.⁴ It states that an axially symmetric solution of the wave equation is known once it is known on the axis and is sufficiently regular (a fact which is true for the plane wave problems treated by Jones, MacCamy and Heins, and Bazer and Brown).

* Received by the PGAP, June 10, 1960.

† Dept. of Math. and Rad. Lab., University of Michigan, Ann Arbor, Mich.

¹ J. Bazer and A. Brown, IRE TRANS. ON ANTENNAS AND PROPAGATION, vol. AP-7, pp. S12-S20; December, 1959.

² D. S. Jones, "A New Method for Calculating Scattering with Particular Reference to the Circular Disk," Electromagnetic Res. Div., Inst. for Math. Sciences, New York University, N. Y., Res. Rept. EM-87; 1955. Also, *Commun. Pure Appl. Math.*, vol. 9, p. 713; 1956.

³ R. C. MacCamy and A. E. Heins, "Axially Symmetric Solutions of Elliptic Differential Equations," Carnegie Inst. of Tech., Pittsburgh, Pa., Tech. Rept. No. 41, Ord. Contract No. DA-36-061-ORD-490; November, 1958. A revised version is to appear in *Z. angew. Math. u. Phys.*

⁴ S. D. Poisson, *J. de l'Ecole Royal Polytechnique*, vol. 12, ch. 19, pp. 215-248; 1823.

With this representation of Poisson and the analytic continuation of the Helmholtz representation into the domain of complex variables, the representation which Bazer and Brown assumed can now be derived directly. The Fredholm integral may be derived by *one* convolution, and does not require successive ones, as Bazer and Brown state. Having accounted for the representation and its brief history, we may question the contribution made by this paper. The solution of such integral equations was discussed in detail by Jones, and is indeed a standard method in the theory of regular Fredholm integral equations.

Reply to A. E. Heins' Remarks⁵

We are pleased to learn that our integral representations can now be derived from the Helmholtz representation, and we look forward to reading the forthcoming revision of the report by MacCamy and Heins,³ where the derivation will presumably be given.

We were fully cognizant of Jones' contribution,² as the passage from our article quoted by Heins already clearly shows. Here, it should be noted that we treated both the first and the second boundary-value problems, whereas Jones treated only the Neumann problem for the disk.

In the passage from our paper quoted by Heins, we used the expression "Fredholm equation," not Heins' expression "Fredholm integral." Surely, he will agree that the inhomogeneous term $N_0^{-1} Mg^{-1}$ in his Fredholm integral equation (5.15)³ involves not one, but two convolutions applied to the aperture field.

Finally, we should stress that we have regarded the integral equations not as ends in themselves, but as tools which, together with our integral representations, could be employed to derive both new and old results in a simple and direct manner. For example, in the second boundary-value for the screen, for all values of ka (k and a are the wave number and aperture radius, respectively) we were able to obtain the form of the edge behavior and give a simple proof of the unique existence of the solution. In addition, we were able, with relatively little effort, to carry out the calculation for the aperture field and the far field amplitude to terms of order (ka) . These results are more accurate than any that have appeared in the literature. Similar remarks apply to the first boundary-value problem.

J. BAZER

A. BROWN

Inst. of Math. Sciences
New York University, N.Y.

⁵ Received by the PGAP, June 25, 1960.

A Concise Formulation of Huygens' Principle for the Electromagnetic Field*

CHEN TO TAI†, SENIOR MEMBER, IRE

THIS communication is to direct attention to the fact that Huygens' principle for the electromagnetic field can be stated in a concise mathematical form by using the unified electromagnetic field vector, together with the dyadic Green's function.

We consider the Maxwellian equations for a harmonically oscillating field defined in a homogeneous and isotropic medium, *i.e.*,

$$\nabla \times \vec{E} = i\omega\mu\vec{H} \quad (1)$$

$$\nabla \times \vec{H} = \vec{J} - i\omega\epsilon\vec{E} \quad (2)$$

Following Bateman¹ and Itoh,² we introduce the unified electromagnetic field vector defined by

$$\vec{F} = \vec{E} + \Gamma\vec{H} \quad (3)$$

where

$$\Gamma = \pm i(\mu/\epsilon)^{1/2} = i\hbar\eta. \quad (4)$$

The ambiguity sign ± 1 , denoted by \hbar , will be used as a separation operator similar to $\sqrt{-1}$ or i in complex number theory. We adopt the rule that $\hbar^2 = 1$. By multiplying (2) by Γ and adding it to (1) we obtain

$$\nabla \times \vec{F} = \kappa\vec{F} + \Gamma\vec{J} \quad (5)$$

where

$$\kappa = -i\omega\epsilon\Gamma = \hbar k \quad (6)$$

with $k = \omega\eta = 2\pi/\lambda$. Eqs. (1) and (2) can be recovered from (5) by separating the parts with and without \hbar . A function, such as

$$f = A + \hbar B, \quad (7)$$

therefore plays a similar role as the function $u + iv$ in complex variable theory. For convenience, we shall call A of (7) the transversal part, and B the longitudinal part.

To integrate (5), we first take the curl of that equation that yields

$$\nabla \times \nabla \times \vec{F} - k^2\vec{F} = \vec{f} \quad (8)$$

where

$$\vec{f} = \Gamma(\kappa\vec{J} + \nabla \times \vec{J}). \quad (9)$$

We introduce now the free-space dyadic Green's function³ defined by

$$\vec{G}_0 = \frac{1}{4\pi} \left(\vec{I} + \frac{1}{k^2} \nabla \nabla \right) \frac{\exp ik|\vec{r} - \vec{r}'|}{|\vec{r} - \vec{r}'|}, \quad (10)$$

which satisfies the equation

$$\nabla \times \nabla \times \vec{G}_0 - k^2\vec{G}_0 = \vec{I}\delta(\vec{r}|\vec{r}'), \quad (11)$$

where \vec{I} denotes the unit dyadic, and $\delta(\vec{r}|\vec{r}')$ the three dimensional delta function. Applying now the vector Green's identity⁴ to (8) and (11), we obtain

$$\begin{aligned} \vec{F}(\vec{r}') = \iiint_V \vec{f} \cdot \vec{G}_0 dV + \oint_S (\vec{F} \times \hat{n}) \\ \cdot (\nabla \times \vec{G}_0 + \kappa\vec{G}_0) dS. \end{aligned} \quad (12)$$

For the case that f does not exist inside V , (12) reduces to

$$\vec{F}(\vec{r}') = \oint_S (\vec{F} \times \hat{n}) \cdot (\nabla \times \vec{G}_0 + \kappa\vec{G}_0) dS. \quad (13)$$

Eq. (13) represents perhaps the most compact expression in describing Huygens' principle as applied to a harmonically oscillating electromagnetic field. By taking the transversal part and the longitudinal part of (13), one obtains, respectively, the expressions of $\vec{E}(\vec{r})$ and $\vec{H}(\vec{r})$ derivable by the conventional method. The formulation described here, of course, does not yield any new information about the Huygens' principle. It merely assembles our known knowledge in a more concise form. It is obvious that the technique outlined here can readily be extended to problems involving dyadic Green's functions which satisfy certain specific boundary conditions, such as the vector Dirichlet and the vector Neumann conditions.⁵

* Received by the PGAP, June 13, 1960. A more detailed exposition of the subject is contained in an article written in Portuguese, to be published by the Brazilian Academy of Sciences.

† Instituto Tecnológico de Aeronáutica, São José dos Campos, Brazil.

¹ H. Bateman, "Electrical and Optical Wave Motion," Dover Publications, Inc., New York, N. Y.; 1955.

² M. Itoh, "The unified electromagnetic equation and its properties in curvilinear coordinate systems," *Rev. Matem. Fis. Teor.* (Tucuman, Argentina), pp. 85-106; 1959.

³ H. Levine and J. Schwinger, "On the theory of electromagnetic wave diffraction by an aperture in an infinite plane conducting plane," *Commun. Pure and Appl. Math.*, vol. 3, pp. 355-391; December, 1955.

⁴ J. A. Stratton, "Electromagnetic Theory," McGraw-Hill Book Co., Inc., New York, N. Y., pp. 464-470; 1941.

⁵ C. T. Tai, "A Glossary of Dyadic Green's Functions," Stanford Res. Inst., Menlo Park, Calif., Tech. Rept. No. 46; 1954.

Gain of Large Scanned Arrays*

M. J. KING† AND R. K. THOMAS†, SENIOR MEMBER, IRE

LARGE electrically scanned arrays have recently become the subject of considerable interest in connection with various proposed applications. Evaluation of the system performance involves the variation of gain with scan angle, and this has generally been assumed to follow a sinusoidal law in accordance with the projected area of the aperture in the scan direction. A verification of this relationship has been established on the basis of the conventional expression for gain in terms of beamwidth.¹ This assumes that the variations in sidelobe power distribution will not produce a significant effect. The purpose of the following analysis is to remove the necessity for this assumption, and to arrive at a derivation for the gain expression which permits calculation of the limiting case of a 90° scan. According to the projected aperture relationship, the gain would be zero for this case which is, of course, not true.

The analysis, for simplicity, will be confined to the case of an aperture having equal amplitude isotropic elements located at half wave spacing. The well-known field expression arising from this model is

$$E \cong \frac{\sin u}{u} \cdot \frac{\sin v}{v}, \quad (1)$$

where

$$u = \frac{a\pi}{\lambda} (\cos \theta - \cos \theta_0), \quad (2)$$

$$v = \frac{b\pi}{\lambda} (\sin \theta \sin \phi - \sin \theta_0 \sin \phi_0). \quad (3)$$

The array is taken to lie in the x, y plane of the coordinate system shown in Fig. 1, and has dimensions b, a along the corresponding axes. Zero scan angle coincides with the z axis, or $\phi_0 = 0, \theta_0 = 90^\circ$. The gain expression is

$$G = \frac{4\pi}{D}, \quad (4)$$

where

$$D = \int_{-\pi/2}^{\pi/2} \int_0^\pi \left(\frac{\sin u}{u} \right)^2 \left(\frac{\sin v}{v} \right)^2 \sin \theta d\theta d\phi.$$

* Received by the PGAP, June 16, 1960.

† Electronic Communications, Inc., Timonium, Md.

¹ R. W. Bickmore, "A note on the effective aperture of electrically scanned arrays," IRE TRANS. ON ANTENNAS AND PROPAGATION, vol. AP-6, pp. 194-196; April, 1958.

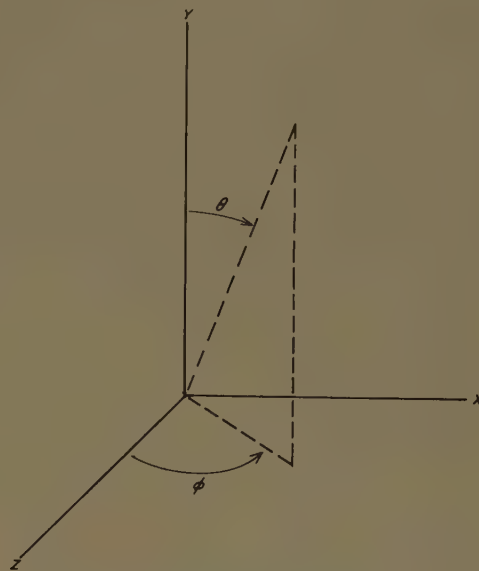


Fig. 1—Coordinate system.

The integration is confined to one hemisphere since the aperture is considered to radiate from one side only.

With no loss in generality the scan may be confined to the plane $\phi = 0$, thus simplifying the expression for v . The integral may be written as

$$D = \int_0^\pi F(\theta) \sin \theta \cdot \left(\frac{\sin u}{u} \right)^2 d\theta \quad (5)$$

where

$$\begin{aligned} F(\theta) &= \int_{-\pi/2}^{\pi/2} \left[\frac{\sin(k \sin \phi)}{k \sin \phi} \right]^2 d\phi \\ &= 2 \int_0^{\pi/2} \left[\frac{\sin(k \sin \phi)}{k \sin \phi} \right]^2 d\phi, \end{aligned}$$

$$v = k \sin \phi,$$

$$k = \frac{b\pi}{\lambda} \sin \theta.$$

We wish to examine the behavior of D where the wavelength λ is small compared to the dimensions a and b . Let us assume that $b/\lambda \gg 1$, and for the present place the restriction $\theta \neq 0$. For $\phi \neq 0$,

$$\left[\frac{\sin(k \sin \phi)}{k \sin \phi} \right]^2 \ll 1$$

and at $\phi=0$

$$\left[\frac{\sin(k \sin \phi)}{k \sin \phi} \right]^2 = 1.$$

The major contribution to the integral $F(\theta)$ occurs then for small ϕ , or

$$F(\theta) \cong 2 \int_0^{\pi/2} \left[\frac{\sin k\phi}{k\phi} \right]^2 d\phi \cong \frac{\pi}{k} = \frac{\lambda}{b \sin \theta}. \quad (6)$$

Substituting this expression into (5), we may remove the restriction $\theta \neq 0$ because the $\sin \theta$ appearing in the numerator of the integrand will cancel the $\sin \theta$ in the denominator of $F(\theta)$, even as $\theta \rightarrow 0$. D may now be written as follows:

$$D \cong \frac{\lambda}{b} \int_0^\pi \left[\frac{\sin u}{u} \right]^2 d\theta = \frac{\lambda}{b} \int_0^\pi \left\{ \frac{\sin \left[\frac{a\pi}{\lambda} (\cos \theta - \cos \theta_0) \right]}{\frac{a\pi}{\lambda} (\cos \theta - \cos \theta_0)} \right\}^2 d\theta. \quad (7)$$

Assuming $a/\lambda \gg 1$, if $\theta \neq \theta_0$,

$$\left\{ \frac{\sin \left[\frac{a\pi}{\lambda} (\cos \theta - \cos \theta_0) \right]}{\frac{a\pi}{\lambda} (\cos \theta - \cos \theta_0)} \right\}^2 = \ll 1$$

but at $\theta = \theta_0$,

$$\left\{ \frac{\sin \left[\frac{a\pi}{\lambda} (\cos \theta - \cos \theta_0) \right]}{\frac{a\pi}{\lambda} (\cos \theta - \cos \theta_0)} \right\}^2 = 1.$$

Therefore, the major contributions to this integral will be in the neighborhood of θ_0 . For $\theta - \theta_0 \ll 1$,

$$\begin{aligned} [\cos \theta - \cos \theta_0] &= -2 \sin \frac{1}{2} (\theta + \theta_0) \sin \frac{1}{2} (\theta - \theta_0) \\ &\cong -(\theta - \theta_0) \sin \frac{1}{2} (\theta + \theta_0). \end{aligned} \quad (8)$$

If θ_0 is not too small the further approximation is made that

$$[\cos \theta - \cos \theta_0] \cong -(\theta - \theta_0) \sin \theta_0.$$

Using this expression, (7) becomes

$$D \cong \frac{\lambda}{b} \int_0^\pi \left\{ \frac{\sin \left[\frac{a\pi}{\lambda} (\theta - \theta_0) \sin \theta_0 \right]}{\frac{a\pi}{\lambda} (\theta - \theta_0) \sin \theta_0} \right\}^2 d\theta. \quad (9)$$

With a change invariable, $r = a\pi/\lambda(\theta - \theta_0) \sin \theta_0$, (9) is

$$\begin{aligned} D &\cong \frac{\lambda^2}{ab\pi \sin \theta_0} \int_{-a\pi/\lambda \theta_0 \sin \theta_0}^{a\pi/\lambda \sin \theta_0 (\pi - \theta_0)} \left(\frac{\sin r}{r} \right)^2 dr \\ &\cong \frac{\lambda^2}{ab \sin \theta_0}. \end{aligned} \quad (10)$$

The expression for the gain then, for θ_0 not too small, becomes

$$G \cong \frac{4\pi ab \sin \theta_0}{\lambda^2} \quad (11)$$

in agreement with the well-known relationship for the case $\theta_0 = 90^\circ$.

As $\theta_0 \rightarrow 0$, this expression is no longer valid due to the nature of the approximation in (8). In order to consider the limiting case, we write D as follows:

$$D \cong \frac{\lambda}{b} \int_0^\pi \left\{ \frac{\sin \left[\frac{a\pi}{\lambda} (\theta - \theta_0) \sin \frac{1}{2} (\theta + \theta_0) \right]}{\frac{a\pi}{\lambda} (\theta - \theta_0) \sin \frac{1}{2} (\theta + \theta_0)} \right\}^2 d\theta. \quad (12)$$

If $\theta_0 = 0$, the major contributions to the integral will be for $\theta \ll 1$, or

$$D \cong \frac{\lambda}{b} \int_0^\pi \left\{ \frac{\sin \left(\frac{a\pi}{2\lambda} \theta^2 \right)}{\frac{a\pi}{2\lambda} \theta^2} \right\}^2 d\theta.$$

Changing the variable of integration to $w = a\pi/2\lambda\theta^2$, we may write

$$\begin{aligned} D &\cong \frac{\lambda}{b} \sqrt{\frac{\lambda}{2a\pi}} \int_0^{a\pi^{3/2}/2\lambda} \left(\frac{\sin w}{w} \right)^2 \frac{dw}{\sqrt{w}} \\ &\cong \frac{2\sqrt{2}}{3} \frac{\lambda^{3/2}}{a^{1/2}b}. \end{aligned} \quad (13)$$

Thus the gain at $\theta_0 = 0$ is approximately

$$G_0 \cong 3\pi \frac{b}{\lambda} \sqrt{\frac{2a}{\lambda}} = 13.3 \frac{b}{\lambda} \sqrt{\frac{a}{\lambda}}. \quad (14)$$

In computing gain for large scan angles (θ_0 near zero), (11) is not valid when it produces a value lower than that given by the limiting case as expressed by (14). Equating the two expressions

$$\frac{4\pi ab \sin \theta_0}{\lambda^2} = 3\pi \frac{b}{\lambda} \sqrt{\frac{2a}{\lambda}},$$

it is seen that (11) should not be used for values of θ_0 less than that defined by

$$\theta_0 \cong \sin \theta_0 = 1.06 \sqrt{\frac{\lambda}{a}}.$$

Second-Mode Operation of the Spiral Antenna*

JOHN R. DONNELLAN†

THE operation of the two-wire Archimedean spiral in the second mode (*i.e.*, the input terminals are fed in phase rather than 180° out of phase) has been described in a previous paper.¹ Currents start out in phase at the center of the spiral (but radiation is suppressed here by a microstrip line) and proceed outward along the spiral arms until—at a circumference of two wavelengths (diameter $= 2\lambda/\pi$)—the currents are again in phase and radiation occurs. This two-wavelength ring produces a null directly on-axis and an essentially omnidirectional pattern in the plane of the spiral (horizontal polarization).

Fig. 1 shows the front and rear views of such a spiral antenna which has been constructed. A type *N* con-

ductor is attached at the center, the inner conductor being connected to the strip and the outer conductor being connected to the group plane underneath. This microstrip line suppresses any radiation which would occur due to the in-phase condition at the input terminals and is continued out until the currents approach an anti-phase condition. The diameter of the spiral is six inches and the diameter of the ground plane is three inches. The experimental work was carried out at a frequency of 1300 Mc ($\lambda = 9''$, $2\lambda/\pi = 6''$), so that the radiation from the two-wavelength ring occurs at the outer portion of the spiral.

In Fig. 2 this antenna is shown fed by a coaxial cable. The solid curve of Fig. 3 shows the omnidirectional nature (within ± 1 db) of the pattern in the plane of the spiral, while the dashed curve shows the predicted null on-axis.

* Received by the PGAP, July 1, 1960.

† Microwave Antennas and Components Branch, Electronics Div., U. S. Naval Res. Lab., Washington 25, D. C.

¹ J. A. Kaiser, "The Archimedean two-wire spiral antenna," IRE TRANS. ON ANTENNAS AND PROPAGATION, vol. AP-8, pp. 312-323; May, 1960.

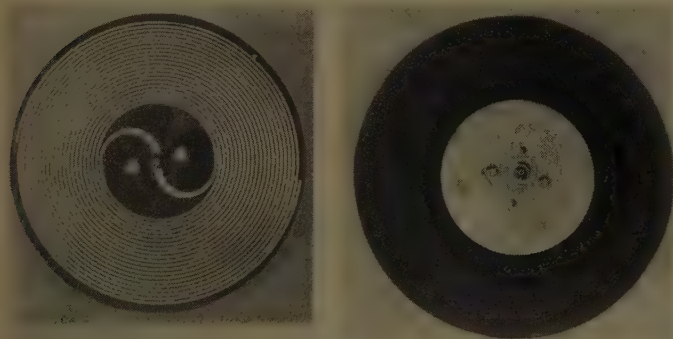


Fig. 1—Front and rear views of second-mode Archimedean spiral antenna.



Fig. 2—Second mode spiral fed at 1300 mc.

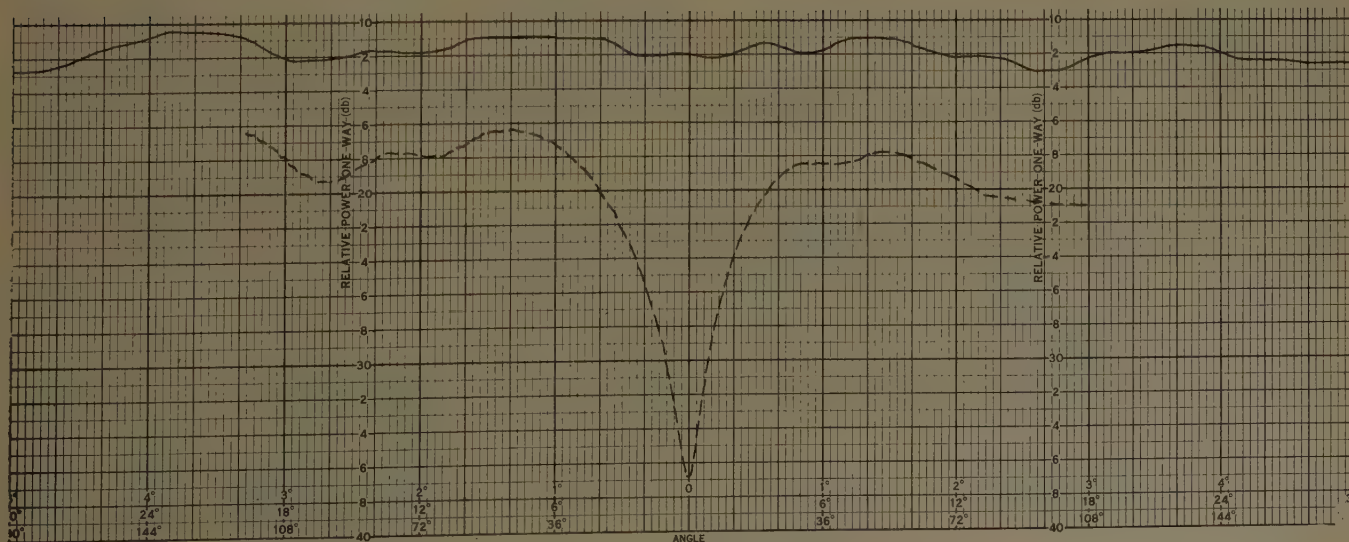


Fig. 3—Beacon pattern in the plane of the spiral (see Fig. 2) and null on-axis. —; pat. in pl. of sp. — —; axial cut.

Contributors

Saburo Adachi (S'57-M'59) was born in Yamagata-Ken, Japan, in 1930. He received the B.E., M.E., and D.E. degrees from the Tohoku University, Sendai, Japan, in 1953, 1955, and 1958, respectively. In 1958 he was appointed an instructor in the Electrical Communications Department of the Tohoku University.



S. ADACHI

From August, 1958, to January, 1960, he was on leave from Tohoku University and worked at the Ohio State University Antenna Laboratory, Columbus, as a research associate. He has been engaged in research on antennas and electromagnetic field problems.

Dr. Adachi is a member of the Institute of Electrical Engineers of Japan, the Institute of Electrical Communication Engineers of Japan, and Sigma Xi.

W. L. Anderson (M'58), for a photograph and biography please see page 531 of the September, 1960, issue of these TRANSACTIONS.

Ross L. Bell (S'57-M'58) was born in Vernon, Texas, on December 30, 1929. He attended the University of Texas, Austin, where he received the B.S. degree in 1957, and the M.S. degree in 1958, both in electrical engineering.



R. L. BELL

While attending graduate school, he worked at Balcones Research Center, the University of Texas, designing refractometers. In 1958 he joined the antenna section of Sylvania's Electronic Defense Laboratory, Mountain View, Calif., where he engaged in design work and near-field studies on log-periodic antennas. His work in this field resulted in a number of patent disclosures. In November, 1959, he joined Granger Associates in Palo Alto, Calif., where he is doing design work and feasibility studies on log-periodic antennas and communication systems.

Donald B. Brick (S'50-A'54-SM'56) was born in Brooklyn, N. Y., on October 1, 1927. He received the A.B. degree in engineering sciences and applied physics in 1950, the M.S. degree in 1951, and the Ph.D. degree in applied physics in 1954, all from Harvard University, Cambridge, Mass.

During 1954 and part of 1955, he was a research fellow at Harvard, doing research in electromagnetic scattering, antennas, and

microwaves. During this period, he was also a consultant to Trans-Sonics, Inc., and Sylvania Electric Products, Inc. Since June,



D. B. BRICK

Dr. Brick is a member of Sigma Xi, the American Physical Society, and the Harvard Engineering Society.

Jack E. Cole (A'56-M'59) was born in Waukesha, Wis., on March 17, 1930. He received the Bachelor of Science degree in electrical engineering from the University of Washington, Seattle in 1954. From 1954 to 1956, he served in the U. S. Air Force as a ground electronics officer. In 1956, he joined the Collins Radio Company at the Collins Propagation Laboratory in Tucson, Ariz., where he has been engaged in tropospheric scatter propagation studies and in the evaluation of scatter systems.



J. E. COLE

Alv Egeland was born in Kristiansand, Norway, on March 22, 1932. He received the Cand.real. degree in physics from Blindern University, Oslo, in 1959. From 1956 to 1959 he was research assistant at the Astrophysical Institute at Oslo, and was engaged in physical studies.



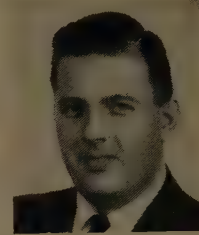
A. EGELAND

Mr. Egeland has been a member of the staff of Kiruna Geophysical Observatory since May, 1959, and has been active in the study of high-latitude radio wave propagation.

Claes T. Elfving (S'53-A'55-M'59) was born in Stockholm, Sweden, on December 18, 1930. He received the B.S. degree in electrical engineering from the University of California, Berkeley, Calif., in January, 1954.

While in school and directly following

graduation he worked with Isoflex Corporation, Burlingame, Calif., where he developed test procedures and designed and built test



C. T. ELFVING

equipment for evaluation of thermal properties of insulation materials. From 1954 to 1956, he served on active duty with the U. S. Army Signal Corps, testing and repairing field radio and aircraft communication equipment. In August, 1956, he joined the antenna section of Sylvania Electronic Defense Laboratories, Mountain View, Calif., where he has been engaged in design of antennas for electronic counter-measures systems. He is presently concerned with logarithmically periodic antenna studies.

Leopold B. Felsen (S'47-A'53-M'54-SM'55), for a photograph and biography, please see page 452 of the July, 1960, issue of these TRANSACTIONS.

Raymond E. Franks (S'49-M'57) was born in Gainesville, Texas, on August 26, 1928. He received the B.S. degree in electrical engineering from Rice Institute, Houston, Texas, in 1950.



R. E. FRANKS

From 1950 to 1957, he was with the Missiles and Ordnance Systems Division of General Electric Company in Pittsfield, Mass., engaged in the design and evaluation of fire control and search radar systems. He joined the Sylvania Electronic Defense Laboratories, Mountain View, Calif., in 1957, and has been engaged in the development of broad-band antenna systems for electronic countermeasures.

Mr. Franks is a member of Tau Beta Pi.

Bengt Hultqvist was born in Småland, Sweden, on August 21, 1927. He received the doctor's degree in physics at the University of Stockholm in 1956. From 1951 to 1956, he was a member of the staff of the Institute of Radiophysics in Stockholm. In 1956, he took over the planning and preparation for the new Kiruna Geophysical Observatory of the Royal Swedish Academy of



B. HULTQVIST

Science. Dr. Hultqvist has been the director of the new Kiruna Geophysical Observatory since its start in 1957.



Richard F. Hyneman (S'49-A'54-M'58) was born in Bloomington, Ind. on April 5, 1928. He received the B.S. degree from



R. F. HYNEMAN

Purdue University, Lafayette, Ind., in 1950, and the Ph.D. degree from the University of Illinois, Urbana, in 1957, both in electrical engineering.

From 1946 to 1948, he served in the U. S. Navy as an electronics technician. While at the University of Illinois, he received an appointment as research associate in the Antenna Laboratory, where he was engaged in studies of microwave antennas. From 1957 to April, 1959, he was employed by the Hughes Aircraft Company as a member of the technical staff of the Microwave Laboratory at Culver City, Calif. During this time, he was engaged in problems involving surface wave antennas and large radar slot arrays. He is presently head of the Microwave Studies Section in the Radar Laboratory at Hughes, Fullerton, Calif.

Dr. Hyneman is a member of Eta Kappa Nu, Tau Beta Pi, and Sigma Xi.



Alan F. Kay (M'55) was born in Newark, N. J., in 1925. He received the B.S. degree from the Massachusetts Institute of Technology, Cambridge, Mass., in 1948, and the Ph.D. degree from Harvard University, Cambridge, Mass., in 1951, both in mathematics.



A. F. KAY

Since 1951 he has worked on microwave and antenna problems. For the last seven years he has been employed by Technical Research Group (TRG Inc.) where he is now Vice President in charge of the Somerville, Mass., branch.

Dr. Kay is a member of SIAM and AMS.



William Lavrench (A'50-M'55) was born in Verigin, Saskatchewan, Canada, on November 8, 1926. He received the B.S. and M.S. degrees in engineering physics from Queen's University, Kingston, Ontario, Canada, in 1948 and 1950, respectively.



W. LAVRENCH

He joined the staff of the National Research Council of Canada in 1949, where he has worked in the Microwave

Section of the Radio and Electrical Engineering Division. His work has been concerned with waveguide components, microwave antennas, and in the past few years with the design and testing of rigid ground radomes.



R. K. Moore (SM'54), for a photograph and biography please see page 352 of the May, 1960, issue of these TRANSACTIONS.



Johannes Ortner was born in Vienna, Austria, on May 31, 1933. He received the degree as Cand. ing. in technical physics from the University of Technology, Vienna, in 1956, and received the Dr. ph. degree in geophysics and meteorology at the University of Vienna in 1960. He has been a member of the staff of Kiruna Geophysical Observatory since October, 1957, where he has been active in the



J. ORTNER

study of high-latitude radio wave propagation.

Dr. Ortner has recently begun working with rocket equipment in the investigation of the ionosphere.



Oliver R. Price (M'54-SM'59) was born in Springfield, Mo., on August 24, 1924. During World War II, he served as a pilot and flight instructor for the U. S. Navy. He received the B.S. degree in physics from California Institute of Technology, Pasadena, in 1953, and the Ph.D. degree in nuclear physics from the University of California, Los Angeles, in 1958. While on a Master's Fellowship from 1954 to 1955 he worked on high-resolution reconnaissance radar at Hughes Aircraft Company.



O. R. PRICE

From 1955 to 1958 he worked on K⁺ meson research (his Ph.D. dissertation) at the Bevatron Accelerator Laboratory, Berkeley, Calif., and at the University of California, Los Angeles. From 1956 to 1958 he also lectured in advanced calculus and physics at West Coast University, Los Angeles. Since June, 1958, he has been in the Antenna Department, Hughes Aircraft Company, Culver City, Calif. He is presently Head of the Advanced Studies Section in the Antenna Department. His recent work, which has been in pattern synthesis, data processing, and reconnaissance radar, has led to the submission of five patent disclosures.

Dr. Price is a member of American Physical Society and Sigma Xi.

Klaus Walther (M'60) was born in Norderney, Germany, on November 27, 1929. He received the degrees of Dipl. Phys.



K. WALTHER

and Dr. rer. nat. from the University of Goettingen, Germany, in 1955 and 1958, respectively. During this time he carried out research work on acoustic and microwave propagation and absorption problems. After one year as research assistant at the University of Goettingen, he joined

the Research Laboratories Division of the Bendix Corporation, Southfield, Mich., in 1959.

His present work includes research in acoustics and microwave techniques.



Lewis B. Wetzel (M'58) was born in Milwaukee, Wis. on March 19, 1925. He received the Bachelor of Science degree in physics from Northwestern University, Evanston, Ill., in 1949, and the M.A. degree in physics and the Ph.D. degree in applied physics from Harvard University, Cambridge, Mass., in 1950 and 1957, respectively.



L. B. WETZEL

From 1956 to 1959 he was a member of the technical staff of Bell Telephone Laboratories, Murray Hill, N. J., where he worked in microwave tube and parametric amplifier development. He is currently an assistant professor in the Division of Engineering at Brown University, Providence, R. I., and is engaged in research on the interaction between electromagnetic waves and plasmas.

Dr. Wetzel is a member of Phi Beta Kappa and Sigma Xi.



Kenneth F. Wright (M'57) was born in West Branch, Iowa, on January 18, 1925. He served in the Navy as an electronic technician from 1943 to 1946. In 1950, he received the Bachelor of Science degree in electrical engineering from the University of Iowa, Iowa City. He joined Collins Radio Company in 1951 as a development engineer. In 1957, Mr. Wright was assigned to the Collins propa-



K. F. WRIGHT

gation Laboratory in Tucson, Ariz., where he has been engaged in tropospheric scatter propagation studies.

IRE Transactions on Antennas and Propagation

Index to Volume AP-8, 1960

Contents

Volume AP-8, Number 1, January, 1960

Back Scattering Cross Sections of Cylindrical Wires on Finite Conductivity, <i>E. S. Cassedy and J. Fainberg</i>	1
A Multipurpose Radar Target, <i>J. W. Carr</i>	7
On Uniform and Linearly Tapered Long Yagi Antennas, <i>Dipak L. Sengupta</i>	11
Design of Circular Apertures for Narrow Beamwidth and Low Sidelobes, <i>T. T. Taylor</i>	17
Tables of Taylor Distributions for Circular Aperture Antennas, <i>R. C. Hansen</i>	23
High-Frequency Diffraction of Electromagnetic Waves by a Circular Aperture in an Infinite Plane Conducting Screen, <i>S. R. Seshadri and T. T. Wu</i>	27
High-Frequency Diffraction of Plane Waves by an Infinite Slit for Grazing Incidence, <i>S. R. Seshadri and T. T. Wu</i>	37
The Calculation of Reflector Antenna Polarized Radiation, <i>Louis E. Raburn</i>	43
Maximum Angular Accuracy of Tracking a Radio Star by Lobe Comparison, <i>Roger Manasse</i>	50
Experimental Studies of Meteor Echoes at 200 MC, <i>J. L. Heritage, S. Weisbrod, and W. J. Fay</i>	57
Scattering by an Infinite Array of Thin Dielectric Sheets, <i>Robert E. Collin</i>	62
Reciprocity Theorems for Electromagnetic Fields Whose Time Dependence Is Arbitrary, <i>W. J. Welch</i>	68
Frequency Scintillations of Satellite Signals Before and After the Argus Experiment, <i>P. R. Arendt</i>	73
Correction to "A Design Procedure for Dielectric Microwave Lenses of Large Aperture Ratio and Large Scanning Angle," <i>F. S. Holt and A. Mayer</i>	77
Antenna Image Quality Evaluation, <i>J. J. Myers</i> Part I—By an Optical Simulation Method.....	78
Part II—By a Mechanical Observer.....	83
Transmission-Line Missile Antennas, <i>Ronold King, C. W. Harrison, Jr., and D. H. Denton, Jr.</i>	88
Radiation Pattern Synthesis with Sources Located on a Conical Surface, <i>A. Ishimaru and G. Held</i>	91
A Slot with Variable Coupling and Its Application to a Linear Array, <i>Raymond Tang</i>	97
Communications:	
Theory of Equilibrium Electron and Particle Densities Behind Normal and Oblique Hypersonic Shock Waves in Air, <i>C. A. Roberts, W. B. Sisco, and J. M. Fiskin</i>	102
A Theorem Regarding the Commutation of Antenna Rotations, <i>L. P. Bolgiano, Jr.</i>	104
Radiation Fields of Circular Loop Antennas by a Direct Integration Process, <i>E. J. Martin, Jr.</i>	105
Refraction VHF Signals at Ionospheric Heights, <i>S. Weisbrod and L. Colin</i>	107
Modified Luneberg Lens for Defocused Source, <i>David K. Cheng</i>	110
Abstracts of Papers from the IRE-URSI Joint Fall Meeting Held October 19-21, 1959—San Diego, Calif.....	112
Contributors.....	123
Announcement of IRE-URSI Joint Spring Meeting.....	126
Annual Index, 1959.....	126

Volume AP-8, Number 2, March, 1960

Frontispiece.....	128
John B. Smyth, Retiring Editor.....	129
Editorial Comment.....	130
Theory of Coupled Folded Antennas, <i>C. W. Harrison, Jr. and Ronald King</i>	131
The Slot Antenna with Coupled Dipoles, <i>R. W. P. King and G. H. Owyang</i>	136
Radiation Patterns of Finite-Size Corner-Reflector Antennas, <i>A. C. Wilson and H. V. Cottony</i>	144

The Flight Evaluation of Aircraft Antennas, <i>George W. Leopard</i>	158
Reciprocity and Scattering by Certain Rough Surfaces, <i>W. S. Ament</i>	167
Backscattering from a Finite Cone, <i>Joseph B. Keller</i>	175
Optimum Radar Integration Time, <i>J. M. Flaherty and E. Kadak</i>	183
Power Spectra of Temperature, Humidity and Refractive Index from Aircraft and Tethered Balloon Measurements, <i>Earl E. Gossard</i>	186
Aircraft Scintillation Spectra, <i>Robert B. Muchmore</i>	201
Apparent Thermal Noise Temperatures in the Microwave Region, <i>Eric Weger</i>	213
Communications:	
Patterns of a Radial Dipole on an Infinite Circular Cylinder: Numerical Values, <i>Curt A. Levis</i>	218
Linear Arrays with Arbitrarily Distributed Elements, <i>H. Unz</i>	222
Synthesis of Nonseparable Two-Dimensional Patterns by Means of Planar Arrays, <i>A. Ksienski</i>	224
A Method to Reduce Antenna Ground Reflections, <i>David Sabih</i>	225
Impulse Excitation of a Conducting Medium, <i>J. Galejs</i>	227
Electromagnetic Transients in Conducting Media, <i>S. H. Zisk</i>	229
Contributors.....	231

Volume AP-8, Number 3, May, 1960

Editorial Comment.....	234
Propagation at 36,000 MC in the Los Angeles Basin, <i>W. L. Flock, R. C. Mackey, and W. D. Hershberger</i>	235
Two Statistical Models for Radar Terrain Return, <i>L. M. Spetner and I. Katz</i>	242
Radar Terrain Return Measured at Near-Vertical Incidence, <i>A. R. Edison, R. K. Moore, and B. D. Warner</i>	246
A New Mathematical Approach for Linear Array Analysis, <i>D. K. Cheng and M. T. Ma</i>	255
Log Periodic Dipole Arrays, <i>D. E. Isbell</i>	260
Beam Pointing Errors of Long Line Sources, <i>M. Leichter</i>	268
Mutual Impedance Effects in Large Beam Scanning Arrays, <i>P. S. Carter, Jr.</i>	276
Mutual Coupling Effects in Large Antenna Arrays: Part I—Slot Arrays, <i>S. Edelberg and A. A. Oliner</i>	286
Spiral Antennas, <i>W. L. Curtis</i>	298
Ground Constant Measurements Using a Section of Balanced Two-Wire Transmission Line, <i>E. J. Kirkscether</i>	307
The Archimedean Two-Wire Spiral Antenna, <i>J. A. Kaiser</i>	312
Coupled Leaky Waveguides I: Two Parallel Slits in a Plane, <i>S. Nishida</i>	323
Experimental Study of a Diffraction Reflector, <i>J. A. Provencher</i>	331
Communications:	
A Note on the Relation Between the "Exact" and "Simplified" Theories for EM Wave Propagation in Ionized Gases, <i>J. M. Anderson</i>	337
A Note on "Effects of Relatively Strong Fields on the Propagation of EM Waves Through a Hypersonically Produced Plasma," <i>J. M. Fiskin and W. B. Sisco</i>	338
A Reciprocity Theorem for Nonperiodic Fields, <i>G. Goubau</i>	339
Checking Design of Stepped Luneberg Lens, <i>H. F. Mathis</i>	342
A Note Concerning the Precise Measurements of Dipole Antenna Impedance, <i>S. Krevsky</i>	343
Fresnel Region Field Distributions of Circular Aperture Antennas, <i>Ming-Kuei Hu</i>	344
On the Beam Deviation Factor of a Parabolic Reflector, <i>Y. T. Lo</i>	347
Announcement of National Bureau of Standards Bibliography on Radio Propagation.....	349
Contributors.....	350

Volume AP-8, Number 4, July, 1960

Coupled Leaky Waveguides II: Two Parallel Slits in a Cylinder, <i>S. Nishida</i>	354
Mutual Coupling Effects in Large Antenna Arrays II: Compensation Effects, <i>S. Edelberg and A. A. Oliver</i>	360
Paraboloidal Reflector Patterns for Off-Axis Feed, <i>S. S. Sandler</i>	368
Unequally-Spaced, Broad-Band Antenna Arrays, <i>D. D. King, R. F. Packard, and R. K. Thomas</i>	380
Resonant Slots with Independent Control of Amplitude and Phase, <i>B. J. Maxum</i>	384
Mutual Coupling of Shunt Slots, <i>A. F. Kay and A. J. Simmons</i>	389
A Wide-Band Transverse-Slot Flush-Mounted Array, <i>E. M. T. Jones and J. K. Shimizu</i>	401
Relation Between a Class of Two-Dimensional and Three-Dimensional Diffraction Problems, <i>L. B. Felsen and S. N. Karp</i>	407
Forward Scatter From Rain, <i>L. H. Doherty and S. A. Stone</i> ..	414
Solution of a Reflection Problem by Means of a Transmission Line Analogy, <i>B. L. Jones and P. C. Patton</i>	418
Experimental Swept-Frequency Tropospheric Scatter Link, <i>W. E. Landauer</i>	423
Energy Density in Continuous Electromagnetic Media, <i>A. Tonning</i>	428

Communications:

Resonant Antenna Array with Tilted Beam, <i>E. M. Rutz</i>	435
Van Atta Reflector Array, <i>E. D. Sharp and M. A. Diab</i>	436
A Circular Loop Antenna with Nonuniform Current Distribution, <i>J. E. Lindsay, Jr.</i>	439
Pattern Synthesis Using Weighted Functions, <i>P. A. Bricout</i> ..	441
On the Excitation of Electromagnetic Surface Waves on a Curved Surface, <i>J. R. Wait</i>	445
Note on "The Excitation of Electromagnetic Surface Waves on a Curved Surface," <i>H. M. Barlow</i>	449
The Structure of HF Signals Revealed by an Oblique Incidence Sweep Frequency Sounder, <i>D. J. Doyle, E. D. DuCharme, and G. W. Jull</i>	449
Contributors.....	452

Volume AP-8, Number 5, September, 1960

Comparison of Experimental with Computed Tropospheric Refraction, <i>W. L. Anderson, N. J. Beyers, and R. J. Rainey</i> ...	456
The Flared Slot: A Moderately Directive Flush-Mounted Broad-Band Antenna, <i>J. W. Eberle, C. A. Levis, and D. McCoy</i>	461
Mathematical and Experimental Studies of a Wide-Band Vertically Polarized Antenna, <i>P. Foldes</i>	466
Maximally Flat and Quasi-Smooth Sector Beams, <i>A. Ksienski</i>	476
A Geometrical Optics Method of Pattern Synthesis for Linear Arrays, <i>Howard E. Shanks</i>	485
Gain Limitations of Large Antennas, <i>Robert C. Hansen</i>	490
Some Equivalences Between Equally and Unequally Spaced Arrays, <i>Sheldon S. Sandler</i>	496
The Efficiency of Launching Surface Waves on a Reactive Half Plane by an Arbitrary Antenna, <i>Julius Kane</i>	500
Surface-Wave Luneberg Lens Antennas, <i>C. H. Walter</i>	508
Correction to "Radiation Fields of Circular Loop Antennas by a Direct Integration Process," <i>E. J. Martin, Jr.</i>	515

Index to Authors

A
 Adachi, S.: Nov 534
 Altshuler, E.: Sep 526
 Ament, W. S.: Mar 167
 Anderson, J. M.: May 337
 Anderson, W. L.: Sep 456, Nov 603
 Arendt, P. R.: Jan 73

B
 Barlow, H. M.: July 449
 Bazer, J.: Nov 633
 Bell, R. L.: Nov 559
 Beyers, N. J.: Sep 456
 Bolgiano, L. P., Jr.: Jan 104

Brick, D. B.: Nov 599
 Bricout, P. A.: Jul 441
 Brown, A.: Nov 633
 Brueckmann, H.: Sep 523

C
 Carr, J. W.: Jan 7
 Carter, P. S.: May 276
 Cassidy, E. S.: Jan 1
 Cheng, D. K.: Jan 110, May 255
 Cole, J. E.: Nov 594
 Colin, L.: Jan 107
 Collin, R. E.: Jan 62
 Conda, A. M.: C Nov 638
 Cottony, H. V.: Mar 144

Communications:

Phenomenological Concepts in Beyond-the-Horizon Tropospheric Propagation, <i>B. J. Starkey</i>	516
The Magneto-Ionic Theory for Drifting Plasma, <i>H. Unz</i>	517
An Endfire Array Continuously Proximity-Coupled to a Two-Wire Line, <i>George R. Forbes</i>	518
Direction Finding in a Two-Component Field, <i>D. N. Travers and W. M. Sherrill</i>	520
Experimental Comparison of Image Line Radiators and Polyrod Antennas, <i>S. P. Schlesinger and A. Vigants</i>	521
Horn Antennas for HF Long-Range Communication, <i>H. Brueckmann and B. G. Hagaman</i>	523
The Measurement of Self and Mutual Impedances, <i>E. Altshuler</i>	526
An Island as a Natural Very-Low-Frequency Transmitting Antenna, <i>M. G. Morgan</i>	528
Contributors.....	531

Volume AP-8, Number 6, November, 1960

A Theoretical Analysis of Semi-Infinite Conical Antennas, <i>S. Adachi</i>	534
Electrical Performance of Rigid Ground Radomes, <i>W. Lavrench</i>	548
Near-Field Measurements on a Logarithmically Periodic Antenna, <i>R. L. Bell, C. T. Elfving, and R. E. Franks</i>	559
Distribution Functions for Monopulse Antenna Difference Patterns, <i>O. R. Price and R. F. Hyneman</i>	567
Radiation from a Tapered Surface Wave Antenna, <i>Leopold B. Felsen</i>	577
Near-Field Gain of Aperture Antennas, <i>A. F. Kay</i>	586
Measured Distribution of the Duration of Fades in Tropospheric Scatter Transmission, <i>K. F. Wright and J. E. Cole</i>	594
An Experimental Investigation of the Fock Approximation for Conducting Cylinders, <i>L. Wetzel and D. B. Brick</i>	599
Frequency Spectra of Transient Electromagnetic Pulses in a Conducting Medium, <i>W. L. Anderson and R. K. Moore</i>	603
Reflection Factor of Gradual-Transition Absorbers for Electromagnetic and Acoustic Waves, <i>Klaus Walther</i>	608
A New Sporadic Layer Providing VLF Propagation, <i>J. Ortner, A. Egeland, and B. Hultqvist</i>	621
Correction to "Pattern of an Antenna on a Curved Lossy Surface," <i>J. R. Wait and A. M. Conda</i>	628

Communications:

Gain of Tchebycheff Arrays, <i>Robert J. Stegan</i>	629
Comment on "Maximum Angular Accuracy of Tracking a Radio Star by Lobe Comparison," <i>Nicholas George</i>	632
Some Remarks on "Diffraction of Scalar Waves by a Circular Aperture," <i>A. E. Heins, J. Bazer, and A. Brown</i>	633
A Concise Formulation of Huygens' Principle for the Electromagnetic Field, <i>Chen To Tai</i>	634
Gain of Large Scanned Arrays, <i>M. J. King and R. K. Thomas</i>	635
Second-Mode Operation of the Spiral Antenna, <i>John R. Donnellan</i>	637
Contributors.....	638
Annual Index.....	Follows page 639

Curtis, W. L.: May 298

Elfving, C. T.: Nov 559

D
 Denton, D. H., Jr.: Jan 88
 Diab, M. A.: Jul 436
 Doherty, L. H.: Jul 414
 Donnellan, J. R.: Nov 637
 Doyle, D. J.: Jul 449
 DuCharme, E. D.: Jul 449

E
 Eberle, J. W.: Sep 461
 Edelberg, S.: May 286, Jul 360
 Edison, A. R.: May 246
 Egeland, A.: Nov 621

F
 Fainberg, J.: Jan 1
 Fay, W. J.: Jan 57
 Felsen, L. B.: Jul 407, Nov 577
 Fiskin, J. M.: Jan 102, May 338
 Flaherty, J. M.: Mar 183
 Flock, W. L.: May 235
 Foldes, P.: Sep 466
 Forbes, G. R.: Sep 518
 Franks, R. E.: Nov 559

G
 Galejs, J.: Mar 227

George, Nicholas: Nov 629
Gossard, E. E.: Mar 186
Goubau, G.: May 339

H

Hagaman, B. G.: Sep 523
Hansen, R. C.: Jan 23, Sep 490
Harrison, C. W., Jr.: Jan 88,
Mar 131
Heins, A. E.: Nov 633
Held, G.: Jan 91
Heritage, J. L.: Jan 57
Hershberger, W. D.: May 235
Holt, F. S.: Jan 77
Hu, M. K.: May 344
Hultqvist, B.: Nov 621
Hyneman, R. F.: Nov 567

I

Isbell, D. E.: May 260
Ishimaru, A.: Jan 91

J

Jones, B. L.: Jul 418
Jones, E. M. T.: Jul 401
Jull, G. W.: Jul 449

K

Kadak, E.: Mar 183
Kaiser, J. A.: May 312
Kane, J.: Sep 500
Karp, S. N.: Jul 407
Katz, I.: May 242

Kay, A. F.: Jul 389, Nov 586
Keller, J. B.: Mar 175
King, D. D.: Jul 380
King, M. J.: Nov 635
King, R.: Jan 88, Mar 131
King, R. W. P.: Mar 136
Kirkscether, E. J.: May 307
Krevsky, S.: May 343
Ksienski, A.: Mar 224, Sep 476

L

Landauer, W. E.: Jul 423
Lavrench, W.: Nov 548
Leichter, M.: May 268
Leopard, G. W.: Mar 158
Levis, C. A.: Mar 218, Sep 461
Lindsay, J. E., Jr.: Jul 439
Lo, Y. T.: May 347

M

Ma, M. T.: May 255
Mackey, R. C.: May 235
Manasse, R.: Jan 50
Martin, E. J., Jr.: Jan 105,
C Sep 515
Mathis, H. F.: May 342
Mayer, A.: Jan 77
Maxum, B. J.: Jul 384
McCoy, D.: Sep 461
Moore, R. K.: May 246, Nov
603
Morgan, M. G.: Sep 528
Muchmore, R. B.: Mar 201

Myers, J. J.: Jan 78

N

Nishida, S.: May 323, Jul 354

O

Oliner, A. A.: May 286, Jul 360
Ortner, J.: Nov 621
Owyang, G. H.: Mar 136

P

Packard, R. F.: Jul 380
Patton, P. C.: Jul 418
Price, O. R.: Nov 567
Provencher, J. A.: May 331

R

Raburn, L. E.: Jan 43
Railey, R. J.: Sep 456
Roberts, C. A.: Jan 102
Rutz, E. M.: Jul 435

S

Sabih, D.: Mar 225
Sandler, S. S.: Jul 368, Sep 496
Schlesinger, S. P.: Sep 521
Sengupta, D. L.: Jan 11
Seshadri, S. R.: Jan 27, Jan 37
Shanks, H. E.: Sep 485
Sharp, E. D.: Jul 436
Sherrill, W. M.: Sep 520
Shimizu, J. K.: Jul 401
Simmons, A. J.: Jul 389

Sisco, W. B.: Jan 102, May 338
Spetner, L. M.: May 242
Starkey, B. J.: Sep 516
Stone, S. A.: Jul 414

T

Tai, C. T.: Nov 634
Tang, R.: Jan 97
Taylor, T. T.: Jan 17
Thomas, R. K.: Jul 380, Nov 635
Tonning, A.: Jul 428
Travers, D. N.: Sep 520

U

Unz, H.: Mar 222, Sep 517

V

Vigants, A.: Sep 521

W

Wait, J. R.: Jul 445, C Nov 628
Walter, C. H.: Sep 508
Walther, K.: Nov 608
Warner, B. D.: May 246
Weger, E.: Mar 213
Weisbrod, S.: Jan 57, Jan 107
Welch, W. J.: Jan 68
Wetzel, L.: Nov 599
Wilson, A. C.: Mar 144
Wright, K. F.: Nov 594
Wu, T. T.: Jan 27, Jan 37

Z

Zisk, S. H.: Mar 229

Index to Subjects

A

Acoustic Waves, Gradual-Transition Absorbers for Electromagnetic and: Nov 608
Aircraft Antennas, Flight Evaluation of: Mar 158
Aircraft Measurements of Temperature, Humidity and Refractive Index: Mar 186
Aircraft Scintillation Spectra: Mar 201
Antennas:
Aircraft, Flight Evaluation of: Mar 158
Aperture, Circular, Fresnel Field of: May 344
Aperture, Circular, Taylor Distributions for: Jan 23
Aperture, Near-Field Gain of: Nov 586
Circular Loop: Jul 439
Commutation of Rotations: Jan 104
Comparison of Image Line Radiators and Polyrod: Sep 521
Corner-Reflector, Radiation Patterns of: Mar 144
Coupled Folded: Mar 131
Dipole Impedance Measurements: May 343
Gain Limitations of Large, Sep 490
Horn, for HF Long-Range Communication: Sep 523
Image Quality Evaluation: Jan 78
Island as a Natural VLF Antenna: Sep 528
Missile Transmission-Line: Jan 88
Monopulse Difference Patterns: Nov 567
Near-Field Measurements on Logarithmically Periodic: Nov 559
Radiation Fields of Circular Loop: Jan 105
Radiation Fields of Circular Loop, Correction: Sep 515
Semi-Infinite Conical: Nov 534
Slot, with Coupled Dipoles: Mar 136

Spiral: May 298

Spiral, Archimedean Two-Wire: May 312

Spiral, Second-Mode Operation: Nov 637

Surface Wave, Tapered, Radiation from: Nov 577

Wide-Band Vertically Polarized: Sep. 466

Yagi, Uniform and Linearly Tapered: Jan 11

Aperture, Circular, Diffraction by a: Jan 27
Apertures, Circular, for Narrow Beamwidth: Jan 17

Aperture, Circular, Taylor Distributions for: Jan 23

Argus Experiment, Frequency Scintillations of Satellite Signals Before and After: Jan 73

Arrays:

Endfire, Coupled to a Two-Wire Line: Sep 518

Equivalences Between Equally and Unequally Spaced: Sep 496

Gain of Large Scanned: Nov 635

Gain of Tchebycheff: Nov 629

Linear Analysis: May 255

Log Periodic Dipole: May 260

Mutual Coupling Effects in Large Antenna: May 286, Jul 360

Mutual Impedance Effects in Large Beam Scanning: May 276

Transverse-Slot Flush-Mounted: Jul 401

Unequally-Spaced, Broad-Band Antenna: Jul 380

Van Atta Reflector: Jul 436

with Arbitrarily Distributed Elements, Linear: Mar 222

with Tilted Beam, Resonant Antenna: Jul 435

B

Beam Pointing Errors of Long Line Sources: May 268

Beams, Sector, Maximally Flat and Quasi-Smooth: Sep 476

Beyond-the-Horizon Tropospheric Propagation, Phenomenological Concepts in: Sep 516

C

Commutation of Antenna Rotations: Jan 104

Corner-Reflector Antennas, Radiation Patterns of: Mar 144

D

Diffraction:

by a Circular Aperture: Jan 27

by an Infinite Slit for Grazing Incidence: Jan 37

of Scalar Waves by a Circular Aperture: Nov 633

Problems, Two and Three-Dimensional: Jul 407

Reflector, Experimental Study of: May 331

Dipole Antenna Impedance, Measurements of: May 343

Dipole Arrays, Log Periodic: May 260

Dipole, Radial, on an Infinite Circular Cylinder: Mar 218

Direction Finding in a Two-Component Field: Sep 520

E

Electromagnetic:

and Acoustic Waves, Gradual-Transition Absorbers for: Nov 608

Fields, Reciprocity Theorems for: Jan 68

Media, Energy Density in Continuous: Jul 428
 Transients in Conducting Media: Mar 229
 Electron Densities Behind Hypersonic Shock Waves: Jan 102
 Energy Density in Continuous Electromagnetic Media: Jul 428

F

Fields, Reciprocity Theorem for Nonperiodic: May 339
 Fock Approximation for Conducting Cylinders: Nov 599
 Fresnel Field of Circular Aperture Antennas: May 344

G

Geometrical Optics Method of Radiation Pattern Synthesis: Sep 490
 Ground Constant Measurements: May 307

H

Horn Antennas for HF Long-Range Communication: Sep 523
 Humidity, Aircraft Measurements of: Mar 186
 Huygen's Principle for the Electromagnetic Field: Nov 634

I

Impedances, Measurement of Self and Mutual: Sep 526
 Impulse Excitation of a Conducting Medium: Mar 227
 Ionized Gases, Propagation in: May 337
 Island as a Natural VLF Transmitting Antenna: Sep 528

L

Lenses:
 Dielectric Microwave of Large Aperture Ratio, Correction to: Jan 77
 Luneberg, Modified for Defocused Source: Jan 110
 Luneberg, Stepped, Checking Design of: May 342
 Luneberg, Surface-Wave Antennas: Sep 508
 Log Periodic Dipole Arrays: May 260
 Logarithmically Periodic Antenna, Near-Field Measurements on: Nov 559
 Luneberg Lens, Modified for Defocused Source: Jan 110
 Luneberg Lens, Stepped, Checking Design of: May 342
 Luneberg Lens, Surface-Wave Antennas: Sep 508

M

Magneto-Ionic Theory for Drifting Plasma: Sep 517
 Meteor Echoes at 200 MC: Jan 57
 Missile Antennas, Transmission-Line: Jan 88
 Monopulse Antenna Difference Patterns: Nov 567

N

Noise Temperatures in the Microwave Region, Thermal: Mar 213

P

Parabolic Reflector, Beam Deviation Factor of: May 347

AP TRANSACTIONS INDEX—4

Paraboloidal Reflector Patterns for Off-Axis Feed: Jul 368
 Plasma, Magneto-Ionic Theory for Drifting: Sep 517
 Plasma, Propagation Through a Hypersonically Produced: May 338
 Propagation:
 at 36,000 MC in Los Angeles Basin: May 235
 in Ionized Gases: May 337
 Through a Hypersonically Produced Plasma: May 338
 VLF, New Sporadic Layer: Nov 621

R

Radar:
 Integration Time, Optimum: Mar 183
 Target, Multipurpose: Jan 7
 Terrain Return Measured at Near-Vertical Incidence: May 246
 Terrain Return, Statistical Models for: May 242

Radiation:

Fields of Circular Loop Antennas: Jan 105
 Fields of Circular Loop Antennas, Correction to: Sep 515
 from a Tapered Surface Wave Antenna: Nov 577
 Pattern of an Antenna on a Curved Lossy Surface, Correction to: Nov 628
 Pattern Synthesis: Jan 91
 Pattern Synthesis, Geometrical Optics Method of: Sep 485
 Pattern Synthesis Using Weighted Functions: Jul 441
 Patterns, Synthesis of Two-Dimensional: Mar 224
 Reflector Antenna, Polarized: Jan 43

Radio Star Tracking by Lobe Comparison, Accuracy of: Jan 50
 Radio Star Tracking by Lobe Comparison, Accuracy of: Nov 632
 Radomes, Electrical Performance of: Nov 548
 Rain, Forward Scatter From: Jul 414
 Reciprocity Theorems for Electromagnetic Fields: Jan 68
 Reciprocity Theorem for Nonperiodic Fields: May 339
 Reflection, Antenna ground, Reducing: May 225
 Reflection Problem Solution by Transmission Line Analogy: Jul 418
 Reflector:
 Antenna Polarized Radiation: Jan 43
 Beam Deviation Factor of a Parabolic: May 347
 Experimental Study of a Diffraction: May 331
 Patterns for Off-Axis Feed, Paraboloidal: July 368
 Refraction of VHF Signals at Ionospheric Heights: Jan 107
 Refraction, Tropospheric: Sep 456
 Refractive Index, Aircraft Measurements of: Mar 186

S

Satellite Signals Before and After the Argus Experiment: Jan 73
 Scanned Arrays, Gain of Large: Nov 635
 Scanning Arrays, Mutual Impedance Effects in Large Beam: May 276

Scatter Propagation, Duration of Fades in Tropospheric: Nov 594
 Scatter Propagation, Swept-Frequency Tropospheric Link: Jul 423
 Scattering of Waves:
 Back Scatter, Cross Sections of Cylindrical Wires: Jan 1
 Back Scatter, From a Finite Cone: Mar 175
 By Rough Surfaces: Mar 167
 By Thin Dielectric Sheets: Jan 62
 Forward Scatter from Rain: Jul 414
 Scintillation Spectra, Aircraft: Mar 201
 Shock Waves, Electron Densities Behind Hypersonic: Jan 102
 Slots:

 Antenna with Coupled Dipoles: Mar 136
 Flared: Sep 461
 Flush-Mounted Array, Transverse: Jul 401
 Mutual Coupling of Shunt: Jul 389
 Resonant, with Independent Control of Amplitude and Phase: Jul 384
 with Variable Coupling: Jan 97
 Spiral Antennas, Archimedean Two-Wire: May 312
 Spiral Antennas: May 298
 Spiral Antennas, Second-Mode Operation of the: Nov 637
 Surface Waves:
 Antenna, Radiation from a Tapered: Nov 577
 Efficiency of Launching: Sep 500
 Excitation on a Curved Surface: Jul 445
 Excitation on a Curved Surface: Jul 449
 Luneberg Lens Antennas: Sep 508
 Sweep Frequency Sounder, Structure of HF Signals Revealed by: Jul 449

T

Taylor Distributions for Circular Aperture Antennas: Jan 23
 Tchebycheff Arrays, Gain of: Nov 629
 Temperature, Aircraft Measurements of: Mar 186
 Thermal Noise Temperatures in the Microwave Region: Mar 213
 Tracking a Radio Star by Lobe Comparison, Accuracy of: Jan 50
 Tracking a Radio Star by Lobe Comparison, Accuracy of, Comment on: 632
 Transient Pulses in a Conducting Medium, Frequency Spectra of: Nov 603
 Transients in Conducting Media, Electromagnetic: Mar 229
 Transmission-Line Missile Antennas: Jan 88
 Tropospheric Refraction: Sep 456
 Tropospheric Scatter Link, Swept-Frequency: Jul 423

V

Van Atta Reflector Array: Jul 436
 VLF Propagation, New Sporadic Layer Providing: Nov 621
 VLF Transmitting Antenna, Island as a Natural: Sep 528

W

Waveguides, Coupled Leaky: May 323, Jul 354

Y

Yagi Antennas, Uniform and Linearly Tapered: Jan 11

INSTITUTIONAL LISTINGS

The IRE Professional Group on Antennas and Propagation is grateful for the assistance given by the firms listed below, and invites application for Institutional Listing from other firms interested in the field of Antennas and Propagation.

AERO GEO ASTRO CORP., 1200 Duke St., Alexandria, Va.

Research and Development; Antennas; Transponders; Command Receivers; Augmenters; Telemetry-Radar.

ANDREW CORPORATION, P.O. Box 807, Chicago 42, Ill.

Antennas, Antenna Systems, Transmission Lines, Development and Production.

ANTLAB, INC., 6330 Proprietors Rd., Worthington, Ohio

Antenna Pattern Range Systems—Recorders & Mounts, & Telemetry Servo Pedestals.

BLAINE ELECTRONETICS, INC., 14757 Keswick St., Van Nuys, Calif.

Antennas, Paraboloids, Scale Models, Antenna Radiation Pattern Measurement Towers.

DEVELOPMENTAL ENGINEERING CORP., Leesburg, Va.; Boston, Mass.; Boulder, Colo.; Washington, D.C.

Antenna Research, Design & Evaluation-Propagation Studies & Communications Systems Engineering

GABRIEL ELECTRONICS, Division of The Gabriel Company, Main & Pleasant Sts., Millis, Mass.

Research, Engineering and Manufacture of Antenna Equipment for Government and Industry.

HUGHES AIRCRAFT COMPANY, Florence and Teale Sts., Culver City, Calif.

Res., Dev., Mfg.: Radar Systems & Components; Antennas, Tubes, Radomes, Solid-State Devices.

I-T-E CIRCUIT BREAKER CO., Special Products Div., 601 E. Erie Ave., Philadelphia 34, Pa.

Design, Development and Manufacture of Antennas, and Related Equipment.

JANSKY & BAILEY, INC., An Affiliate of Atlantic Research Corp.,

1339 Wisconsin Ave., N.W., Washington, D. C.

Complete Engineering Services for Antennas and Propagation Programs.

MARK PRODUCTS CO., 5439 W. Fargo Ave., Skokie, Ill.

Antennas for Two-Way Communications, Grid Parabolas, Research & Development.

TECHNICAL APPLIANCE CORP., 1 Taco St., Sherburne, N. Y.

Des., Dev., & Mfg.: Antennas & Antenna Systems for Communications, Telemetry, & Tracking.

WEINSCHEL ENGINEERING COMPANY, INC., Kensington, Md.

Antenna Pattern Receivers; Bolometer Amplifiers; Modulated Microwave Sources;
Insertion Loss Measuring Systems.

WHEELER LABORATORIES, INC., Great Neck, N. Y.; Antenna Lab., Smithtown, N. Y.

Consulting Services, Research and Development, Microwave Antennas and Waveguide Components.

The charge for Institutional Listing is \$25 for one issue or \$100 for six consecutive issues (one year). Application may be made to the Technical Secretary, The Institute of Radio Engineers, Inc., 1 East 79 Street, New York 21, N. Y.